The Development of a Flexible Rotor Active Magnetic Bearing System

---

A dissertation presented to

The School of Electrical and Electronic Engineering

North-West University

In partial fulfilment of the requirements for the degree

Magister Ingeneriae

in Electrical and Electronic Engineering

by

Eugén O. Ranft

Supervisor: Prof. G. van Schoor

May 2005

Potchefstroom Campus

SUMMARY

The School of Electrical and Electronic Engineering at the North-West University is in the process of developing an Active Magnetic Bearing (AMB) research laboratory. The aim is to establish a knowledge base on AMBs in support of industries that make use of this environmentally friendly technology. AMB technology is seen as one of the technology drivers for the Pebble Bed Modular Reactor (PBMR) currently in development in South Africa and is predicted to become largely conventional in this application.

In the process of developing an AMB laboratory some basic models are constructed to establish infrastructure for research investigations. The aim of this project is to develop a flexible rotor double radial AMB system. The system comprises a laminated heteropolar magnetic actuator, eddy-current position sensors, switch-mode power amplifiers and a digital controller. Emphasis is placed on stable suspension of a flexible rotor through the first three critical frequencies. This project also caters for future work on high speed losses in AMB systems.

A design process comprising aspects of modelling and analysis is developed, implemented and verified for a flexible rotor AMB system. The design commences with a system specification followed by an iterative process comprising electromagnetic design, detailed system modelling and rotordynamic analysis, and is concluded with design implementation and verification.

The system design includes two interchangeable rotors; a flexible rotor for rotordynamic analyses and a rigid rotor for high speed loss analyses. The flexible rotor system is specified to experience the first three critical frequencies up to an operating speed of 10,000 rpm. The rigid rotor maximum operating speed is specified as 30,000 rpm. Rotor stability at critical frequencies places specific constraints on the equivalent stiffness and damping parameters of the AMB.

An iterative design process is then initiated by an analytical electromagnetic design of the radial AMBs conducted in MathCAD®. The magnetic actuator utilizes a 0.6 mm air gap and has a maximum load capacity of 500 N. A force slew rate specification of 5×10^6 N/s is obtained from the system's equivalent stiffness (500 N/mm) and damping (2.5 N.s/mm) parameters resulting in a 3 kVA power amplifier requirement. These parameters are used in the detailed MATLAB® modelling of the system. Stiffness and damping parameters as well as system dynamic response are verified and used to design a flexible rotor. The magnetic bearing locations, displacement sensor locations and rotordynamic response are verified using finite element

methods. The design of the rotor stands central to the iterative design process since it impacts on the forces experienced by the AMBs as well as the critical frequencies of the AMB system.

The most important outcome of the iterative design process is a dimensioned electromagnetic configuration and two rotor designs. The flexible rotor spans 500 mm and weighs 7.72 kg whereas the rigid rotor has the same length and weighs 12.5 kg. A centre mass on the flexible rotor lowers the first three critical frequencies to below the maximum operating speed.

A 3 kVA (300 V, 10 A) switch-mode, current controlled power amplifier (PA) is developed in-house as part of the outcome of the study. The topology used is a two-quadrant controlled H-bridge, switched at 100 kHz and controlled in current-mode. The design is thoroughly verified through a process of prototyping and includes aspects of electromagnetic compatibility and protection in terms of over-current and temperature. The PA exhibits a 6 kHz bandwidth and linear characteristics and plays a critical role in the AMB system performance.

The AMB controller is realised with a dSPACE® real-time development tool (DS1104), located inside a personal computer (PC). The rotational speed is monitored with an optical speed sensor while the shaft is propelled via an air turbine unit.

Once constructed the actual AMB stiffness and damping parameters as well as its dynamic response are obtained. Discrepancies between the analytically predicted, simulated and experimentally obtained results are addressed and clarified. The sensitivity of the system to parameter changes is obtained as a measure of marginal stability. The rotordynamic response is characterised by measuring the rotor displacement at pre-defined locations as the rotor traverses the critical frequencies. These results show good correlation with the predicted rotordynamics.

This study emphasises the importance of extensive modelling and analyses in the design of AMB systems to guarantee the required performance of the end product in terms of its dynamic performance and stability. The most important outcome of this project is a working high speed AMB model complete with integrated control. The system is versatile and allows for a variety of investigations including advanced control investigations and high speed magnetic bearing loss analyses. This project uniquely contributes to the research currently underway in the field of AMBs in the School of Electrical and Electronic Engineering.

OPSOMMING

Die Skool vir Elektriese en Elektroniese Ingenieurswese by die Noordwes Universiteit is in die proses om 'n Aktiewe Magnetiese Laer (AML) laboratorium te ontwikkel. Die doel is om kundigheid te vestig in die veld van AMLs ter ondersteuning van industrieë wat van hierdie omgewingsvriendelike tegnologie gebruik maak. AML tegnologie word gesien as een van die tegnologiedrywers vir die Korrelbed Modulêre Reaktor wat tans in Suid Afrika ontwikkel word en is voorspel om algemeen in die toepassing te word.

In die AML laboratorium ontwikkelingsproses word basiese modelle gebou om infrastruktuur te skep vir navorsingsondersoeke. Die doel van hierdie projek is om 'n buigbare rotor dubbel-radiale AML stelsel te ontwikkel. Die stelsel behels 'n gelamineerde heteropolêre magnetiese aktueerder, werwelstroom posisiesensors, skakelmodus kragversterkers en 'n digitale beheerder. Klem word geplaas op stabiele suspensie van 'n buigbare rotor deur die eerste drie kritiese frekwensies. Die projek maak ook voorsiening vir toekomstige werk op hoëspoed verliese in AML stelsels.

'n Ontwerpsproses wat aspekte van modellering en analise insluit word ontwikkel, geïmplementeer en geverifieer vir 'n buigbare rotor AML stelsel. Die ontwerp word begin met 'n stelselspesifikasie en vervolg met 'n iteratiewe proses bestaande uit 'n elektromagnetiese ontwerp, gedetailleerde stelselmodellering en rotordinamiese analise. Die ontwerp word afgesluit met ontwerpsimplementering en verifikasie.

Die stelselontwerp sluit twee omruilbare rotors in; 'n buigbare rotor vir rotordinamiese analises en 'n rigiede rotor vir hoëspoed verliesanalises. Die buigbare rotor stelsel word gespesifiseer om die eerste drie kritiese frekwensies tot en met 10,000 opm te ondervind. Die rigiede rotor se maksimum bedryfspoed word gespesifiseer as 30,000 opm. Rotorstabiliteit by die kritiese frekwensies plaas spesifieke beperkings op die ekwivalente styfheid en dempingparameters van die AML.

Die iteratiewe ontwerpsproses word geïnisieer deur 'n analitiese elektromagnetiese ontwerp van die radiale AMLs in MathCAD®. Die magnetiese aktueerder maak gebruik van 'n 0.6 mm luggaping en het 'n maksimum drakrag van 500 N. 'n Krag sloerheidspesifikasie van $5x10^6$ N/s word verkry vanaf die ekwivalente styfheid- (500 N/mm) en demping- (2.5 N.s/mm) parameters en lei tot 'n 3 kVA kragversterkervereiste. Hierdie parameters word gebruik in die gedetailleerde

MATLAB®-modellering van die stelsel. Die styfheid- en dempingparmeters asook die dinamiese gedrag van die stelsel word geverifieer en gebruik om die buigbare rotor te ontwerp. Die plasing van die AMLs en die posisiesensors asook die rotordinamiese gedrag word deur eindige element metodes geverifieer. Die rotorontwerp staan sentraal tot die iteratiewe ontwerpsproses aangesien dit die kragte wat die AMLs ondervind asook die kritiese frekwensies van die AML stelsel bepaal

Die belangrikste uitkoms van die iteratiewe ontwerpsproses is 'n gedimensioneerde elektromagnetiese opstelling en twee rotorontwerpe. Die buigbare rotor span 500 mm en weeg 7.72 kg terwyl die rigiede rotor dieselfde lengte is, maar 12.5 kg weeg. 'n Sentermassa op die buigbare rotor verlaag die eerste drie kritiese frekwensies tot onder die maksimum bedryfspoed.

'n 3 kVA, skakelmodus, stroombeheerde kragversterker word in-huis ontwikkel as deel van die studie se uitkoms. 'n Tweekwadrant-beheerde H-brug konfigurasie wat teen 100 kHz geskakel word en in stroommodus beheer word, word gebruik. Die ontwerp is deeglik geverifieer deur 'n proses van prototipering en bevat aspekte van elektromagnetiese versoenbaarheid en beskerming in terme van oor-stroom en temperatuur. Die kragversterker toon 'n wye liniêre bereik met 'n bandwydte van 6 kHz en speel 'n kritiese rol in die gedrag van die AML stelsel.

Die AML beheerder word geïmplementeer met dSPACE® intydse ontwikkelingsgereedskap (DS1104) in 'n persoonlike rekenaar. Die rotasiespoed word deur middel van 'n optiese sensor gemonitor en die as word deur 'n lugdrukturbine aangedryf.

Na konstruksie word die fisiese AML model se styfheid- en dempingparameters asook die dinamiese gedrag van die stelsel opgemeet. Afwykings tussen die analitiese, gesimuleerde en eksperimentele resultate word aangespreek en uitgeklaar. Die sensitiwiteit van die stelsel vir parameterveranderinge word ook bepaal as 'n maat van marginale stabiliteit. Die rotordinamiese gedrag word gekarakteriseer deur die rotorverplasing op voorafbepaalde posisies te monitor soos die rotor deur die kritiese frekwensies gaan.

Die studie beklemtoon die belangrikheid van uitgebreide modellering en analise in die ontwerp van AMLs om die verlangde gedrag in terme van dinamiese gedrag en stabiliteit te waarborg. Die belangrikste uitkoms van die projek is 'n werkende hoëspoed AML model kompleet met geïntegreerde beheer. Die stelsel is meerdoelig en laat 'n verskeidenheid van ondersoeke toe wat gevorderde beheertoepassings en hoëspoed verliesanalises insluit. Hierdie projek dra uniek by tot die navorsing op AMLs tans onderweg in die Skool vir Elektriese en Elektroniese Ingenieurswese.

ACKNOWLEDGEMENTS

I would like to firstly thank M-Tech Industrial and THRIP for funding this research and granting me the opportunity to further my studies.

I would also like to acknowledge the following people, in no particular order, for their contributions during the course of this project.

- Professor George van Schoor, my supervisor, for his guidance, advice and support that stood central to the success of this project.
- J. Roberts for his work on the rotordynamics and mechanical design.
- Instrument Manufacturers at North-West University and ALSTOM for the manufacturing of the model hardware.
- My fiancé, Desré Lindeque, for her love, support and understanding.
- My father Louis Ranft for his help, advice and support.
- My family for their love and loyalty.
- My friends, Zebedee, Hannes and André

"The Lord God is my Strength, and he will give me the speed of a deer and bring me safely over the mountains." Habakkuk 3:19

TABLE OF CONTENTS

NOMENCLATURE

LIST OF FIGURES

LIST OF TABLES

LIST OF ABBREVIATIONS

ac	Alternating current
ADC	Analogue to digital converter
AMB	Active Magnetic Bearing
CAD	Computer Aided Design
DAC	Digital to analogue converter
dc	Direct current
EM	Electromagnetic
EMC	Electromagnetic Compatibility
EMI	Electromagnetic Interference
FEM	Finite Element Method
IC	Integrated circuit
IGBT	Insulated-gate bipolar transistor
MGD	MOS-gate driver
MMF	Magneto Motive Force
MOSFET	Metal-oxide semiconductor field-effect transistor
PA	Power Amplifier
PBMR	Pebble Bed Modular Reactor
PC	Personal Computer
PCB	Printed Circuit Board
PWM	Pulse Width Modulation
rms	Root mean square
rpm	Revolutions per minute

LIST OF SYMBOLS

A_g	Air gap area
B	Magnetic flux density
b_{eq}	Equivalent damping
C	Capacitance
d	Duty cycle
E	Electrical energy
F, F_m	Electromagnetic force
g, g_0	Air gap length
$G_s(s)$	System open loop transfer function
H	Magnetic field intensity
I	rms / dc value of current
i	Instantaneous current
i, i_0, i_m	Control, bias and electromagnet currents respectively
K_D	Differential gain of the PD controller
k_{eq}	Equivalent position stiffness
k_i	Force-current factor
k_m	Electromagnet constants
K_P	Proportional gain of the PD controller
k_s	Force-displacement factor
ℓ	Magnetic path length
L_c	Coil inductance
m	Suspended body mass / current slope
N	Number of coil turns
P	Electrical power
$P.O.$	Percentage overshoot
Q	Electrical charge / thermal power
R	Electrical resistance
R_{coil}	Coil resistance
R_θ	Thermal resistance
S	Apparent power
s	Complex frequency
T	Temperature
t_{rr}	Reverse recovery time
T_s	Settling time

V	rms / dc value of voltage
v	Instantaneous voltage
x, x_0, x_s	Rotor position
ω	Rotational speed
ω_n	Natural frequency
ζ	Damping factor
Φ	Magnetic flux
θ	The stator pole pitch

1 Chapter

Introduction

This chapter provides introductory information on the pebble bed modular reactor and active magnetic bearings in general. The problem statement is supplied and followed by the issues to be addressed and the methodology. A concise overview of the document is also presented.

1.1 Background

The School of Electrical and Electronic Engineering at the North-West University is in the process of developing an Active Magnetic Bearing (AMB) research laboratory. The aim is to establish a knowledge base on AMBs in support of industries that make use of this environmentally friendly technology. AMB technology is seen as one of the technology drivers for the Pebble Bed Modular Reactor (PBMR) currently in development in South Africa and is predicted to become largely conventional in this application.

1.1.1 The Pebble Bed Modular Reactor

The Pebble Bed Modular Reactor (PBMR) is a South-African initiated project with international partners involving a closed cycle (Brayton-cycle) based nuclear power generation plant. The inherent safety and modularity of the design renders it an ideal alternative to meet the future energy needs of not only South-Africa, but the world in general. Part of the New Partnership for Africa's Development (NEPAD) initiative would be to electrify Africa. The PBMR technology lends itself to the modular electrification of Africa, supplying energy where needed.

The primary objective of the PBMR is to achieve a plant that has no physical process that could cause a radiation hazard beyond the plant site boundary. Producing approximately 110 MW of electrical power the PBMR module is the smallest standalone component of the PBMR power generation system. The module can produce power in a standalone mode, or as part of a power plant that consists of up to ten units [1].

The system will make use of helium in the closed loop gas cycle to transfer the heat from the nuclear fusion elements to the power turbine. Since helium is both chemically and radiologically inert, nuclear contamination to the plant and environment is prevented [2]. Other possible sources of nuclear contamination are oil or dust within the gas cycle. Oil film bearings pose a risk since the lubricant becomes a gas at the working temperature causing contamination of the plant. To overcome this problem magnetic bearings, which require no lubrication, are used. Figure 1-1 displays a schematic diagram of the PBMR system layout implementing a Brayton cycle.

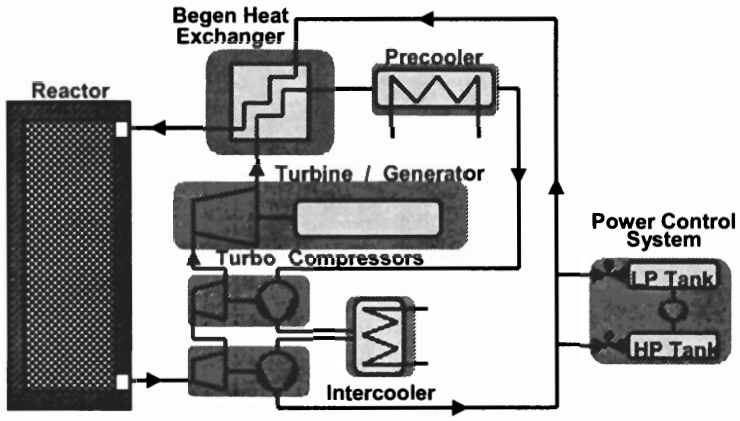

Figure 1-1: PBMR System Layout [1]

In the Brayton cycle helium gas is heated in the reactor and circulates through turbines, compressors and heat exchangers to generate electrical power.

1.1.2 Active Magnetic Bearings

Initially active magnetic bearings (AMBs) were designed to overcome limitations posed by conventional bearings. Their ability to work in vacuum with no lubrication and contamination, or to run at high speed, rendered AMBs the preferred option in research laboratories. Since the introduction of AMBs to industry their application has grown extensively.

AMBs have a number of novel qualities rendering them invaluable machine components in the modern day industry [3]. Their ability to suspend a rotor without mechanical contact results in a no wear and no lubrication configuration. This renders the AMB an environmentally friendly technology that results in the reduction of machine maintenance and waist associated with the replacement of lubrication and bearings [4].

Historically there are two types of machinery which were outfitted with AMBs on a commercial basis:

- Equipment under the category of turbomachinery, including centrifugal compressors, turbo-expanders and turbines, among others and
- Turbomolecular pumps, such as those used in the semiconductor industry to create ultra high vacuum environments.

With advances in the semiconductor industry, digital controller industry and magnetic materials, AMBs are more compact less expensive and even more reliable.

Figure 1-2 displays a functional diagram of an AMB system. A position sensor monitors the rotor displacement and supplies the information to the controller which generates an appropriate control signal. A power amplifier converts the control signal to a power signal which drives the electromagnetic actuator. The actuator in turn exerts a force on the rotor to correct the displacement.

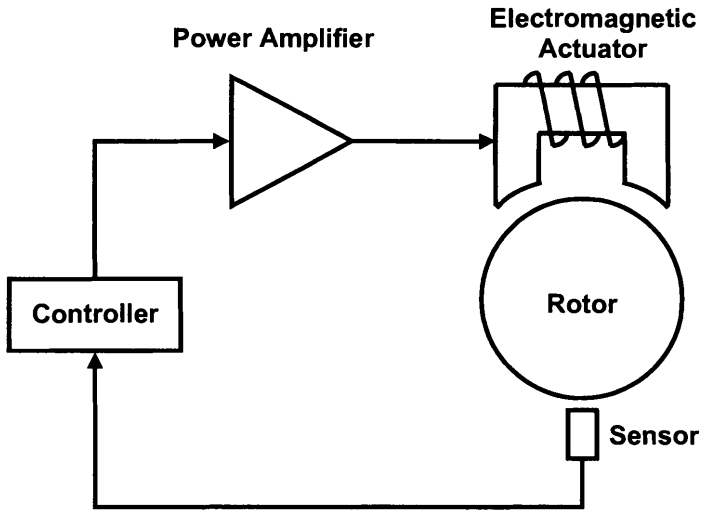

Figure 1-2 AMB functional diagram

1.2 Problem statement

The purpose of this project is the development of a double radial, flexible rotor active magnetic bearing model. Emphasis is placed on the stable suspension of a flexible rotor through the first three critical frequencies. A second (rigid) rotor must be easily interchangeable and will allow for high speed loss analyses. A switch-mode power amplifier will be used to enable future self-sensing investigations. A detailed design process, considering high speed limitations as well as

rotordynamics, will be developed. Flexible rotordynamics are also analysed and play a fundamental role in the design specifications.

The double radial AMB model will not only enable research on complex control strategies but may also facilitate future work on high speed losses. This will greatly contribute to the research currently under way on AMBs in the School of Electrical and Electronic Engineering. Figure 1-3 displays a basic drawing of the proposed heteropolar model that will be developed. This model comprises two heteropolar radial AMBs, one on each end of a flexible shaft. A lumped mass on the centre of the shaft will serve as an air pressure turbine and will also lower the critical frequencies.

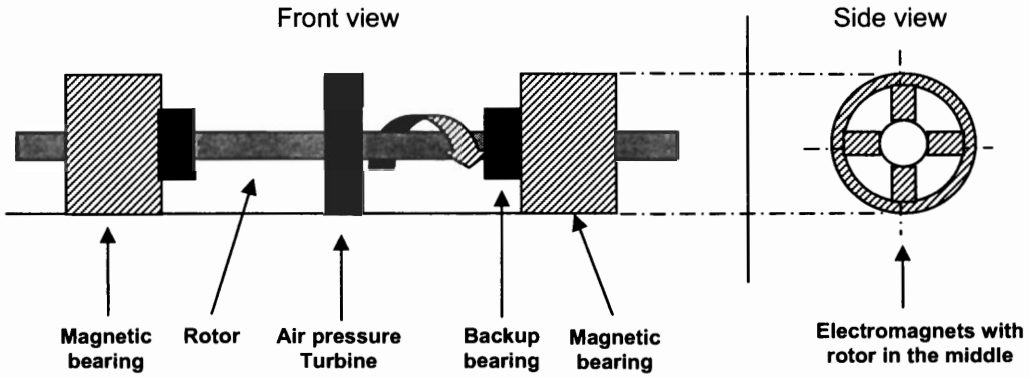

Figure 1-3: Simplified heteropolar radial AMB system

1.3 Issues to be addressed and methodology

This high speed AMB system can be divided into four main components, each with its own sub-systems, constraints and design considerations. Figure 1-4 displays a system diagram, with the different components and their interconnection. The system comprises a controller, power amplifiers, the physical model and position sensors. The position sensors generate signals representative of the rotor position. These signals are fed to the controller which generates appropriate current reference signals. The power amplifiers convert the current reference signals to currents through the electromagnets. The electromagnets then generate appropriate forces to suspend the rotor in the desired position.

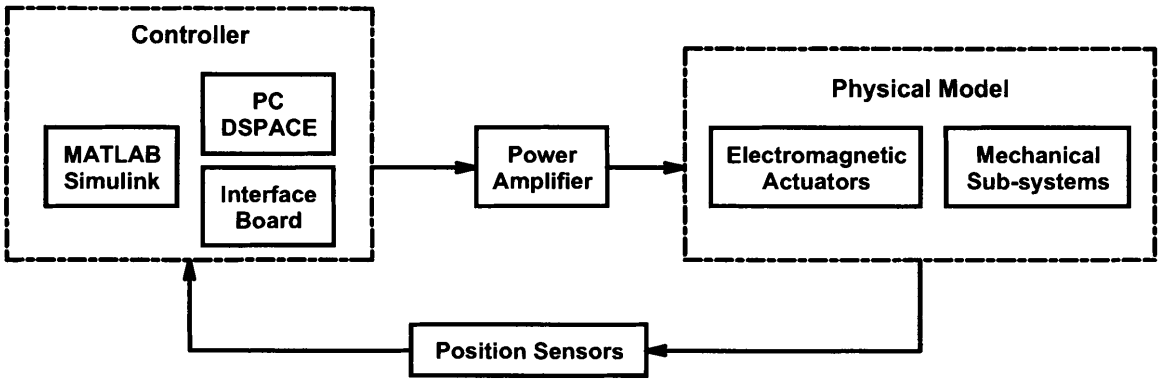

Figure 1-4: Basic AMB system diagram

1.3.1 Design process

In order to design the elaborate system depicted in Figure 1-4, a comprehensive design process is essential. This multi-discipline system comprising two radial magnetic bearings, a four degree of freedom controller, sensors and power amplifiers, require extensive modelling and detailed planning to ensure component compatibility and model functionality.

1.3.2 System specification

The first step in developing an AMB system is to generate a detailed system specification addressing all the relevant requirements. System parameters which include maximum rotational speed, shaft characteristics and mechanical layout will be specified and used as a point of departure for the system design. The purpose and future use of the model also places constraints on the system which influences the specifications.

1.3.3 Electromagnetic design

The electromagnetic design is initiated by stipulating certain design choices and performance requirements. One such a design choice is selecting a specific electromagnetic configuration. There are two topologies to choose from, heteropolar or homopolar (refer to section 2.2.1) each with its own advantages and disadvantages. Once the topology is selected the amplifier specification is compiled from the performance requirements. This is followed by the journal sizing, stator design and control parameters design.

1.3.4 System modelling

An accurate simulation model of the complete system must be developed from the physical model design parameters. The simulation forms an integral part of the design process and will be used to confirm the design and verify analytical predictions. Parameters for the controller, sensor and power amplifier will be verified with the detailed system simulation.

1.3.5 Rotor design and dynamic analysis

In order to design a flexible rotor AMB system to experience three critical frequencies of which the third is the first bending mode, a detailed rotordynamic analysis is needed. The maximum electromagnetic carrying force, stiffness and damping parameters as well as bearing position is determined by the rotordynamic analyses. The dynamic characteristics of the rotor and bearing combination must be designed to ensure no-mechanical-contact between rotating and stationary parts, due to rotor vibrations.

1.3.6 Design implementation

Design implementation comprises detailed mechanical design incorporating all system components into a functional and aesthetically pleasing model. The physical model will be designed using CADKEY®, a computer aided design (CAD) software package. Detailed manufacturing drawings of the different sub-systems will be compiled from which the model will be constructed.

1.3.7 Power amplifier development

While the physical model is in construction a switch mode power amplifier (PA) will be developed according to specifications obtained from the electromagnetic design. The development process will entail a prototype amplifier followed by a printed circuit board (PCB) prototype and then the final design PCB version. The PA plays an integral role in the AMB system and great care will be taken to develop a high bandwidth amplifier with wide range and exceptional linearity.

1.3.8 System Integration

After the development of a physical model, the design and implementation of a controller, amplifier and sensor, the different components must be integrated into a fully functional model. In order to successfully integrate the system the following two issues must be addressed:

dSPACE®

dSPACE® is a real-time control software package which will be used to implement the control system. The program along with its real-time development card is installed in a standard personal computer with a Windows XP operating system. The dSPACE® kit, ACE 1104 is specially designed for Universities [5]. The software is closely integrated with MATLAB® and the Simulink® environment which allows for modelling of the system and controller design. When the control model is ready it is loaded into the dSPACE® card from where it controls the physical system in real-time.

Electrical interface

The electrical interface is used to interface the dSPACE® real time development card (DS1104) with the physical system. The main objectives of the interface are to isolate the DS1104 card from high voltages and to scale the system signals to make them compatible with the card inputs. The electrical interface will also interface the power amplifiers and sensors with the model and the DS1104 card.

1.3.9 System evaluation

After completion of the system integration, the model should be evaluated. The measured stiffness and damping values will be compared to the predicted values. Emphasis will be placed on the rotor response. The rotor displacements will be plotted against rotational speed in order to determine the critical frequencies. The predicted critical frequencies will be compared to the actual results and the degree of correlation will determine the effectiveness of the design process.

1.4 Overview of the dissertation

Chapter 2 contains a detailed literature study on the different aspects involved in designing and developing an AMB system. The background obtained from this study will enable the designer to base design and implementation decisions on previous work. This chapter serves as a basis for the system design.

Chapter 3 contains a detailed system design, initiated by a description of the iterative design process that was followed. The system specifications are listed and used in the electromagnetic

design. The power amplifier specifications, journal and stator dimentions as well as the PD control parameters are obtained from the electromagnetic design and incorporated in the detailed system simulation. Analytical predictions are verified and used to conduct the rotor design and dynamic analysis. Chapter 3 is concluded with the design implementation which constitutes the mechanical design.

The power amplifier (PA) design is discussed in chapter 4. The design commences with a detailed specification followed by the power circuit design. The gate drive circuit and the pulse width modulated (PWM) controller circuit designs are discussed in detail. Some consideration is also given to electromagnetic compatibility (EMC). Thermal protection, short circuit protection and soft start are incorporated in the final design to ensure a well rounded product. Finally the circuit layout and packaging receives attention and the PA is characterised.

With the development of the different sub-systems completed, the system integration issues are addressed in chapter 5. The magnetic bearing hardware integration is discussed followed by the controller implementation. The electrical interface is discussed with some protection designs and the chapter is concluded by a discussion on the final system assembly.

The developed AMB system is characterised in chapter 6 using methods defined in chapter 2 and 3. Equivalent stiffness and damping parameters are obtained by means of steady state tests as well as system step responses followed by the system sensitivity measurement at standstill. The rotordynamic performance is recorded and compared to the predicted results.

Chapter 7 contains a section on system simulation refinement where discrepancies between the analytical predictions and the simulation as well as discrepancies between the experimental results and the simulation are discussed. Non-ideal system characteristics are discussed and some areas are identified where future work is needed.

Chapter 1 gave some background on the PBMR and AMBs which were followed by the problem statement. The issues that need to be addressed are highlighted as well as the methodology that will be followed. A short overview of the dissertation is also presented. Chapter two contains a detailed literature study on some of the aspects needed to successfully complete the project.

2
Chapter
Literature Study

Chapter 2 contains a detailed literature study on Active Magnetic Bearings (AMBs). It starts with an introduction to AMBs discussing the basic operating principles, some advantages and limitations as well as design considerations. The components contained in the AMB loop are then discussed; the electromagnetic actuator, sensors, controller and power amplifiers. Rotordynamics are also discussed since it plays a crucial role in the design of this specific system. Finally the power losses encountered in AMBs are discussed.

2.1 Active Magnetic Bearings

2.1.1 Introduction

Initially active magnetic bearings (AMBs) were designed to overcome limitations posed by conventional bearings. Their ability to work in vacuum with no lubrication and contamination, or to run at high speed, rendered AMBs the preferred option in research laboratories. Since the introduction of AMBs to industry their application has grown extensively. With a number of novel features AMBs have become valuable machine elements with a diverse range of applications [3]. AMBs are well suited to applications such as canned pumps, turbomolecular vacuum pumps, turboexpanders, and centrifuges where conventional oil bearings cannot be used.

The principle that is most often used to obtain magnetic suspension is that of the active electromagnetic bearing. Figure 2-1 explains the components and the function of a simple AMB. A sensor measures the displacement of the rotor from the reference position. A controller then derives the appropriate control signal which is converted into a control current by the power amplifier (PA). The control current then generates the magnetic forces required within the electromagnetic actuator to stably suspend the rotor at the reference position.

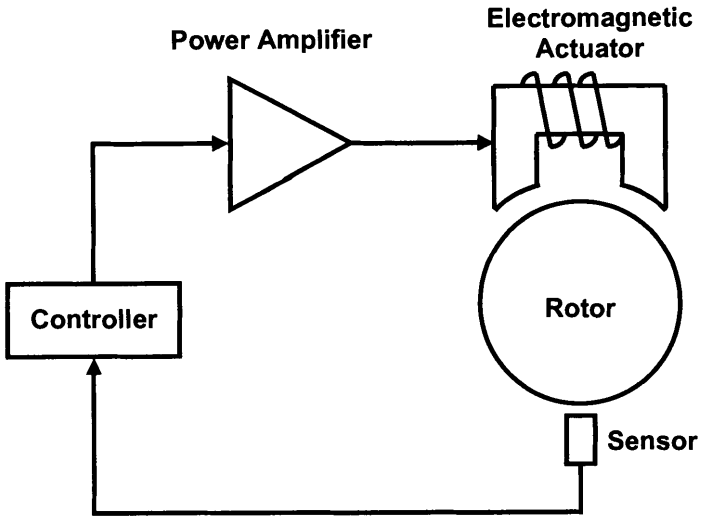

Figure 2-1 AMB functional diagram

2.1.2 Basic operating principles

Contrary to forces acting on conductors in a magnetic field (Lorentz force), the attraction force of magnets (reluctance force) is generated at the boundaries of differing permeability μ. Figure 2-2 displays a simple magnetic bearing arrangement [6].

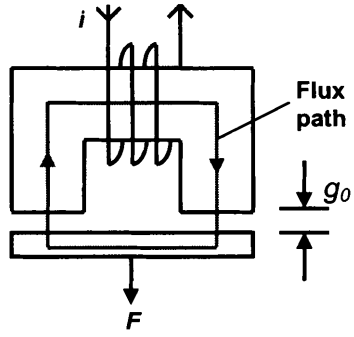

Figure 2-2 Simple magnetic bearing arrangement [7]

The flux always flows perpendicular to the surface of the different materials, and the greater the difference in permeability, the greater the force. The magnetic resistance of an arrangement is called reluctance and it is inversely proportional to the permeability μ. The force is acting in such a way that it tends to reduce the reluctance of the mechanical arrangement. This force is derived from the energy stored in the magnetic field which can be converted to mechanical energy [8].

In order to provide non-contact support for a rotor, the reluctance forces generated by the electromagnets must be controlled to vary with change in rotor position. Without closed loop

control it is impossible to suspend a rotor in such a way. The electromagnet forms part of a control loop as shown in Figure 2-1.

2.1.3 Advantages of AMBs

AMBs display a number of novel qualities which render them indispensable machine components in modern industry. The ability of AMBs to provide contact free rotation allows for high rotational speeds without lubrication, avoiding contaminating wear. This renders AMBs ideal for vacuum applications or processes where no lubrication and contaminating wear is allowed. The maintenance cost is drastically reduced due to the no-mechanical-contact arrangement.

When compared to fluid film bearings, AMBs display remarkably low bearing losses. Typically 5 to 20 times lower than conventional bearings at high operating speeds. Typical AMB losses include: active power losses (controller, coil and amplifier losses), parasitic losses (eddy currents and hysteresis) and windage losses [9]. Losses in fluid film bearings include: pump power, cooling power, oil shear losses and friction losses.

AMBs make it possible to adapt the stiffness and damping of the bearing to optimally suit the specific application. By adjusting the controller the bearing supports can be made more flexible. There are two major advantages from a rotordynamics point of view to have the supports more flexible than the rotor:

- The dynamic loads transmitted through the bearings to the non-rotating structure are reduced, thus prolonging machine life and minimizing structural vibration.
- Damping in bearings operates more effectively, thus attenuating rotor whirl amplitude at critical speeds.

Advanced control algorithms like μ and H^{∞} have the ability to precisely control the position of a flexible shaft within microns. To implement such an active vibration control system the kind of disturbance and its frequency must be known [10]. This also makes it possible to compensate for external disturbances on the machine [11] [12].

AMBs inherently allow for condition monitoring due to the availability of current and position signals. Potential AMB failure could be predicted and appropriate measures taken. A faulty AMB coil could for example be detected before it actually fails. Due to redundancy built into some AMB configurations such a faulty coil could simply be deactivated and the required force divided among the remaining active coils. The machine may then be operated until the next scheduled

maintenance stop. Systems fitted with AMBs can thus be operated more reliably than systems with conventional bearings.

2.1.4 Limitations of AMBs

AMBs are quite expensive due to limited application and the complexity of the arrangement. The initial installation cost is much higher than that of conventional bearings because of expensive amplifiers and control systems. This is however counteracted by low maintenance cost and longer machine life.

A major barrier facing designers is the question of what happens when the power fails. Power outages cause magnetically levitated shafts to rapidly de-levitate. Passive backup bearing systems are used to support the rotating shaft under these conditions. Backup bearing systems normally consist of conventional bearings with relatively large clearances between the shaft and inner bearing. This may cause large rotor transient vibrations during de-levitation of the rotor [4].

A maximum load capacity per unit area constraint is placed on an AMB due to material properties such as flux saturation and maximum current density. This load capacity is lower than that of conventional bearings resulting in an increase in envelope size for AMB installations [3].

2.1.5 AMB design considerations

The application of AMBs in rotating machinery requires consideration of the following [13]:

- **Machine layout** – The most important consideration in machine layout is the bearing location. Second to this is the sensor location. It is important to choose the location of the radial sensor in such a way that the movement experienced by the bearing is sensed by the sensor without any attenuation or phase change.
- **Magnetic bearing hardware** – The load capacity which comprises static and dynamic capacity determines the hardware design. Static capacity is a function of the magnetic material used, the pole face area and flux density designed into the system, whereas dynamic capacity is a function of system characteristics which include sensor bandwidth, power amplifier slew rate and controller performance. The material used in the magnetic circuit is important. The type of material, lamination thickness, the method used to fit the material to the shaft, and the tolerances used in the manufacturing are all critically important. The backup bearing location, the type of material used and the clearance between the bearing and the shaft should also be considered.

- **Power Amplifier** – The type of amplifier used is an important consideration. It determines the actuator slew rate and plays a dominant role in overall system performance. It also poses layout considerations in terms of electromagnetic compatibility (EMC).
- **Sensors** – Different applications pose unique constraints for sensors. The operating environment, the accuracy, linearity, tolerances and compatibility are all factors taken into account when choosing a sensor.
- **Control** – Consider analogue or digital control. An analogue controller offers simplicity whereas a digital controller offers greater flexibility in the control algorithm. The digital controller is specified by the type of control that the specific application requires. The sampling rate and controller cycle time are important considerations.
- **Diagnostic information** – AMBs inherently provide an enormous amount of information with respect to the health of the machine. Information on dynamic bearing loads enables the identification of shaft unbalance. Information on static loads enables the identification of changing machinery conditions, internal mechanical damage to stationary components, or design problems. The data acquisition tool is a consideration of the type of fault diagnostics performed.

2.2 Electromagnetic Actuator

2.2.1 Configurations

There are two basic configurations for radial AMBs; heteropolar and homopolar. Heteropolar magnetic bearings primarily have a radial flux path as shown in Figure 2-3 (a) whereas homopolar magnetic bearings have a flux path with both radial and axial components as shown in Figure 2-3 (b).

The heteropolar design is similar to that of electromotors and relatively easy to manufacture. The hysteresis losses are kept as low as possible by laminating the stator and the magnetically active part of the rotor. The homopolar arrangement keeps the hysteresis losses low and laminating may not be necessary. This configuration is most often used when lamination of the rotor is not possible.

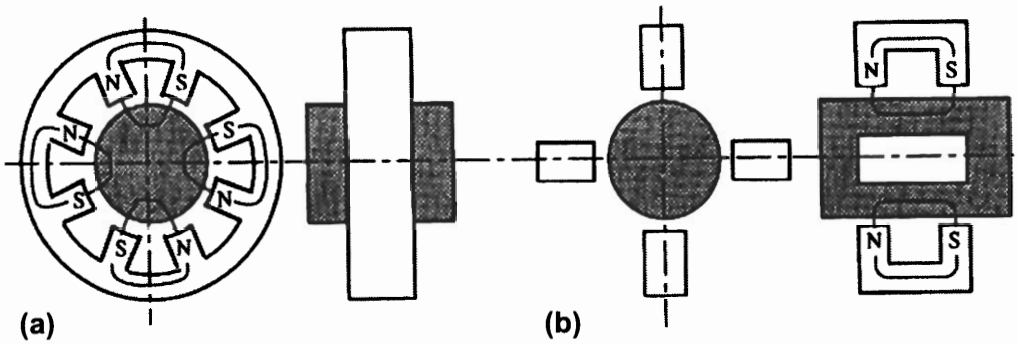

Figure 2-3 Structural shapes of (a) Heteropolar and (b) Homopolar radial AMBs

The advantages of the eight-pole radial bearing shown in Figure 2-3 is that two geometrically opposing pole pairs can respectively be assigned to Cartesian coordinates x and y. The simulation of the mechanical system, controller design and rotor motion measurement are usually based on these coordinates. This simplifies bearing control.

2.2.2 AMB Force

Ampere's circuital law states that the magnetic field intensity H induced by N turns carrying current i, wrapped around a closed magnetic path with length ℓ is given by:

$$H = \frac{Ni}{\ell} \tag{2-1}$$

It is assumed that the magnetic field intensity direction is parallel to the magnetic path and that the current in the wire is perpendicular to the magnetic path. The quantity Ni is called the magnetomotive force (MMF). The magnetic flux Φ in the circuit equals the product of the flux density B and the pole face area A_g which is also the area of the air gap.

$$\Phi = BA_g \tag{2-2}$$

In magnetic circuits most of the magnetic resistance (reluctance) resides in the air gaps. Air and other nonferrous material have nearly the same magnetic properties as free space. The flux density in such materials is related to the magnetic field intensity by the linear relation

$$B = \mu_0 H \tag{2-3}$$

where the permeability of free space is given by

$$\mu_0 = 4\pi \times 10^{-7} \text{ [H/m]}. \tag{2-4}$$

The magnetic path material used for magnetic bearings is normally ferrous material and the air gaps are made as small as possible to reduce the required MMF.

Consider the magnetic circuit shown in Figure 2-4. Due to the high relative permeability of the materials used for the magnetic circuit, such as silicon steel, the reluctance of the material can be neglected compared to the reluctance of the air gaps. The flux density in each air gap is obtained using (2-5) which is derived from (2-1) and (2-3) using $\ell = 2g$.

$$B = \frac{\mu_0 N i_m}{2g} \tag{2-5}$$

As stated previously the attraction force is generated at the boundaries between differing permeability μ. The calculation of these forces is based on the field energy. The energy W stored in the homogeneous field in the air gaps is obtained using (2-6).

$$W = \frac{1}{2} BHV = \frac{1}{2} BHA_g 2g \tag{2-6}$$

For small displacements dg the magnetic flux BA_g remains constant. When the air gap increases by dg the volume $V = 2gA_g$ increases and the energy stored in the field increases by dW. This increase in energy is mechanically supplied where an attractive force must be overcome.

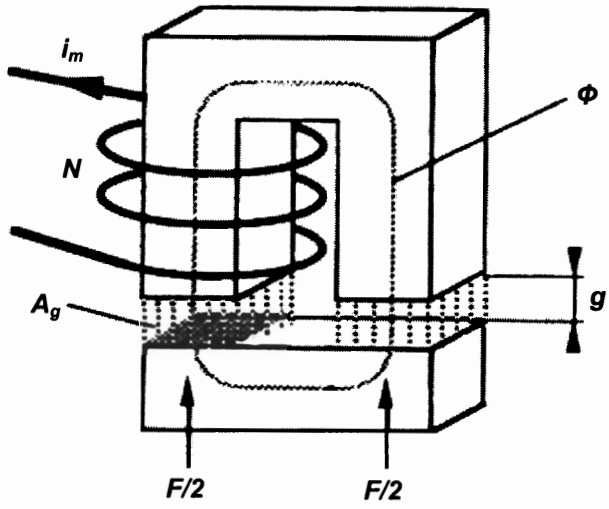

Figure 2-4 Force of a magnet

The attractive force is determined by obtaining the partial derivative of the field energy W with respect to the air gap g.

$$F_m = \frac{dW}{dg} = BHA_g = \frac{B^2 A_g}{\mu_0} \tag{2-7}$$

Equation (2-7) remains valid when the flux density remains constant. By substituting (2-5) into (2-7) the force is obtained as a function of coil current and the air gap:

$$F_m = \frac{\mu_0 N^2 i_m{}^2 A_g}{4g^2} \tag{2-8}$$

In the heteropolar configuration the poles are located 22.5° (θ) with respect to the vertical. This must be taken into account when obtaining the force component in the vertical direction. The pole form also influences the force and a term is included for this. The derivation of the correction factor due to the pole geometry is included in Appendix A. The resulting force produced by a single pole pair is then estimated using (2-9).

$$F_m = \frac{\mu_0 N^2 i_m{}^2 A_g}{4g^2} \cos(\theta) \left(\frac{\sin\left(\frac{\theta}{2}\right)}{\frac{\theta}{2}} \right)^2 \quad \textbf{(2-9)}$$

It should be noted that this estimation for force may be optimised since it does not provide for fringing and leakage of flux nor does it allow for some losses in MMF across the magnetic circuit.

2.3 Sensors

The accuracy and stability of the displacement sensor used in an AMB play an important part in the performance of the AMB. Contact free sensors must monitor the rotating surface which implies that the surface quality and the homogeneity of the material will influence the measuring result. The bandwidth of the sensor must also exceed the power amplifier bandwidth. Commercial application requires low cost sensors that are durable and stable. The sensors should also display low noise susceptibility [6].

2.3.1 Sensor considerations

Measuring range: The measuring range of a sensor is the range in which an approximately linear correlation between the measured quantity and the sensor output signal is achieved. The sensor range must correspond with the maximum displacement of the physical system.

Linearity: The linearity is normally represented as a percentage of the maximum measuring range. This is an indication of the extent to which the measured quantity deviates from the linear relation between the measured quantity and the sensor output signal.

Sensitivity: The sensitivity indicates the ratio of the output signal and the measured quantity. For displacement sensors the sensitivity is indicated, for instance, in mV/µm. The sensitivity can be enhanced by electronically amplifying the output signal.

Resolution: Apart from the signal describing the measured quantity each sensor also generates noise. The value of the signal which can be distinguished from the noise (usually peak to peak value) is called resolution. The resolution is normally indicated in absolute values (μm for displacement sensors) and cannot be improved by amplification. The resolution can however be improved by low-pass filtering at the expense of frequency range.

Frequency range: The frequency where the sensitivity is reduced by 3 dB is known as the cut-off frequency. It is important to keep in mind that the signal may already show a significant phase lag at the cut-off frequency [6].

2.3.2 Displacement measurement

In AMBs the rotor position is monitored using displacement sensors which play an important role in the AMB closed loop. Apart from the measuring range, linearity, sensitivity, resolution and frequency range which must be taken into account, the sensor's temperature range and noise immunity is also important. A wide variety of displacement sensors are used in AMB applications. A few of them are discussed in sections to follow.

Inductive displacement sensors

This sensor incorporates a ferrite inductor as part of an oscillating circuit. As a ferrous object of which the position is to be measured, approaches the ferrite inductor, its inductance changes and the oscillating circuit is detuned. By demodulating and linearising the oscillating circuit output, a signal proportional to the distance between the sensor and the object to be measured is produced. Two opposing sensors are frequently implemented differentially in a bridge circuit at a constant frequency. This configuration produces a nearly linear signal.

The modulation frequency ranges from 5 kHz up to 100 kHz and the cut-off frequency of the output signal ranges between one tenth and one fifth of the modulation frequency. Inductive sensors are normally not very sensitive to the magnetic fields near the bearing magnets since they are shielded by the ferrite core. They may however display massive disturbances when a switching power amplifier is used with a switching frequency close to that of the modulation frequency.

Eddy-current sensors

A coil encapsulated in the probe tip, radiates a high frequency magnetic field into the observed target. As a conductive surface approaches, eddy currents are induced which weaken the

magnetic field. The amplitude of the oscillation is dependant on the clearance and once demodulated and linearised a voltage proportional to the clearance is produced.

A reduction in resolution may result from disturbances caused by non-homogeneities in the measured rotating material. The sensitivity of the sensor is dependant on the type of material being measured and is specified by the manufacturer. Eddy-current sensors must be shielded for applications where they are located near high frequency magnetic fields. Other mounting considerations, for instance minimum clearance between sensors, are specified in the installation manuals for the different manufacturers.

Capacitive displacement sensors

Capacitive displacement sensing is implemented by realising a plate capacitor with one electrode the sensor and the other the object to be measured. The capacitance of the plate capacitor varies with the clearance of the electrodes. An alternating current with a fixed frequency is generated which runs through the sensor. The voltage amplitude as measured across the electrodes is proportional to the displacement. Circuitry then demodulates and amplifies this signal to produce a linear displacement signal.

Commercially available capacitive sensors display very high resolution (for instance 0.02 µm at a measuring range of 0.5 mm), but are very expensive. The sensor is sensitive to dirt in the air gap which changes the dielectric constant, as well as electrostatic charging of the contact-less rotor.

Magnetic displacement sensors

The air gap in a magnetic loop with a constant current can be measured using the flux density *B*. When two sensors are configured so that they oppose each other, and the flux densities are subtracted from each other, a well linearised displacement signal is obtained. The flux density is measured with Hall sensors or with field plates. These sensors are sensitive to interferences caused by external magnetic fields.

Optical displacement sensors

There are several topologies utilising light to measure displacement. The simplest configuration employs a light source and a light sensitive sensor opposite to the light source. The object to be measured blocks the light from the light source and the light intensity measured on the sensor serves as a measurement of the position of the object. By selecting the correct components a nearly linear displacement signal is produced.

A similar topology reflects the light by the object to be measured. The light intensity measured by the sensor changes according to the position of the object. Optical displacement sensors are very sensitive to dirt and the resolution is limited due to diffraction effects which renders them inappropriate for some applications [6].

2.4 Controller

2.4.1 Introduction

The designation "active" magnetic bearing implies actively controlled magnetic forces. Basic bearing properties such as stiffness, damping, rotor positioning, unbalance response and many others are determined by the controller.

The force generated by the electromagnet, as given by (2-9), is directly proportional to the square of the coil current and indirectly proportional to the square of the air gap. The electromagnet is a nonlinear system with negative position stiffness, rendering the magnetic bearing open loop unstable. In order to achieve stable suspension of the rotor, feedback control must be implemented.

To achieve stable suspension of the rotor the electromagnet must apply a force equal to the gravitational force acting on the suspended rotor. The gravitational force *mg* and the magnetic force F_m must be in equilibrium. The resultant force *F* applied to the suspended body is obtained using (2-10).

$$F = F_m - mg \tag{2-10}$$

Figure 2-5 (a) displays the electromagnet force-current relationship and (b) the force-displacement relationship.

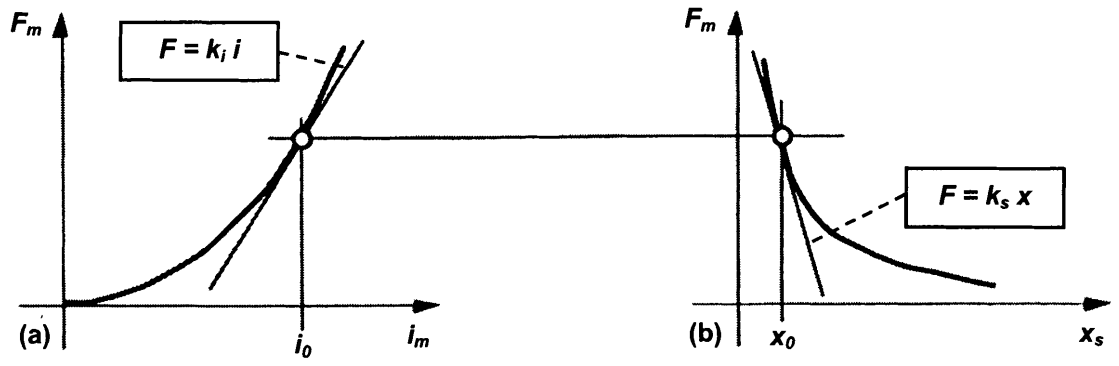

Figure 2-5 Magnetic force F_m as a function of (a) current and (b) air gap [6]

It is sufficient for controller design to consider only the slopes of the nonlinear force-current and force-displacement curves at the operating point. Figure 2-5 (a) shows the linearization of the force-current function. A new variable i is introduced for the deviation of the winding current i_m from the operating point i_0.

$$i = i_m - i_0 \tag{2-11}$$

The slope of $F(i)$ is called the force-current factor k_i and the unit is Newton/Ampére (N/A). The linearization of the force-displacement function $F(x)$ is shown in Figure 2-5 (b). Here too a new variable x is introduced which describes the deviation from the operating point x_0. Take note that from this point onwards positive displacement is towards the magnet (see Figure 2-6), this implies positive values for k_s.

$$x = x_0 - x_s \tag{2-12}$$

The slope of $F(x)$ is called the force-displacement factor k_s and the unit is N/m, the same as mechanical stiffness. All three variables, force, displacement, and current, have constant operating point values (mg, x_0 and i_0) and variables (F, x, i) for deviations from this operating point. The resulting instantaneous force F as a function of displacement and current as linearised around the working point is:

$$F(x,i) = k_s x + k_i i \tag{2-13}$$

The values of k_i and k_s can be obtained by determining the partial derivative of the nonlinear force equation (2-9) with respect to displacement and current at the working point.

2.4.2 Closing the control loop

The first goal of control design is to stabilise the contact-free equilibrium. The controller must provide a restoring force similar to that of a spring suspension and damping to attenuate oscillations. This is achieved by applying forces proportional to displacement and rate of displacement. This simple design is useful as a starting and reference point in theory and application.

Figure 2-6 (a) displays a spring-mass-damper model with a stiffness of value k and a damping of value b. The resulting force F for such a suspension in response to a displacement x is:

$$F = -kx - b\dot{x} \tag{2-14}$$

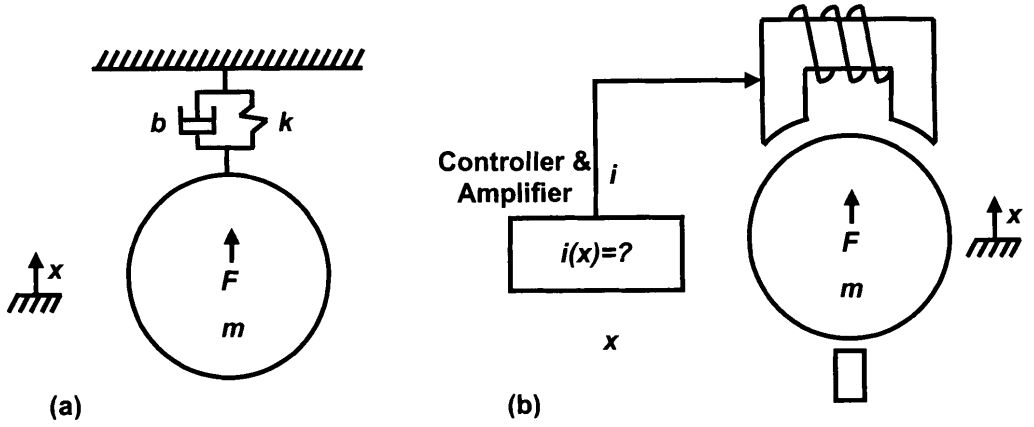

Figure 2-6 Simple controller design as to emulate spring-damper behaviour [6]

The controller function *i(x)* must now be designed in order to achieve the same stiffness of value *k* and damping value *b*. This is accomplished by solving *i* from (2-13) and (2-14):

$$i(x) = -\frac{(k + k_s)x + b\dot{x}}{k_i} \tag{2-15}$$

Assuming an ideal (linear) sensor and power amplifier, without noise and time delays, the dynamic behaviour of the masses in Figure 2-6 (a) and (b) are equivalent. Contact free suspension is realised. The characteristic equations for these two systems are given in (2-16).

$$s^2 + \left(\frac{b}{m}\right)s + \frac{k}{m} = s^2 + \left(\frac{b_{eq}}{m}\right)s + \frac{k_{eq}}{m} \tag{2-16}$$

2.4.3 Nonlinear System

The control configuration used in this project incorporates two opposing electromagnets with two current controlled power amplifiers and a single PD controller to achieve magnetic suspension in a single axis. Figure 2-7 displays the nonlinear system block diagram for this configuration with k_{m1} and k_{m2} the top and bottom electromagnet constants respectively.

An error signal is produced by subtracting the rotor position from a reference position. The error signal is scaled via the proportional constant (K_P) and the derivative of the error signal via the derivative constant (K_D) to produce a current reference signal (i_{ref}). The current reference signal is added and subtracted from a bias current reference signal (i_{0ref}) to produce reference current signals for the top and bottom power amplifiers (PAs) respectively.

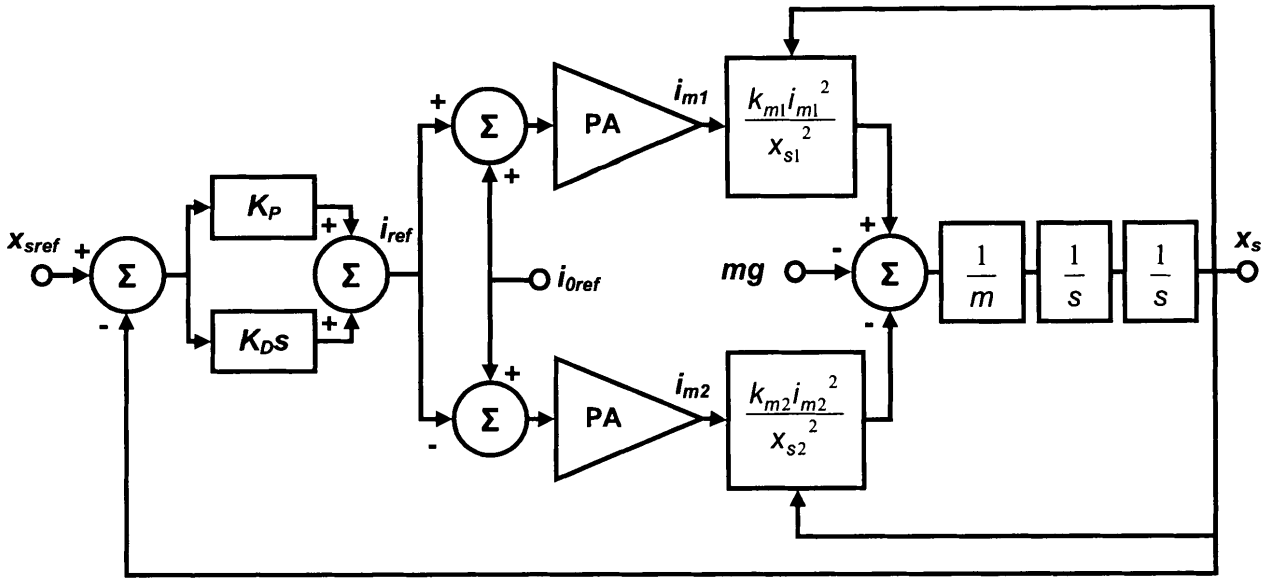

Figure 2-7 Nonlinear system block diagram

2.4.4 *Linearised Model*

The nonlinear model of the AMB shown in Figure 2-7 is linearised around the working point to obtain the linear system block diagram shown in Figure 2-8. Take note that for this model it is assumed that the force-current and force-displacement factors for the two magnets are the same. This is however only valid if the working points of the two magnets are the same. For horizontal suspension where no gravity applies this assumption is valid for small perturbations around the geometrical centre between the magnets. The PAs are assumed to be ideal with unity gain.

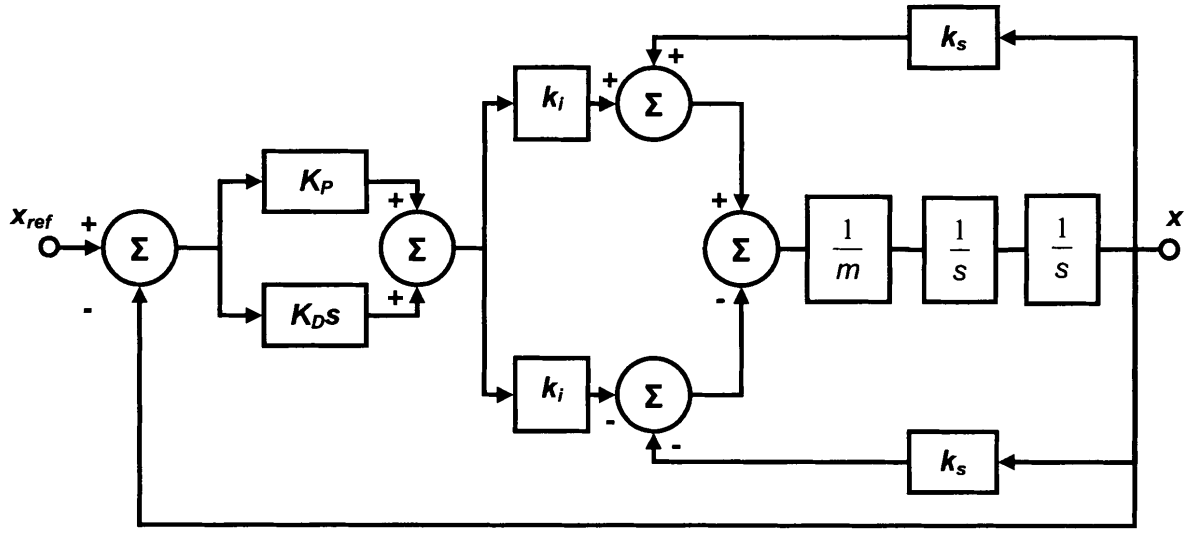

Figure 2-8 Linear system block diagram

Figure 2-9 displays a signal flow diagram derived from the system block diagram shown in Figure 2-8.

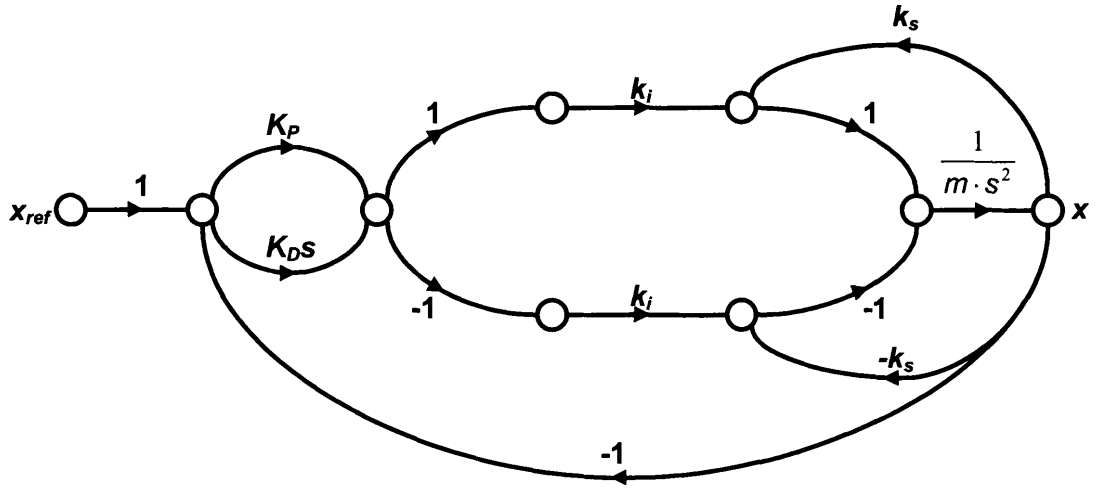

Figure 2-9 Signal flow diagram

From the signal flow diagram in Figure 2-9 the forward paths connecting the input to the output are:

$$P_1 = \frac{K_P k_i}{ms^2},\ P_2 = \frac{K_D k_i s}{ms^2} = \frac{K_D k_i}{ms} \qquad \textbf{(2-17)}$$
$$P_3 = \frac{K_P k_i}{ms^2},\ P_4 = \frac{K_D k_i s}{ms^2} = \frac{K_D k_i}{ms}$$

Six loops are identified:

$$L_1 = \frac{k_s}{ms^2},\ L_2 = \frac{k_s}{ms^2},\ L_3 = \frac{-K_P k_i}{ms^2} \qquad \textbf{(2-18)}$$
$$L_4 = \frac{-K_D k_i}{ms^2},\ L_5 = L_3,\ L_6 = L_4$$

Loops L_1 through to L_6 touches, therefore the determinant is:

$$\Delta = 1 - (L_1 + L_2 + L_3 + L_4 + L_5 + L_6) \qquad \textbf{(2-19)}$$

The cofactor of each forward path is evaluated by removing the loops that touch that specific path from the determinant. Therefore the cofactors are:

$$\Delta_1 = \Delta_2 = \Delta_3 = \Delta_4 = 1 \qquad \textbf{(2-20)}$$

The system transfer function is obtained using (2-21).

$$T = \frac{P_1 \cdot \Delta_1 + P_2 \cdot \Delta_2 + P_3 \cdot \Delta_3 + P_4 \cdot \Delta_4}{\Delta} \qquad \textbf{(2-21)}$$
$$= \frac{\frac{2K_P k_i}{ms^2} + \frac{2K_D k_i}{ms}}{1 - \left(\frac{2k_s}{ms^2} - \frac{2K_P k_i}{ms^2} - \frac{2K_D k_i}{ms}\right)}$$
$$= \frac{2K_P k_i + 2K_D k_i s}{ms^2 + 2K_D k_i s + (2K_P k_i - 2k_s)}$$

The resulting characteristic equation for this system is as given by (2-22).

$$q(s) = s^2 + \frac{2K_D k_i}{m} s + \frac{2K_P k_i - 2k_s}{m} \qquad (2\text{-}22)$$
$$= s^2 + \frac{b_{eq}}{m} s + \frac{k_{eq}}{m}$$

The result in (2-22) is the same as that of (2-16) which implies that the AMB system with a single controller and two electromagnets will display dynamic behaviour equivalent to that of a spring-mass-damper system. The equivalent damping for this system is derived from (2-22) as

$$b_{eq} = 2K_D k_i \qquad (2\text{-}23)$$

and the equivalent stiffness as

$$k_{eq} = 2K_P k_i - 2k_s \qquad (2\text{-}24)$$

The results obtained in (2-23) and (2-24) can now be used to design a simple PD controller which will result in a stable system with the desired equivalent stiffness and damping values.

2.5 Power Amplifiers

Power amplifiers (PAs) control the flow of energy between a power source and a load. In the case of magnetic bearings, PAs control the amount of magnetic energy in the electromagnets. This implies that the PA provides a mechanism to add energy to the magnetic field, extract energy from the magnetic field or maintaining the magnetic field energy at a constant level.

There are two main types of PAs; linear amplifiers and switch-mode amplifiers. A linear amplifier behaves like an adjustable resistor in series with the load and controls the voltage or current by adjusting the resistance seen by the power source. This type of amplifier displays poor efficiency, typically in the order of 5 %. A major advantage of linear amplifiers is that they do not generate switching noise.

In switch-mode PAs switches are operated in saturation where the switch impedance is either very low or very high. In order to control the rate of energy addition or extraction, pulse width modulation (PWM) is implemented. By controlling the amount of energy added or extracted in a short interval the average level of energy can be controlled. Figure 2-10 displays the H-bridge topology used to achieve energy addition and extraction.

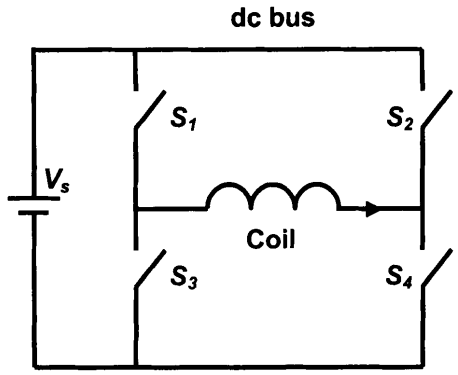

Figure 2-10 H-bridge principle [13]

There are two methods of implementing the PWM control; two-state control and three-state control. With two-state control energy is added to the magnetic field by closing switches S_1 and S_4 which results in a positive coil current. When energy must be extracted switches S_1 and S_4 are opened and switches S_2 and S_3 are closed. The rate at which energy can be added and extracted is a function of the dc bus voltage and the coil inductance. This determines the PA's slew rate (dynamic performance) [13].

Three-state PWM control introduces a third state where the coil current is allowed to free-wheel through switches S_3 and S_4 when switches S_1 and S_2 are opened. The coil current decreases very slowly with a time constant determined by the coil inductance and coil resistance. This topology greatly reduces the ripple component of the coil current. Since only two devices are switched in each cycle the switching losses are reduced by a factor two.

The decision of when energy must be added, extracted or maintained is based on the parameter being controlled. There are three parameters which are typically controlled in PAs [13];

- the coil current (current controlled) - most common
- the air gap flux - next most common
- the coil voltage (voltage controlled) - least common

In all three cases the controlled variable is monitored and compared to the reference value. This error signal is then used as basis for controlling the H-bridge switching.

Switch-mode PAs are superior to linear amplifiers in the sense that they are very efficient (up to 90 %). The losses in switch-mode PAs are mainly due to switching and conduction losses of the switches.

A PA is specified in terms of its peak and continuous current rating as well as its voltage. The current is specified to meet the force requirements, whereas the rated power supply voltage is specified to obtain the desired force slew rate (dynamic performance).

2.6 Rotordynamics

Rotordynamic analysis enables the machine designer to accomplish the following objectives in modern machine design:

- Critical speeds prediction
- Design modifications to change critical speeds
- Determine balance correction masses and location from measured vibration data
- Predict amplitudes of synchronous vibration caused by rotor imbalance

Rotordynamic analysis is accomplished by either constructing analytical models of the rotor or by finite element methods (FEM). The latter is the preferred approach since modern FEM packages allow the machine designer to perform very accurate analysis of structural dynamics using the three dimensional computer aided design (CAD) model of the rotor. The same CAD model can then be used for the finite element analysis and for compiling manufacturing drawings.

A rotor-bearing system has a number of discrete natural frequencies of lateral vibration. Every natural frequency can be associated with a mode shape which can be seen as a snapshot of the rotor deflection curve at the moment of maximum strain during the vibration.

Critical speed is defined as the shaft speed that coincides with the natural frequency which is excited by a rotor imbalance rotating at shaft speed. Therefore the rotor does not vibrate as it appears to an external stationary observer, but rather is bowed into the mode shape associated with the particular natural frequency. The shaft whirls about the bearing centreline.

In mathematical terms a natural frequency is an eigenvalue and a mode shape is an eigenvector. A distributed mass-elastic system has an infinite number of eigenvalues and associated eigenvectors in theory, but in practice only the lowest three or four critical speeds and associated whirl modes are excited in the operating speed range of a high speed machine [14].

Mode shapes are determined by the distribution of mass and stiffness along the rotor, as well as the bearing support stiffnesses. The first three modes associated with the lowest three natural frequencies of a uniform shaft vary with increased support stiffness as shown in Figure 2-11.

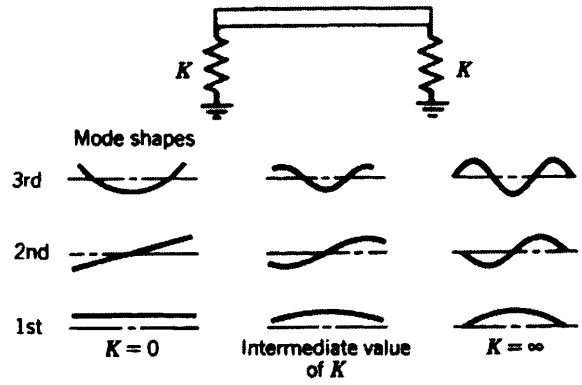

Figure 2-11: Effect of bearing support stiffness *K* on lateral vibration modes of a uniform shaft [14]

The first two modes with low support stiffness ($K \approx 0$) involve a negligible amount of shaft bending. These two rigid-rotor modes for a rotor with two massive disks are shown in Figure 2-12. If the disks are identical and evenly spaced from the rotor mid-span, and if the bearing supports have equal stiffness, then the first rigid-rotor mode will trace a cylinder and the second will trace two cones with a common apex at mid-span. Rotor asymmetry or unequal bearing stiffness will somewhat modify these mode shapes.

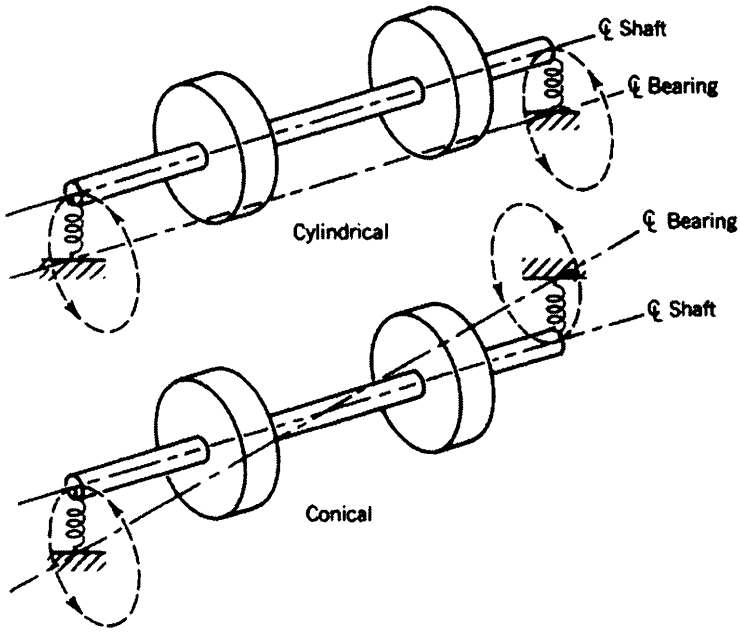

Figure 2-12: Rigid-rotor modes of whirling for a symmetrical rotor [14]

With moderate damping, the synchronous response of the rotor-bearing system of Figure 2-12 would appear as shown in Figure 2-13. The whirling amplitude measured at the bearings,

caused by imbalance, is plotted as a function of shaft speed. The peaks of the whirl amplitude for each of the two modes identify the critical speeds.

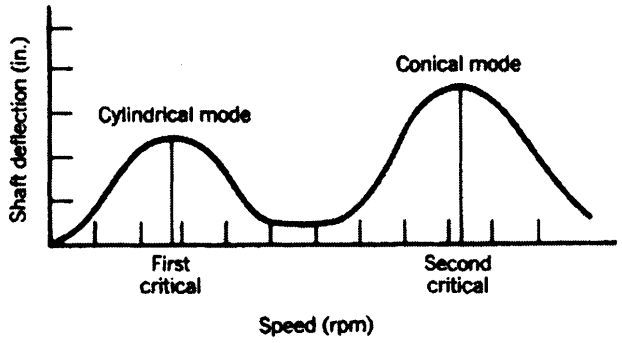

Figure 2-13: Synchronous response to unbalance through both rigid-body modes [14]

For a shaft speed beyond the conical critical, a third critical speed is reached that involves shaft bending, as shown on the top left of Figure 2-11. For very slack support, this mode is equivalent to a free-free (unsupported) mode.

The first three critical speeds typically vary with support stiffness, as shown in Figure 2-14. This type of plot is referred to as a critical speed map. The insensitivity of the third critical speed to support stiffness allows a range of operating speeds that does not traverse any of the critical speeds, (see the vertical arrow of Figure 2-14). This is good machine design practice, from a rotordynamics standpoint. The modern trend toward higher speeds however makes it difficult to avoid approaching or traversing the third critical speed [14].

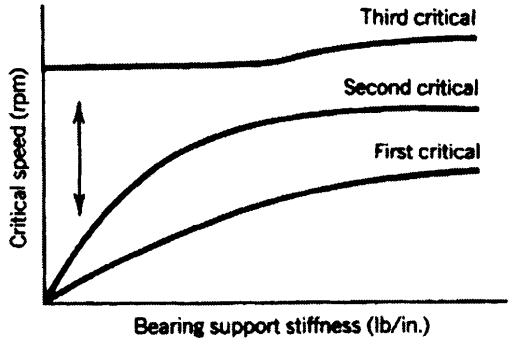

Figure 2-14: Critical speed map for three modes [14]

Machines with oil film bearings can have enough support damping to make one or both of the rigid-rotor critical speeds disappear. In such a case, the third calculated critical speed may become the first or second observed critical speed. This is sometimes called the first bender due to the mode shape.

If the bearing supports are stiffened, the modes become more like those shown on the right of Figure 2-11. For a symmetric rotor with two identical discs on an elastic shaft, the first two modes of operation on rigid supports are shown in Figure 2-15. The top and bottom mode shapes are approximated by a half and a full sine wave respectively. Since rigid bearing supports cannot dissipate energy, and since internal damping in a rotor is destabilising at high speeds, this type of design can create severe rotordynamic problems. Almost all flexing is in the rotor, rather than in the supports [14].

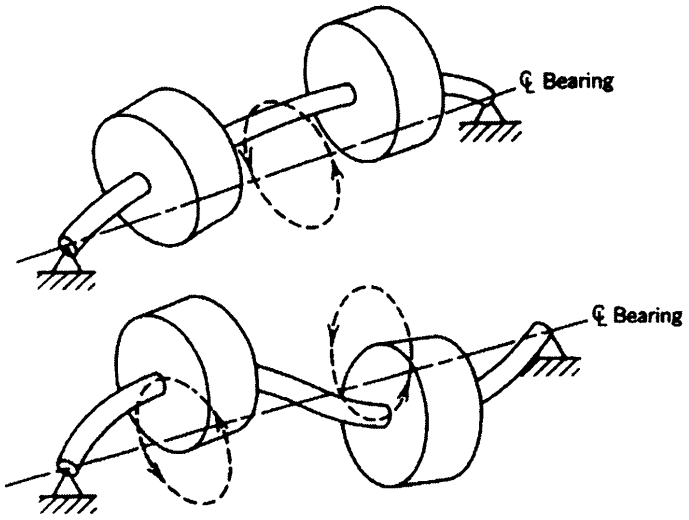

Figure 2-15: First two rigid-support modes of whirling for a symmetric elastic two-disk rotor [14]

Since the dynamic properties of an AMB are controlled electromagnetically, the bearing stiffness and damping coefficients can be chosen within certain physical limits. This enables the attenuation of vibration amplitudes.

Rotordynamics play an integral role in the final design of the rotor-bearing system. The design must display robust dynamic characteristics to ensure no-mechanical-contact between stationary and rotating parts due to vibrations. Critical factors contributing to these robust dynamics are bearing stiffness and damping as well as bearing position [15].

2.7 AMB losses

One of the most impressive features of AMBs is their ability to sustain high rotation speeds. Jesse Beams, a physics professor at the University of Virginia received a patent for a device which spins small steel balls (1/32 in. diameter) at 4,000,000 revolutions per second [4]. In

today's industrial applications rotational speeds that have been realised are in the range of about 3 kHz for a grinding spindle, or about 5 kHz for small turbo-machinery.

AMBs operating at high speeds display a number of losses and in order to fully utilise the many advantages posed by AMBs the ability to accurately predict losses becomes a necessity. These losses can lead to excessive heating in large electric motors or compressors, and may need to be removed by external cooling. Losses should also be minimised in applications such as energy storage flywheels, in order to maximise the length of time the rotating machine can operate at a fixed energy [16] [17].

The losses encountered in an AMB system may be categorised as follows:

- Coil losses
- Iron losses
- Air losses

Coil losses are the resistive losses due to current in the electromagnetic coils and are quite accurately determined from basic formulas. Iron losses in the rotor constitute three components: eddy current losses, alternating hysteresis losses and rotational hysteresis losses. These losses are critical to the design process of an AMB system. Air losses are generated by the windage friction loss due to the gasses or liquids surrounding the rotor. These losses may be significant in high speed applications and should be determined to assess its impact [16] [18].

All the components contained in the AMB loop were discussed in detail and the knowledge contained in each paragraph will be used in chapter 3 to design the AMB system. The choice of actuator configuration and power amplifier topology can now be based on knowledge obtained from previous work. The type of sensor to use with a specific power amplifier was also discussed and will influence the final decision. Some valuable information about the controller design was also discussed which enables the designer to obtain the controller parameters from the specified stiffness and damping values of the system. The rotordynamics gives background on system behaviour and what to expect during system operation. The losses which can be expected in an AMB system were also discussed. The next chapter contains a detailed design of the system.

3
Chapter
System Design

Chapter 3 contains a detailed system design. First the design process that was followed is explained. This is followed by a detailed system specification which highlights all the aspects that should be considered in the design process. The electromagnetic design is then discussed followed by the MATLAB® simulation of the system. The results obtained from the electromagnetic design together with simulation results are used to design the rotor and perform rotordynamic analyses. Finally the design implementation is discussed.

3.1 Design process

An active magnetic bearing (AMB) system involves an interconnection of mechanical and electrical components as well as a large amount of software. This renders the system a typical product of mechatronics which is an interdisciplinary area of engineering science based on the classical fields of mechanical and electrical engineering as well as computer science.

The iterative design process outlined in Figure 3-1 shows the first step as a complete system specification. From the system specification a maximum carrying force along with a force slew rate is estimated and used to compile a preliminary electromagnetic (EM) design using MathCAD®. Parameters obtained from the EM design along with the calculated controller parameters are now used to simulate the complete system. The stiffness and damping parameters as well as the system's dynamic response are verified using the simulation.

A rotor is now designed with the physical sizes obtained from the EM design. Dynamic analyses are performed on the rotor, using the verified stiffness and damping parameters, in order to obtain the rotor forces and displacements in the magnetic bearings. These results are compared to the maximum carrying force and allowable displacement due to the bearing geometry. If the forces or displacements are out of range the electromagnetic design is reviewed and the process is repeated. When these specifications are within range the focus shifts to the rotordynamic performance.

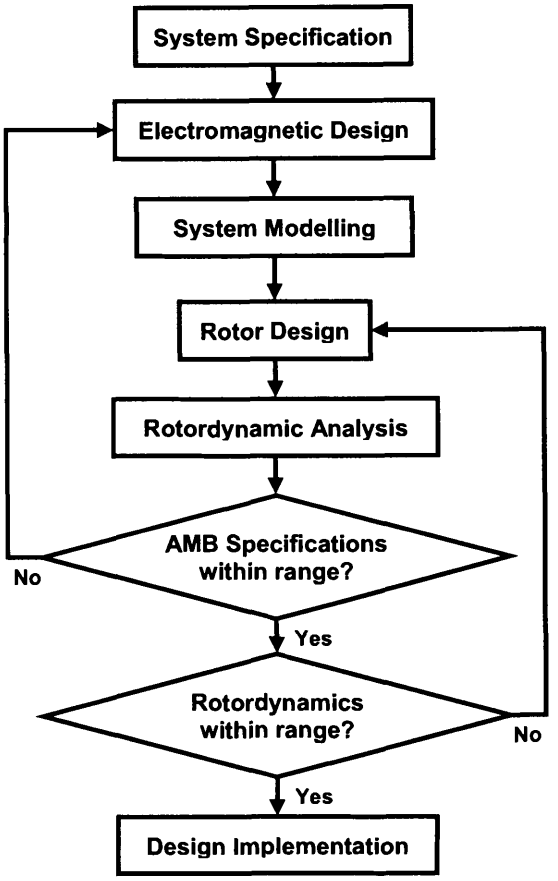

Figure 3-1 Design Process

The magnetic bearing location as well as the rotor response is verified and if either of these parameters is out of range the rotor design is reviewed. The rotor forces and displacements are again verified and once the rotordynamic performance is within range, the design can be implemented. In the following sections the final iteration of the design process depicted in Figure 3-1 is discussed in detail.

3.2 System specification

3.2.1 Research outcomes

North-West University is currently in the process of establishing AMB technology in the School of Electrical and Electronic Engineering. An axial AMB and single radial AMB systems have been developed to date and the next step in establishing the relevant technology is to develop a double radial AMB system.

Developing AMB hardware is an expensive exercise and care should be taken to ensure that the hardware is functional and if possible allows for multiple research applications. The following areas of research were identified:

- Flexible rotor analysis
- High speed loss analysis
- Self-sensing position estimation

The hardware is designed with the mentioned research areas in mind. This implies that the model will comprise a flexible rotor, rigid rotor and switch-mode power amplifiers which are compatible with self-sensing techniques.

3.2.2 Main area of focus

Information gathered from literature, prior work and discussions with PBMR consultants indicated that the main area of focus for this project should be to stably suspend a flexible rotor through its first bending mode.

A flexible rotor must be designed and detailed rotordynamic analyses must be performed to ensure that it is possible to stably suspend the rotor through the first bending mode. Bearing stiffness and damping are taken into account as well as maximum carrying force.

Although the model is designed with high speed loss analyses as well as self-sensing position estimation in mind, the main area of focus is rotordynamic analyses. The design does not cater for propulsion of the rigid rotor to very high speeds and no self-sensing position estimation design is included.

3.2.3 System specifications

A double radial AMB model must be developed which caters for:

Flexible rotor analyses

A flexible rotor must be designed that has a maximum operating speed of 10,000 rpm. The rotor should pass through its first three critical frequencies of which the third should be the first bending mode before reaching maximum operating speed. The AMB must be able to stably suspend the flexible rotor through these critical frequencies and allow for advanced control implementation.

High speed loss analyses

Together with the flexible rotor a rigid rotor should be designed with a maximum operating speed of 30,000 rpm. This maximum operating speed allows for relevant high speed loss analyses which may be compared to previous work [16]. The rotor must have an uncomplicated design to simplify the windage calculations. The rotor should also remain rigid for speeds up to the maximum operating speed to eliminate unwanted transients that may influence the analysis. The two rotors must also be interchangeable with minimum adjustments.

Self-sensing position estimation

The power amplifiers that are used must cater for self-sensing position estimation. The self-sensing position estimation technique determines the rotor position from the change in the coil inductance. This is measured by measuring the current slope while applying a square voltage wave across the coil. A switch-mode power amplifier must be developed to satisfy these criteria.

3.3 Electromagnetic Design

The electromagnetic design is performed using MathCAD® calculation software. This software allows the designer to create a design using variables which can be manipulated. The variables are easily adjusted to reduce the time it takes to obtain the optimal design. The calculations used in this design are based on the heteropolar radial bearing design process outlined in [13].

3.3.1 Design choices and performance requirements

A previous model that was developed made use of a homopolar configuration with linear power amplifiers and the magnetic circuit was manufactured from solid mild steel. The proposed double radial system makes use of switch-mode power amplifiers. For propulsion the double radial AMB system makes use of compressed air that is projected onto a machined profile on the shaft. This topology has limited energy transfer capability that is difficult to determine. To ensure that the model is capable of high rotation speeds, the losses in the magnetic circuit should be minimized. In order to reduce the high speed losses, the magnetic circuit is laminated. Since it is very difficult to manufacture a laminated homopolar configuration it was decided to implement a heteropolar design. The process of designing and manufacturing a laminated heteropolar configuration was strategic to establish knowledge on this topic at the North-West University.

Other choices which simplify the design are:

- Poles are paired which implies no flux splitting (NNSSNNSS). This configuration does not make effective use of the magnetic material but does simplify the control and reduces power losses.
- Quadrant control is implemented. Each pole pair (NS) is wound in series and powered by a single power amplifier.
- Removable coils are used.

Figure 3-2 displays a standard 8-pole configuration with removable coils that will be used in this design. As shown in Figure 3-2 the magnetic material is not optimally utilised since there are areas in the material which experience no flux. This configuration however simplifies the control requirements.

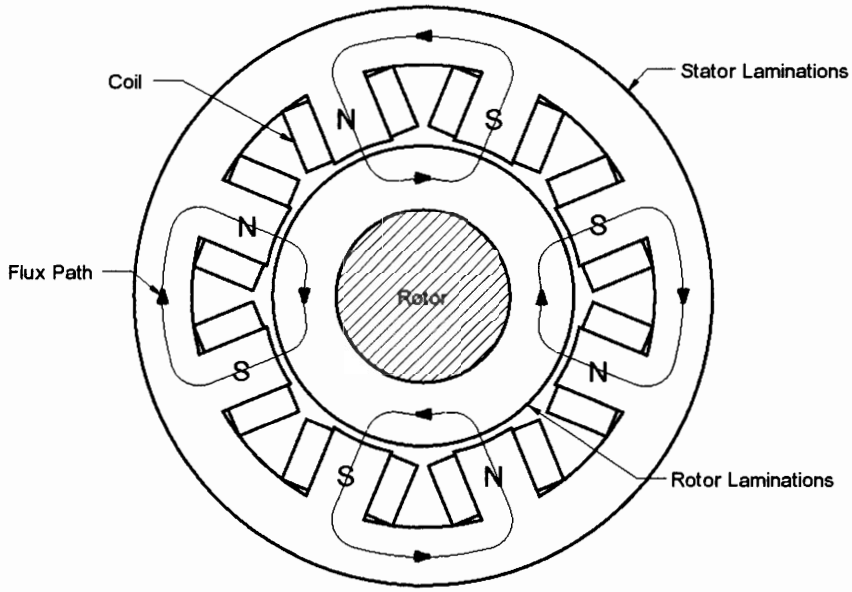

Figure 3-2 Standard 8-pole Heteropolar radial bearing [13]

The material used for the laminations is cogent^{TM} silicon steel (M330-50A). This is machine grade silicon steel with a lamination thickness of 0.5 mm. This is not the optimal lamination thickness for high speed operation but was the only readily available option. For operation at 10,000 rpm the predicted core losses are acceptable but at 30,000 rpm the losses are predicted to be excessive. Since this project focuses on the flexible rotor operating at 10,000 rpm it was not seen as a problem. The rigid rotor operating at 30,000 rpm would pose high losses which would enable relevant high speed loss analyses. Unfortunately the propulsion needed to reach such high speeds is predicted to be a problem.

Through the iterative process that was followed the following performance requirements were compiled from the rotordynamic analysis and mechanical configuration:

- Rotor laminations inside diameter ($2r_r$) are equal to 31.75 mm. This specification is placed by the Trantorque GT™ Miniature Series components that are used to secure the two rotor lamination packs as well as a centre mass to the flexible shaft.
- Peak load capacity (F_{max}) of 500 N and an rms load capacity (F_{rms}) of 200 N. These constraints were determined by the rotordynamic analysis.
- Bearing stiffness k_{eq} of 500 N/mm or 500×10^3 N/m
- Bearing damping b_{eq} of 2.5 N.s/mm or 2.5×10^3 N.s/m
- The air gap (g_0) is equal to 0.6 mm which was chosen to represent a typical air gap that is used.
- A maximum rotational speed constraint of 30,000 rpm is placed by the mechanical strength of the rigid rotor.

3.3.2 Amplifier specification

The amplifier specifications are obtained from the maximum slew rate needed to implement the desired control. The maximum slew rate is calculated by determining the maximum change in force over a period of time. The maximum rotational speed of 30,000 rpm relates to a rotational frequency (f_{rot}) of 500 Hz. The resulting force caused by an unbalance on the shaft will represent a sinusoidal function with the same frequency as the rotational frequency. In order to utilise the full range of the magnetic arrangement the maximum amplitude of this unbalance force is chosen to be 500 N. The unbalance force will increase from zero to the maximum amplitude in a quarter of the period. A redundancy factor (RF) of 5 is included to ensure that the maximum specified slew rate will be greater than the maximum slew rate required by the physical system. The maximum slew rate is determined using (3-1).

$$\begin{aligned} \frac{dF}{dt} &= RF \cdot F_{\max} \cdot f_{rot} \cdot 4 \\ &= 5 \cdot 500 \cdot 500 \cdot 4 \ \text{N/s} \\ &= 5 \times 10^6 \ \text{N/s} \end{aligned} \tag{3-1}$$

The power amplifier maximum VA rating is now determined using (3-2) with the maximum slew rate.

$$\begin{aligned} VA_{\max} &= \frac{dF}{dt} \cdot g_0 \\ &= 5 \times 10^6 \cdot 0.6 \times 10^{-3} \ \text{VA} \\ &= 3 \times 10^3 \ \text{VA} \end{aligned} \tag{3-2}$$

With the maximum VA rating specified the maximum voltage is chosen to be 310 V which is equal to the rectified 220 V supply and the current rating is obtained using (3-3).

$$I_{sat} = \frac{VA_{max}}{V_{max}} \quad (3\text{-}3)$$
$$= \frac{3\times10^{3}}{\sqrt{2}\cdot 220} \text{ A}$$
$$= 9.64 \text{ A}$$

The number of turns per coil is now determined using (3-4).

$$N = \frac{B_{sat}\cdot g_0}{I_{sat}\cdot \mu_0} \quad (3\text{-}4)$$
$$= \frac{1\cdot 0.6\times10^{-3}}{9.64\cdot 4\cdot \pi\times10^{-7}} \text{ turns}$$
$$\approx 50 \text{ turns}$$

3.3.3 *Journal sizing and stator design*

Figure 3-3 displays the mechanical layout of the electromagnetic design with the relevant dimensions.

r_s	stator radius
r_c	coil space radius
r_j	journal radius
r_r	rotor shaft radius
r_p	pole radius
g_0	air gap
w	pole width
n	number of poles
l	axial length
a_r	journal stator aspect ratio $(r_j-r_r)/w$
A_g	air gap area
N	number of coil turns

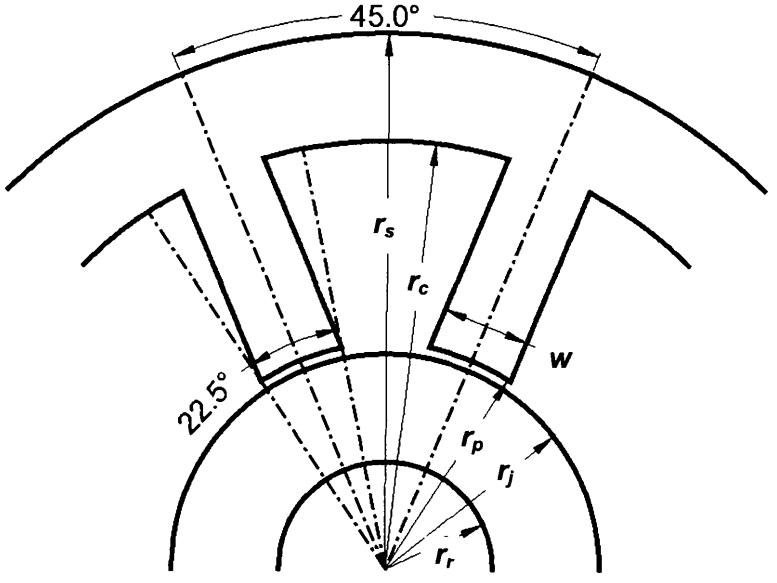

Figure 3-3 Stator iron geometry [13]

A maximum load capacity per unit area constraint is placed on an AMB due to material properties such as flux saturation and maximum current density. This implies that the peak load

capacity dictates the air gap area. Using the configuration as shown in Figure 3-3 and (2-9) the air gap area is obtained using (3-5).

$$A_g = \frac{\mu_0 \cdot F_{max}}{B_{sat}^{\ 2} \cdot \cos(\theta) \cdot \left(\frac{\sin\left(\frac{\theta}{2}\right)}{\frac{\theta}{2}} \right)^2} \tag{3-5}$$

$$= 688.895 \times 10^{-6} \text{ m}^2$$

Using an aspect ratio (AR) of 1.368 between the rotor lamination material width (r_j - r_r) and the pole width (w), the pole width is determined using (3-6).

$$w = \frac{\theta \cdot (r_r + g_0)}{1 - \theta \cdot AR} \tag{3-6}$$

$$= 13.98 \times 10^{-3} \text{ m}$$

The journal outside radius is now determined using (3-7).

$$r_j = w \cdot AR + r_r \tag{3-7}$$

$$= 35 \times 10^{-3} \text{ m}$$

The axial length of the journal can now be determined using (3-8)

$$l = \frac{A_g}{w} \tag{3-8}$$

$$= 49.277 \times 10^{-3} \text{ m}$$

$$\cong 50 \times 10^{-3} \text{ m}$$

3.3.4 Coil design

Since this is a test model, removable coils are implemented in order to allow the interchanging of coils. Figure 3-4 displays the removable coil configuration with the applicable coil design parameters.

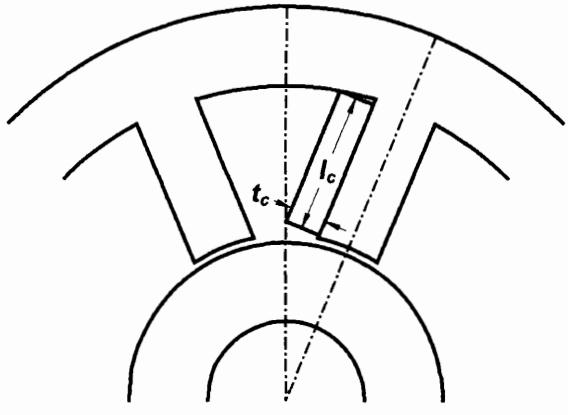

Figure 3-4 Removable coil configuration [13]

These parameters are obtained using:

$$t_c = r_p \cdot \tan\left(\frac{\pi}{n}\right) - \frac{w}{2} \qquad (3\text{-}9)$$
$$= 7.756 \times 10^{-3} \text{ m}$$

with n the number of pole pairs [13]. Using the thermal limit of 3x10^6 A/m^2 (J_{rms}), and a copper fill factor of 0.5 (FF_c), the coil window area is determined using (3-10).

$$A_v = \frac{N \cdot I_{rms}}{FF_c \cdot J_{rms}} \qquad (3\text{-}10)$$
$$= 166.667 \times 10^{-6} \text{ m}^2$$

From (3-9) and (3-10) l_c is obtained using (3-11).

$$l_c = \frac{A_v}{t_c} \qquad (3\text{-}11)$$
$$= 21.489 \times 10^{-3} \text{ m}$$

The coil space radius r_c can now be determined using (3-12).

$$r_c = \sqrt{\left(l_c + r_p\right)^2 + \left(\frac{w}{2} + t_c\right)^2} \qquad (3\text{-}12)$$
$$= 58.963 \times 10^{-3} \text{ m}$$
$$\cong 60 \times 10^{-3} \text{ m}$$

The pole length is obtained from the coil space radius r_c and the pole radius r_p using (3-13).

$$l_p = r_c - r_p \qquad (3\text{-}13)$$
$$= 24.4 \times 10^{-3} \text{ m}$$

The stator radius is obtained using (3-14).

$$r_s = r_c + w \qquad (3\text{-}14)$$
$$= 73.98 \times 10^{-3} \text{ m}$$
$$\cong 75 \times 10^{-3} \text{ m}$$

3.3.5 Coil resistance and inductance

The wire size needed for this configuration is determined using (3-15).

$$r_{wire} = \sqrt{\frac{FF_c \cdot A_v}{\pi \cdot N}} \qquad (3\text{-}15)$$
$$= 0.73 \text{ mm}$$

A standard wire diameter of $1.4\text{x}10^{-3}$ mm is sourced. The wire copper area is now obtained using (3-16).

$$A_{wire} = \pi \cdot (r_{wire})^2 = 1.539 \times 10^{-6} \text{ m}^2 \quad \textbf{(3-16)}$$

The coil length (l_{coil}) is obtained by determining the pole perimeter using (3-17).

$$l_{coil} = 4 \cdot N \cdot [(t_c + w) + (t_c + l)] = 15.898 \text{ m} \quad \textbf{(3-17)}$$

A copper specific resistance (ρ_c) of $1.912\text{x}10^{-8}$ Ω.m is used to determine the coil resistance as shown in (3-18).

$$R_{coil} = \rho_c \cdot \frac{l_{coil}}{A_{wire}} = 0.197 \ \Omega \quad \textbf{(3-18)}$$

The coil inductance (L_c) is now obtained using (3-19).

$$L_c = \frac{2 \cdot \mu_0 \cdot A_g \cdot N^2}{g_0} = 7.2 \text{ mH} \quad \textbf{(3-19)}$$

3.3.6 AMB stiffness and damping

Magnetic actuator forces change with both current and air gap. A linearized equation for the instantaneous force as a function of current and displacement is given by (3-20).

$$F(x,i) = k_s x + k_i i \quad \textbf{(3-20)}$$

The ratio of a change in force due to a change in current is called the current gain (k_i) and the ratio of a change in force due to a change in position is called the position stiffness (k_s). As discussed in section 2.4.1, it is clear that the position stiffness and current gain can now be determined by calculating the partial derivative of the force equation with respect to displacement and current at the working point. The force generated by a single power amplifier and a set of coils can be described by (3-21).

$$F = \frac{B^2 A_g}{\mu_0} \cos(\theta) = \frac{\mu_0 N^2 {i_m}^2 A_g}{{x_s}^2} \cos(\theta) \quad \textbf{(3-21)}$$

The correction factor due to the pole geometry found in (2-9) is excluded in (3-21) resulting in a 1.6 % error which is acceptable for this application.

The current gain for a single actuator is defined as

$$k_i = \left.\frac{\partial F}{\partial i_m}\right|_{i_m=i_0,\ x_s=g_0} = 2\frac{\mu_0 N^2 i_0 A_g}{g_0^{\ 2}}\cos(\theta) \tag{3-22}$$

where the derivative is evaluated with a control current equal to zero and a rotor position of $x = 0$. The current gain is positive because an increase in current produces an increase in force. The position stiffness for a single actuator is defined as

$$k_s = \left.\frac{\partial F}{\partial x_s}\right|_{i_m=i_0,\ x_s=g_0} = -2\frac{\mu_0 N^2 i_0^{\ 2} A_g}{g_0^{\ 3}}\cos(\theta) \tag{3-23}$$

where the derivative is evaluated with a control current equal to zero and a rotor position of x = 0. The position stiffness is negative as the force increases with a decreasing air gap.

To obtain the desired bearing stiffness and damping the PD controller parameters are determined using (2-23) and (2-24). The proportional constant is obtained using (3-24).

$$K_P = \frac{\frac{k_{eq}}{2} + k_s}{k_i} = 12502 \tag{3-24}$$

Take note, k_s assumes positive values due to chosen position reference. The derivative constant is determined using (3-25).

$$K_D = \frac{b_{eq}}{2k_i} = 37.5 \tag{3-25}$$

3.4 System Modelling

In the process of designing and implementing a controller for a system such as an AMB an accurate model of the system becomes an invaluable tool. Figure 3-5 displays a nonlinear model that was used to simulate the system in MATLAB®.

The actual rotor position is subtracted from the reference position to generate an error signal. A single PD controller then generates an appropriate current reference signal (i_{ref}). The current reference signal is then added and subtracted from a bias current signal (i_{0ref}) to produce reference signals i_{m1ref} and i_{m2ref} for the top and bottom power amplifiers (PAs) respectively. The actuator characteristic equation then converts the currents produced by the PAs to forces. The two forces are opposing and therefore subtracted from each other. The rotor acceleration is obtained by dividing the resulting force with the rotor mass. The rotor position is then determined from the rotor acceleration.

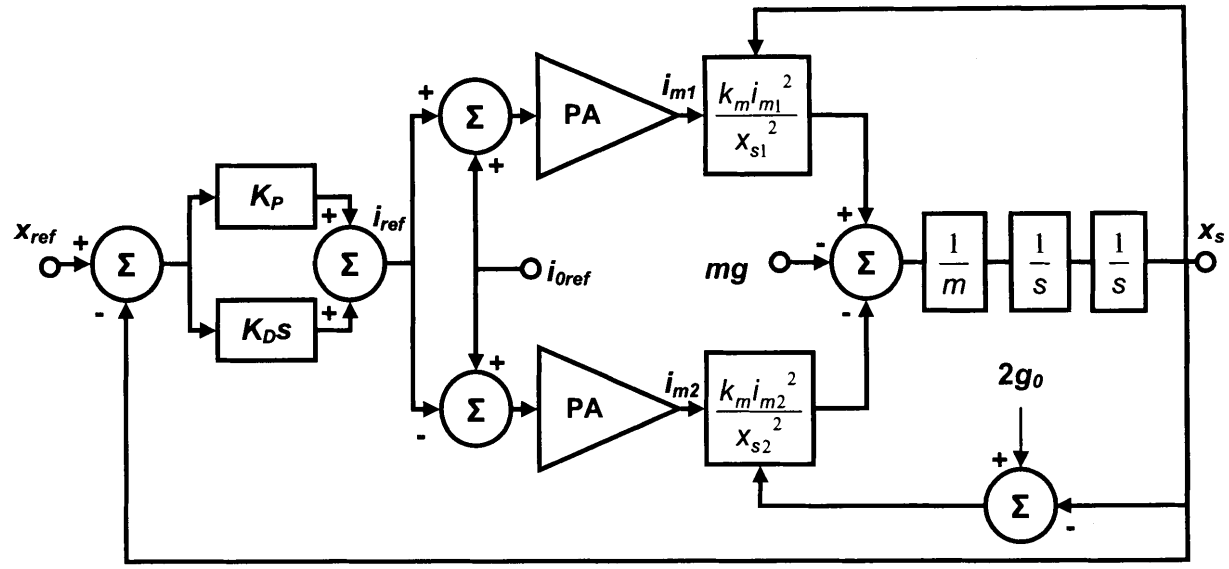

Figure 3-5 Simulation block diagram

The simulation program contains the nonlinear force to displacement relationship as well as the nonlinear force to current relationship. It also accurately simulates the switch-mode PA which switches at a 100 kHz. The simulation sampling rate was chosen to be 10 MHz which is a factor 100 greater than the switching frequency. The digital controller that will be implemented with dSPACE® however cannot operate at such high frequencies and practical sampling rates are in the order of 20 kHz. In order to accurately simulate the PA and at the same time implement realistic controller sampling rates, the simulation was programmed so that the controller operates at a fixed frequency much lower than the simulation sampling rate. The MATLAB® source code for the simulation can be found on the data CD in Appendix E

The analytical bearing stiffness and damping are now verified using the simulation. Since only proportional and differential control are implemented a relatively large (79 µm) steady state error occurs in the vertical axis due to the rotor mass as shown in Figure 3-6 where zero indicates the rotor centre position.

The result obtained from the vertical step response may not show satisfactory correlation to the calculated values since the calculation utilises linearised force functions which is only valid if the rotor is in the centre of the two actuators. The steady state error may however be used to calculate the bearing stiffness as shown in (3-26).

$$k_{eq} = \frac{F}{x} = \frac{mg}{x} = \frac{3.86 \cdot 9.81}{79 \times 10^{-6}} \text{ N/m} \qquad \textbf{(3-26)}$$
$$= 479 \times 10^3 \text{ N/m}$$

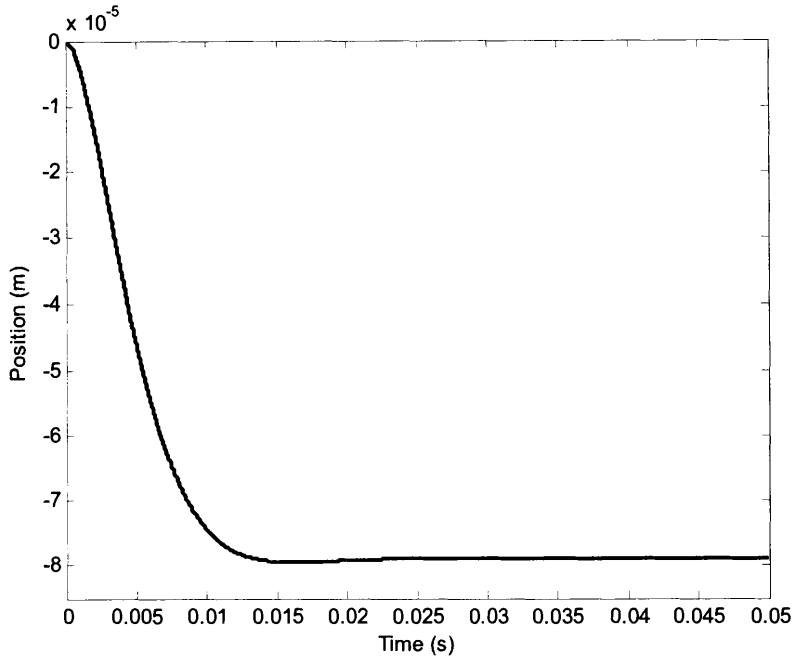

Figure 3-6 Steady state error due to rotor mass

This result reveals a 4.2 % deviation between the calculated and simulated responses. In order to verify the calculated bearing stiffness and damping using a step response a moderate (0.05 mm) step is taken in the positive direction on the horizontal axis. Figure 3-7 shows the step at 0.0125 s.

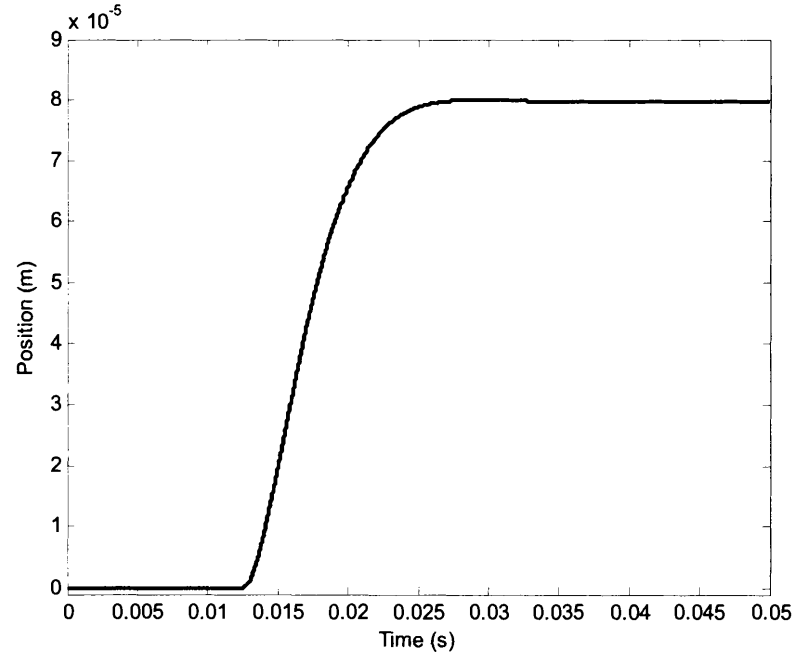

Figure 3-7 Step Response in horizontal axis

From Figure 3-7 the percentage overshoot (*P.O.*) is obtained using (3-27)

$$P.O. = \frac{80.046\times10^{-6} - 79.632\times10^{-6}}{79.632\times10^{-6}}\times 100\ \% \qquad (3\text{-}27)$$
$$= 0.52\%$$

and settling time (T_s) (to within 2 % of the final value) is determined as 0.0117 s. As shown in section 2.5 this system can be seen as a second-order system close to its working point. It is for this reason that a step response can be used to obtain the equivalent stiffness and damping value of the system. The equivalent bearing stiffness and damping are now obtained using the process outlined in [19]. The system damping ratio is obtained using (3-28).

$$P.O. = 100e^{\frac{-\pi\zeta}{\sqrt{1-\zeta^2}}} \qquad (3\text{-}28)$$
$$\therefore\ \zeta = 0.859$$

The natural frequency of the system is now determined using (3-29).

$$\omega_n = \frac{4}{T_s\zeta} = 396.8\ \text{rad/s} \qquad (3\text{-}29)$$

The equivalent stiffness for the system is now obtained using (3-30).

$$k_{eq} = \omega_n{}^2 m = 608\times10^3\ \text{N/m} \qquad (3\text{-}30)$$

The system's equivalent damping value is determined using (3-31).

$$b_{eq} = \zeta\left(2\sqrt{k_{eq}\cdot m}\right) = 2.63\times10^3\ \text{N.s/m} \qquad (3\text{-}31)$$

From these results a 22 % deviation from the predicted value for the equivalent stiffness is noted and a 5.2 % deviation in the equivalent damping value. These deviations may be attributed to the accuracy of the determined *P.O.* and T_s values and other nonlinearities such as slope compensation incorporated in the simulation. Since the amplifier controls the maximum peak current, slope compensation causes the average coil current to be less than the desired current. This in effect lowers the bias current (i_0) level so that k_i decreases proportionally as shown in (3-22) and k_s decreases in the square as shown in (3-23). This will cause the equivalent stiffness to increase as shown in (2-24) and explains the deviation of the simulated and analytical results. When the amount of slope compensation added to the current signal is reduced the results obtained from the step response correlates more closely to the predicted results.

In order to verify the simulation model with the physical model a series of step responses are performed in both the vertical and horizontal axes. The step size is enlarged to ensure that the nonlinear nature of the system can be compared to that of the simulation model. Figure 3-8 displays a 100 µm step in the positive direction on the horizontal axis. The 100 µm step in the

reference position is implemented at 0.0125 s. The system displays very little overshoot and a rather large steady-state error (58 μm). The parameters obtained from the step response are as follows: $P.O.$ = 0.32 %, ζ = 0.877, T_s = 0.012 s, k_{eq} = 555x10^3 N/m and b_{eq} = 2.569 x10^3 N.s/m.

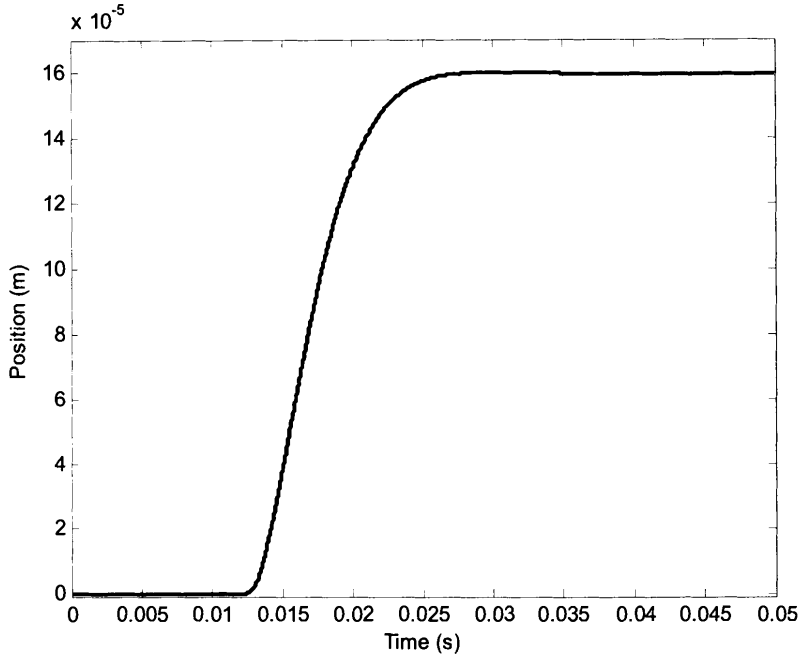

Figure 3-8 Step response in horizontal axis (100 μm reference)

Figure 3-9 displays a 100 μm step in the positive direction on the vertical axis. This predicted response will also be compared to the system's actual response and is a good measure to correlate the nonlinearities.

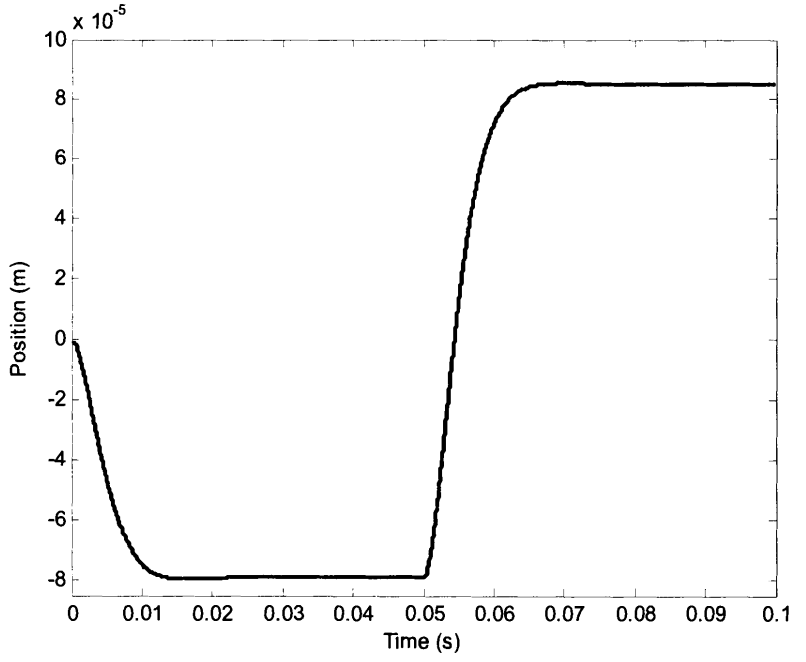

Figure 3-9 Step response in vertical axis (100 μm reference)

3.5 Rotor design and dynamic analysis

Taking into account the maximum model size and the maximum operating speed as well as the third critical frequency, a shaft is designed. Rotordynamic analyses are done using analytical methods and rotordynamics software. The rotor design is adapted until it displays the desired characteristics. The required bearing stiffness, damping and positions are obtained from the rotor analyses.

Dyrobes® rotordynamic analysis software is used to conduct the finite element rotordynamic analyses. Figure 3-10 displays the rotor model used in the dynamic analyses. A stiffness value of 500×10^3 N/m and a damping value of 2.5×10^3 N.s/m is used to simulate the AMBs at stations 5 and 31. An imbalance of 35 g.mm is assumed since this represents a realistic imbalance value obtainable during rotor manufacturing.

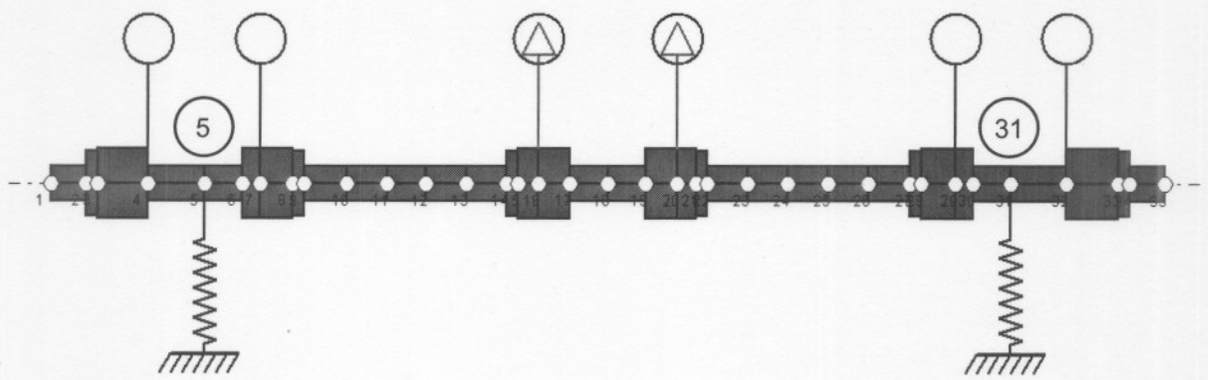

Figure 3-10 AMB flexible rotor test model

Figure 3-11 displays the first predicted critical frequency and the corresponding mode shape. This is the first rigid-rotor mode, since very little shaft bending is involved, where the shaft traces a cylinder.

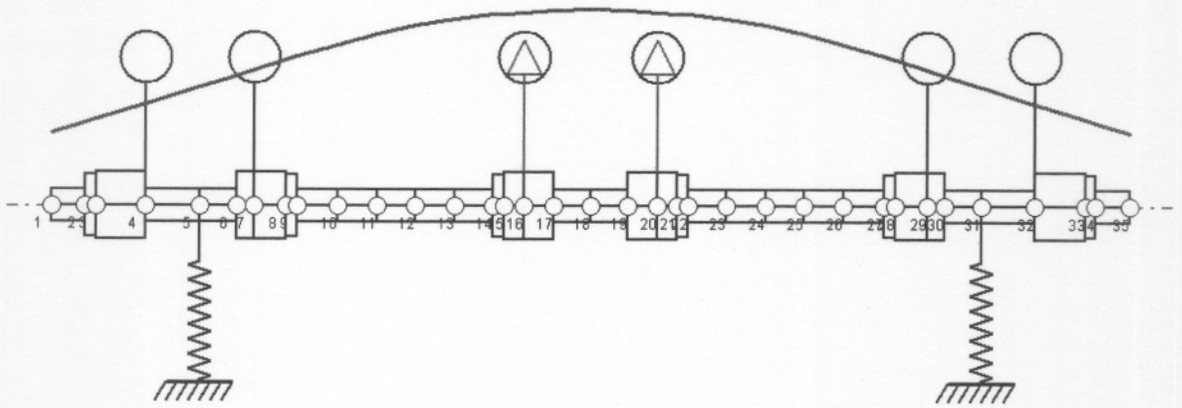

Figure 3-11 First critical speed mode shape (2,947 rpm)

The second rigid-rotor mode will trace two cones with a common apex at mid-span as shown in Figure 3-12. This critical frequency is predicted at 4,637 rpm.

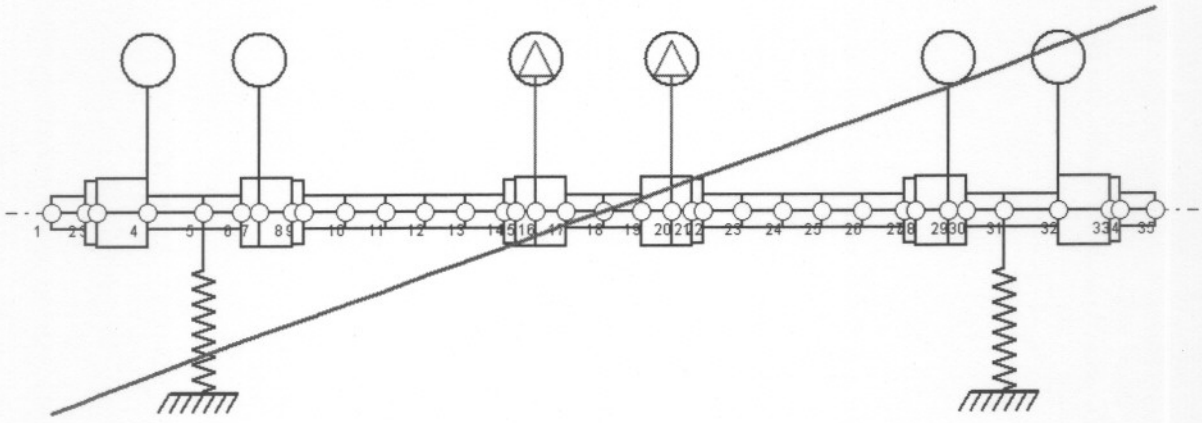

Figure 3-12 Second critical speed mode shape (4,637 rpm)

The third critical frequency involves shaft bending and is known as the first bending mode. Figure 3-13 displays the first bending mode shape at 7,276 rpm.

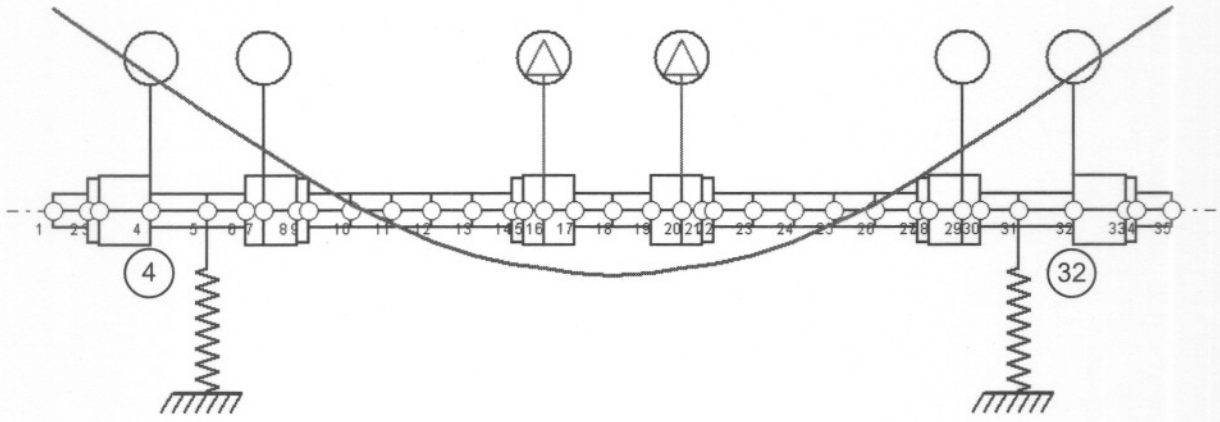

Figure 3-13 Third critical speed mode shape (7,276 rpm)

Important to note in Figure 3-13 is the shaft displacement at the magnetic bearing locations. It is very important to ensure that the AMBs are capable of implementing damping in order to attenuate the maximum bending amplitude. Another crucial factor is to ensure that there are no nodes between the AMB location and the displacement sensor. The displacement sensors will be located at stations 4 and 32.

The first three critical frequencies are well below the maximum operating speed of 10,000 rpm. The shaft is also analysed to ensure the structural integrity at 10,000 rpm. The fourth critical frequency is also analysed to ensure that it does not fall within the shaft's operating range.

Figure 3-14 displays the fourth critical frequency and corresponding mode shape. This critical frequency is predicted at 26,533 rpm which is well above the maximum operating speed of the shaft. This mode shape traces a sinusoidal function and as shown has very little displacement at the AMB locations.

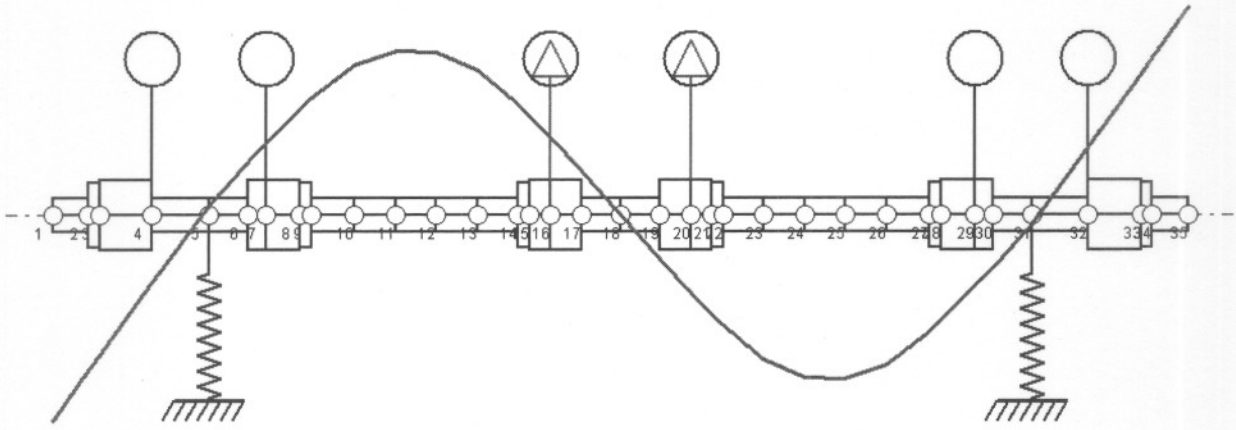

Figure 3-14 Fourth critical speed mode shape (26,533 rpm)

A critical speed map for the first four critical frequencies is displayed in Figure 3-15. From the results it is clear that the first two rigid-rotor critical frequencies are sensitive to the amount of support stiffness involved while the third and fourth critical frequencies (bending modes) display very little sensitivity to support stiffness.

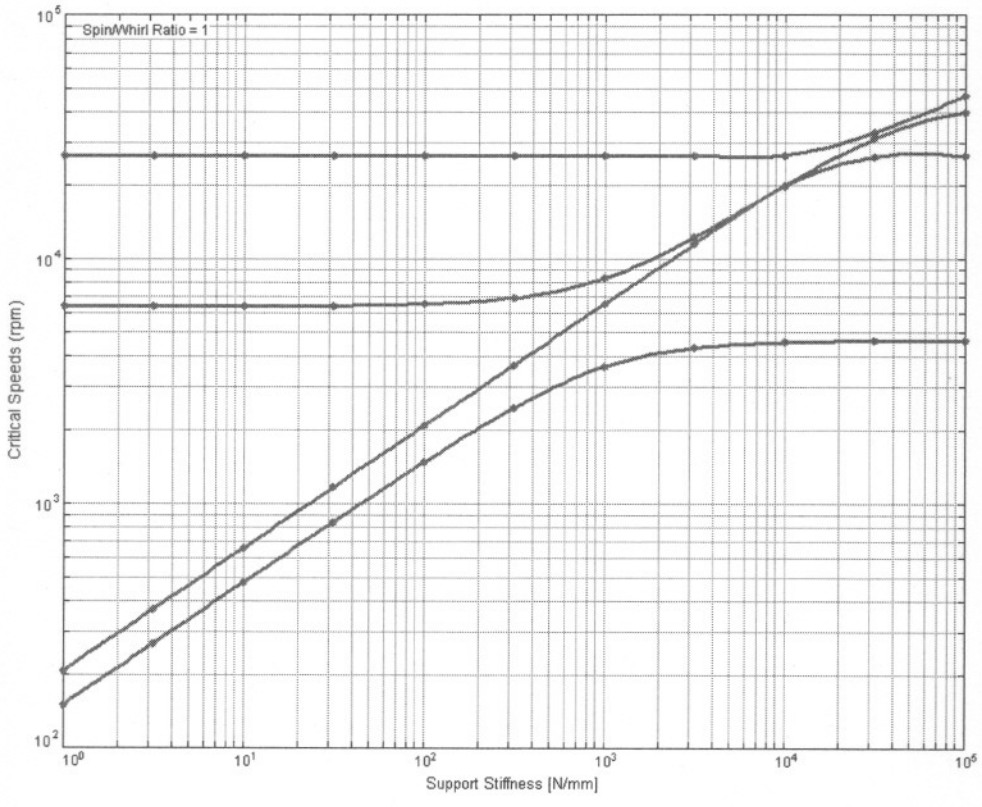

Figure 3-15 Critical speed map

Figure 3-16 displays the rotor unbalance response displacements at stations 5 and 18 respectively. Station 5 represents the magnetic bearing centre and can be compared to the displacement sensor data. Station 18 represents the centre mass and can be compared to the data obtained from the displacement sensor situated at station 16.

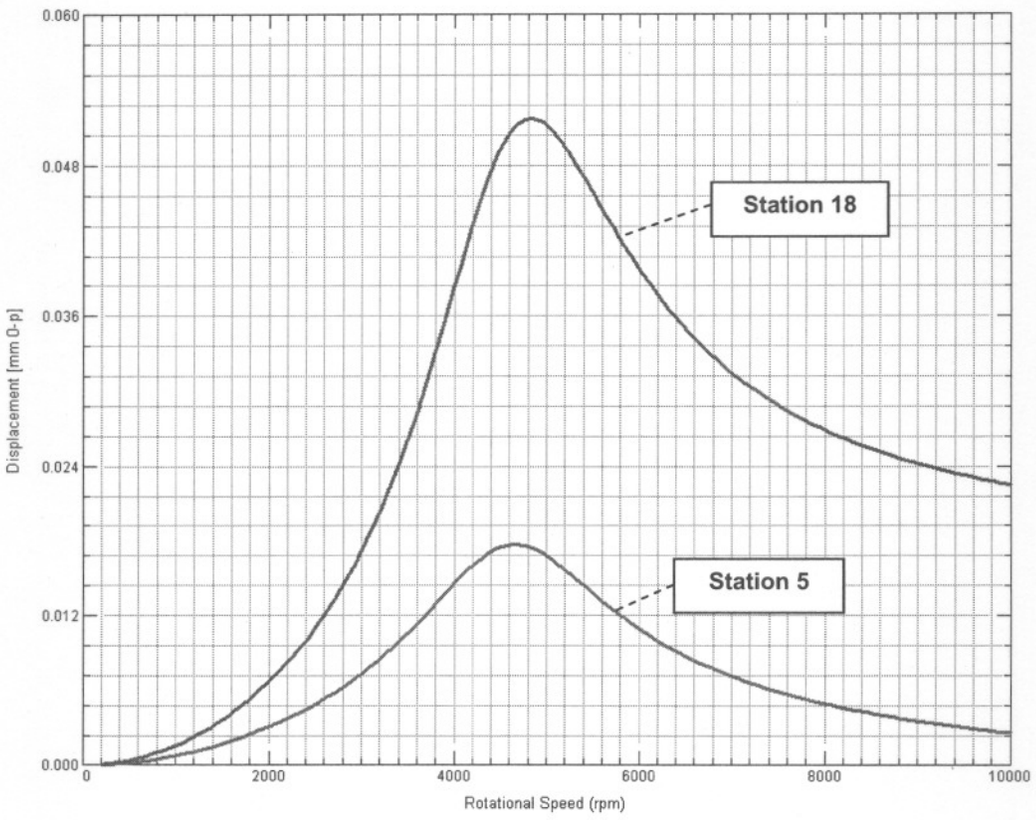

Figure 3-16 Unbalance response: Displacement at Station 5 (peak response = 0.0177 mm at 4,600 rpm) Station 18 (peak response = 0.0518 mm at 4,800 rpm)

The predicted displacements are within range and the dynamic analysis confirms that the rotor will be stably suspended up to the maximum working speed of 10,000 rpm.

3.6 Design implementation

The magnetic circuit is manufactured from silicon steel laminations. The rotor lamination inside diameter is punched to ensure precision and repeatability. A H7T6 press fit is used to secure the rotor laminations to a mild steel bobbin which in turn is secured to the 16 mm stainless steel shaft by means of Trantorque units. The centre mass is also fitted to the shaft with Trantorque units.

Figure 3-17 displays the CADKEY® model of the flexible rotor. This configuration was chosen since it simplifies the manufacturing process.

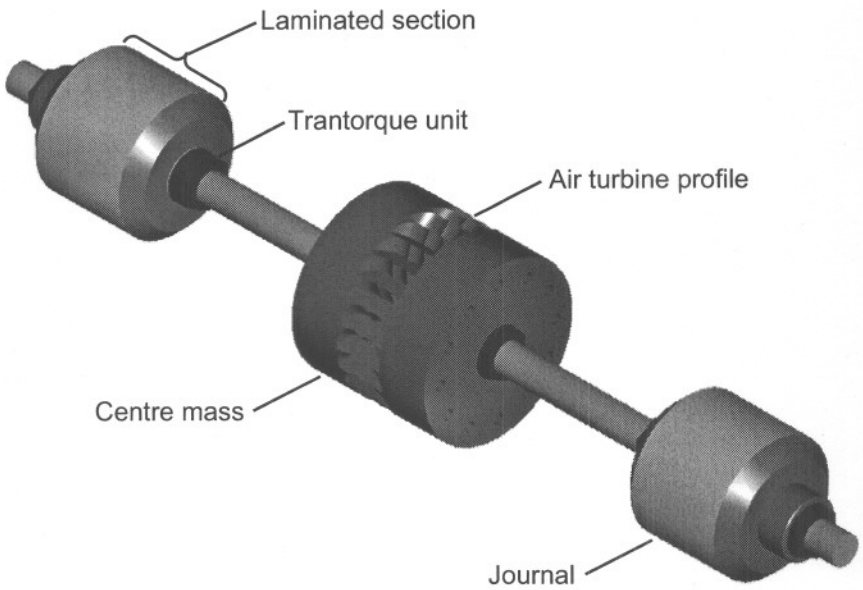

Figure 3-17 Flexible rotor CADKEY model

The tapped holes on the sides of the centre mass are included for unbalance response measurements and the machined profile on the centre mass is part of the air turbine propulsion system. Detailed manufacturing drawings of the flexible rotor are included in Appendix B

Figure 3-18 displays the AMB stator housing and connector box. The eight-pole heteropolar stator lamination pack and coils are also visible. The connector box houses 4 sub-D type connectors which are used to connect each pole pair to a power amplifier.

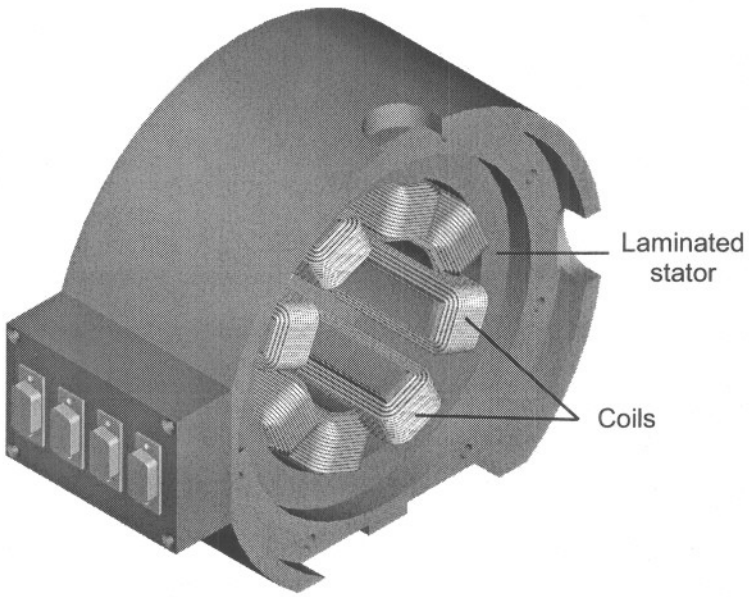

Figure 3-18 AMB Stator housing

The stator laminations are laser cut from the same material used to manufacture the rotor laminations. The stator packs are interference fitted in the stator housing which are manufactured from 220 mm aluminium round bar. Aluminium is used since it is a nonferrous material and aesthetically appealing. Detailed manufacturing drawings are included in Appendix B.

Figure 3-19 displays the double radial AMB model overview which comprises two heteropolar radial AMBs, an air turbine propulsion unit and a flexible shaft. The backup bearing is manufactured from a material called vesconite used in preference to brass. These components are fitted to a 25 mm mild steel base plate. The space on the front of the base plate is used to house the eight power amplifiers.

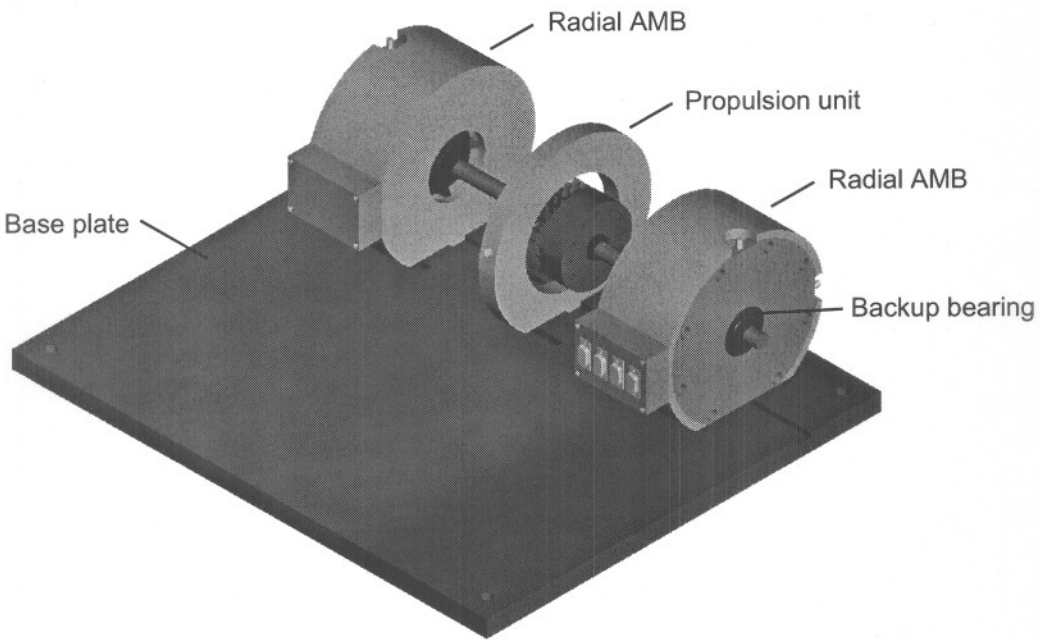

Figure 3-19 Double radial AMB model overview

The power amplifiers used for this specific application are designed in chapter 4 and the system interface is discussed in chapter 5.

Chapter 3 discussed the design process involved in developing a double radial flexible rotor AMB system. A detailed electromagnetic design as well as a system simulation and rotordynamic analysis are also included. The design implementation is also briefly discussed. The power amplifier design and development are discussed in chapter 4.

4
Chapter
Power Amplifier Design

Chapter 4 contains detailed design discussions of the power amplifier imbedded in the active magnetic bearing system. A detailed specification is followed by designs of the various components contained in the switch-mode peak current-mode controlled power amplifier. In conclusion some results obtained during testing are shown.

4.1 Power Amplifier Specification

Power amplifiers (PAs) are essential components of any active magnetic bearing (AMB) system. A PA converts a control signal, produced by the dSPACE® real-time development tool, to a current in an AMB coil to generate the force required to stably suspend a body at the reference position. The AMB is thus current controlled. Figure 4-1 displays a functional block diagram of the power amplifier.

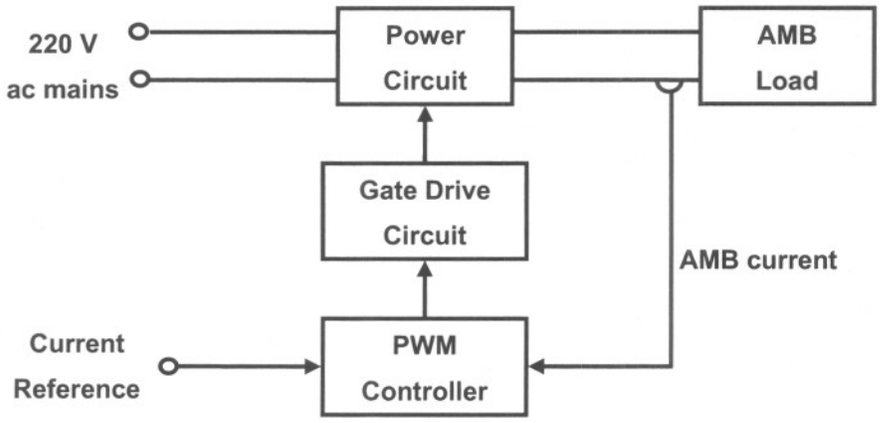

Figure 4-1 Power Amplifier functional block diagram

The power amplifier maximum ratings are obtained from section 3.3.2. By rectifying the 220 V alternating current (ac) mains a direct current (dc) bus voltage of 310 V is obtained. The PWM controller senses the coil current and generates the appropriate PWM control signal which is applied to the switching components by the gate drive circuit. The PWM controller adjusts the

PWM signal to ensure that the actual coil current follows the reference current. The coil current should be adjustable from a minimum of 0 A to a maximum of 10 A. The PA should also display a linear relationship between the reference current signal and the coil current. As stated in section 3.4 a switching frequency of 100 kHz is used and an H-bridge with two quadrant control is implemented. The PA bandwidth is specified as 5 kHz, an order in magnitude higher than the maximum rotating frequency of the system (500 Hz).

The PA must operate at a maximum ambient temperature of 25 °C and must be thermally protected. The PA must also be short-circuit protected. Appropriate electromagnetic compatibility (EMC) measures should be taken to prevent the PA from interfering with the AMB.

4.2 Power Circuit Design

The power circuit is divided into three sub-systems; the rectifier, input filter and the H-bridge. Figure 4-2 displays the functional block diagram of the power circuit.

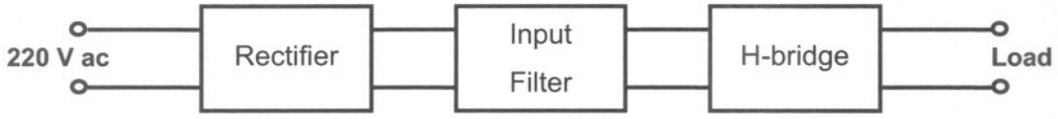

Figure 4-2 Power circuit functional block diagram

The following sections contain detailed design discussions of the sub-systems mentioned.

4.2.1 H-bridge Design

Figure 4-3 displays the H-bridge which comprises two controllable switches and two diodes. For the purpose of this discussion a decoupling capacitor (C_{dec}) is assumed part of the H-bridge. The first step in designing the H-bridge is the process of specifying the switching components.

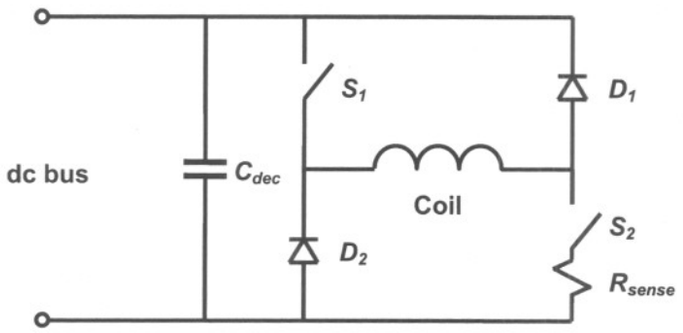

Figure 4-3 H-Bridge

There are several factors to take into account when specifying controllable switches:

- Power capability (Voltage and current rating)
- Switching speed (Hard/soft switching)
- Drive circuit requirements
- Protection
- Losses

The specific controllable switch must be able to withstand a dc voltage of at least 310 V, conduct a maximum current of 10 A at 50 % duty cycle and must be able to operate at a switching frequency of 100 kHz in the hard switched mode. Two types of controllable switching devices are typically considered for this specific application; the metal-oxide semiconductor field-effect transistor (MOSFET) and the insulated-gate bipolar transistor (IGBT).

Both the MOSFET and the IGBT meet the required power capability and switching speed for this specific configuration. They both require relatively simple drive circuits and with the correct layout require no protection in the form of snubber circuits.

The MOSFET displays a significant increase in on-state resistance with an increase in temperature while the corresponding increase in on-voltage in an IGBT is very small. This results in an increase of up to a factor 3 in the on-state voltage of the MOSFET with only a small increment in the on-state voltage of the IGBT when the temperature rises from room temperature to the maximum value. This renders the IGBT ideally suited for applications which require operation at high temperatures. The on-state voltage of the MOSFET also increases as the blocking voltage specification increases while identical conditions result in a relatively small increase in the IGBT on-state voltage. In conclusion, MOSFETs are suited for applications which require low blocking voltages and high operating frequencies whereas IGBTs are the preferred devices for applications requiring high blocking voltages and lower operating frequencies [20].

As this PA requires a medium operating frequency and a high blocking voltage both devices were considered. An IGBT device, the IRG4PC50W, specifically designed for switch-mode power supplies were compared to a MOSFET device, the APT5020BNFR which displays very low on resistance. Both these devices were tested in the PA circuit with and without external snubbering circuits. The root mean square (rms) input current for the different configurations was recorded at an H-bridge voltage of 310 V and an average output current of 9 A . These results are summarised in Table 4-1.

The total power loss of the PA and coil can be expressed as

$$P_{loss} = V_{rms} I_{rms} PF \tag{4-1}$$

with V_{rms} the rms input voltage, I_{rms} the rms input current and PF the power factor. Since V_{rms} remains the same for all the configurations and with an insignificant variation in PF, the rms input current is a good indication of the amount of power being dissipated. The voltage applied to the coil and the coil current also remain unchanged which implies that the change in rms input current is due to the change in the switching losses.

Table 4-1 Comparison of MOSFET and IGBT device losses

	MOSFET APT5020BNFR	**IGBT IRG4PC50W**
With snubber	I_{rms} = 0.870 A	I_{rms} = 0.750 A
Without snubber	I_{rms} = 0.820 A	I_{rms} = 0.650 A

Table 4-1 shows that the configuration which incorporates the IGBTs without the snubber circuit displays the lowest losses. The IRG4PC50W IGBT device is chosen and implemented in the design.

When specifying power diodes the following factors are taken into account:

- Current carrying capability (I_F)
- Reverse blocking voltage specification (V_R)
- Reverse recovery time (t_{rr})

There are several types of power diodes available, each suited for a particular application. For this specific application, a fast recovery diode will be used. Fast recovery diodes are required for operation in high-frequency circuits in combination with controllable switches to minimise device losses. An ultrafast soft recovery diode the HEXFRED HFA15PB60 was identified which is ideally suited for applications in power supplies and power conversion systems.

With the switching components identified the next step is the decoupling capacitor design. This capacitor provides a low impedance path for the high frequency currents. The WIMA MKP 10 capacitor is especially designed for applications in switch-mode power supplies. Situating the capacitor as close as possible to the H-bridge with the correct layout, as discussed in section 4.8, together with the capacitor's low equivalent series resistance (ESR) realise a low impedance path for the high frequency currents. This eliminates voltage spikes due to stray inductances and reduces noise transmission due to high frequency current loops.

The capacitance value is determined from the amount of current drawn from the capacitor and the allowable voltage ripple across the H-bridge. The AMB is simulated with an unbalance force equal to the maximum carrying force of the electromagnetic design at a frequency of 100 Hz. Figure 4-4 displays the simulated coil current of the top vertical actuator. This current is representative of the nominal load condition that the PA will be exposed to.

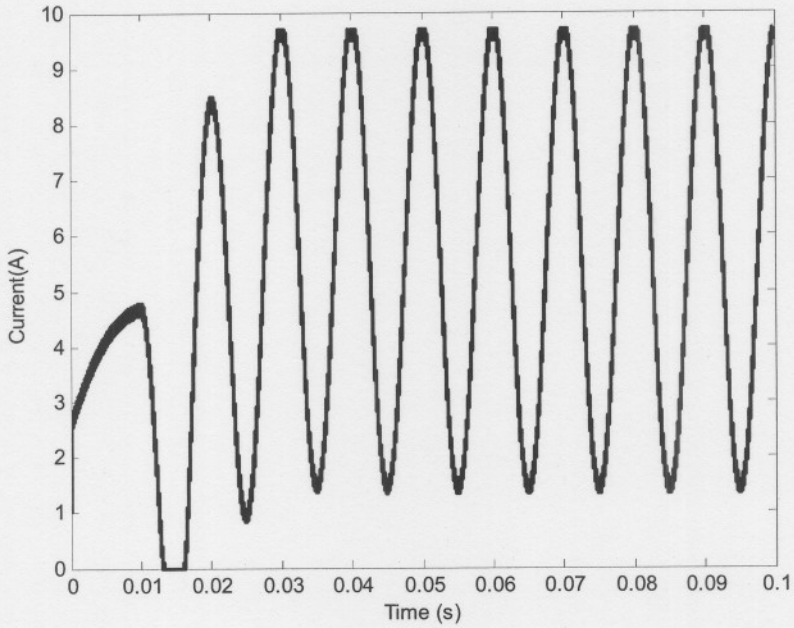

Figure 4-4 Simulated top vertical coil current

From the simulation the rms value of the coil current is determined to be 6.3 A and the average coil current 5.6 A. The average value for a maximum continuous current is determined to be 9.6 A. The decoupling capacitor should display a voltage ripple component of less than 10 % while supplying the maximum current. The capacitor value is determined using (4-2).

$$i = C_{dec}\frac{dv}{dt} \tag{4-2}$$

$$\therefore C_{dec} = i\frac{\Delta t}{\Delta v}$$

$$= 9.6\frac{5\times10^{-6}}{0.1\cdot 310}\ \text{F}$$

$$= 1.55\ \mu\text{F}$$

A 1.5 µF capacitance value is chosen. The dissipation factor (*DF*) for the 1.5 µF MKP 10 capacitor at 100 kHz is estimated from the data sheet to be $20\text{x}10^{-4}$. This value may however be highly inaccurate. The ESR of the capacitor is determined using (4-3).

$$\text{ESR} = \frac{\tan\delta}{2\pi fC} \tag{4-3}$$

$$= \frac{20\times10^{-4}}{2\pi\cdot 100\times10^{3}\cdot 1.5\times10^{-6}}\ \Omega$$

$$= 2.12\ \text{m}\Omega$$

The power dissipation due to the capacitor's ESR and the rms current is obtained using (4-4).

$$P_{cap} = I_{rms}^{\ 2}\,\mathrm{ESR} \qquad (4\text{-}4)$$
$$= 6.3^2 \cdot 2.12 \times 10^{-3}\ \mathrm{W}$$
$$= 84.2\ \mathrm{mW}$$

The temperature rise (ΔT) as a result of the power dissipation is now determined using the specific dissipation (SD) obtained from the data sheet.

$$\Delta T = \frac{P_{cap}}{SD} \qquad (4\text{-}5)$$
$$= \frac{84.225 \times 10^{-3}}{0.025}\ ^{\circ}\mathrm{C}$$
$$= 3.4\ ^{\circ}\mathrm{C}$$

Voltage derating for this specific device only applies to temperature rises above 85 °C which implies that the maximum voltage rating of 400 V dc applies. This theoretical estimate of the temperature rise seems too low. The actual temperature rise will be measured.

Switch losses

The switching components incorporated in the H-bridge display non-ideal characteristics. These non-ideal characteristics cause the components to consume power. As the IGBT is operated in the hard switched mode it displays both conductive and switching power losses. The conductive losses are due to the on-state voltage drop across the device whereas the switching losses are due to the finite switching times.

From the data sheet of the IRG4PC50W the worst case total switching energy loss (E_{ts}) is given as 1.14 mJ under specific test conditions. These test conditions along with the conditions at which the IGBTs are operated in the power amplifier are summarised in Table 4-2.

Table 4-2 Total switching loss conditions

	Parameter	Test Conditions	Application Conditions
T_j	Junction temperature	150 °C	150 °C
I_C	Collector current	27 A	5.6 A
V_{cc}	Collector voltage	480 V	310 V
V_{GE}	Gate – Emittor voltage	15 V	15 V
R_G	Gate resistor	5 Ω	8 Ω

In order to use the total switching loss parameter obtained from the data sheet it must be scaled according to the varying factors. These factors are; the collector current, collector voltage and

gate resistor value. All of these factors are directly proportional to the switching losses. An estimate of the total switching energy is made using (4-6).

$$E_{ts-new} = \frac{I_{C-new}}{I_{C-old}} \frac{V_{CC-new}}{V_{CC-old}} \frac{R_{G-new}}{R_{G-old}} E_{ts-old} \tag{4-6}$$
$$= \frac{5.6}{27} \cdot \frac{310}{480} \cdot \frac{8}{5} \cdot 1.14 \times 10^{-3} \text{ J}$$
$$= 244.3 \times 10^{-6} \text{ J}$$

The switching power losses are now determined using the total switching energy together with the operating frequency in (4-7).

$$P_{sw} = E_{ts} f_s \tag{4-7}$$
$$= 244.3 \times 10^{-6} \cdot 100 \times 10^{3} \text{ W}$$
$$= 24.4 \text{ W}$$

The IGBT also displays conductive losses due to the on-state voltage drop across the collector-emittor terminals. The conductive losses are obtained from (4-8)

$$P_{on} = V_{CE(on)} I_C d \tag{4-8}$$
$$= 2.3 \cdot 5.6 \cdot 0.5 \text{ W}$$
$$= 6.4 \text{ W}$$

where d is the duty cycle and I_C the average collector current. The H-bridge is operated at a duty cycle close to 50 %.The total power losses for a single IGBT switch are determined using (4-7) and (4-8) in (4-9).

$$P_{IGBT} = P_{sw} + P_{on} \tag{4-9}$$
$$= 24.4 + 6.4 \text{ W}$$
$$= 30.8 \text{ W}$$

The losses contributed by the diodes can also be divided into switching losses and conductive losses. Using information obtained from the HFA15PB60 data sheet the switching losses for a single diode are estimated using (4-10)

$$P_{sw} = \frac{V_R I_{RRM} t_{rr} f_s}{2} \tag{4-10}$$
$$= \frac{310 \cdot 6.5 \cdot 74 \times 10^{-9} \cdot 100 \times 10^{3}}{2} \text{ W}$$
$$= 7.5 \text{ W}$$

where I_{RRM} is the maximum reverse recovery current and t_{rr} the reverse recovery time. The conductive losses are determined from the diode typical maximum forward voltage (V_{FM}) parameter obtained from the data sheet. The conductive losses are obtained from (4-11)

$$P_{on} = V_{FM} I_F d \tag{4-11}$$
$$= 1.3 \cdot 5.6 \cdot 0.5 \text{ W}$$
$$= 3.6 \text{ W}$$

with I_F the average forward current through the diode and d the duty cycle at 50 %. Using (4-10) and (4-11) the total power losses in one diode are determined using (4-12).

$$\begin{aligned} P_{Diode} &= P_{sw} + P_{on} \\ &= 7.5 + 3.6 \ \text{W} \\ &= 11.1 \ \text{W} \end{aligned} \tag{4-12}$$

Sense resistor losses

The last loss component in the H-bridge is the resistor used for current sensing. The choice of the specific resistor value is motivated and discussed in par 4.4.3. A 0.1 Ω sense resistor is used and situated just below switch S_2 in Figure 4-3. The resistor losses are determined using the rms current and the resistor value.

$$\begin{aligned} P_{R_{sense}} &= I_{rms}{}^2 R_{sense} d \\ &= 6.3^2 \cdot 0.1 \cdot 0.5 \ \text{W} \\ &= 2 \ \text{W} \end{aligned} \tag{4-13}$$

A non-inductive power metal film resistor was identified from the CADDOCK MP915 series. It is a heat sink mountable resistor capable of dissipating the specified power.

Total power losses

The total power losses in the H-bride are determined using (4-14).

$$\begin{aligned} P_{H-Bridge} &= 2(P_{IGBT}) + 2(P_{Diode}) + P_{R_{sense}} \\ &= 2(30.8) + 2(11.1) + 2 \ \text{W} \\ &= 85.8 \ \text{W} \end{aligned} \tag{4-14}$$

These losses are transformed into heat which is conducted away from the components using a heat sink. In section 4.2.4 an appropriate heat sink is specified which ensures that the devices operate within their specified safe operating limits. Figure 4-5 displays the final H-bridge circuit diagram.

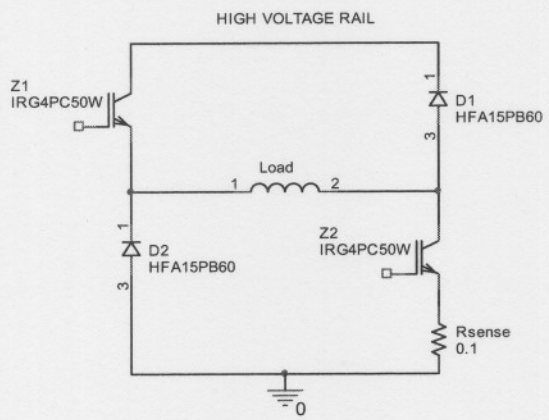

Figure 4-5 Final H-bridge circuit diagram

4.2.2 Rectifier Design

The rectifier generates the dc bus voltage by rectifying the ac supply voltage. It also supplies the power dissipated in the H-bridge and load. In order to specify and design the components involved, the load power is first determined. Figure 4-6 displays the proposed rectifier circuit diagram.

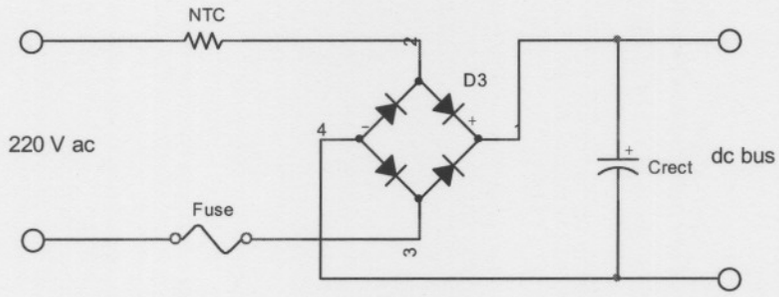

Figure 4-6 Rectifier circuit diagram

Load Power

The load power supplied by the power amplifier may be divided into three components namely copper losses, core losses and work done on the suspended body. The copper losses together with the losses due to the work done on the suspended body are obtained from the simulation. With a sinusoidal disturbance force of 500 N at a frequency of 100 Hz the losses obtained from the simulation are 34.2 W. This result is obtained by determining the average power supplied by the H-bridge to the load. Using the simulated rms coil current of 6.3 A together with the copper resistance of 0.172 Ω, the copper losses are determined using (4-15).

$$P_{copper} = I_{rms}^{\ 2} R_{coil} \qquad \textbf{(4-15)}$$
$$= 6.3^2 \cdot 0.172 \ \text{W}$$
$$= 6.8 \ \text{W}$$

From this result it is possible to obtain the work done on the suspended body using (4-16).

$$P_{work} = P_{sim} - P_{copper} \qquad \textbf{(4-16)}$$
$$= 34.2 - 6.8 \ \text{W}$$
$$= 27.4 \ \text{W}$$

The remaining loss component, the core losses, are determined from loss data obtained from the material data sheet. Cogent™ M330-50A silicon steel laminations are used as the core material in the magnetic circuit. From the data sheet the total losses in watt per kg for a flux excursion of 1 T at a frequency of 400 Hz are given as 28.1 W/kg. The effective core material volume for a single PA is obtained using computer aided design (CAD) software (CADKey) and

determined to be 85.2x10^{-3} dm^3. Using the material conventional density of 7.60 kg/dm^3 and the volume obtained from CADKey the effective material mass is:

$$M_{eff} = 85.2\times10^{-3}\cdot 7.6 \text{ kg} = 0.65 \text{ kg} \quad (4\text{-}17)$$

The core losses are now obtained using (4-18).

$$P_{core} = P_{spec}\, M_{eff} = 28.1\cdot 0.65 \text{ W} = 18.3 \text{ W} \quad (4\text{-}18)$$

The core losses determined in (4-18) are for the worst case scenario. A rotational speed of 24,000 rpm is assumed which is above the maximum operating speed. The total load power is obtained from (4-15), (4-16) and (4-18) and is determined using (4-19).

$$P_{Load} = P_{copper} + P_{work} + P_{core} = 6.8 + 27.4 + 18.3 \text{ W} = 52.5 \text{ W} \quad (4\text{-}19)$$

The total power supplied by the rectifier is determined from (4-14) and (4-19) using (4-20).

$$P_{rect} = P_{H-Bridge} + P_{Load} = 96 + 52.5 \text{ W} = 148.5 \text{ W} \quad (4\text{-}20)$$

The average supply current is determined from (4-20) using (4-21).

$$I_{rect} = \frac{P_{rect}}{V_{dc-bus}} = \frac{148.5}{310} \text{ A} = 479 \text{ mA} \quad (4\text{-}21)$$

A single phase bridge rectifier, the BR06 is chosen to convert the ac voltage to dc. The 100 Hz smoothing capacitor is designed to limit the voltage ripple to less than 10 % of the total voltage while supplying the average current obtained. The capacitance value is obtained in (4-22).

$$C_{rect} = I_{rect}\frac{dt}{dv} = 0.5\frac{10\times10^{-3}}{0.1\cdot 310} \text{ F} = 161 \text{ µF} \quad (4\text{-}22)$$

A Rubycon 220 µF, 450 V large can type electrolytic capacitor is chosen for this application. A negative temperature coefficient (NTC) resistor is connected in series with the capacitor to limit the inrush current. The resistance value decreases during continuous operation due to a rise in

temperature. The maximum rating for the peak forward surge current (I_{FSM}) is obtained from the BR64 data sheet and used to determine the NTC resistance value.

$$R_{NTC} = \frac{V_{DC}}{I_{FSM}} \qquad (4\text{-}23)$$
$$= \frac{310}{125} = 2.48\ \Omega$$

In the process of sourcing the NTC a component that was able to withstand the instantaneous energy was identified with a resistive value of 5 Ω. The BR64 bridge is capable of supplying a constant current of 6 A and to safeguard this component a 5 A fuse is connected in series with the input.

4.2.3 Input Filter Design

An input filter is designed to prevent the high frequency H-bridge current from reflecting on the 220 V ac mains. Figure 4-7 displays the filter schematic, where the 220 µF capacitor is the rectifier capacitor and the 1.5 µF capacitor is the H-bridge decoupling capacitor. The inductor *L* needs to be designed to form a high impedance path for the high frequency H-bridge currents.

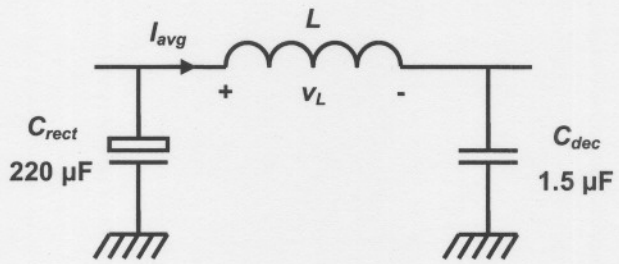

Figure 4-7 Input filter

Figure 4-8 and Figure 4-9 respectively display the inductor current and voltage waveforms. The inductor average current is equal to the rectifier average current and the ripple current should be restrained to within 10 % of this value.

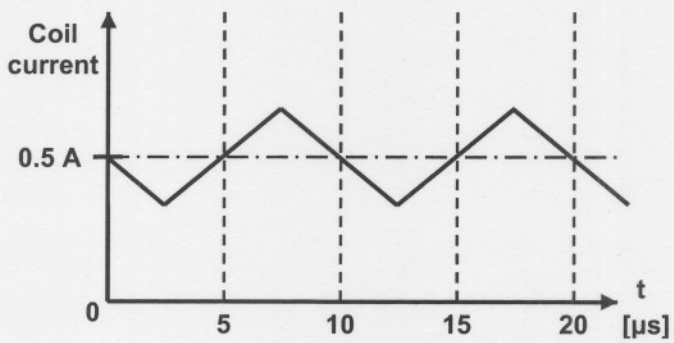

Figure 4-8 Filter inductor current waveform

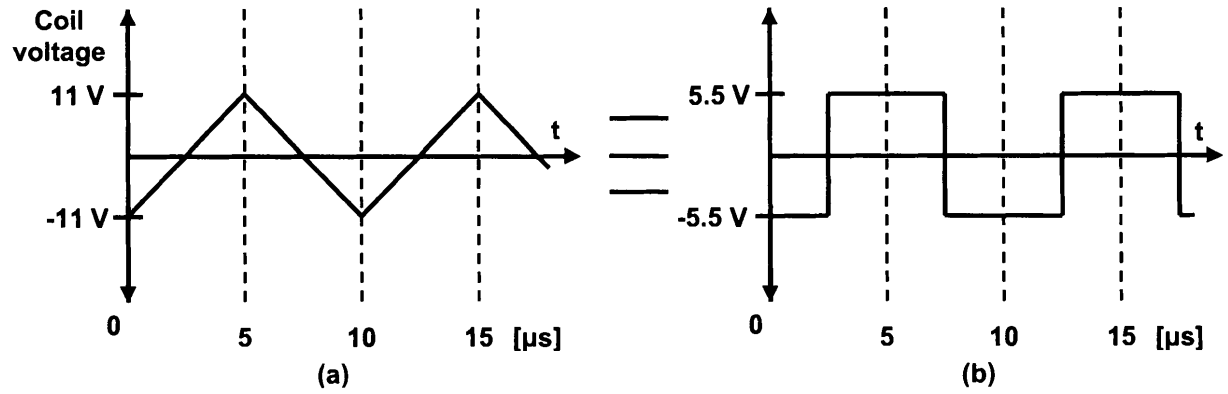

Figure 4-9 Filter inductor (a) actual and (b) equivalent voltage waveform

Figure 4-9 (a) displays the actual voltage across L and (b) displays an equivalent voltage waveform. The voltage waveform in (a) is due to the voltage ripple component on the H-bridge decoupling capacitor caused by the load current. Using waveform (b) and the ripple current specification, the filter inductance value is determined using (4-24).

$$v_L = L\frac{di}{dt} \tag{4-24}$$

$$\therefore L = v_L \frac{\Delta t}{\Delta i}$$

$$= 5.5 \cdot \frac{5\times10^{-6}}{0.1\cdot 0.5}\ \text{H}$$

$$= 550\ \mu\text{H}$$

A Micrometals iron powder toroidal core was identified as most suitable for the inductor and the inductor designed using an iterative design process. Iron powder cores are used due to their high saturation flux density. The number of turns wound onto the toroid is determined using (4-25)

$$N = \sqrt{\frac{L\,\ell_c}{\mu_0\,\mu_r\,A_c}} \tag{4-25}$$

$$= \sqrt{\frac{550\times10^{-6}\cdot 5.14\times10^{-2}}{4\pi\times10^{-7}\cdot 75\cdot 0.347\times10^{-4}}}\ \text{turns}$$

$$\cong 93\ \text{turns}$$

where ℓ_c is the average flux path length and A_c the toroid cross sectional area as obtained from the T80-26B component data sheet. A total of 93 turns are used. The wire diameter is obtained by specifying a safe current density and using the average inductor current. A current density of 3 A/mm^2 is specified and a minimum safe copper area of 0.2 mm^2 is obtained.

By specifying the wire diameter (D_{wire}), the copper area needed is determined using (4-26).

$$A_{wire} = N\left(\frac{D_{wire}}{2}\right)^2 \pi \tag{4-26}$$
$$= 93\left(\frac{0.8\times10^{-3}}{2}\right)^2 \pi \ \text{m}^2$$
$$= 46.7\times10^{-6} \ \text{m}^2$$

A fill factor (FF) of 0.4 is specified and used in (4-27) to determine the available window area.

$$A_{window} = FF\,\pi\left(\frac{ID}{2}\right)^2 \tag{4-27}$$
$$= 0.4\pi\left(\frac{12.6\times10^{-3}}{2}\right)^2 \ \text{m}^2$$
$$= 49.9\times10^{-6} \ \text{m}^2$$

ID is the inside diameter of the toroid. The window area available for the TB80-26B core is $49.9\text{x}10^{-6}$ m^2 which is larger than the copper area needed for the specific design.

During testing an oscillation was observed in both the H-bridge current and voltage waveforms. Upon further investigation it was identified as a resonance phenomenon of the input filter. The LC filter damping is obtained from (4-28)

$$\zeta = \frac{R}{2}\sqrt{\frac{C_{dec}}{L}} \tag{4-28}$$
$$= \frac{1.224}{2}\sqrt{\frac{1.5\times10^{-6}}{550\times10^{-6}}}$$
$$= 0.032$$

with R the coil resistance and capacitor ESR in series. A system is critically damped for a $\zeta = 1$ and will not display oscillations for $\zeta \geq 1$. In order to increase the system damping to 1, a 220 µF capacitor is placed in parallel with the WIMA capacitor and a series resistor is added. The resistance value is determined in (4-29)

$$R_s = \frac{2\zeta}{\sqrt{\frac{C_{eq}}{L}}} - R \tag{4-29}$$
$$= \frac{2}{\sqrt{\frac{110\times10^{-6}}{550\times10^{-6}}}} - 1.224 \ \Omega$$
$$= 3.2 \ \Omega$$

where C_{eq} is the series combination of C_{rec} and the 220 μF capacitor placed in parallel with the WIMA capacitor. The underdamped oscillation was excited during testing by an at the time noise problem in the circuit. It proved not to be a problem in the final circuit where the series resistor was removed.

4.2.4 Thermal Design

The power electronic components in the H-bridge display losses as discussed in section 4.2.1. In order to keep the temperature of the components within safe operating levels a heat sink is used which reduces the thermal resistances of the components with respect to the ambient. Figure 4-10 displays the equivalent circuit of the thermal system with R_{IGBT}, R_{DIODE} and R_{Rsense} the respective thermal resistances between the component junctions and the heat sink and R_{SA} the heat sink to ambient thermal resistance. Q_{IGBT}, Q_{DIODE} and Q_{Rsense} respectively refer to the power dissipated in the components.

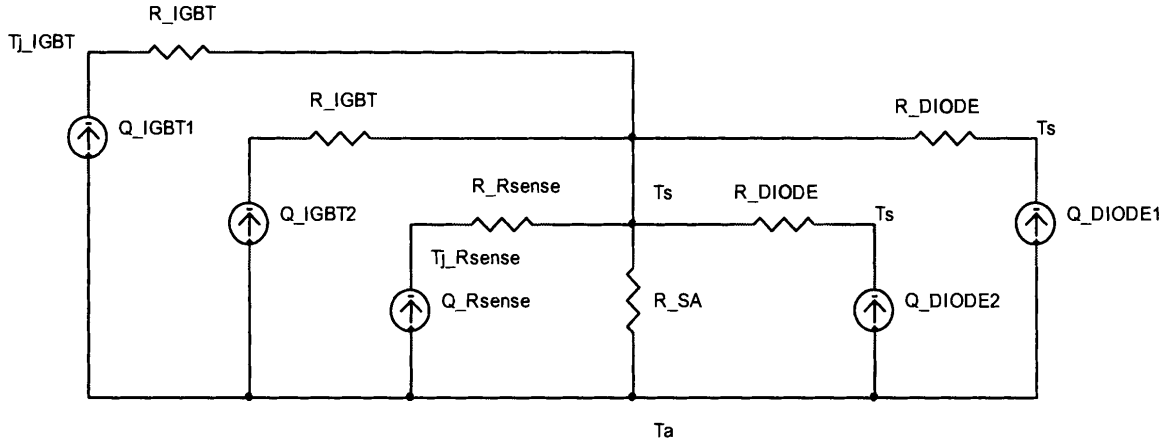

Figure 4-10 Equivalent circuit of thermal system

The switching devices along with the sense resistor are mounted on a single heat sink. The heat sink thermal resistance is obtained using the total power contributed by the devices and specifying the maximum heat sink temperature. The heat sink temperature (T_S) is specified by determining which component necessitates the lowest T_S in order to stay within safe operating temperatures. The components are mounted on the heat sink using ISOSTRATE 2000 K3 electrically-isolating thermal interface pads which display a thermal impedance of 0.23 °C-in^2/W. The IGBTs and diodes are packaged in a TO-247 package of which the case to sink thermal resistance is obtained using (4-30).

$$R_{\theta CS} = \frac{0.23}{0.8 \cdot 0.626} \ ^\circ\text{C/W} = 0.46 \ ^\circ\text{C/W} \quad \textbf{(4-30)}$$

The CADDOCK MP915 series sense resistor is packaged in a TO-126 package. The case to sink thermal resistance of this package is obtained from (4-31).

$$R_{\theta CS} = \frac{0.23}{0.32 \cdot 0.44} \ ^\circ\text{C/W} = 1.63 \ ^\circ\text{C/W} \tag{4-31}$$

Table 4-3 summarises the thermal characteristics of the H-bridge components.

Table 4-3 Thermal characteristics of devices

Parameter	Discription	IRG4PC50W	HFA15PB60	R_{sense} (CADDOCK)
T_j	Operating Junction	150 °C	150 °C	-
$R_{\theta JC}$	Junction - Case	0.64 °C/W	1.7 °C/W	-
$R_{\theta CS}$	Case - Sink	0.46 °C/W	0.46 °C/W	1.63 °C/W

The allowable heat sink temperature of the IGBT device under normal load conditions is obtained in (4-32) using the power dissipated in a single IGBT and the relevant thermal resistances.

$$T_S = T_j - Q_{IGBT}(R_{\theta JC} + R_{\theta CS}) = 150 - 30.8(0.64 + 0.46) \ ^\circ\text{C} = 116.1 \ ^\circ\text{C} \tag{4-32}$$

The heat sink temperature must be kept below 116 °C to keep the IGBT below its maximum allowable junction temperature. The allowable heat sink temperature of the diode is obtained in (4-33) using the power dissipation in a single diode and the relevant thermal resistances.

$$T_S = T_j - Q(R_{\theta JC} + R_{\theta CS}) = 150 - 11.1(1.7 + 0.46) \ ^\circ\text{C} = 126 \ ^\circ\text{C} \tag{4-33}$$

The sense resistor has a power rating of 15 W at a case temperature of 25 °C which decreases to 0 W at 150 °C. This results in a derating factor of 0.12 W/°C which is used in (4-34) to obtain the allowable heat sink temperature for a 2 W power loss.

$$T_S = \frac{125(18 - Q)}{15} - QR_{\theta CS} = \frac{125(18 - 2)}{15} - 2 \cdot 1.63 \ ^\circ\text{C} = 130.1 \ ^\circ\text{C} \tag{4-34}$$

The IGBT has the lowest heat sink temperature requirement at a temperature of 116 °C. At this heat sink temperature the IGBT devices will be on their thermal limit under normal load conditions. A rise in the average coil current will result in thermal destruction of the devices.

Thermal protection is included in the design to protect the circuit under prolonged operation above normal load.

The worst case scenario for the power amplifier occur when a continuous maximum coil current of 9.6 A is supplied to the coil. For the circuit to protect itself against thermal destruction the power dissipation in the H-bridge must be terminated when the heat sink reaches a certain temperature. To achieve this, a thermal switch is incorporated in the circuit, which switches the PA to the off mode until it has cooled down.

The heat sink temperature at which the PA should be turned off to protect itself is obtained from the IGBT power losses in the worst case scenario. As the average current rises to 9.6 A the losses in the IGBT increase from 30.8 W to 52.8 W. The maximum allowable heat sink temperature is obtained using the power dissipation and thermal resistances in (4-35).

$$\begin{aligned} T_S &= T_j - Q(R_{\theta JC} + R_{\theta CS}) \\ &= 150 - 52.8(0.64 + 0.46)\ ^\circ\text{C} \\ &= 91.9\ ^\circ\text{C} \end{aligned} \tag{4-35}$$

A derating factor of 15 % is included to ensure that the IGBTs stay within their safe operating area. This reduces the heat sink temperature to 78 °C. A thermal switch with a transition temperature of 75 °C is chosen for this specific application.

The thermal switch will now terminate the coil current as soon as the heat sink temperature rises above 75 °C. This implies that the heat sink temperature must stay below 75 °C while the power amplifier is operated under normal load conditions. The maximum thermal resistance of the heat sink is obtained from (4-36).

$$\begin{aligned} R_{\theta SA} &= \frac{T_S - T_A}{Q_{H-Bridge}} \\ &= \frac{75 - 25}{85.8}\ ^\circ\text{C/W} \\ &= 0.58\ ^\circ\text{C/W} \end{aligned} \tag{4-36}$$

Apart from the thermal resistance, the heat sink geometry also plays an important role in the process of sourcing a suitable heat sink. A finned aluminium heat sink 200 mm wide and 40 mm high displays a thermal resistance of 0.65 °C/W for a length of 100 mm. For the final configuration four PAs are mounted on a heat sink 500 mm in length. A cooling fan is integrated into the final heat sink configuration in order to lower the thermal resistance for each PA well below 0.58 °C/W.

4.3 Gate Drive Circuit Design

4.3.1 Gate Drive Requirements for High-Side Device

The gate drive requirements for a MOS-gated device such as an IGBT utilised as a high-side switch (collector connected to the high voltage rail) and operated in hard switched mode can be summarised as follows [21]:

- Gate voltage must be 10 – 15 V higher than the collector voltage. Being a high side switch the gate voltage must be higher than the rail voltage which is frequently the highest voltage available in the system.
- The gate voltage must be controllable from the logic which is normally referenced to ground. The control signal must be level-shifted to the emittor of the high side device which in this case swings between the two rails.
- The gate drive circuit should not significantly affect the overall efficiency.

4.3.2 Component Selection

An International Rectifier MOS-gate driver (MGD), the IR2113, was identified for this specific application. The MGD integrates most of the functions required to drive one high-side and one low-side IGBT. With the addition of a few components, this device provides very fast switching speeds and low power dissipation. The device operates either on the bootstrap principal or with a floating power supply. In order to minimise components the bootstrap principal is utilised in the design. Figure 4-11 displays the proposed gate drive circuit diagram.

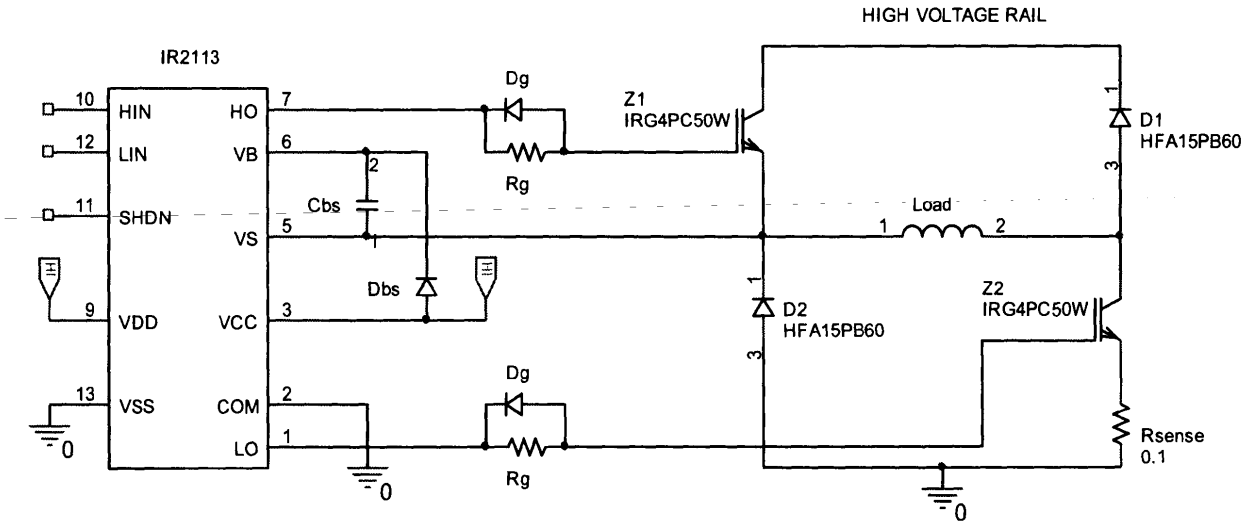

Figure 4-11 Gate drive circuit diagram

The IR2113 is capable of sourcing gate currents up to 2 A. To make best use of this feature the gate resistor R_g is chosen in accordance. The resistor value is obtained from (4-37)

$$R_g = \frac{V_{cc}}{I_{g-\max}} = \frac{15}{2}\ \Omega = 7.5\ \Omega \tag{4-37}$$

where V_{CC} is the supply voltage and $I_{g\text{-}max}$ the maximum peak gate current specified by the gate driver. An 8 Ω, ¼ W gate resistor is chosen for this specific application. Small signal diodes (1N4148) are placed in parallel with the gate resistors to speed up the turn off of the IGBTs. This will reduce the current-tail effect of the IGBT.

The gate charge for the high side IGBT (Z1) shown in Figure 4-11 is provided by the bootstrap capacitor (C_{bs}). The capacitor is charged by the V_{CC} supply through the bootstrap diode (D_{bs}) during the time the device is off. This is due to the fact that V_S swings to ground when the diodes D_1 and D_2 conduct. Since the capacitor is charged from a low voltage source, the power consumed to drive the gate is small.

4.3.3 Bootstrap Components Design

As shown in Figure 4-11 the bootstrap diode and capacitor are the only external components strictly required for operation in this specific application. Local decoupling capacitors on the V_{CC} and V_{DD} supplies are useful in practice to compensate for the inductance of the supply lines.

There are five factors influencing the supply capacity of bootstrap capacitors [21]:

1. Gate charge required to enhance the IGBT
2. I_{qbs} – quiescent current for the high side driver circuitry
3. Currents within the level shifter of the control IC
4. IGBT gate-source forward leakage current
5. Bootstrap capacitor leakage current

The fifth factor is only relevant if the bootstrap capacitor is an electrolytic capacitor. Ignoring the bootstrap capacitor leakage current as well as the IGBT gate-source leakage current due to their insignificant small values, the bootstrap capacitor's minimum charge requirement is obtained from (4-38) [22]

$$Q_{bs} = 2Q_g + \frac{I_{qbs}}{f} + Q_{ls} = 2\left(180\times10^{-9}\right) + \frac{125\times10^{-6}}{100\times10^{3}} + 5\times10^{-9}\ \text{C} = 366.3\ \text{nC} \tag{4-38}$$

where:

Q_g = Total gate charge of high-side IGBT

I_{qbs} = Quiescent V_{bs} supply current

f = Frequency of operation

Q_{ls} = Level shift charge required per cycle (5 nC)

The bootstrap capacitor must be able to supply the minimum charge as determined while retaining its voltage. This is necessary to reduce ripple on the bootstrap voltage (V_{bs}) as well as preventing V_{bs} from dropping below the IR2113 under-voltage lockout value. Therefore the charge in C_{bs} must be a minimum of double the value previously determined. The minimum capacitance value for C_{bs} is obtained using (4-39) [22]

$$C_{bs} = \frac{2Q_{bs}}{V_{cc} - V_f - V_{LS} - V_{Min}} \quad \textbf{(4-39)}$$

$$= \frac{366.3 \times 10^{-9}}{15 - 1.25 - 1.3 - 8.2} \text{ F}$$

$$= 86.2 \text{ nF}$$

where:

V_f = Forward voltage drop across the bootstrap diode

V_{LS} = Voltage drop across the diode D_2 when bootstrap capacitor is charging

V_{Min} = Minimum voltage between V_B and V_S ($V_{bs\text{-}min}$)

As stated previously, the capacitance value obtained in (4-39) for C_{bs} is the absolute minimum required. Due to the nature of the bootstrap circuit operation, a small value capacitor can lead to overcharging which could in turn damage the IC. In order to minimise the risk of overcharging and to further reduce the ripple component on the V_{bs} voltage, the capacitance value obtained from the above equation should be multiplied by a factor 15 (rule of thumb). This results in a capacitance value of 1.3 µF and for this specific application a 2.2 µF tantalum capacitor is chosen.

The bootstrap diode (D_{bs}) shown in Figure 4-11 should be able to withstand the full rail voltage. It should also be an ultra-fast recovery device to minimise the amount of charge fed back from the C_{bs} capacitor to the V_{cc} supply. The high temperature reverse leakage characteristics of the diode may also prove to be a determining factor when the capacitor has to hold the charge for a prolonged period of time which is not the case in this application.

The current rating of the diode is the product of the charge obtained in (4-38) and the switching frequency [21]. The current rating is now obtained from (4-40).

$$\begin{aligned} I_F &= Q_{bs} f \\ &= 366.3 \times 10^{-9} \cdot 100 \times 10^{3} \text{ A} \\ &= 36.6 \text{ mA} \end{aligned} \tag{4-40}$$

The D_{bs} diode characteristics are summarised as follows:

V_{RRM} = 310 V (minimum)

max t_{rr} = 100 ns

I_f = 36.6 mA

The MUR150 diode which satisfies all the mentioned criteria is used in the final design.

4.4 PWM Controller Design

4.4.1 Peak Current-Mode Control

Current-mode control is implemented in this switching power amplifier by sensing and controlling the peak IGBT collector current. In systems such as these where the load ripple current is relatively small, peak current control is nearly equivalent to average current control. The load current as well as the current flowing through the IGBTs are shown in Figure 4-12.

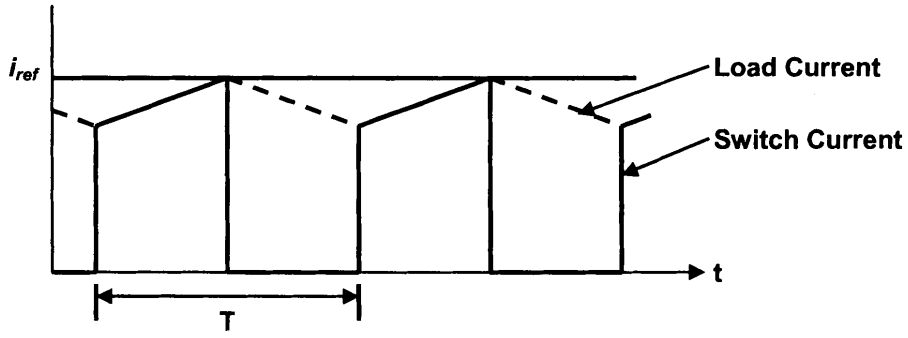

Figure 4-12 H-Bridge current waveforms

Figure 4-13 displays a schematic diagram of the peak current-mode control configuration. The current flowing through the IGBT is sensed using a sense resistor. An oscillator produces a pulse train at a fixed frequency which is used to set a latch. Each time the latch is set, the gate drive switches on the IGBTs. The device remains in the on state until the v_{Rsense} signal exceeds the v_{iref} reference signal. At this instant the latch is reset and the IGBTs are turned off.

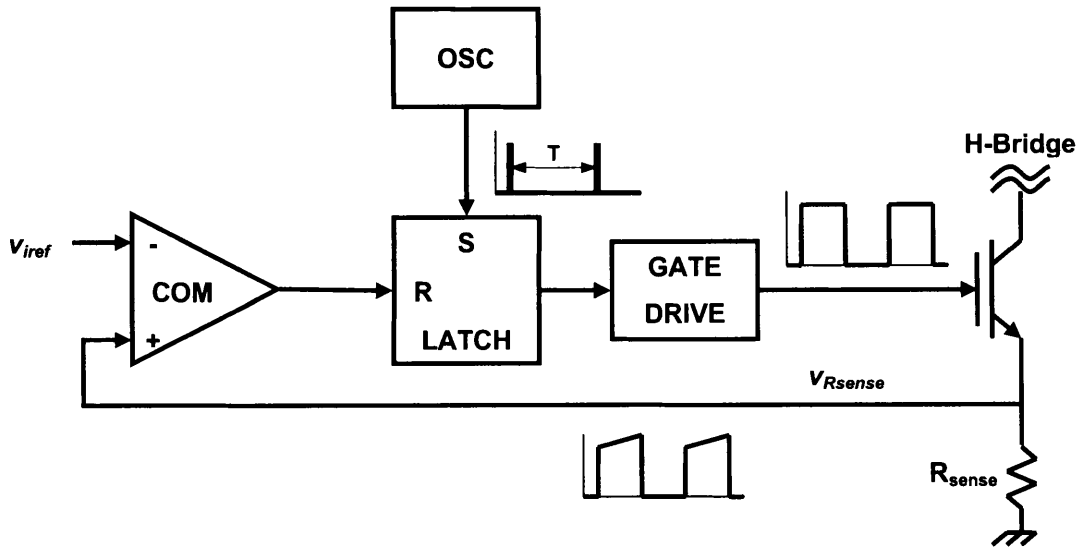

Figure 4-13 Peak current-mode control schematic diagram

The fixed frequency peak-sensing current-mode converter displays several drawbacks which include:

1. Open loop instability above 50 % duty cycle
2. Less than ideal loop response caused by peak instead of average inductor current sensing
3. Tendency towards sub-harmonic oscillations
4. Noise sensitivity, especially when inductor ripple current is small

Fortunately a simple solution is available. It has been shown by a number of authors that by adding slope compensation to the current waveform, the system is stabilised for operation above 50 % duty cycle. This technique also minimises the mentioned drawbacks. A more detailed discussion of slope compensation can be found in section 4.4.4.

4.4.2 Integrated Controller Selection

The UC3842 is a pulse width modulation (PWM) integrated circuit (IC) which provides all the necessary features to implement a fixed frequency current-mode control scheme with the minimum external component count. The device is capable of operation at duty cycles approaching 100%. Internally implemented circuits include: under-voltage lockout, a precision reference trimmed for accuracy at the error amp input and a PWM comparator which also provides current limit control. Figure 4-14 displays a block diagram of the UC3842.

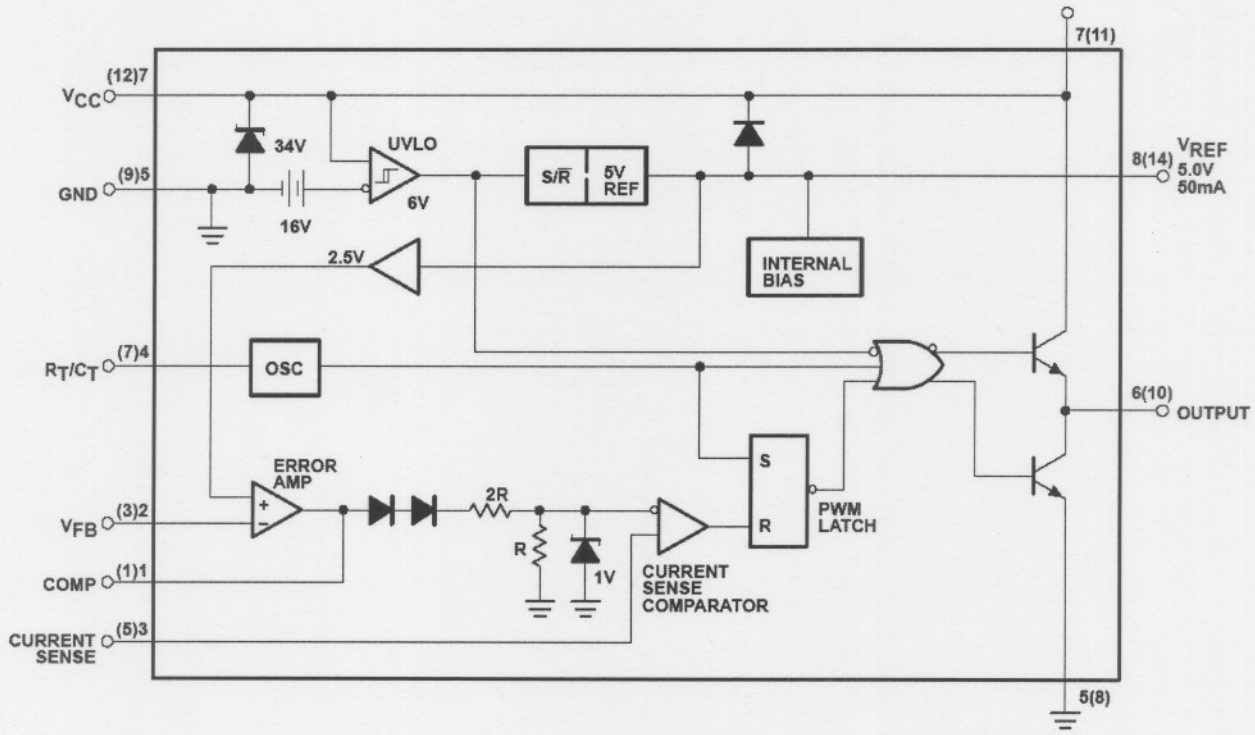

Figure 4-14 UC3842 Current-mode PWM controller block diagram

The pin numbers in parenthesis refer to the D package. For this design the 8-pin P-DIP package is used. The following sections contain a detailed discussion of the control design which incorporates the UC3842.

4.4.3 Current Sense Circuit

The current flowing through the load while the IGBTs are conducting is sensed using a sense resistor. Figure 4-15 displays the proposed current sense circuit.

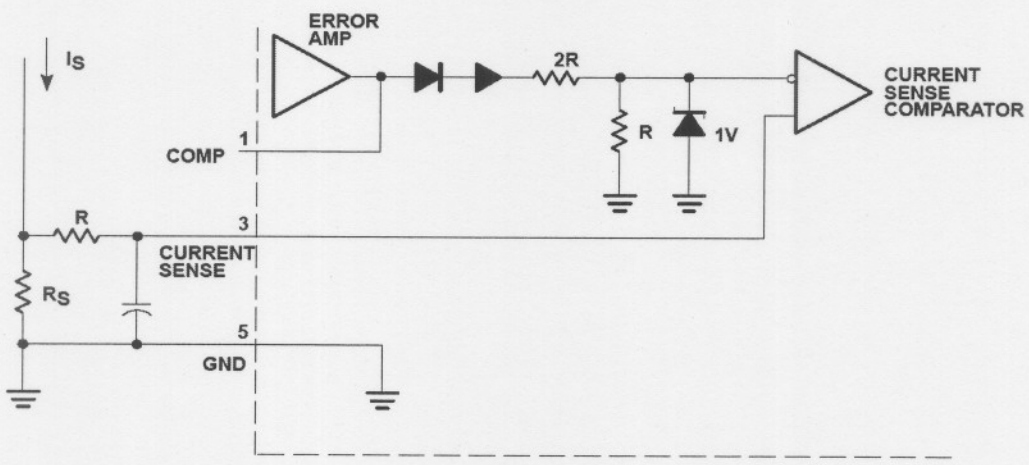

Figure 4-15 Current sense circuit

The current sense comparator compares the voltage signal applied to the current sense pin to a voltage produced by the error amplifier. The error amplifier input to the current sense comparator is limited by a 1 V zener diode. The current sense signal should thus not exceed a value of 1 V at the peak current. With a specified peak coil current of 10 A, the sense resistor value is obtained from (4-41).

$$R_{sense} = \frac{V_{Rs-max}}{I_{S-max}} \qquad (4\text{-}41)$$
$$= \frac{1}{10}\ \Omega$$
$$= 0.1\ \Omega$$

As discussed in section 4.2 a non-inductive power metal film sense resistor is chosen for this application. A small RC filter is included in the design in order to suppress switching transients. The values of the RC filter resistor and capacitor are obtained in section 4.4.4 where the slope compensation is discussed.

4.4.4 Slope Compensation

Slope compensation is the process where an artificial slope is either added to the current sense waveform or subtracted from the control signal. As stated in section 4.4.1 peak current-mode converters display several drawbacks which can be minimised by implementing slope compensation. Slope compensation is described in detail in [23]. Figure 4-16 displays typical slope compensation waveforms where in (a) no slope compensation is added, (b) an artificial slope is subtracted from the control signal and in (c) the artificial slope is added to the current sense waveform.

The amount of slope added is determined by the specific application. Optimal current control is obtained by using an artificial slope equal to one half of the decaying coil current slope (m_2). With the slope $m = -½m_2$ the average coil current follows the control signal so that, in the small signal analysis, the coil acts as a controlled current source. This amount of slope compensation benefits all current-mode controlled converters, whether they operate above 50 % duty cycle or not.

Slope compensation also improves the noise immunity of a current-mode controlled converter. A small ripple component on the coil current presents only a shallow slope on the current sense signal. This may lead to pulse width jitter caused by both random and synchronous noise. In order to benefit from this technique the slope compensation m should be considerably greater than m_2. Unfortunately this presents a trade-off since any slope greater than $½m_2$ will cause the

converter to behave less like an ideal current-mode converter and more like a voltage mode converter.

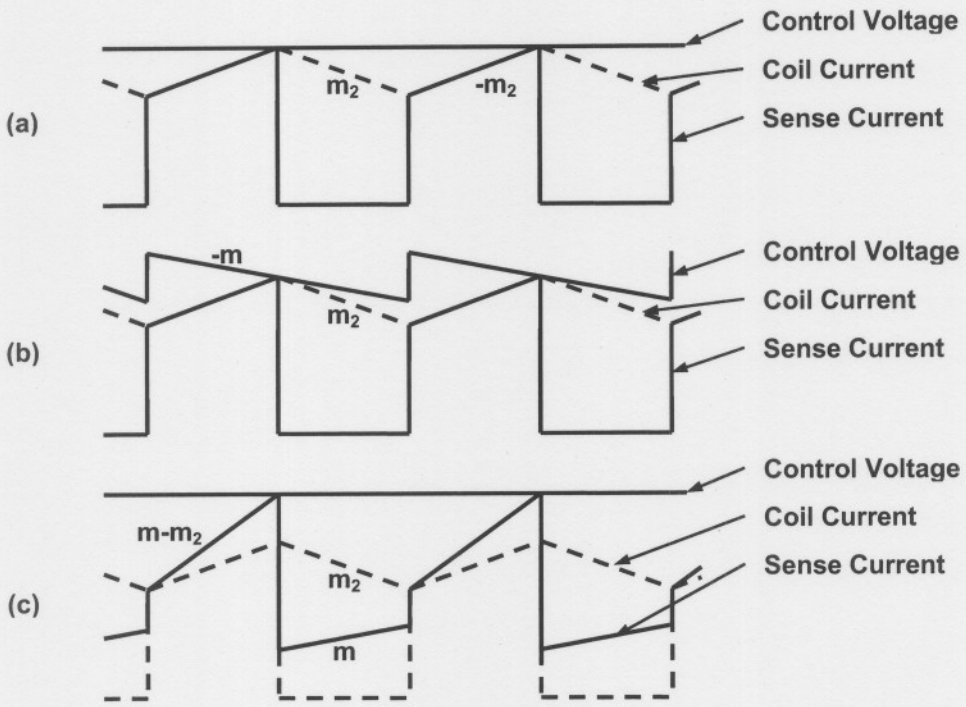

Figure 4-16 Slope compensation waveforms (a) no slope compensation, (b) artificial slope subtracted from control voltage, (c) artificial slope added to current sense signal

Slope compensation is implemented on the UC3842 with the addition of only two external components. Since the PMW controller allows access to the oscillator ramp a simple voltage divider circuit is used to add slope to the current sense signal. Figure 4-17 displays the proposed slope compensation circuit diagram.

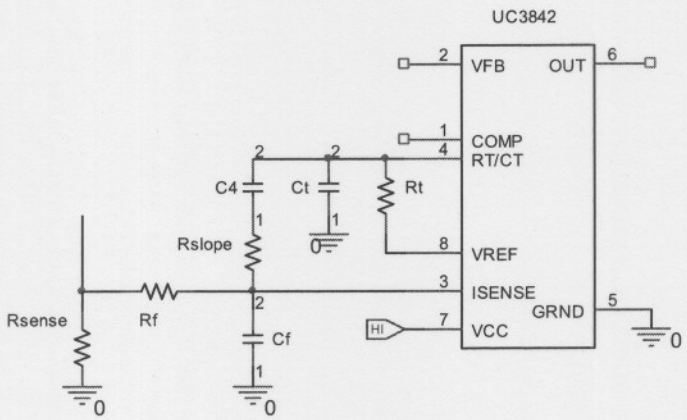

Figure 4-17 Slope compensation circuit diagram

The oscillator frequency is determined by the resistor R_t and the capacitor C_t. Values for these two components which produce an operating frequency of 100 kHz is found in the UC3842 data sheet. For this application these values are: R_t = 8.2 kΩ and C_t = 2.2 nF.

The circuit components are dimensioned to add a ramp equivalent to the inductor current down slope. The inductor current down slope (m_2) is obtained using (4-42).

$$\begin{aligned} m_2 &= \frac{di}{dt} \\ &= \frac{V_{dc-bus}}{L_c} \\ &= \frac{310}{5\times10^{-3}} \text{ A/s} \\ &= 62000 \text{ A/s} \end{aligned} \tag{4-42}$$

The inductor current down slope is scaled by R_{sense} to obtain the equivalent down slope (m_2').

$$\begin{aligned} m_2' &= m_2 R_{sense} \\ &= 62000 \cdot 0.1 \text{ V/s} \\ &= 6200 \text{ V/s} \end{aligned} \tag{4-43}$$

This desired ramp value is tapped from the oscillator signal via C_4 and R_{slope}. The oscillator ramp signal is determined using (4-44).

$$\begin{aligned} m_{osc}' &= \frac{\Delta V}{T} \\ &= \frac{1.7}{9.5\times10^{-6}} \text{ V/s} \\ &= 178.95\times10^{3} \text{ V/s} \end{aligned} \tag{4-44}$$

Capacitor C_4 acts as an ac coupling capacitor which eliminates the dc offset voltage on the oscillator ramp. Due to the choice of the decoupling capacitor value (10 nF), the oscillator ramp scaling is governed by the resistive voltage divider network formed by R_{slope} and R_f. Figure 4-18 displays the simplified slope compensation circuit.

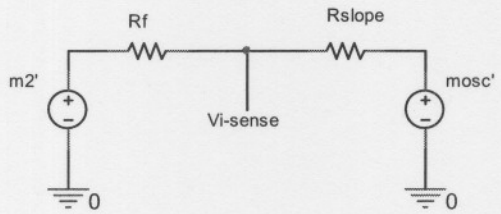

Figure 4-18 Simplified slope compensation circuit

Using superposition the slope of the $V_{i\text{-}sense}$ signal ($m_{Vi\text{-}sense}$) is as given by (4-45).

$$m_{Vi-sense} = m_2' \cdot \frac{R_{slope}}{R_{slope}+R_f} + m_{osc}' \cdot \frac{R_f}{R_f+R_{slope}} \tag{4-45}$$

By choosing the amount of slope compensation to be equal to one half of the equivalent coil current down slope, the two terms on the right hand side of (4-45) are manipulated as follows:

$$\frac{m_2'}{2} \cdot \frac{R_{slope}}{R_f+R_{slope}} = m_{osc}' \cdot \frac{R_f}{R_f+R_{slope}} \tag{4-46}$$

The component value for R_{slope} is now obtained by solving (4-46) for R_{slope} and by choosing R_f = 1 kΩ.

$$R_{slope} = 2R_f \frac{m_{osc}'}{m_2'} \tag{4-47}$$

$$= 2 \cdot 1 \times 10^3 \cdot \frac{179 \times 10^3}{6200} \ \Omega$$

$$= 57.7 \ \text{k}\Omega$$

A 56 kΩ resistor is used to implement the artificial slope of m = -½m_2. The first order low pass filter is designed for a cut-off frequency of 333 kHz. The capacitance value for C_f is obtained from (4-48).

$$C_f = \frac{1}{2\pi \cdot f \cdot R_f} \tag{4-48}$$

$$= \frac{1}{2\pi \cdot 333 \times 10^3 \cdot 1 \times 10^3} \ \text{F}$$

$$= 478 \ \text{pF}$$

A 470 pF, 35 V capacitor is used.

4.4.5 Error Amplifier Design

This section of the design must satisfy two objectives; isolating the dSPACE® current reference signal from the PA, and establishing a linear relationship between the current reference signal and the actual coil current.

The current reference signal produced by the dSPACE® card is a voltage signal. The signal is generated by one of the analogue output ports with a range of ±10 V and a 5 mA current source or sink capability. The PA supply is a rectified mains supply which implies that the electronic ground is floating with respect to earth. Since the dSPACE® ground is connected to earth, the PA must be electrically isolated from the dSPACE® card. Electrical isolation is achieved by using an optocoupler as interface. A high-speed optocoupler, the 6N136, is sourced. This device is typically used as a feedback element in switch-mode power supplies and for analogue signal ground isolation.

The optocoupler output is powered from a regulated 5 V, 50 mA supply on the UC3842. In order to utilise the full range of the optocoupler output, it is connected to the error amplifier input via a voltage divider network. Figure 4-19 displays the proposed interface circuit.

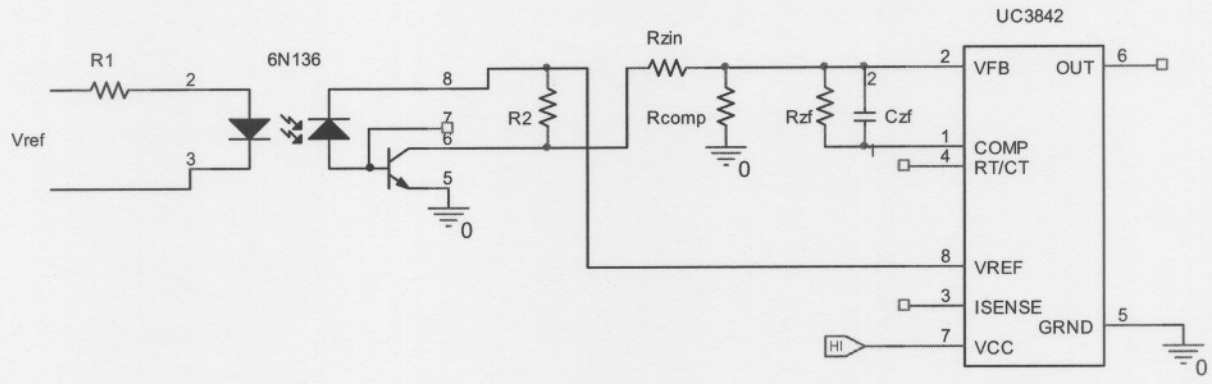

Figure 4-19 Error amplifier circuit diagram

The resistance R_1 is chosen in order to ensure that the 5 mA source capability of the dSPACE® analogue output is not exceeded, whereas R_2 is a function of the current transfer ratio of the optocoupler at the specific working point. Values for R_1 and R_2 are obtained and implemented after which they are refined in order to produce the desired response. The optimal resistance values are: R_1 = 2.7 kΩ and R_2 = 4.7 kΩ. Figure 4-20 displays the optocoupler's measured response which shows excellent linearity between the reference voltage and the output voltage.

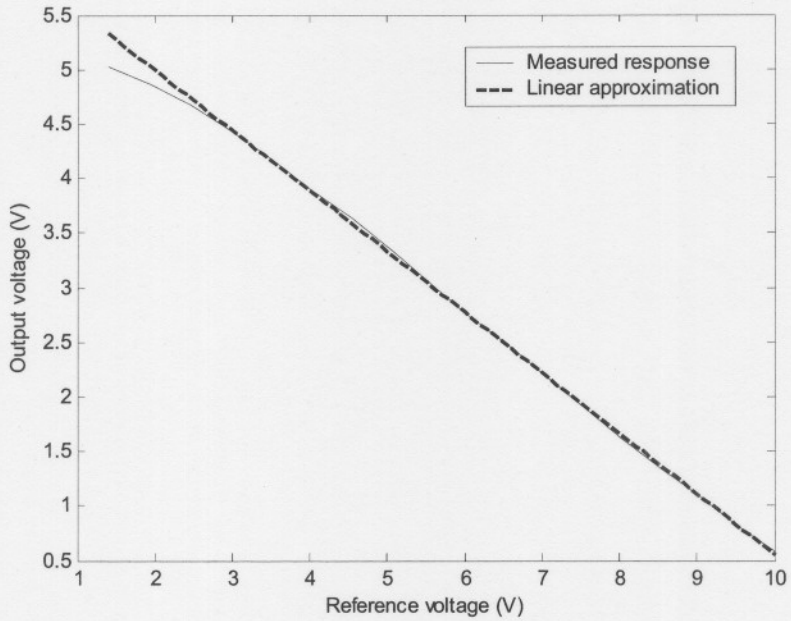

Figure 4-20 Optocoupler input output response

The minimum and maximum values of the optocoupler's linear range are obtained from Figure 4-20 and are summarised in Table 4-4.

The minimum and maximum values of the error amplifier output voltage (v_e) are determined by the internal circuitry. Figure 4-21 shows v_e experiencing a voltage drop of two diodes and a

voltage divider network before being applied to the current sense comparator. The reference voltage applied to the current sense comparator should range from 0 V to a maximum of 1 V. The error amplifier output should therefore range from a minimum of 1.4 V to a maximum of 4.4 V. Table 4-4 shows the voltage values for the minimum and maximum conditions at the respective locations.

Table 4-4 Optocoupler input output relationship

Output conditions	Optocoupler input voltage	Optocoupler output voltage (v_i)	Desired Error Amp output (v_e)
Min	2.5 V	4.6 V	1.4 V
Max	10 V	0.6 V	4.4 V

The error amplifier output voltage (v_e) can be described by:

$$v_e = 2.5 + 2.5\frac{R_{zf}}{R_{comp}} + (2.5 - v_i)\frac{R_{zf}}{R_{zin}} \tag{4-49}$$

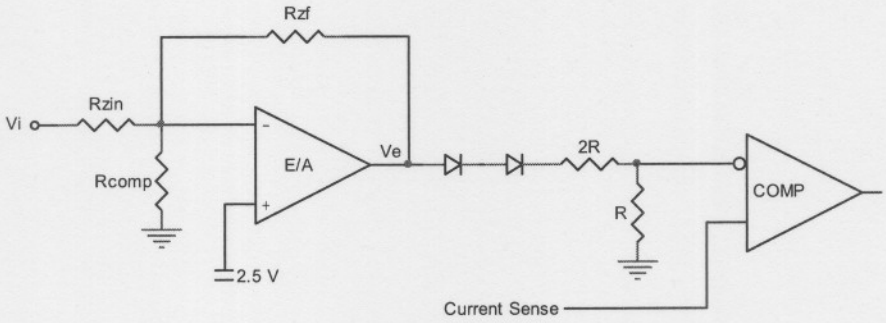

Figure 4-21 Error amplifier internal circuit diagram

By substituting the values of v_i and v_e, which corresponds to the minimum output condition, into (4-49), the result in (4-50) is obtained.

$$1.4 = 2.5 + 2.5\frac{R_{zf}}{R_{comp}} + (2.5 - 4.6)\frac{R_{zf}}{R_{zin}}$$

$$\frac{R_{zf}}{R_{zin}} = 0.52 + 1.19\frac{R_{zf}}{R_{comp}} \tag{4-50}$$

The corresponding maximum output condition values of V_i and V_e reveals the result in (4-51).

$$4.4 = 2.5 + 2.5\frac{R_{zf}}{R_{comp}} + (2.5 - 0.6)\frac{R_{zf}}{R_{zin}}$$

$$\frac{R_{zf}}{R_{zin}} = 1 - 1.32\frac{R_{zf}}{R_{comp}} \tag{4-51}$$

In order to obtain component values the right hand terms of (4-50) and (4-51) are set equal.

$$0.52 + 1.19\frac{R_{zf}}{R_{comp}} = 1 - 1.32\frac{R_{zf}}{R_{comp}}$$

$$\frac{R_{zf}}{R_{comp}} = 0.19 \qquad \textbf{(4-52)}$$

After choosing the resistance value of R_{zf} = 39 kΩ, the remaining two component values are obtained from (4-51) and (4-52). They are: R_{comp} = 220 kΩ and R_{zin} = 47 kΩ.

The low pass filter created by the capacitor C_{zf} in the feedback loop of the error amplifier as seen in Figure 4-19 is designed with a -3 dB cut-off frequency of 8.5 kHz. This cut-off frequency is experimentally obtained as the best trade-off between amplifier bandwidth and noise suppression. The capacitor value is obtained in (4-53).

$$C_{zf} = \frac{1}{2\pi R_{zf} f} \qquad \textbf{(4-53)}$$

$$= \frac{1}{2\pi \cdot 39 \times 10^3 \cdot 8.5 \times 10^3} \text{ F}$$

$$= 480 \text{ pF}$$

A 470 pF capacitor is used.

4.5 EMC Considerations

The power amplifier applies a square voltage wave to the coil with amplitudes of ± 310 V which results in average coil currents of up to 9.6 A. The switching times of the IGBTs are extremely fast (60 ns) which result in very high di/dt and dv/dt excursions. These conditions result in a very noisy environment, especially when more than one amplifier is operating in close proximity. Common mode noise may cause pulse width jitter which may result in less than adequate response. This problem is addressed in the following sections.

4.5.1 Synchronisation

The AMB system requires a total of eight power amplifiers. Due to the system layout the PAs will be situated in close proximity. The PAs are synchronised to all turn on their respective switches at precisely the same time. This will not only reduce the possibility of spurious turn-on due to noise coupling among the PAs, but will also ensure more deterministic system behaviour. Each PA terminates its own gate pulses when the coil current exceeds the reference value. The noise effect during turn-off might be a factor. This will however be investigated during testing.

Synchronisation is obtained by adding a sync pulse to the oscillator voltage ramp. By applying the same sync pulse to the different PAs, each amplifier's voltage ramp is forced through the oscillator's internal upper threshold at the precise same time. The simplest method of synchronisation utilises the timing capacitor (C_t) in near standard configuration. Instead of connecting C_t directly to ground a small resistor is placed in series with C_t to ground. The resistor acts as a point of input for the sync pulse raising the C_t voltage above the oscillator's internal upper threshold.

The sync pulse is generated by a standard circuit of which the design is readily available. The sync circuit is also electrically isolated in order to protect the timing pulse circuit and since the ground voltages differ from each other. Figure 4-22 displays the proposed synchronisation circuit diagram.

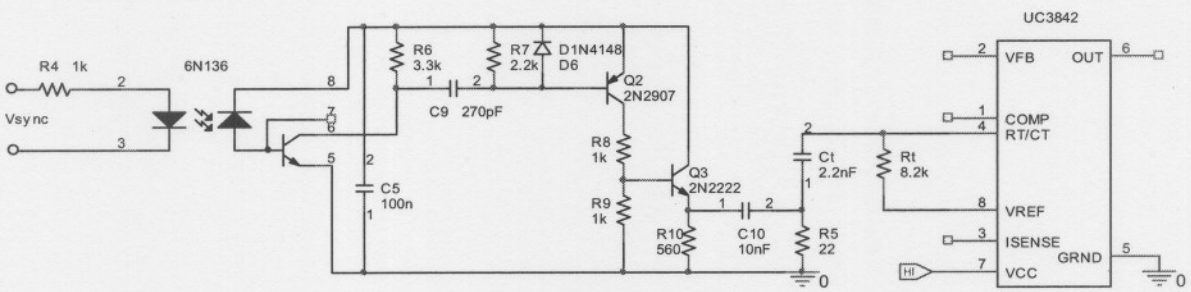

Figure 4-22 Synchronisation circuit diagram

4.5.2 Common Mode Filter

Since the AMB coils are actuated by 100 kHz, 620 V peak to peak square wave voltages and the coils are in close proximity, capacitive coupling among the coils are inevitable. This capacitive coupling could pose a problem when reflected as noise on the current signals. The current signals are used for control and ideally also for position estimation. This source of noise is classified as common mode noise. The common mode noise can be reduced by realising a common mode filter in line with the PA output. Figure 4-23 displays the common mode filter realised by a common mode inductor L_{cm} and an equivalent capacitance formed by the shields around the conductors that are grounded on the one side.

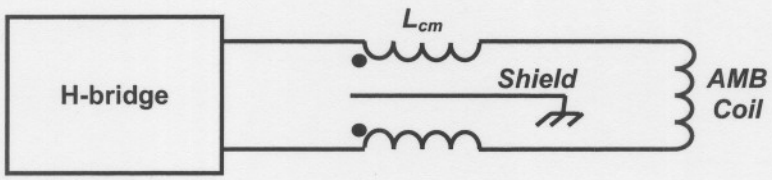

Figure 4-23 Common mode filter implementation

The equivalent common mode filter realised by this circuit is illustrated in Figure 4-24. The noise sources V_N represent the coupling from adjacent AMB coils.

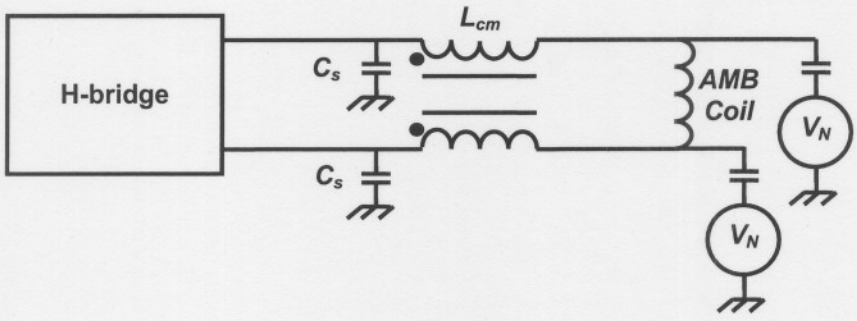

Figure 4-24 Equivalent common mode filter

The capacitance (C_s) is parasitic due to the shield and L_{cm} is simply chosen to obtain maximum common mode inductance. L_{cm} is realised by using a ferrite toroid core with a high permeability (μ) and the maximum number of turns. A MMG M_n-Z_n coated toriod (28-780C36) is used with five common turns.

A twisted pair shielded cable is used to connect the coil to the PA. The shield is connected to the PA heat sink which in turn is connected to ground. This reduces the radiated noise as well as common mode noise coupling.

4.6 Protection

4.6.1 Soft Start

When the PA is switched on while a positive reference current voltage is applied, it will attempt to provide the specified coil current as soon as the UC3842 under voltage lockout level is traversed. At this point the H-bridge voltage along with the electronics power supply is not yet stabilised which may result in a condition where some of the components are strained. To avoid this condition a soft start is implemented on the PA.

Soft start prevents the PA from delivering a coil current directly after it is switched on. The error amplifier output is shorted to ground using a PNP transistor (Q_1). Figure 4-25 displays the soft start circuit diagram. As soon as the electronics power supply voltage exceeds the UC3842 under voltage threshold the UC3842 switches on. At this time the error amplifier output (V_e) is still shorted to ground. The 5 V reference is high and the capacitor C_{ss} starts charging through

the resistor R_{ss}. The time it takes Q_1 to switch off completely is determined by the $R_{ss}C_{ss}$ time constant. A soft start delay of 1 s is implemented with the following component values: R_{ss} = 1 MΩ and C_{ss} = 1 µF.

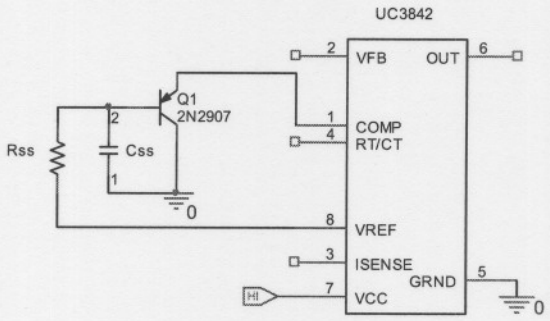

Figure 4-25 Soft start circuit diagram

4.6.2 Short Circuit Protection

The slope of the coil current produced by the power amplifier is a function of the coil inductance. When the inductance decreases the slope increases and in the event of a short circuit on the output of the PA, the inductance seen by the H-bridge reduces to a very small value. This causes the current to rise very rapidly and high peak currents may result before the gate pulses can be terminated by the PWM controller. The switching components of the H-bridge will not be able to withstand these repetitive peak current pulses and will fail.

To protect the circuit under short circuit conditions, some circuitry is added to disable the gate pulses as soon as a certain current limit is exceeded. A simple latch circuit is used to implement the proposed protection. Figure 4-26 displays the short-circuit protection circuit diagram which is implemented on the shutdown pin of the IR2113 gate drive unit.

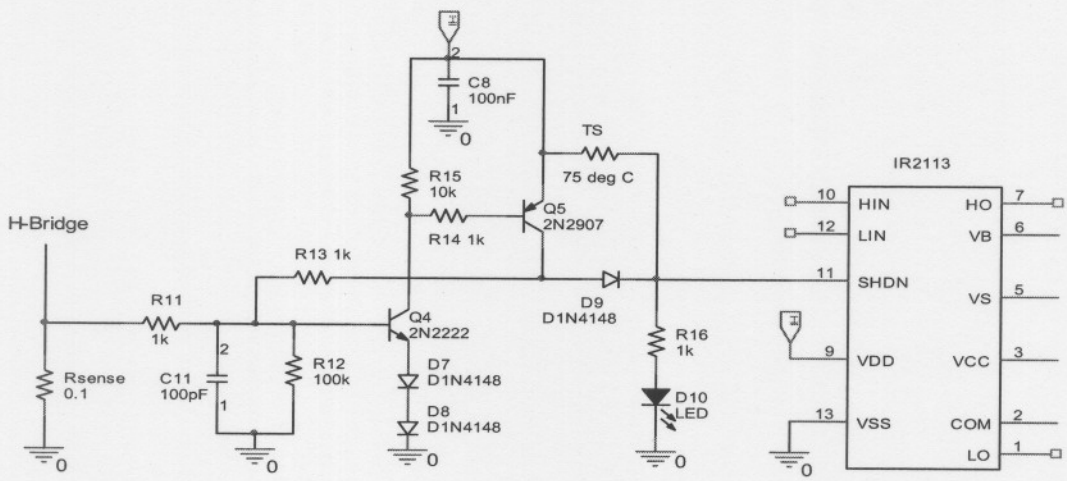

Figure 4-26 Short-circuit protection circuit diagram

As soon as the current sense voltage produced by the R_{sense} resistor exceeds the voltage drop produced by the two diodes (D_7 and D_8) and the NPN transistor (Q_4), the circuit latches and applies 15 V to the shutdown pin on the IR2113 which in turn terminates the gate pulses.

When the voltage produced by R_{sense} exceeds the voltage drop across D_7, D_8 and Q_4, a base current starts to flow in Q_4. The collector current now flowing causes Q_5 to turn on which in turn drives Q_4 into saturation and causes the circuit to latch. The component values are chosen in such a way to ensure the shortest latch time possible.

4.6.3 Thermal Protection

As mentioned in section 4.2.4 thermal protection is also included in the design. A thermal switch with a transition temperature of 75 °C is included to turn off the PA when the safe operating temperature limits of the components are approached. The thermal switch (T_S) is shown in Figure 4-26. Under normal conditions T_S has a high resistance value (≈100 kΩ) and as soon as the transition temperature is traversed, the resistance value decreases dramatically (≈100 Ω). When this takes place the shutdown pin on the IR2113 is pulled high and the gate drive signals are terminated. The thermal switch returns to its original state once the heat sink temperature drops below the transition temperature.

4.7 Electronics Supply Design

The power amplifiers are designed as modular units which may be used as standalone components or in an integrated system. For this reason each PA is equipped with its own electronic supply.

4.7.1 Transformer Specification

The transformer specification is obtained from the current requirements of the PA electronic circuit. During testing, the total current drawn by the electronic circuits was found to be 60 mA at a supply voltage of 17 V. These requirements result in a power rating of just over 1 VA. For this specific application a 1.5 VA, 220-12 V transformer is used.

4.7.2 Rectifier Design

The transformer secondary is rectified using a DB105 full wave rectifier which has ample power capacity. The smoothing capacitor value for a voltage ripple of less than 5% is obtained using (4-54).

$$C = i_{rect}\frac{dt}{dv} \tag{4-54}$$
$$= 0.06\frac{10\times10^{-3}}{0.05\cdot17}\ \text{F}$$
$$= 706\ \mu\text{F}$$

A 1000 µF, 25 V smoothing capacitor is used.

4.8 Circuit Layout and Packaging

During the PA development some critical factors with respect to circuit layout were identified. These are:

- H-bridge layout
- H-bridge decoupling capacitor position with respect to H-bridge and
- IR2113 placement with respect to the IGBTs

Stray inductances in the H-bridge and the use of an inductive sense resistor were the cause of major noise problems during the prototyping phase of the PA. Oscillations caused by these stray inductances rendered the system unstable. This problem was solved by rearranging the H-bridge components and using a non-inductive power metal film sense resistor.

The first prototype of the PA also damaged the high-side output of the IR2113 driver. This was due to the stray inductance found in the path between the V_s pin and the high-side IGBT's source. This caused a negative voltage spike on the V_s pin which damaged the device. The H-bridge components were rearranged in order to locate the IR2113 driver as close as possible to the high-side IGBT in order to keep the connection between the IGBT's source and the V_s pin as short as possible. This reduced the negative voltage spike to within safe operating limits.

By keeping the high *di/dt* current loops small and the high *dv/dt* surfaces small the transmitted noise is reduced. Figure 4-27 displays the optimal H-bridge component layout which was implemented. From this layout it can be seen that the IGBTs (Z_1 and Z_2) and the power diodes (D_1 and D_2) along with R_{sense} which constitutes the H-bridge are arranged in close proximity to

minimise path inductances. The decoupling capacitor (WIMA) is also positioned very close to H-bridge to provide a low impedance source for the high frequency currents.

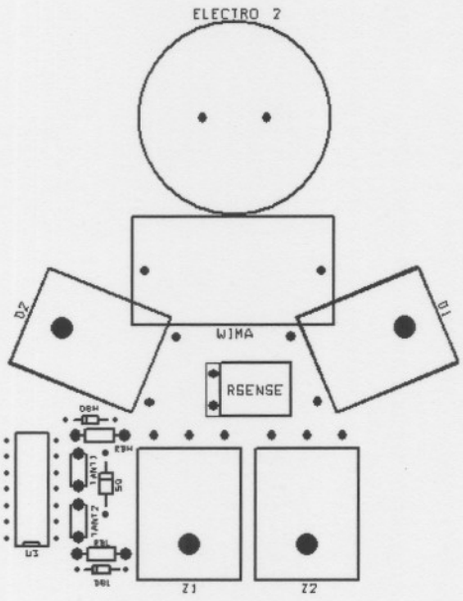

Figure 4-27 H-bridge layout

A complete circuit diagram is included in Appendix C.

4.9 Power Amplifier Characterisation

This section contains results obtained form actual measurements on the final design that was implemented.

4.9.1 H-Bridge

Figure 4-28 displays the measured coil currents at minimum, an average of 5.6 A and at maximum. The positive and negative slopes of the current ripple are equal as predicted and can now be used to obtain the actual coil inductance.

$$L = V\frac{\Delta t}{\Delta i} \qquad \textbf{(4-55)}$$

$$= 310\frac{3.04\times10^{-6}}{193\times10^{-3}}\ \text{H}$$

$$= 4.88\ \text{mH}$$

The actual coil inductance is only 68 % of the predicted value of 7.2 mH. This implies that the force slew rate will improve but the current ripple on the coil current will increase. An increase in

current ripple leads to an increase in the offset value between the reference current and actual coil current. This has a major influence on the AMB stiffness and damping parameters. The coil resistance is measured as 0.187 Ω, closely correlating with the analytically predicted value of 0.197 Ω.

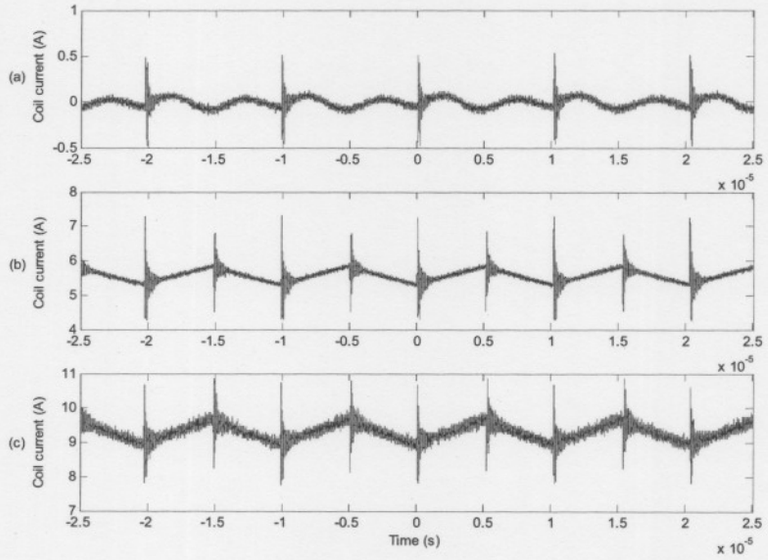

Figure 4-28 Power amplifier coil current waveforms: (a) minimum, (b) average of 5.6 A and (c) maximum

Figure 4-28 (c) shows the current for the case where the reference signal is set at 1 V, which translates to a current reference of 10 A. Note that the maximum value of the current is 10 A due to the peak current-mode control method implemented. The voltage ripple as measured across the H-bridge 310 V dc-bus is shown in Figure 4-29 for an average coil current of 9.6 A.

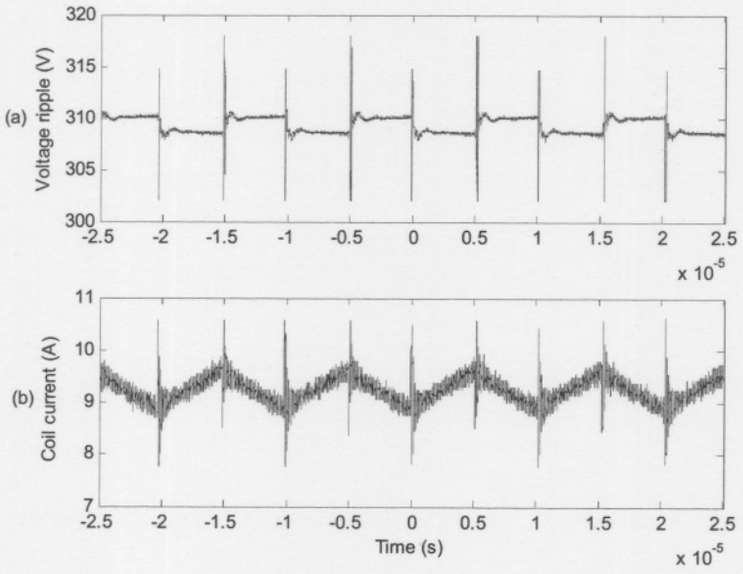

Figure 4-29 H-bridge waveforms: (a) voltage ripple, (b) coil current

Figure 4-30 (a) displays the square wave voltage which is applied to the coil in order to produce an average coil current of 5.6 A. Note that for the positive current slope the IGBTs are conducting and 310 V is applied to the coil. When the IGBTs are switched off the current flows through the diodes and the coil experiences -310 V which produces an equal but negative current slope.

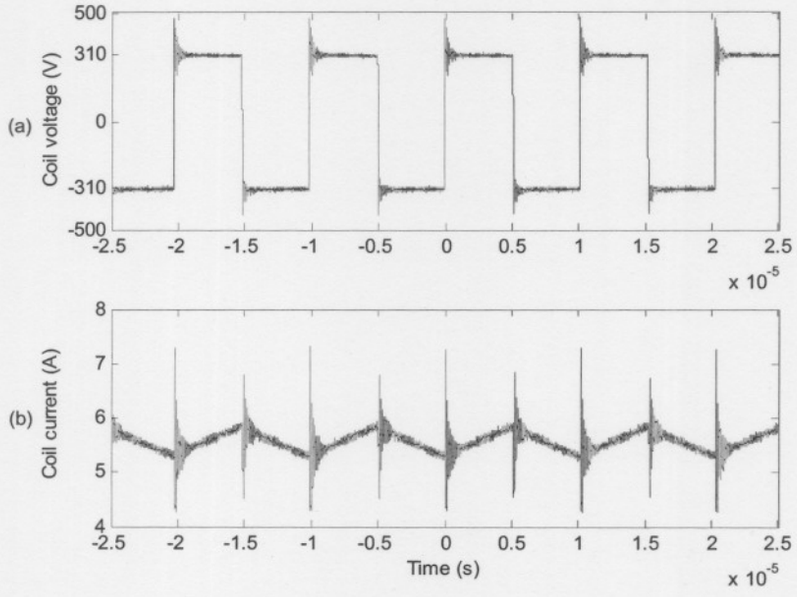

Figure 4-30 Coil waveforms: (a) applied voltage, (b) coil current

The voltage and current waveforms of the low-side IGBT device are shown in Figure 4-31. Note that only the positive slope part of the coil current is conducted by the device. The switching transients are discussed in more detail in the remainder of this section.

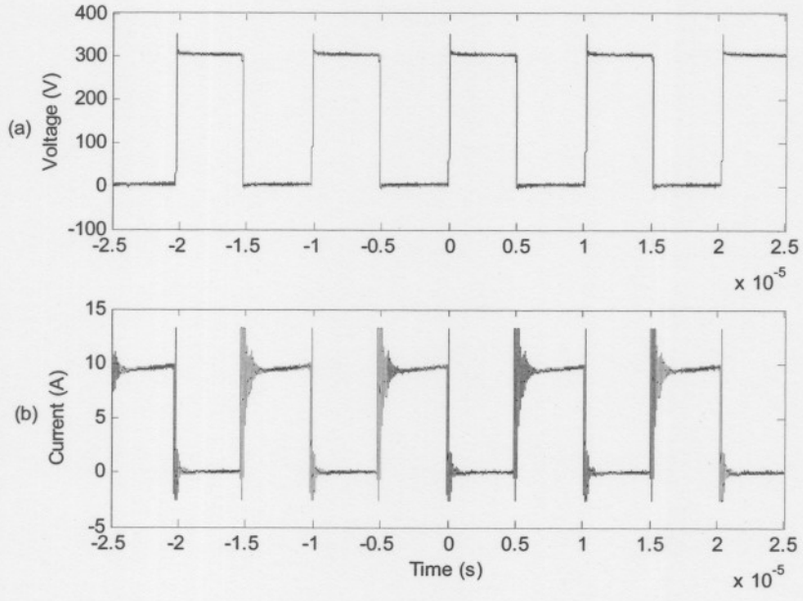

Figure 4-31 Low-side IGBT (a) voltage and (b) current waveforms

Figure 4-32 displays the IGBT's switch on transient with the drain source voltage in (a) and the drain current in (b). The drain current is obtained by measuring the voltage across R_{sense} and scaling it by a factor 10. As shown, the switching time for the device is in the vicinity of 75 ns. This translates to a power loss of approximately 12 W.

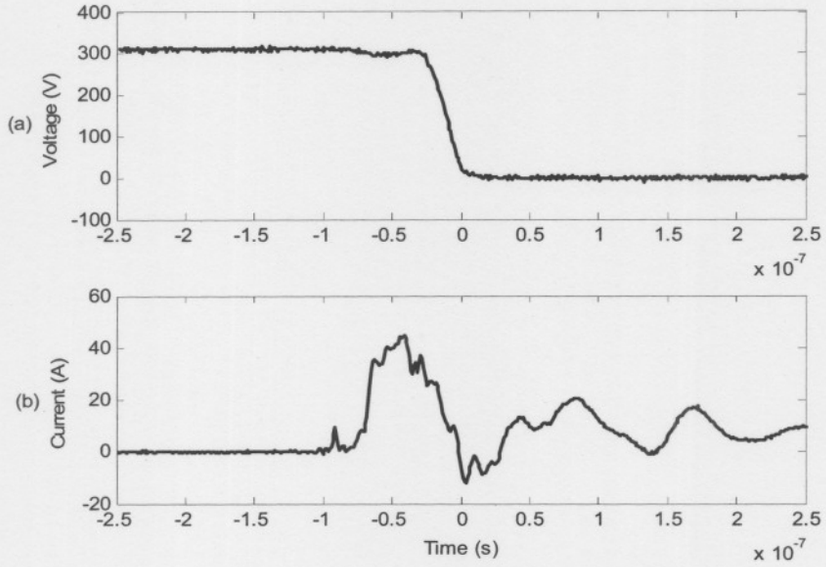

Figure 4-32 IGBT switch on (a) voltage and (b) current waveforms

The switch-off transient is shown in Figure 4-33 where a 120 ns switching time is recorded. This translates to a power loss of approximately 18 W. With the conductive losses estimated at 7 W, the total IGBT losses are estimated at 37 W. This is lower than the predicted value due to the reverse diode included across the gate drive resistor to reduce the loss effect of the current tail inherent to IGBT devices.

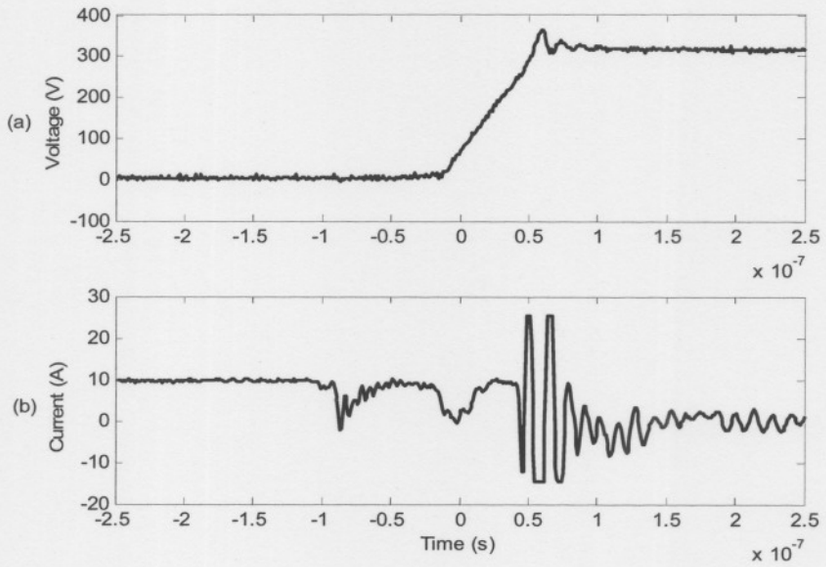

Figure 4-33 IGBT switch off (a) voltage and (b) current waveforms

4.9.2 Control

Figure 4-34 (a) displays the R_{sense} voltage waveform for an average coil current of 9.6 A, and (b) the corresponding filtered and slope compensated waveform. The leading and trailing edges of the square wave are rounded due to the low pass filter and the slope is increased due to the slope compensation.

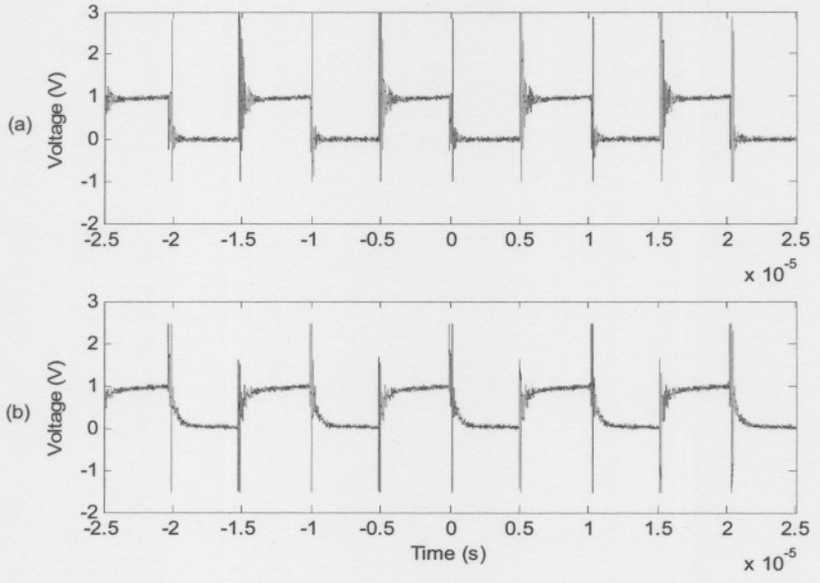

Figure 4-34 Current sense voltage (a) across R_{sense} and (b) after low pass filter and slope compensation

The power amplifier average output current is plotted against the input reference voltage in Figure 4-35. A large range with excellent linearity is displayed which verifies the component values specified in section 4.4.5.

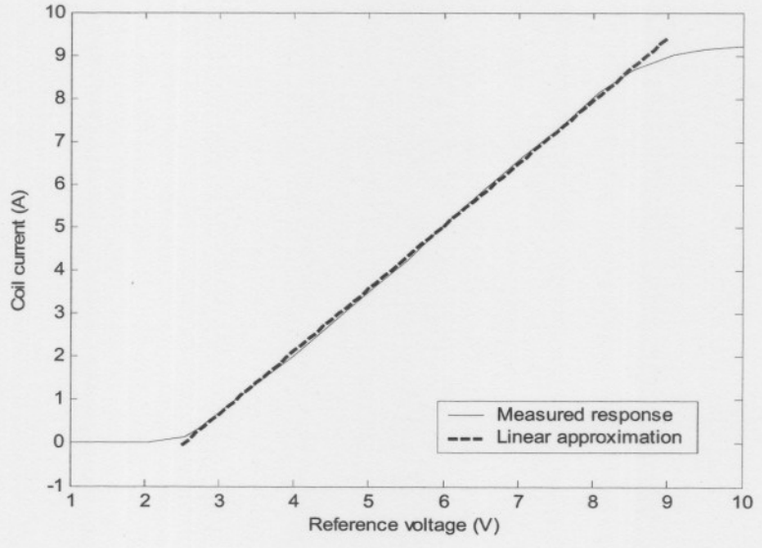

Figure 4-35 Power amplifier input – output characteristics

The power amplifier bandwidth is obtained by determining the -3 dB cut-off frequency. A sinusoidal reference voltage is applied to the PA which produces a corresponding current waveform. Figure 4-36 (a) displays the coil current at a frequency of 35 Hz without any attenuation and (b) the coil current at the point of 3 dB attenuation. The -3 dB frequency is found to be 6 kHz. Note that the -3 dB point is taken as the point where the fundamental of the triangular current waveform is attenuated by 3 dB.

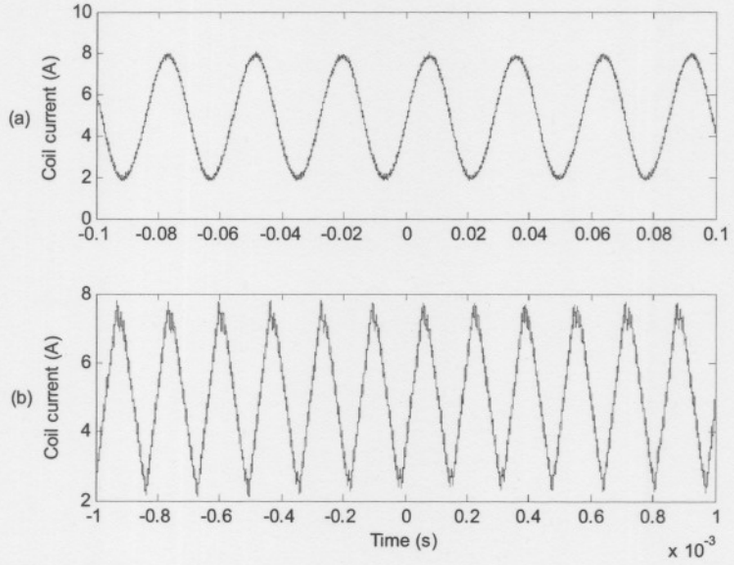

Figure 4-36 Resulting coil current for a sinusoidal reference voltage of (a) 35 Hz and (b) 6 kHz

Figure 4-37 displays a step response with (a) the reference voltage and (b) the resulting coil current. From this result the slew rate of the system can be estimated as 67143 A/s.

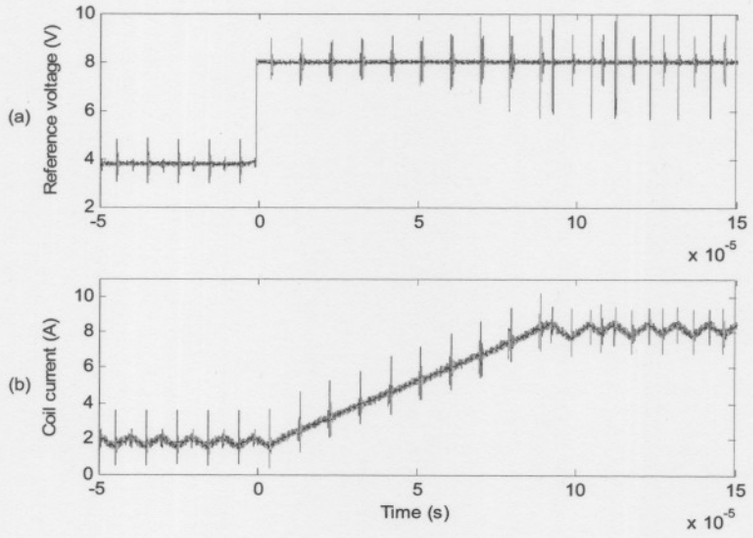

Figure 4-37 Power amplifier step response waveforms: (a) reference voltage, (b) coil current

The oscillator voltage ramp is shown in Figure 4-38 (a) without the sync pulse and (b) with the sync pulse applied. By closely observing the waveforms, it can be seen that the frequency of the synchronised timing ramp is slightly higher than the unsynchronised timing ramp.

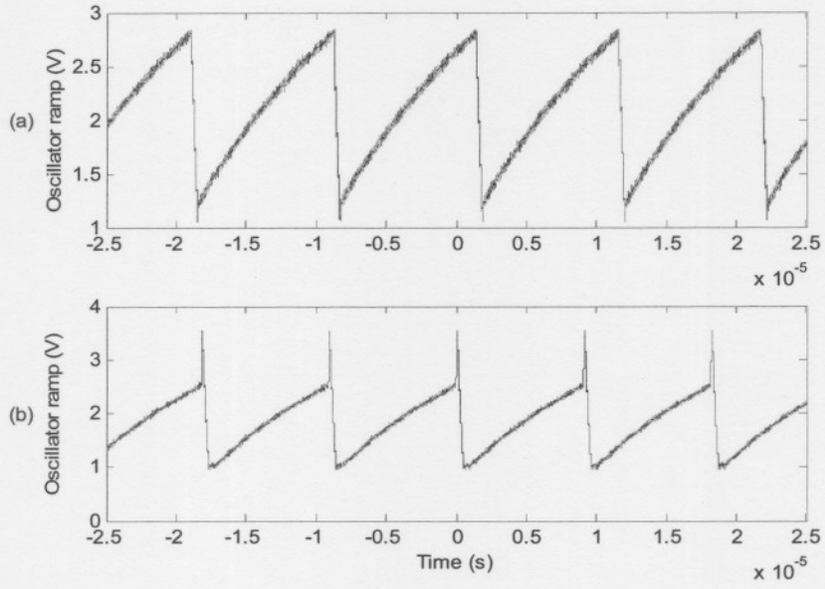

Figure 4-38 Oscillator (a) timing ramp and (b) synchronised timing ramp

4.9.3 Protection

During a short-circuit condition the latch described in section 4.6.2 pulls high the shutdown pin of the IR2113 which terminates the gate pulses. Figure 4-39 displays the shutdown pulse (a) as well as the resulting current waveform (b).

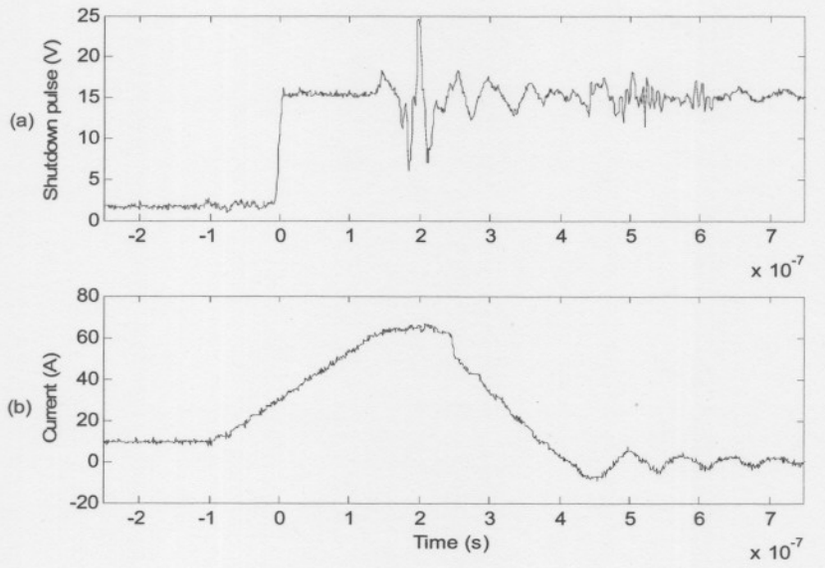

Figure 4-39 Short-circuit (a) shutdown pulse and (b) current waveforms

From the measurement it is clear that the latching speed is in the vicinity of 50 ns and the time to turn off the H-bridge in the region of 200 ns. The peak current of 65 A is well below the non-repetitive peak current rating of the diodes (150 A) and IGBTs (220 A).

4.9.4 Thermal measurements

During thermal testing the power amplifier is operated at an average current of 5.6 A and at an ambient temperature of 28 °C. The heat sink temperature is gradually increased by reducing the effectiveness of the cooling fan. This raises the heat sink thermal resistance to the point where the heat sink will not reach thermal equilibrium below the thermal switch threshold. The thermal switch activates just before the fan is completely removed, which indicates that the heat sink's thermal resistance is only slightly too high for operation without added cooling. Figure 4-40 displays the locations at which the temperature readings were taken.

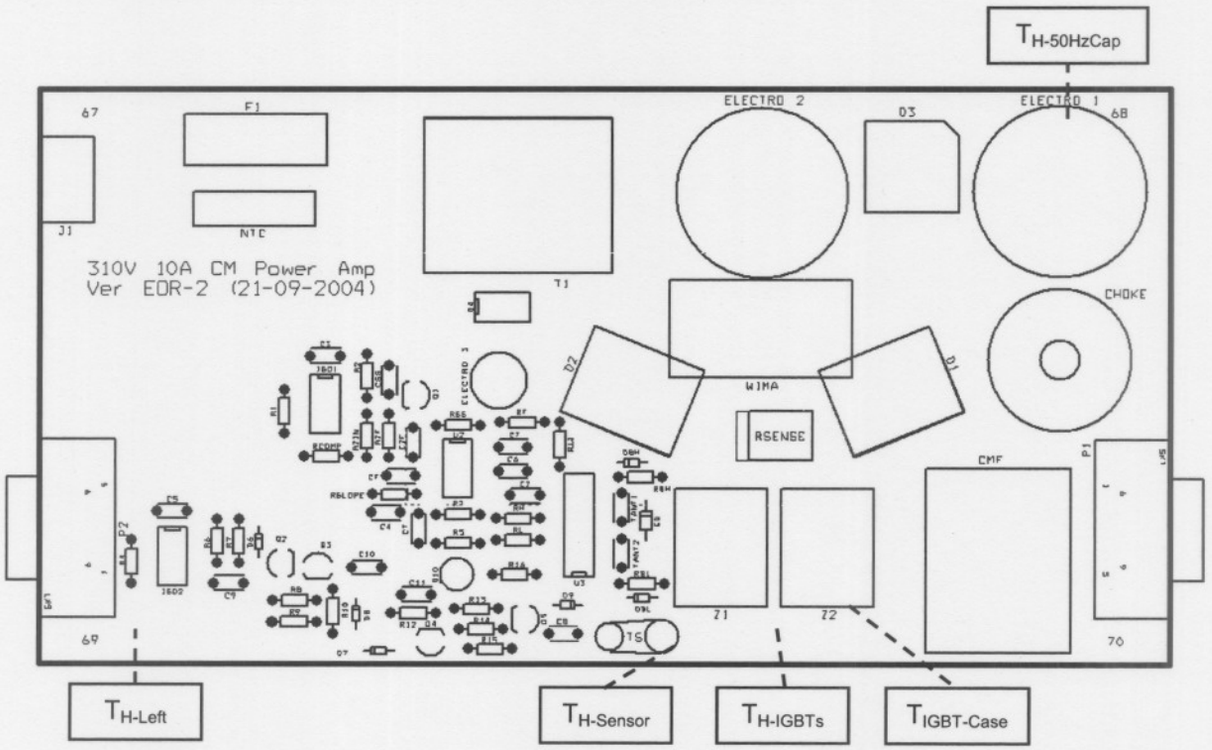

Figure 4-40 Temperature measurement locations

The temperatures recorded at the moment the thermal switch shuts down the PA are as follows:

- $T_{IGBT\text{-}Case}$ = 74 °C (IGBT case temperature)
- $T_{H\text{-}Sensor}$ = 63 °C (Heat sink temperature near thermal switch)
- $T_{H\text{-}IGBTs}$ = 65 °C (Heat sink temperature near IGBTs)
- $T_{H\text{-}50HzCap}$ = 62 °C (Heat sink temperature near 50 Hz smoothing capacitor)
- $T_{H\text{-}Left}$ = 50 °C (Heat sink temperature near control connector)

Using the case to sink thermal resistance of the IGBT the amount of power dissipated by a single device at an average coil current of 5.6 A is given by (4-56).

$$Q_{IGBT} = \frac{T_C - T_S}{R_{\theta CS}} = \frac{74-65}{0.46}\ \text{W} = 19.6\ \text{W} \tag{4-56}$$

An estimated power loss value using the switching times and an average coil current of 5.6 A results in (4-57):

$$Q_{IGBT} = \frac{V I_{avg}}{2} t_{sw} f + V_f I_{avg} d = \frac{310 \cdot 5.6}{2} \cdot \left(120 \times 10^{-9} + 75 \times 10^{-9}\right) \cdot 100 \times 10^{3} + 1.3 \cdot 5.6 \cdot 0.5\ \text{W} = 20.6\ \text{W} \tag{4-57}$$

This result verifies that the thermal resistance of the material used to isolate the components from the heat sink is accurate.

The following measurements are obtained at thermal equilibrium, with external cooling representative of the final configuration.

- $T_{IGBT\text{-}Case}$ = 65 °C
- $T_{H\text{-}Sensor}$ = 53 °C
- $T_{H\text{-}IGBTs}$ = 56 °C
- $T_{H\text{-}50HzCap}$ = 48 °C
- $T_{H\text{-}Left}$ = 45 °C

From these results it is evident that the devices are operated well below their recommended maximum thermal ratings.

In chapter 4 a switch-mode power amplifier using peak current-mode control was designed implemented and tested. It was found that the PA displayed excellent linearity over a wide input range which renders it ideal for the application it was designed for. The PA displays a very high bandwidth (6 kHz) *which is required for efficient control implementation in high speed AMB systems. Short-circuit protection as well as over temperature protection is included to safeguard the PAs from fault conditions that may occur during operation. With the AMB hardware and PAs developed, the next step is system integration which will be discussed in detail in chapter 5.*

5
Chapter
System Integration

Chapter 5 contains a detailed discussion on system integration. Figure 5-1 *displays the system interface block diagram which shows the system comprises a controller, electrical interface and magnetic bearing hardware.*

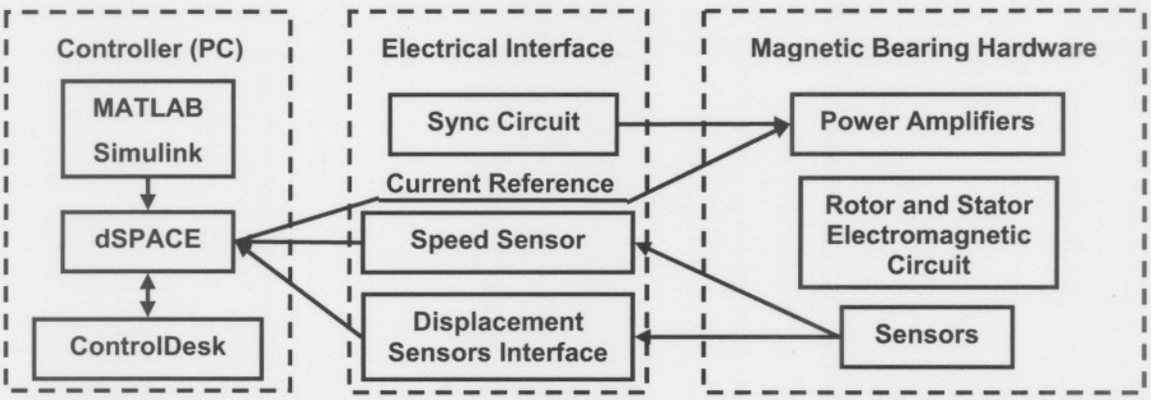

Figure 5-1 System interface block diagram

The controller is housed on a personal computer (PC) and comprises dSPACE® hardware, ControlDesk® interfacing software and MATLAB's Simulink® environment. The magnetic bearing hardware consists of power amplifiers, stator and rotor electromagnetic circuits, a speed sensor and displacement sensors. The dSPACE® card located in the PC receives (transmits) analogue signals from (to) the hardware. This is accomplished through an electrical interface. The electrical interface houses the synchronisation circuitry for the PAs, speed sensor circuitry for the optical speed sensor and displacement sensor interfacing circuitry. The following sections contain detailed discussions of the system components.

5.1 Magnetic Bearing Hardware

5.1.1 Power Amplifiers

Although some thought was given to conducted Electromagnetic Interference (EMI) in the previous chapter, little consideration was given to limiting radiated emissions. The contributors to radiated EMI are categorised depending on how the energy is generated. The energy may result from an electric field, which is generated by a changing voltage (dv/dt) on a conductive surface, or from a magnetic field which is generated by a changing current (di/dt) in a conductive path.

In order to limit the radiated EMI the eight PAs are electrically shielded from one another and external circuitry by means of mild steel sheet metal enclosures which are connected to ground. This material is both conductive and ferrous and by placing each PA in its own compartment both the electric and magnetic fields are attenuated. The compartments are however not completely sealed off and slot antennas may still pose a problem. This will be investigated during laboratory testing.

The PAs are mounted on two separate heat sinks which are located back to back and cooled by two external 220 V ac cooling fans. Detailed CAD drawings of this configuration are included in the mechanical design shown in Appendix B. Figure 5-2 displays the heat sink–PAs arrangement with the PAs uncovered.

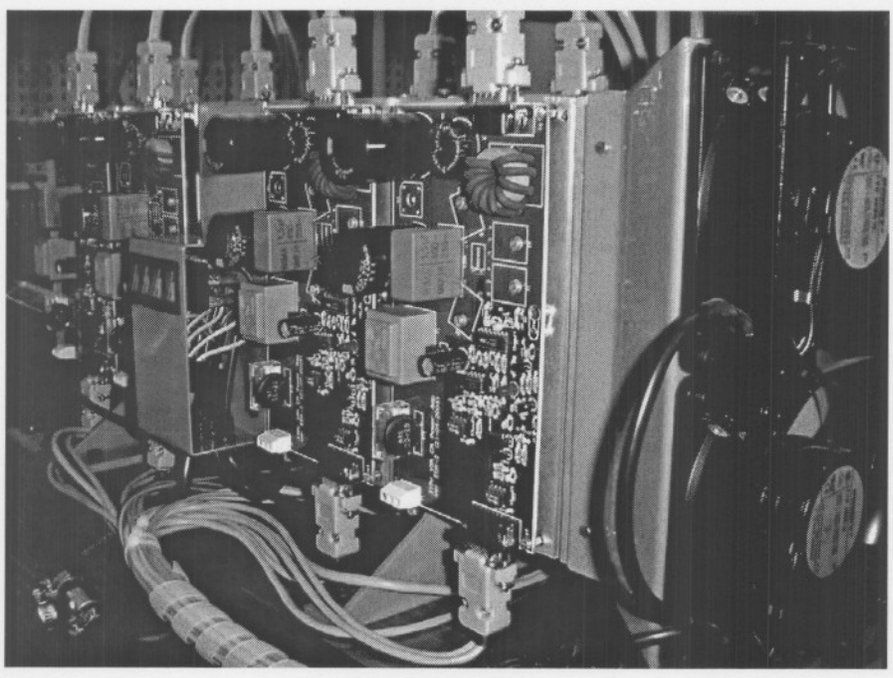

Figure 5-2 Power amplifier heat sink layout

5.1.2 Rotor and Stator Electromagnetic Circuit

As stated in section 3.3.1 the rotor and stator electromagnetic circuits are manufactured from silicon steel laminations. Figure 5-3 displays the cleated stator lamination packs as well as both the rigid and flexible rotor lamination packs.

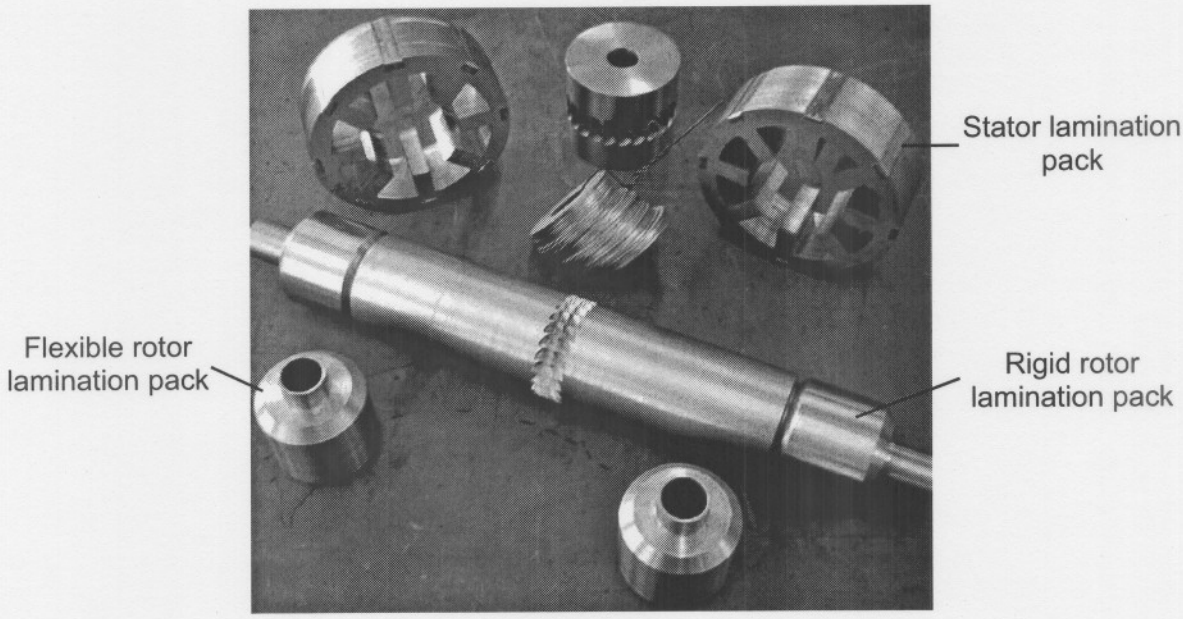

Figure 5-3 Rotor and stator electromagnetic circuits

5.1.3 Sensors

Eddy current sensors were chosen to monitor rotor displacement due to their immunity to the high frequency noise generated by the PAs. The eddy current sensor that was sourced is the SKF CMSS65/CMSS665 series 5 mm Eddy Probe System. Figure 5-4 displays the probe tip of one of the sensors.

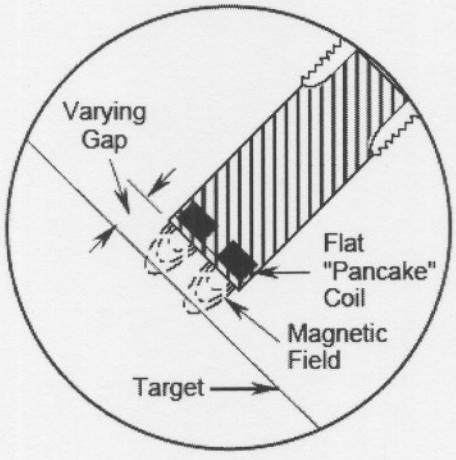

Figure 5-4 Eddy current probe tip

The encapsulated coil, situated in the probe tip, radiates a high frequency magnetic field into the observed target. This magnetic field is generated by a driver circuit. As a conductive surface approaches the probe tip, eddy currents are induced which weakens the magnetic field. The driver produces a dc voltage representing the field strength which decreases as a conductive surface nears the probe tip.

The driver linearises and normalises its output to a specific sensitivity (7.87 mV/micron) throughout its working range. The eddy probe system has a useable sensing range of 2 mm and a dynamic range of dc up to 10 kHz (-3dB). Since the maximum rotating frequency of the rigid rotor is 500 Hz, a 10 kHz bandwidth is more than adequate. The driver power requirements are: 15 mA from a -24 V dc supply. The minimum calibrated load resistance of the driver is 3 kΩ and the driver output is protected against faulty wiring.

Two sensors are located in each stator in order to monitor the vertical (y-axis) and horizontal (x-axis) axes. The voltage signals representing the rotor position are fed to the analogue to digital converters (ADCs) located on the dSPACE® card. Figure 5-5 displays the eddy current probes as integrated in the stator.

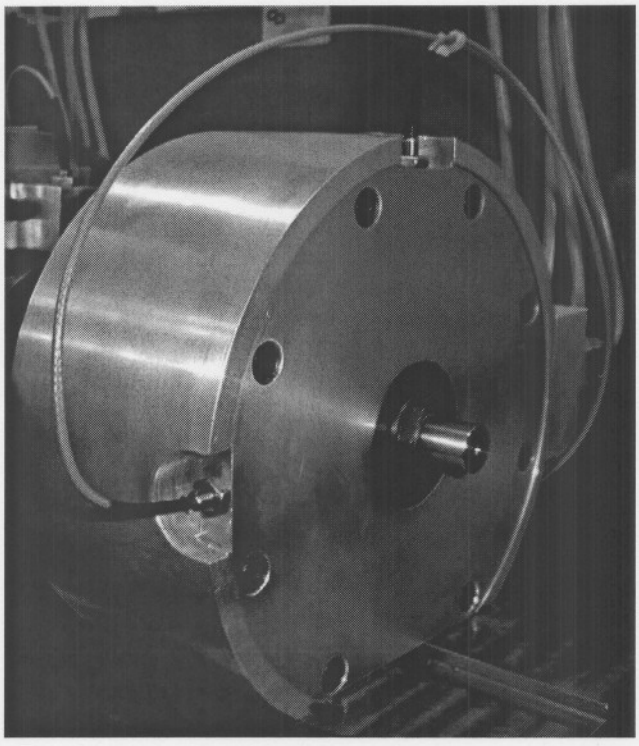

Figure 5-5 Integrated eddy current probes

The developed flexible rotor AMB hardware necessitates a speed sensor to characterise the system and determine the critical frequencies. An optical sensor is used to monitor the rotational frequency. Figure 5-6 displays the optical speed sensor arrangement. The sensor operation is discussed in detail in section 5.3.3.

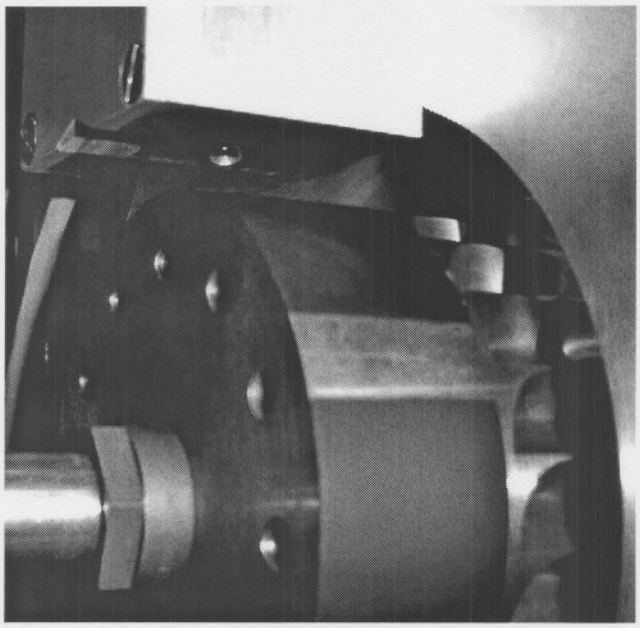

Figure 5-6 Speed sensor

5.2 Controller

A digital controller is used for this specific application. Since a current controlled PA is used a simple PD controller is adequate to control the rotor in its reference position. The magnetic circuit design does not allow flux splitting which simplifies the control requirements even further. Since no flux splitting takes place the y-axis and x-axis of each AMB are controlled independently. The control parameters obtained from the MATLAB® simulation model in chapter 3 are now implemented in a Simulink® model of the system.

5.2.1 Simulink®

As stated above the respective y and x-axis of each magnetic bearing is controlled separately. Due to the magnetic circuit's symmetrical design and ignoring the effect of gravity, the control for all four axes are identical. Figure 5-7 displays the Simulink® model of the control for a single axis, the left bearing vertical axis in this case. The rotor displacement is monitored by the SKF

eddy probe system which produces an analogue voltage signal. This signal is converted into a 16-bit digital value via the analogue to digital converter (ADC) shown on the left of Figure 5-7.

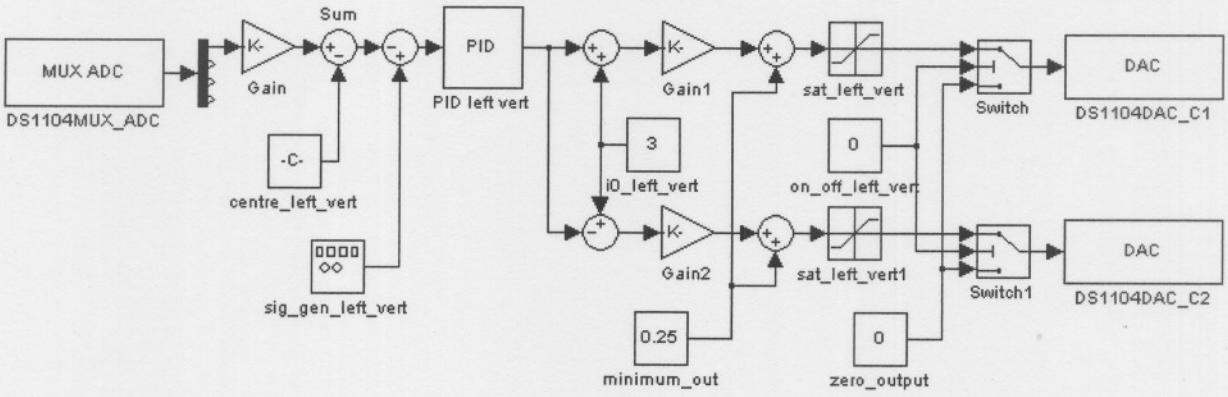

Figure 5-7 Simulink® model of a single axis controller

The dSPACE® card converts a voltage of 10 V to a digital floating point value representing 1. In order to correlate the controller parameters with the simulation parameters the input is scaled to convey the rotor position in meters. The sensor's sensitivity of 7.87 mV/micron is further attenuated by a factor 10 due to the ADC. The scaling factor (Gain in Figure 5-7) which converts the input to meters is obtained using (5-1).

$$Sensitivity = \frac{7.87\times10^{-3}}{10\cdot1\times10^{-6}} \ V/m \qquad \textbf{(5-1)}$$

$$\Delta x = \frac{10\cdot1\times10^{-6}}{7.87\times10^{-3}}\Delta v \ [m]$$

$$= 1.27\times10^{-3}\cdot\Delta v \ [m]$$

The centre position reference is subtracted from the position signal in order to obtain the error signal which is fed to the digital PD controller. A signal generator is also implemented in order to change the position reference.

The PD control element generates a control current reference signal which is added to the bias current signal for the one PA and subtracted for the other. This then generates the current reference signal for each PA. The PAs however do not respond to reference voltages below 2.5 V. Since the PA output range is 10 A for an input range of 7.5 V, the current reference signal is scaled by a factor 0.75 and an offset value corresponding to the 2.5 V is added.

Finally a switch is implemented in order to force the PA reference current to zero which shuts it down. The output of the switch is connected to the DAC which produces an analogue output for

each PA. The DAC increases the current reference signal fed to it by a factor 10 which is also taken into account.

The program cycle time is determined by the complexity of the model and is obtained experimentally. For this specific application a cycle time of 50 µs which relates to a sampling frequency of 20 kHz is implemented.

5.2.2 dSPACE®

Real time development is a vital tool in control engineering. The same is true for the automatic generation of real-time code which can be implemented on the hardware. Real-Time Interface (RTI)/RTI-MP) carries out this linking function for dSPACE® systems. Together with Real-Time Workshop from The MathWorks it automatically generates real-time code from Simulink® models and implements this code on the dSPACE® real-time hardware.

The dSPACE® real-time development hardware contains four 16-bit analogue to digital converters (ADCs) and four 12-bit ADCs. It also houses eight 12-bit digital to analogue converters (DACs). The four 16-bit ADC inputs are used to convert the analogue position signals generated by the sensors into digital values. The controller then generates the appropriate digital control values which are converted to analogue signals via the eight DACs.

5.2.3 ControlDesk®

ControlDesk®, dSPACE's well established experiment software, provides all the functions to control, monitor and automate experiments and make the development of controllers much more efficient. ControlDesk® allows the control engineer to access all the parameters incorporated in the Simulink® model. The parameters may be manipulated or monitored in order to optimise the control or to conduct certain experiments on the system.

Figure 5-8 displays the main ControlDesk® interface window for this project which allows access to the control parameters of the Simulink® model. X-Y plots of both the left and right stator's x and y positions as well as the values of the control parameters of all four controllers are displayed. The PID constants as well as the bias current level for each control axis can be manipulated individually. Each control axis can also be switched off individually which may be required for certain experiments. The rotational speed is monitored with an optical speed sensor and displayed.

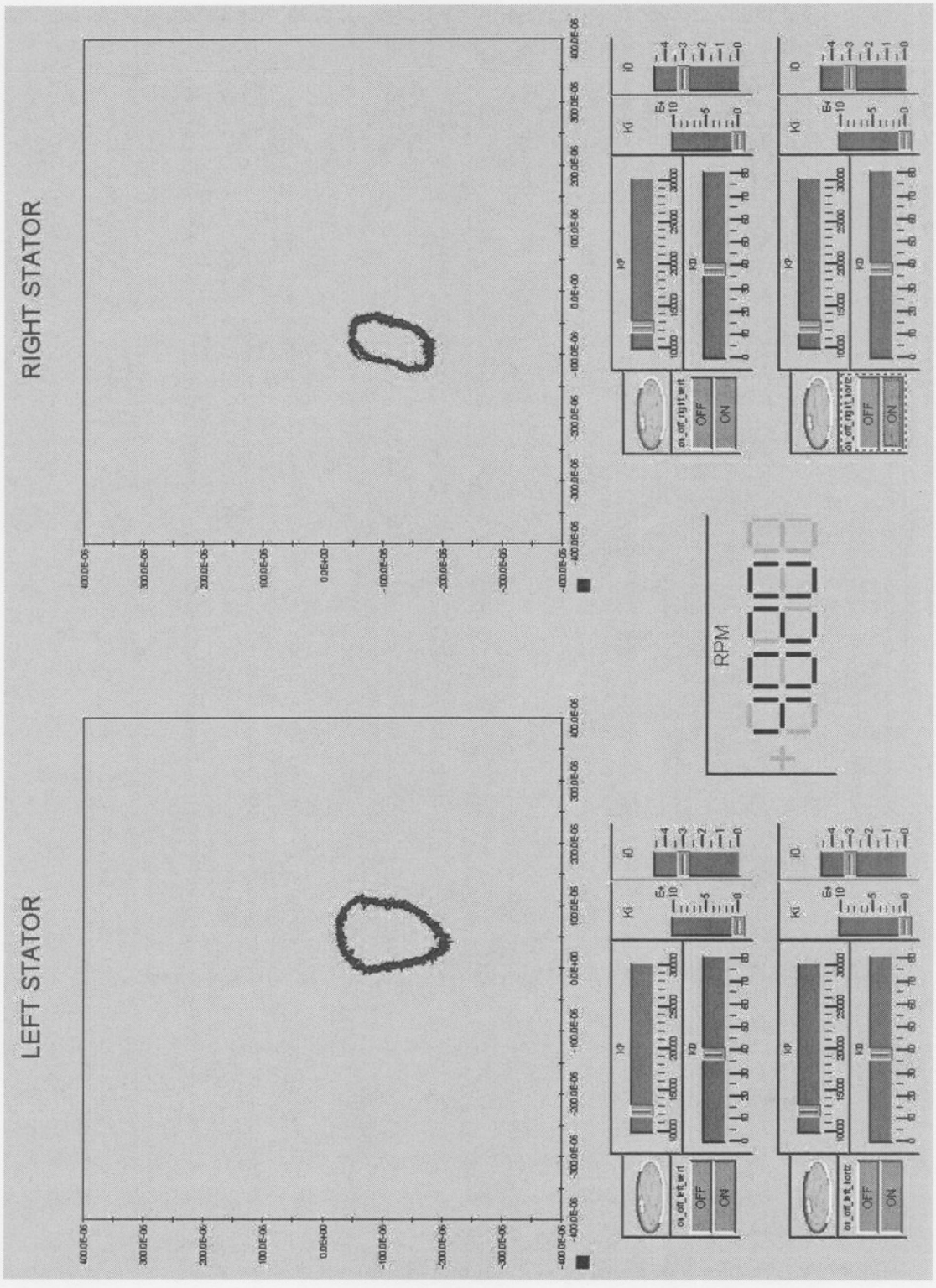

Figure 5-8 ControlDesk® main interface window

Figure 5-9 displays the ControlDesk® interface window that is used to capture system data. In the right top corner the centre mass vertical position is plotted against time. The left stator vertical and horizontal positions are plotted in the left bottom corner, top and bottom graphs

respectively. The right stator vertical and horizontal positions are plotted in the right bottom corner, top and bottom graphs respectively. The interface window also allows the user to apply position reference changes and conduct step response measurements on all four axes.

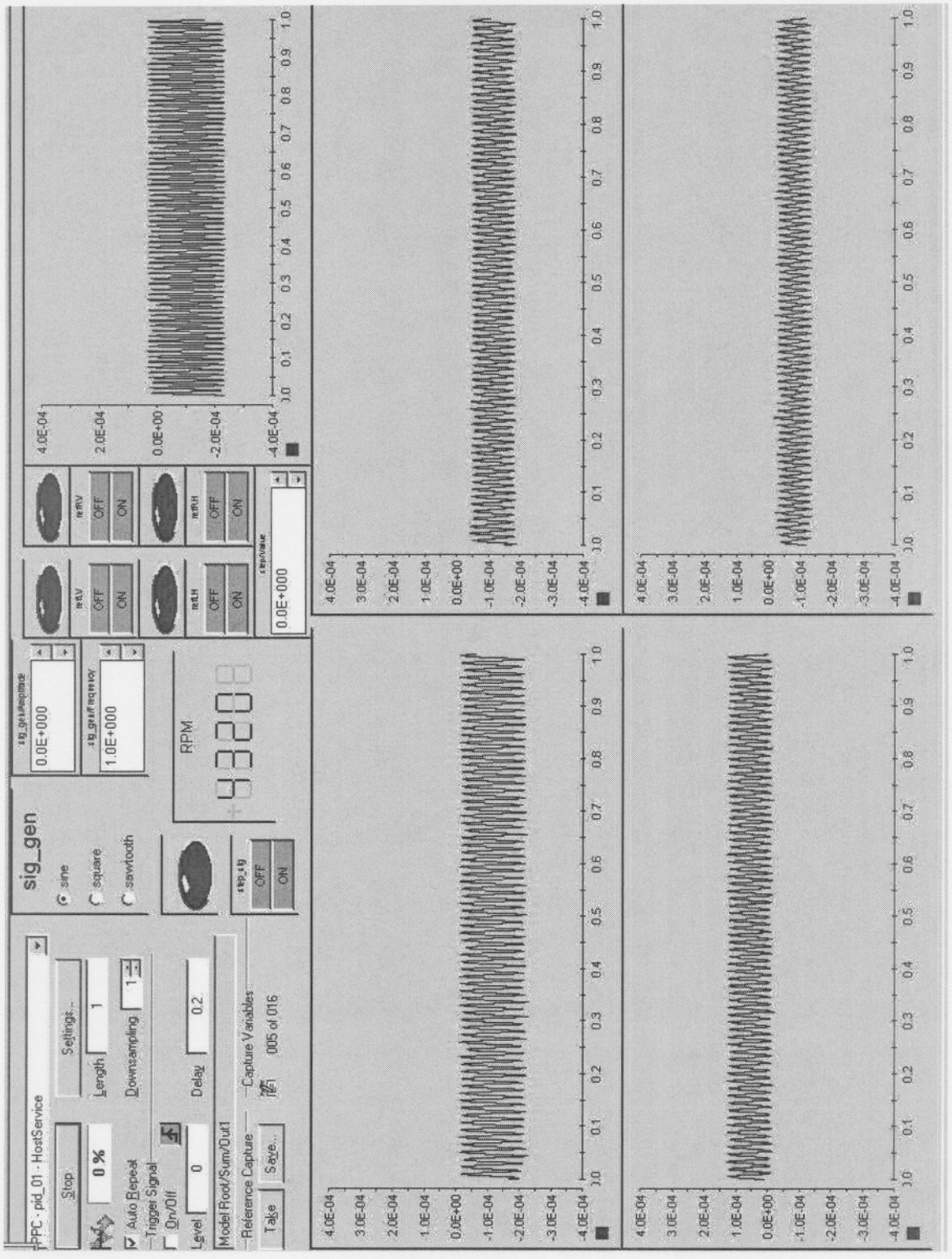

Figure 5-9 ControlDesk® data capture interface window

5.3 Electrical Interface

The dSPACE® DS1104 real-time development card which is located in the PC has a 100-pin, high density KEL I/O connector (P1) which is used to obtain access to the I/O signals of the board. Connector P1 in turn is connected to two Sub-D connectors, P1A and P1B. These connectors are plugged into the enclosure designed to house all of the circuitry needed to interface the DS1104 card with the AMB hardware. Each relevant I/O pin is connected to the corresponding AMB hardware signal. The enclosure is manufactured from mild-steel and is grounded to reduce EMI.

Figure 5-10 shows the electrical interface enclosure with the synchronisation circuit at the top, the speed sensor circuitry in the middle and the displacement sensor interface circuitry at the bottom. The five black units on the left are the eddy current probe drivers. The electrical interface connects to the PC via a ribbon cable.

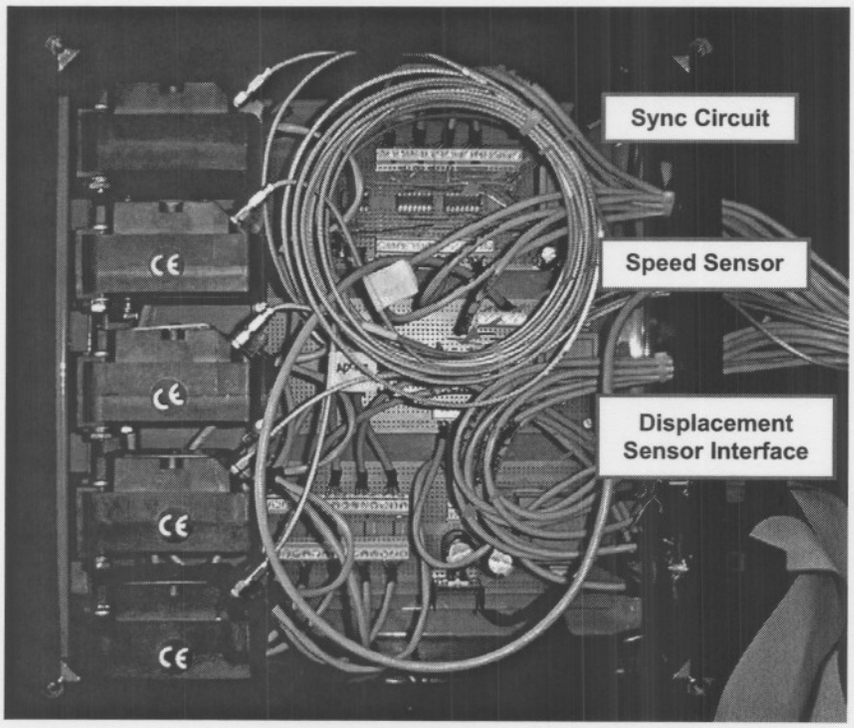

Figure 5-10 Electrical interface

5.3.1 Synchronisation circuit

The synchronisation circuit comprises an oscillator and a network of fast comparators. Figure 5-11 displays a schematic diagram of the synchronisation circuit located in the electrical interface. The oscillator generates a 100 kHz, 5 V square wave which is compared to a 2.5 V

reference by LM399 comparators. The comparators are used to drive the optocoupler input of the synchronisation circuitry located on the PAs.

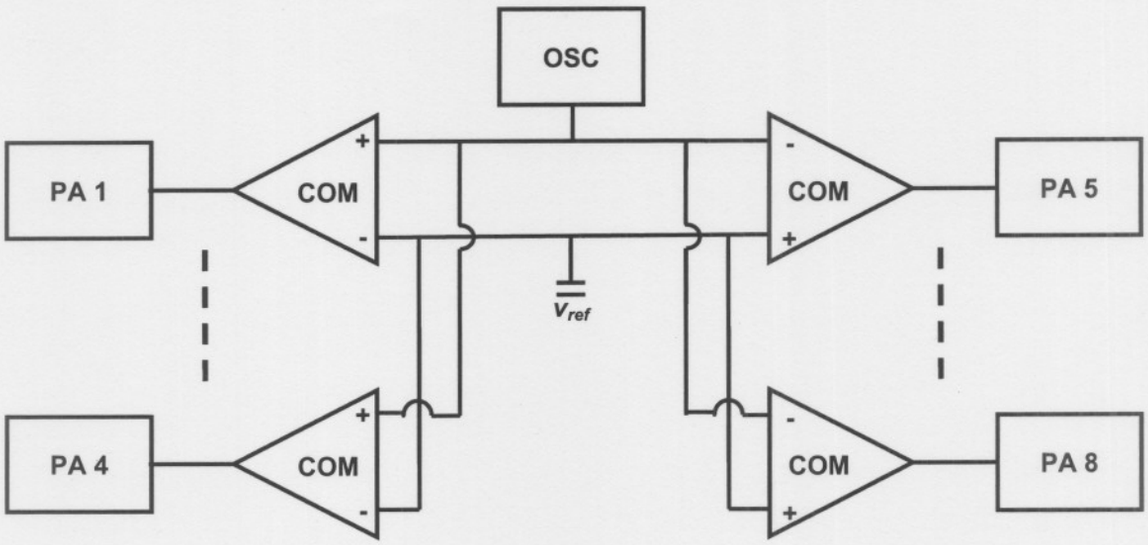

Figure 5-11 Synchronisation schematic diagram

5.3.2 Control reference

The digital PD controller, housed on the DS1104 real-time development card, generates an appropriate current reference signal for each PA. The I/O pins on which the signals are generated are connected to the corresponding PA optocoupler inputs. The optocoupler electrically isolates the DS1104 card from the PA which protects it from fault conditions that may result during testing.

5.3.3 Speed Sensor

As stated in section 2.6 critical speed is defined as the speed at which vibration due to rotor imbalance is at a maximum. In order to characterise the developed system and determine the critical frequencies, the rotational speed must be monitored. An optical speed sensor is realised using an infrared LED and a pin-diode. The two components are aligned so that the infrared light is reflected onto the pin diode by the centre mass. The reflecting area on the centre mass is painted black except for a 10 mm strip. This will generate a transition in the amount of light received by the pin-diode.

Figure 5-12 displays the circuit diagram of the optical speed sensor. The output of the circuit is a 5 V pulse train with a frequency equal to the rotational frequency. This signal is applied to a

digital input on the dSPACE® card where the rotation speed is obtained by measuring the frequency of the pulse train.

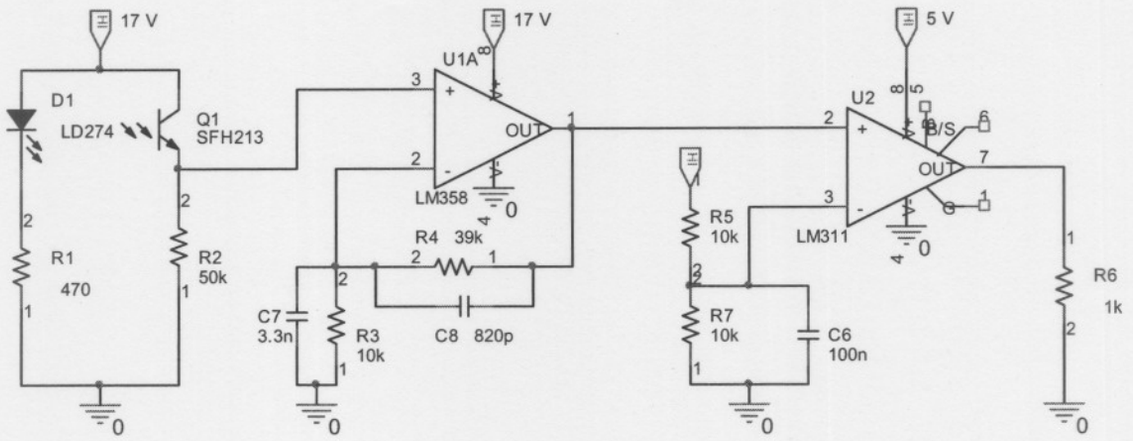

Figure 5-12 Speed sensor circuit diagram

5.3.4 Displacement Sensor Interface

The SKF eddy current probe drivers require a -24 V dc supply with a minimum current capability of 75 mA. Figure 5-13 displays the proposed power supply circuit diagram.

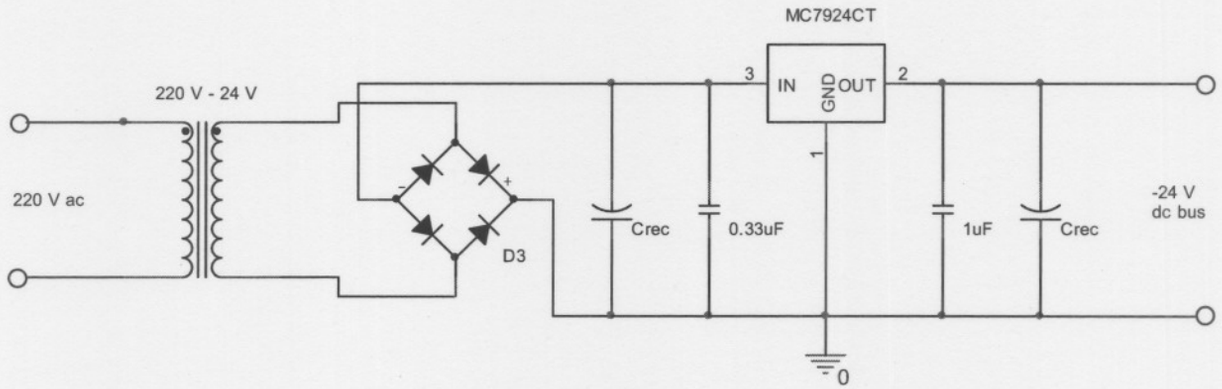

Figure 5-13 Sensor power supply circuit diagram

The transformer's VA rating (S_{tr}) is obtained in (5-2) by using the 24 V ac rectified value and six times the supply current required by one eddy current sensor (15 mA).

$$\begin{aligned} S_{tr} &= \sqrt{2} \cdot V_{ac} \cdot i_{dc} \\ &= \sqrt{2} \cdot 24 \cdot 90 \cdot \times 10^{-3} \ \text{VA} \\ &= 3.1 \ \text{VA} \end{aligned} \tag{5-2}$$

A 3.2 VA, 220 V to 24 V transformer was sourced. The rectifier capacitor value for a voltage ripple component of less than 2.5 % is obtained using (5-3).

$$C_{rect} = i_{dc}\frac{dt}{dv} \tag{5-3}$$
$$= 90\times10^{-3}\cdot\frac{10\times10^{-3}}{0.025\cdot34}\ \text{F}$$
$$= 1060\ \mu\text{F}$$

A 1000 µF, 63 V capacitor is used.

The sensor output varies from 0 to -24 V while dSPACE® only allows an input of ±10 V. Some circuitry is added in order to protect the dSPACE® card from sensor inputs above the maximum ratings.

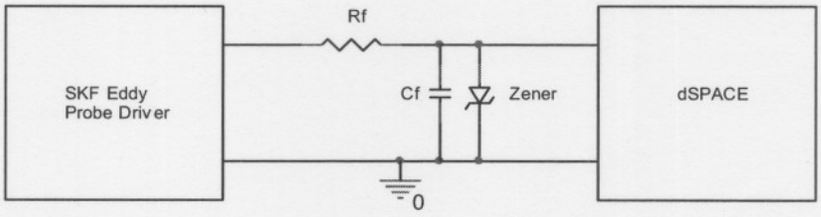

Figure 5-14 Sensor over voltage output protection

An 11 V zener diode is used to limit the voltage input to the DS1104 card. The minimum value for R_f is obtained using (5-4).

$$R_f = \frac{V_{max} - V_{zener}}{I_{max}} \tag{5-4}$$
$$= \frac{24-11}{8\times10^{-3}}\ \Omega$$
$$= 1.6\ \text{k}\Omega$$

R_f is chosen as a 3.3 kΩ resistor. The filter capacitor's (C_f) value is obtained using (5-5) for a cut-off frequency of 5 kHz.

$$C_f = \frac{1}{2\pi R_f f} \tag{5-5}$$
$$= \frac{1}{2\pi\cdot3.3\times10^{3}\cdot5\times10^{3}}\ \text{F}$$
$$= 9.6\ \text{nF}$$

A 10 nF ceramic capacitor is used.

5.4 System Assembly

Special care is taken with general system layout, shielding and system grounding to ensure that the noise embedded in the system does not render it unstable. Figure 5-15 displays the system shielding and grounding diagram. One central earth point is used with a star configuration to ensure that earth loops are not created. The shielding is also configured to ensure low levels of noise coupling.

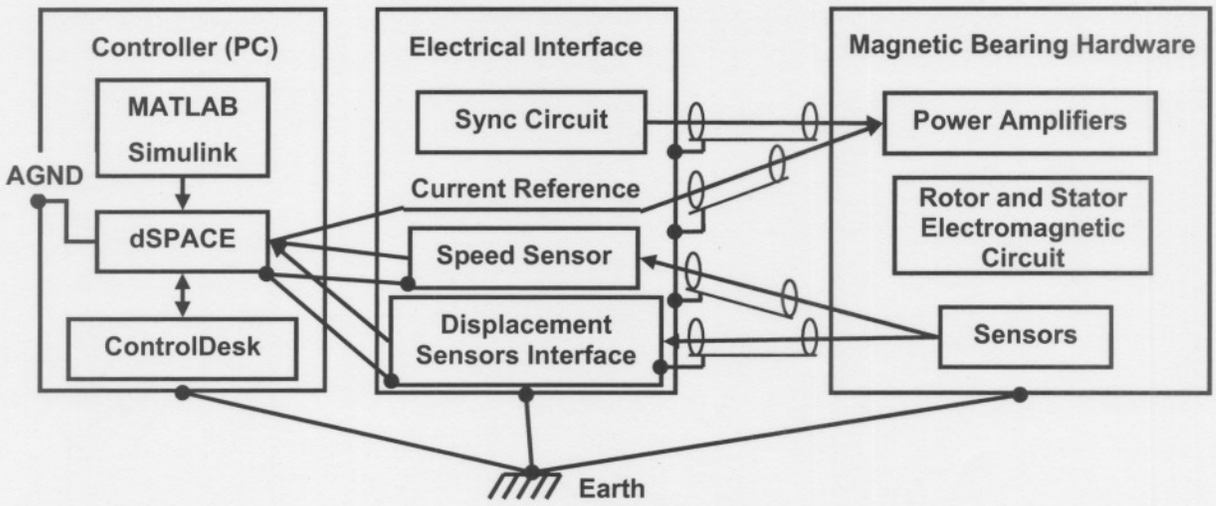

Figure 5-15 System shielding and grounding diagram

Figure 5-16 shows the final magnetic bearing hardware model that was developed. The PAs, both stators and the air pressure turbine are located on the base plate. The end result is an aesthetically pleasing model.

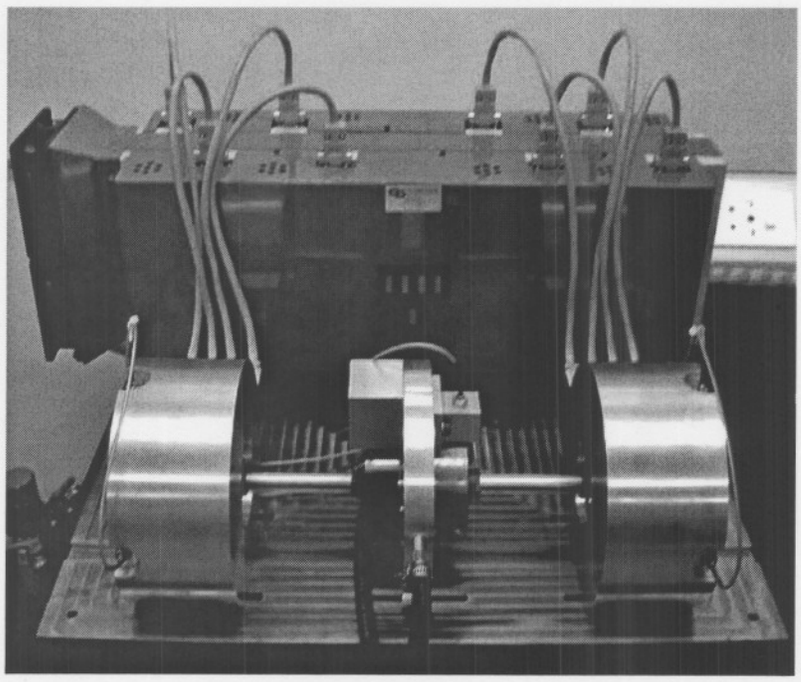

Figure 5-16 Flexible rotor AMB model

Chapter five discusses the system integration with emphasis on the electrical interface, dSPACE® implementation, general system layout and shielding and grounding. The system will now be characterised in chapter 6.

6
Chapter
System Characterisation

Chapter 6 contains results obtained from the physical flexible rotor AMB model. The system dynamic performance is first analysed. The equivalent stiffness is obtained from the steady state deflection due to gravitational force on the rotor and the equivalent damping from a step response. The system's sensitivity is measured and compared to ISO standards and finally the system's rotordynamic performance is recorded and discussed.

6.1 AMB Dynamic Performance

6.1.1 Equivalent stiffness and damping

The AMB stiffness can be obtained from the deflection due to a disturbance force. Figure 6-1 displays the right stator steady state vertical position where zero represents the magnetic bearing centre position. The deflection is due to the gravitational force exerted on the rotor.

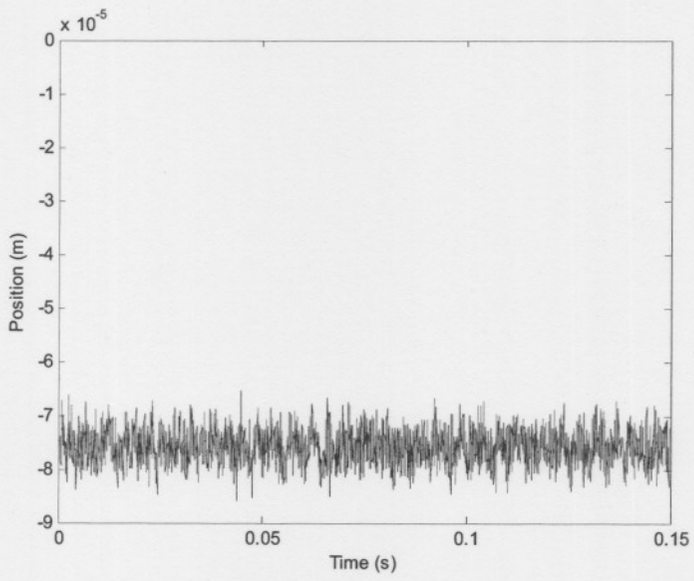

Figure 6-1 Steady state error due to rotor mass

The steady state error together with one half of the rotor mass is used to obtain the equivalent stiffness using (6-1).

$$k_{eq} = \frac{F}{x} = \frac{mg}{x} = \frac{3.86 \cdot 9.81}{75 \times 10^{-6}} \text{ N/m} \qquad \textbf{(6-1)}$$
$$= 505 \times 10^{3} \text{ N/m}$$

The system was designed for a stiffness of 500×10^3 N/m (refer to chapter 3 section 3.3.1). This result reveals a 99 % correspondence between the predicted and experimental results. The simulated stiffness obtained from the steady state error due to a disturbance force (479×10^3 N/m) is much lower than the predicted and experimental results. These phenomena will be addressed in chapter 7. The system equivalent damping is obtained using a step response. Figure 6-2 displays the experimental and simulated results obtained from a 50 µm step in the positive horizontal axis.

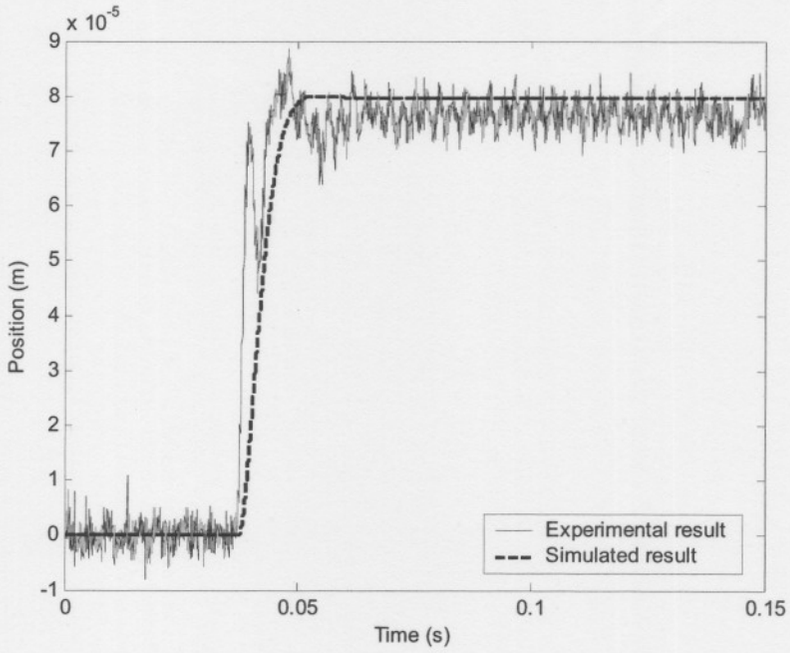

Figure 6-2 Horizontal step response (50 µm step)

Although there is good correlation between the settling values of the experimental result and the simulated result, the rise times differ. The practical rise time is much shorter than the simulated response. The practical damping is much lower than the simulated damping as revealed by the percentage overshoot (*P.O.*) and oscillations. This explains the difference in rise times since the rise time can be shortened by lowering the system damping. The practical result also reveals a 130 Hz oscillatory component on the step response during the step transition.

The noisy displacement signal obtained from the physical system is fed through a low pass filter to remove the high frequency noise components. Figure 6-3 displays the filtered version of the step response. Due to the noise it is not possible to accurately determine the settling time of the step response. The equivalent damping can be determined from the equivalent stiffness and the *P.O.* using (6-2). The *P.O.* is estimated as 11.7 % resulting in a ζ of 0.564.

$$b_{eq} = \zeta\left(2\sqrt{k_{eq} \cdot m}\right) = 1.585 \times 10^3 \text{ N.s/m} \quad \textbf{(6-2)}$$

The physical system displays a much lower damping which may be due to the extra pole introduced in the differential gain path at 1000 rad/s. The lower damping and the oscillatory response of the practical system will be further investigated in chapter 7.

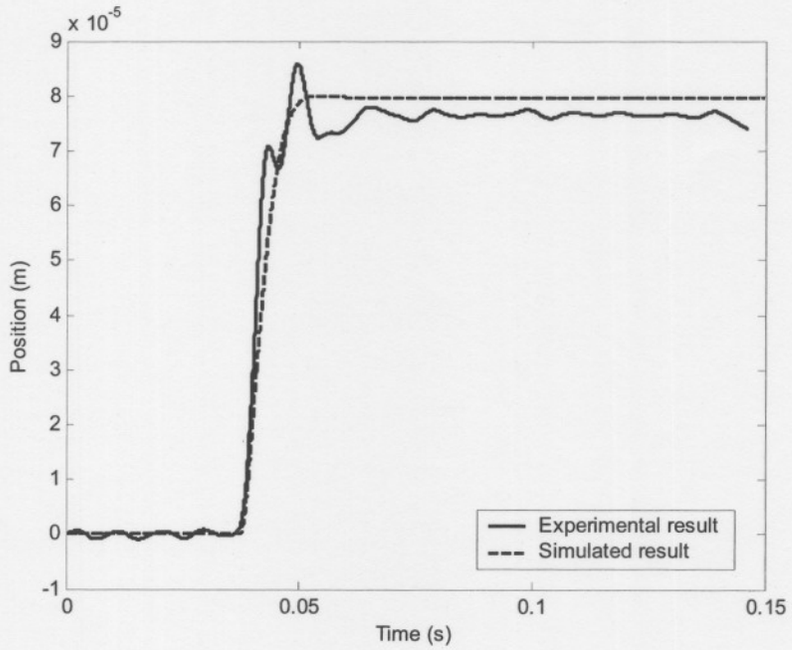

Figure 6-3 Horizontal step response (50 µm step, filtered)

Figure 6-4 displays the experimental and simulated responses to a step of 100 µm. Again there is very little variation in settling values and a significant variation in rise times. What is important to note is the fact that this is a rather large step away from the working point and confirms that the simulation is accurate.

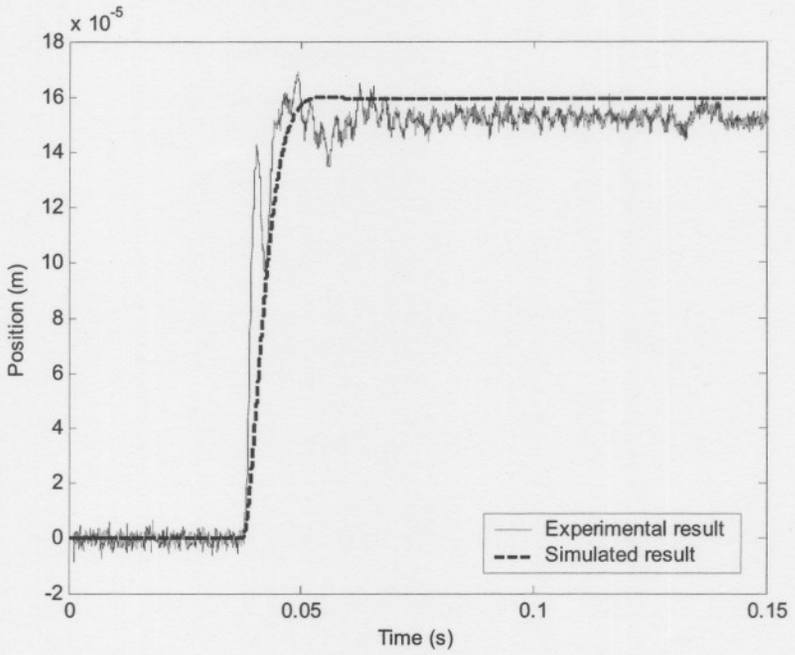

Figure 6-4 Horizontal step response (100 µm step)

A 100 µm step in the position reference value is introduced for the vertical axis and the result shown in Figure 6-5. The simulation response correlates remarkably well with the results obtained from the physical system in terms of settling values. This step response reveals the system's nonlinear nature since the rotor moves from one side of the working point to the other with a relative large displacement and verifies the simulation.

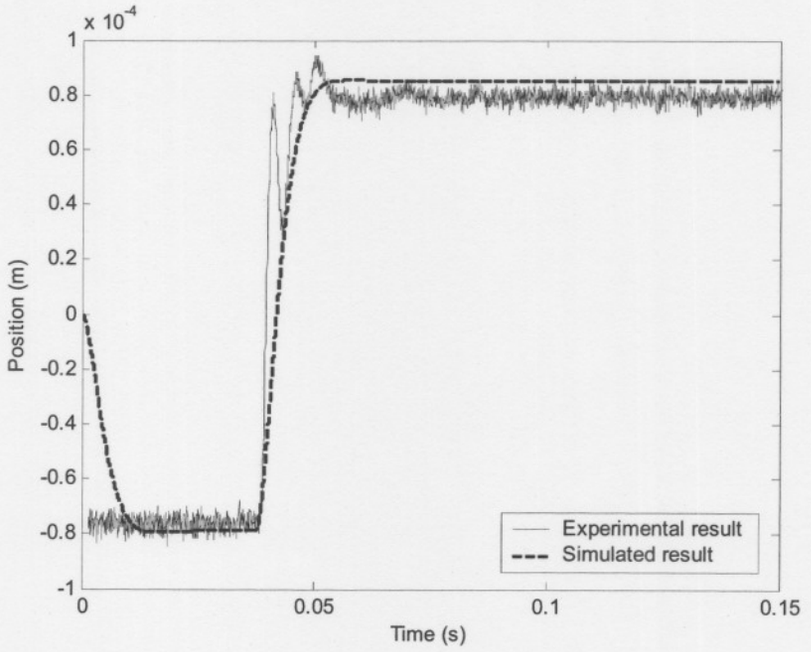

Figure 6-5 Vertical step response (100 µm step)

6.1.2 System Sensitivity

The stability robustness of an AMB is critically important to ensure stable operation amidst changes in the system parameters. Stability robustness refers to the stability margin of the system and can be determined through frequency domain analyses. Although the Nyquist plot can be used to determine marginal stability, the method proposed by ISO CD14839-3 [24] is the sensitivity function.

The sensitivity function is defined as the ratio of v_R over v_D where v_D is a sinusoidal disturbance of which the frequency is varied. The system sensitivity (in dB) is obtained using (6-3).

$$G_s(s) = 20 \cdot \log \frac{V_R(s)}{V_D(s)} \tag{6-3}$$

Figure 6-6 shows the system block diagram and the locations where v_D is introduced and v_R is measured.

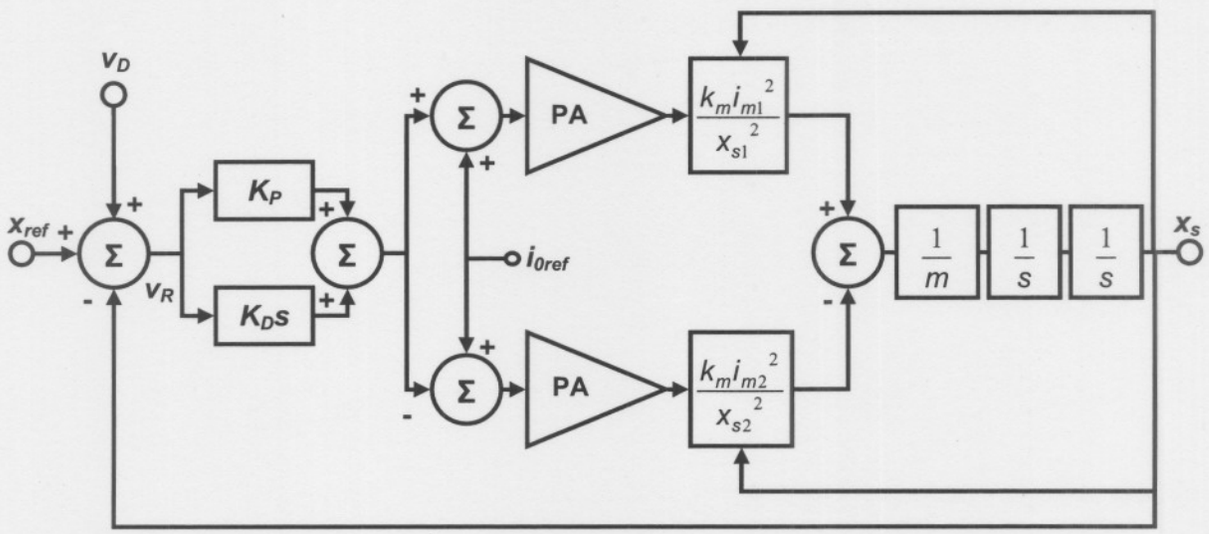

Figure 6-6 Block diagram of the nonlinear system

The sensitivity as a function of frequency is shown in Figure 6-7. Since the flexible rotor has a maximum operating rotational frequency of 167 Hz, the sensitivity is characterised up to 200 Hz. In practice the upper limit is normally specified the highest of 3 times the maximum operating speed or 2 kHz.

The sensitivity must be measured at rotor standstill and at operating speed. The measurement shown in Figure 6-7 was done at rotor standstill. The system's sensitivity at nominal operating speed was not determined.

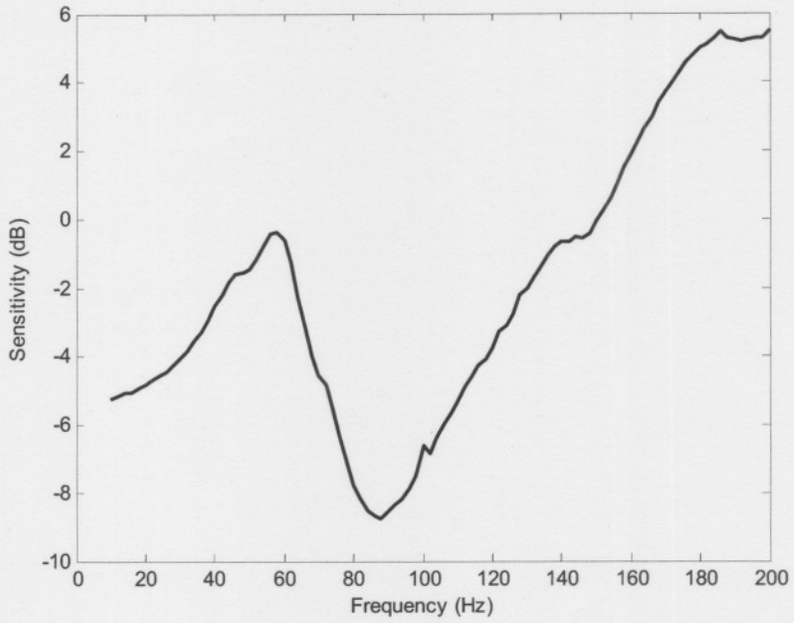

Figure 6-7 System sensitivity

According to ISO CD14839-3 [24], the sensitivity function of newly commissioned machines should fall within zone A which implies that the sensitivity should be below 8 dB. This international standard applies to industrial machines operating at nominal power greater than 15 kW, and is not limited by size or operational speed.

Table 6-1 Criteria of zone limits [24]

Zone	Peak of sensitivity
A/B	8 dB
B/C	12 dB
C/D	14 dB

Zone A: The sensitivity function of newly commissioned machines would normally fall within this zone.

Zone B: Machines with the sensitivity functions within this zone are normally considered acceptable for unrestricted long-term operation.

Zone C: Machines with the sensitivity functions within this zone are normally considered unsatisfactory for long-term continuous operation.

Zone D: The sensitivity function of machines within this zone is normally considered to be sufficiently severe to cause damage to the machine [24].

6.2 Rotordynamic Performance

The rotordynamic response of the physical system is now compared to the predicted response. The rotordynamic analyses predicted the first critical frequency (cylindrical) at 2,947 rpm, the second (conical) at 4,637 rpm and the third critical frequency (first bending mode) at 7,276 rpm. Figure 6-8 displays (a) the vertical and (b) the horizontal peak to peak displacement of the left stator.

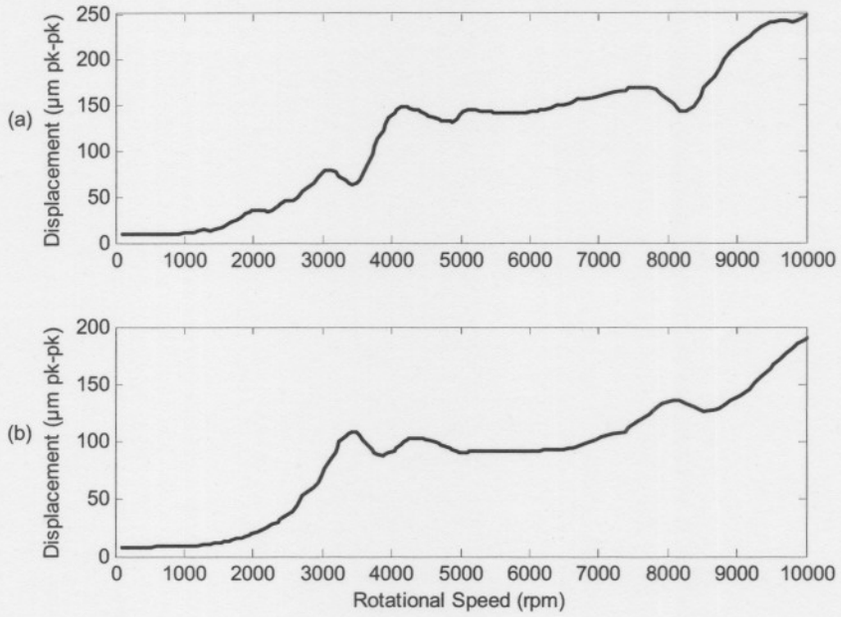

Figure 6-8 Left stator (a) vertical, (b) horizontal displacement vs. rotational frequency

Critical frequencies are observed at 3,000 rpm, 4,100 rpm, and 7,800 rpm on the vertical displacement. The horizontal displacement shows critical frequencies at 3,400 rpm, 4,400 rpm and 8,100 rpm. The displacement amplitude is much higher than the predicted amplitudes due to a rather large imbalance on the left journal.

The vertical (a) and horizontal (b) peak to peak displacements for the right stator are shown in Figure 6-9. Here critical frequencies on the vertical displacement are observed at 2,900 rpm, 4,000 rpm and 8,200 rpm. The horizontal displacement shows critical frequencies at 3,300 rpm and 4,300 rpm. The right stator is balanced to a much higher degree than the left stator. The predicted maximum displacement is located at 4,600 rpm with a peak to peak amplitude of 35 µm. The actual peak to peak displacements are much higher than the predicted values due to a much larger imbalance on the physical system.

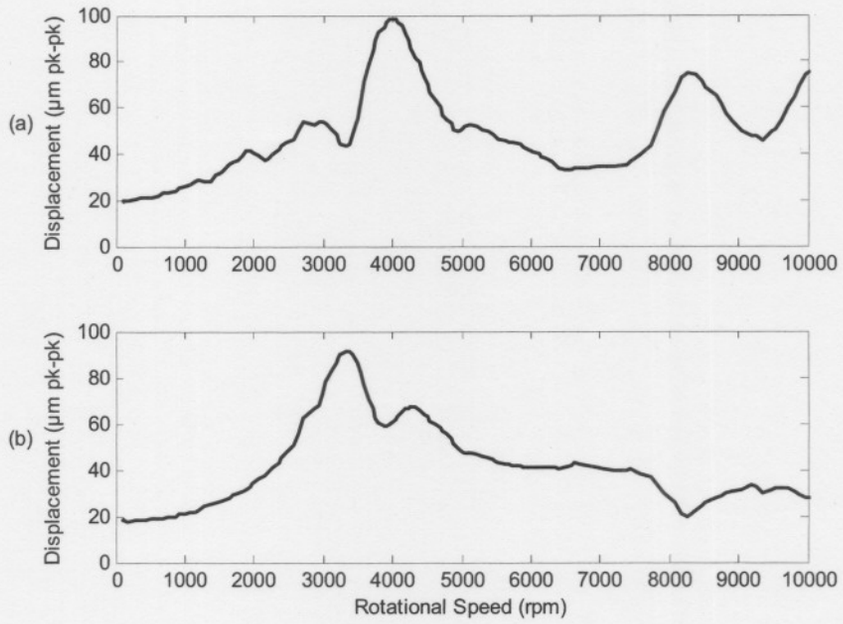

Figure 6-9 Right stator (a) vertical, (b) horizontal displacement vs. rotational frequency

The measured maximum displacement is observed at 4,000 rpm with a peak to peak amplitude of 100 µm. Compared to the predicted maximum peak to peak displacement of 35 µm this amplitude is still relatively high but much lower than that of the left stator indicating a smaller imbalance on the right stator.

The centre mass peak to peak displacement as a function of rotational frequency is shown in Figure 6-10. Critical frequencies are shown at 3,000 rpm, 4,000 rpm and 5,050 rpm.

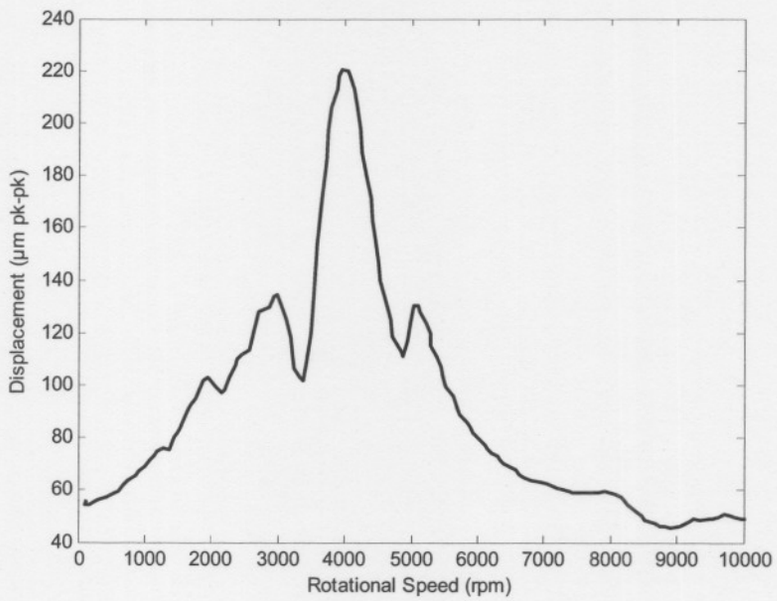

Figure 6-10 Centre mass displacement vs. rotational frequency

The maximum displacement is observed at 4,000 rpm with a peak to peak displacement of 220 μm. The predicted maximum peak to peak displacement of the centre mass is located at 4800 rpm with an amplitude of 104 μm.

The measured critical frequencies are higher than the predicted critical frequencies. This may be attributed to the higher stiffness of the physical system due to the lower level of bias current. Looking at the system's critical speed map shown in Figure 3-15 it is evident that an increase in equivalent stiffness will result in an increase in the critical frequencies.

The high peak to peak displacements may be contributed to high imbalance forces and low damping values. A decrease in system damping due to the lower level of bias current results in an increase in peak to peak displacements.

An X-Y plot of the rotor position in the right stator is displayed in Figure 6-11 at a rotational frequency of 4,000 rpm. The rotor follows a distorted elliptical path due to the imbalance forces and the rotordynamic response at the critical frequency.

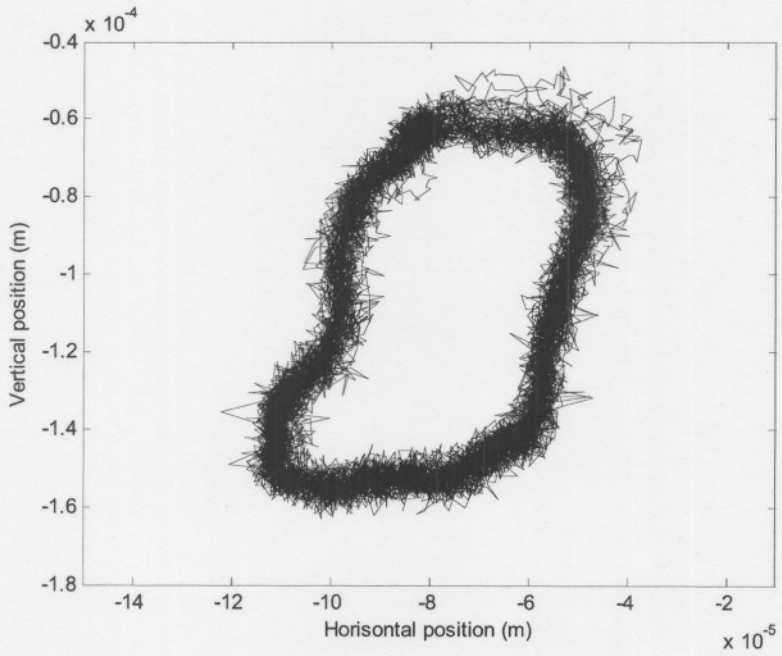

Figure 6-11 Right stator XY plot at maximum vertical displacement

Figure 6-12 displays an X-Y plot of the rotor position in the left stator. The path is much more elliptical than that of the right stator because of the more dominant imbalance forces.

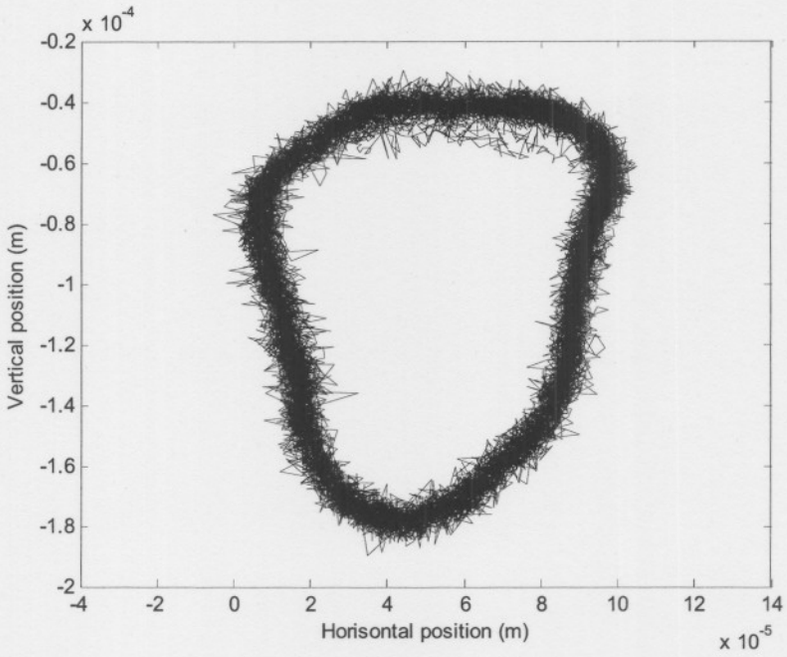

Figure 6-12 Left stator XY plot at 4,000 rpm

Figure 6-13 displays the X-Y plot of the rotor position in the right stator at 10,000 rpm. As shown the rotor traces a figure eight.

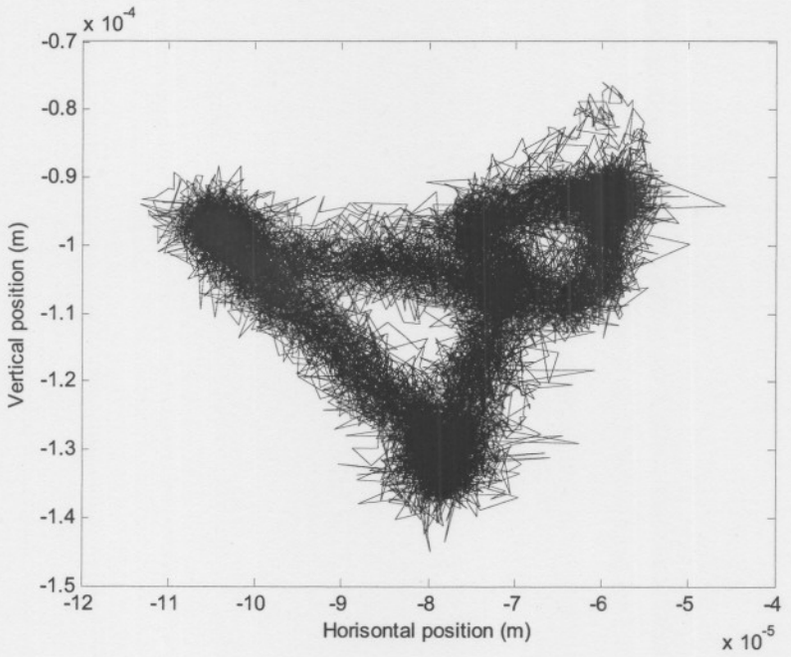

Figure 6-13 Right stator XY plot at 10,000 rpm

Chapter 6 discusses the characterisation of the realised hardware model of the flexible rotor AMB system. The simulation model and the rotordynamic analysis package are verified with results obtained from the physical system. The system's sensitivity function was determined and found to be within ISO standards for large machines. The deviations between the predicted, simulated and experimental results are addressed in chapter 7.

7
Chapter
Conclusions and Recommendations

Chapter 7 starts off with a system simulation refinement section where discrepancies between the analytical, simulated and experimental results are explained. This is followed by some insight on the losses encountered in the magnetic circuit. Section 7.3 highlights the areas identified where future work may be conducted and this is followed by a conclusion.

7.1 System Simulation Refinement

The MATLAB® simulation of the AMB system shows relatively good correlation to the analytical predictions as well as the experimental results. Further refinement of the simulation model is however needed to better explain the deviations in the results.

The first step in refining the system simulation is to explain the deviation between the analytically predicted equivalent stiffness and damping values and the simulated results. As stated in section 3.4 the bias current level will definitely influence these values since k_i is proportional to, and k_s proportional to the square of the bias current as seen in (3-22) and (3-23). By increasing the bias current reference (i_{0ref}) value to 3.305 A the actual bias current level is increased to 3 A. This is done to overcome the effect of the artificial slope that is added to the current sense signal. Figure 7-1 displays the steady state position error due to the rotor mass with the increased bias current level.

From Figure 7-1 a steady state error of 76.486×10^{-6} m is observed which translates to an equivalent stiffness of 495×10^3 N/m. The equivalent stiffness has increased from 479×10^3 N/m as obtained using (3-26) to within 1 % of the predicted equivalent stiffness. This result confirms the accuracy of the linear analytical model close to its working point with regards to the simulation.

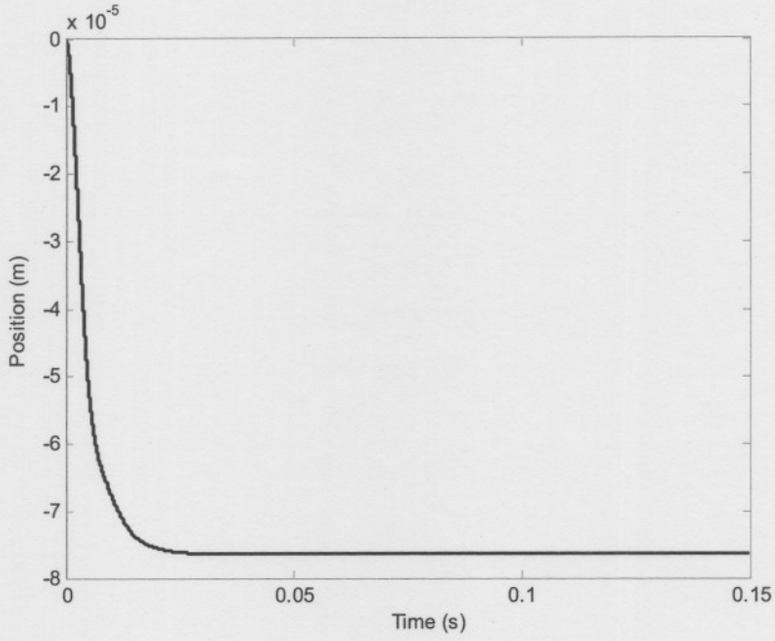

Figure 7-1 Steady state error due to rotor mass

Figure 7-2 shows the system's step response in the horizontal axis from which the equivalent stiffness and damping values can be obtained. The values are k_{eq} = 482x10^3 N/m and b_{eq} = 2.452x10^3 N.s/m which correlate much closer to the analytically designed values of 500 N/m and 2.5 N.s/m respectively. The results show that (3-24) and (3-25) can be used to design a PD controller with high accuracy for an AMB system with this specific configuration.

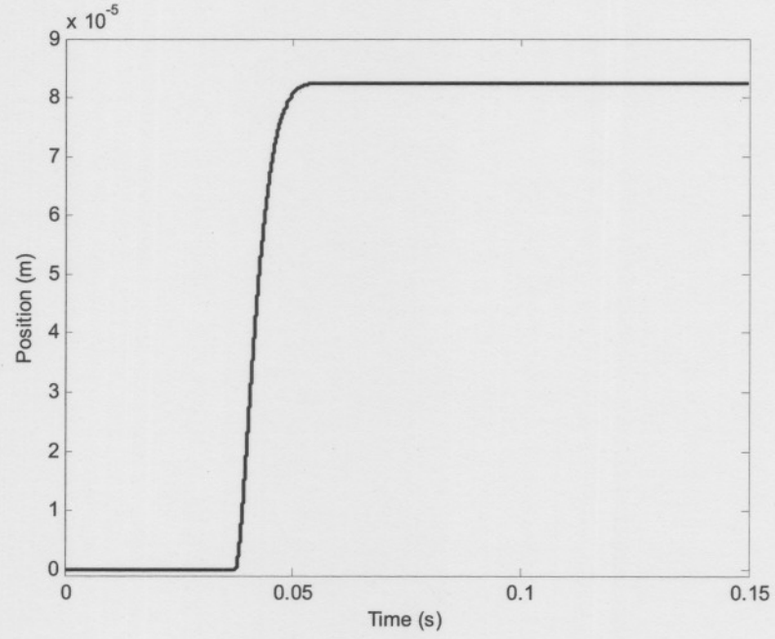

Figure 7-2 Horizontal step response (50 µm step)

The next step in the refinement process is to correlate the simulation with the physical system. From section 6.1.1 a relatively large discrepancy was shown between the simulated and experimental results. It was also suggested that the cause might be the additional pole included in the differential path of the physical system. This assumption is further investigated by including the pole in the simulation.

From a differentiator's frequency response it can be seen that as the frequency increases, the differentiator gain also increases. To ensure that the high frequency noise does not become dominant, an additional pole is introduced that limits high frequency gain. The transfer function is given by (7-1).

$$G_D(s) = \frac{s\omega_n}{s + \omega_n} \tag{7-1}$$

The additional pole in the differentiator path is included in the simulation and the coil inductance is also lowered to the measured value. Figure 7-3 displays a simulated and experimental step response (50 µm step) in the horizontal axis. The rise times and settling values of the simulated and experimental results now shows good correlation.

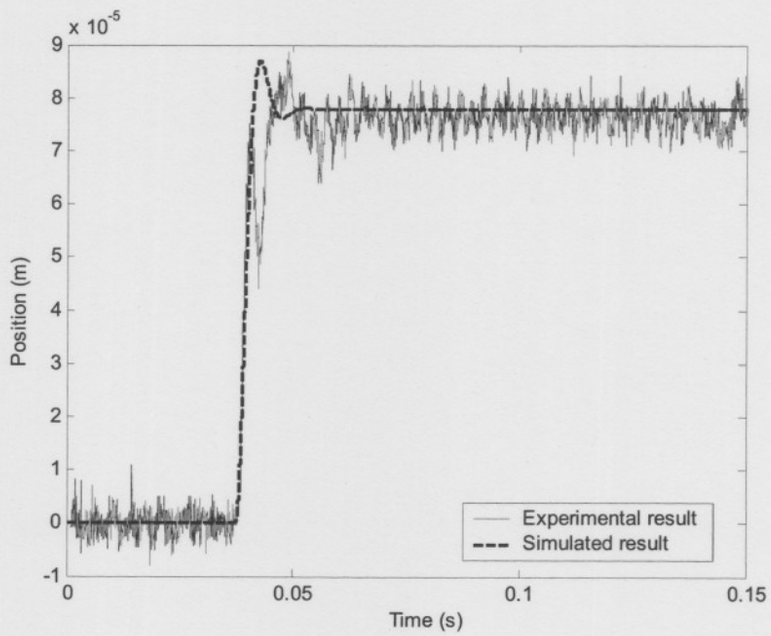

Figure 7-3 Horizontal step response (50 µm step)

From Figure 7-3 the following parameters are obtained: k_{eq} = 1.654x10^6 N/m and b_{eq} = 2.843x10^3 N.s/m. Using an equivalent stiffness of 1.654x10^6 N/m and the system's critical speed map shown in Figure 3-15 the critical frequencies are estimated at 4,000 rpm, 8,200 rpm and 9,800 rpm. When comparing these results to that of the right stator shown in Figure 6-9 (a), remarkable correlation is observed. This confirms the high equivalent stiffness value predicted by the simulation.

The simulation also shows good correlation with experimental results over a large operating range as shown by the step response in the vertical axis displayed in Figure 7-4.

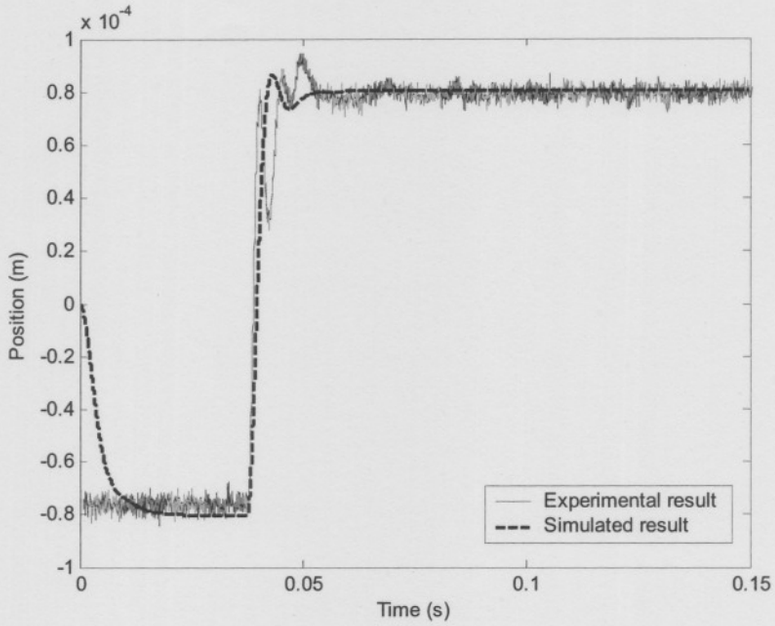

Figure 7-4 Vertical step response (100 µm step)

The analytical and experimental results however do not show good correlation. With the experience gained in simulation refinement it is predicted that the correlation between the analytical and experimental results will be improved by including the additional pole in the differentiator path.

The experimental results also reveal discrepancies between the equivalent stiffness values obtained from steady state analyses and those obtained from the system's dynamic response. Further investigation into this phenomenon will improve the research group's understanding of the concept of equivalent stiffness in AMBs.

An oscillation on the experimental result which does not appear on the simulated result is observed on the rising edges of Figure 7-3 and Figure 7-4. This oscillatory response cannot be reproduced in simulation and further investigation into the source is needed.

The physical system displays a relatively high level of noise due to the switching power amplifiers. The noise spectrum was analysed and the main contributing components were included in the simulation to analyse the effect the noise has on the system. Figure 7-5 displays the same step response as shown in Figure 7-3 with the added noise.

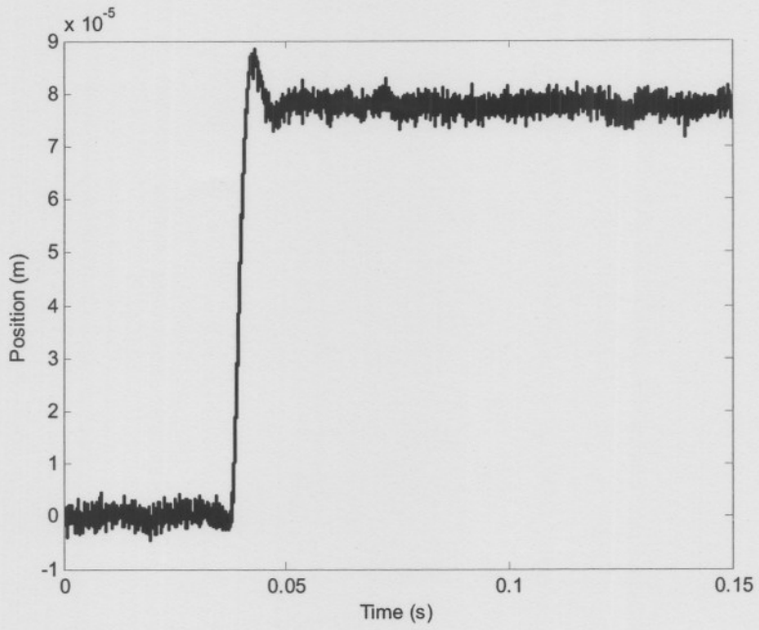

Figure 7-5 Horizontal step response with noise (50 µm step)

From this result it is clear that the level of noise is unacceptable since it influences the rotor position. The noise levels must be further attenuated to improve system performance.

7.2 Magnetic Circuit Losses

Power dissipation in the magnetic circuit is observed to be excessive. The magnetic material of the rotor journals heats up due to eddy-current losses induced by the 100 kHz switching frequency and the 400 mA current ripple. From the coil current waveform in Figure 4-30 (b) an oscillation is also observed at a much higher frequency. This oscillation also contributes to induced eddy-currents.

Temperature readings on the two stators indicate that one of the journals experiences higher losses than the other. The rotor was turned around in the stator and the same journal heated up which indicated that there might be a difference in the magnetic material of the two journals. The journal temperatures were measured after the rotor was accelerated up to 10,000 rpm and allowed to run down which takes approximately 7 minutes. The left journal's temperature measured 73 °C whereas the right journal measured 56 °C.

7.3 Future Work

7.3.1 Power Amplifiers

The power amplifiers (PAs) that were developed display excessively high slew rates which imply that the voltage level on the dc link may be reduced. Lowering the dc link voltage will reduce the current ripple which in turn reduces eddy-current losses.

Another way of reducing the ripple current component is by implementing tri-state amplifier control. Apart from the two states currently in place where energy is either added to or extracted from the coil, a third state is introduced where the coil current is allowed to freewheel.

Since the eddy-current losses are proportional to the square of the switching frequency it may also be advantageous to investigate lower switching frequencies.

7.3.2 Magnetic circuit configuration

In the current configuration each PA is responsible for the bias flux as well as the control flux of the coils it is connected to. Other topologies exist where separate windings are used to establish the bias flux. The bias flux coils are energised by a dc current with very low ripple component. The bias flux can also be established with permanent magnets.

One of the advantages of this topology is that a single PA can be used to control one degree of freedom. The control coils are connected in series and configured so that one opposes the bias flux and the other is added to the bias flux.

Another advantage is that this configuration places lower requirements on the control PA. Since the bias flux is produced by a separate set of coils, the number of control coil turns is reduced, resulting in lower inductance which in turn lowers the dc link voltage requirements. These lower power requirements are favourable since it extends the PA lifetime.

7.3.3 Magnetic Material

Losses experienced in the magnetic circuit may also be reduced by choosing the correct material for the circuit. Currently Cogent M330-50A silicon steel is used. The 0.5 mm laminations are well suited for low loss applications in 50 Hz machines. They are however not suited for high frequency applications. The heteropolar design incorporates eight poles which

implies that the maximum rotating frequency may be multiplied by eight resulting in an effective frequency of 1333 Hz experienced by the rotor magnetic material.

For high frequency applications thinner laminations should be used since the eddy current losses are proportional to the square of the lamination thickness.

7.3.4 Advanced Control Algorithms

The digital controller incorporated in the flexible rotor AMB system is ideal for the implementation of a variety of control algorithms. The overall system performance can be greatly improved and different control strategies can be compared. Active vibration control may also be implemented to reduce vibration amplitudes at critical frequencies.

Advanced current allocation control algorithms as well as low or zero bias current topologies may also be used to reduce losses in the magnetic circuit.

7.3.5 Power Losses Analyses

During the design of the AMB system, special care was taken to make provision for high speed loss analysis. Together with the flexible rotor a rigid rotor was designed with critical frequencies above the maximum operating speed. The two rotors are easily interchangeable and require the minimum adjustments.

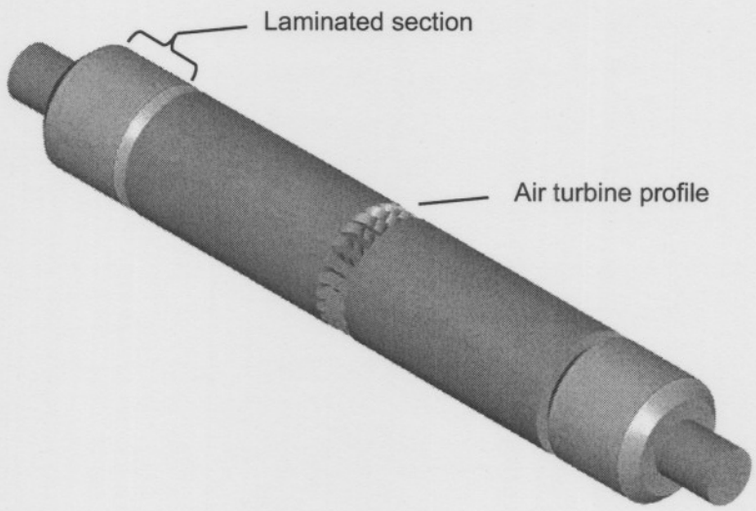

Figure 7-6 Rigid rotor CADKEY model

The rigid rotor displayed in Figure 7-6 has an uncomplicated profile which simplifies the windage loss calculations. The rotor is propelled by projecting high pressure air onto the machined profile at the centre of the rotor. This propulsion method has a limited energy transfer capability that may not be able to propel the rotor to very high speeds as required for high speed loss analyses.

During testing a maximum speed of 6,000 rpm was reached and the rotor displayed a high level of unbalance. The maximum rotor speed can be increased by improving rotor balancing and adjusting the air turbine nozzle positions. Alternative methods of propulsion may however be needed to propel the shaft to 20,000 rpm.

7.3.6 System noise levels

As shown in the experimental result of Figure 7-3 the system reveals a high noise level. This reduces the overall system performance and complicates accurate measurements. A simplified first order low pass filter is implemented to reduce aliasing. For a 16-bit analogue to digital converter (ADC) 96 dB attenuation is required at the Nyquest frequency. The simple low pass filter does not satisfy this criterion and therefore aliasing takes place.

Future work will include research on more advanced anti-aliasing filters and overall system noise reduction. Special consideration may also be given to electromagnetic compatibility issues.

7.3.7 Design process refinement

The system design constitutes electromagnetic design, detailed system analysis and modelling. In the analytical analyses of the electromagnetic design no consideration is given to losses, leakage and fringing effects encountered in the electromagnetic circuit.

A detailed electromagnetic circuit design method must be put in place which accurately predicts the losses induced by certain PA topologies. The need for a detailed design process incorporating an analytical design, finite element method (FEM) design verification, detailed loss predictions and a detailed system simulation is apparent.

After refinement of the bias current level, the analytical results correlated closely with the simulation (additional pole in the differentiator path however not included). This version of the simulation does not show satisfactory correlation with the experimental results. The pole in the

differentiator path is added in the simulation which results in an improved correlation between the simulation and the experimental results. Discrepancies now exist between the analytical and simulation results.

Future work is needed to include the additional pole in the differentiator path in the analytical model of the AMB system. The analytical and simulation models may also be further refined to include actual system dynamics and nonlinearities currently not modelled e.g. magnetic material properties.

7.4 Conclusion

The objective of this project was to develop a flexible rotor double radial active magnetic bearing system. The rotor had to be stably suspended through the first three critical frequencies of which the third is the first bending mode. From the results it is shown that such a system was realised in an aesthetically pleasing well rounded model.

The versatile system allows for many different investigations which include advanced control investigations as well as work on high speed magnetic bearing losses.

APPENDIX

Appendix A: Force correction due to pole geometry [25].

The force that the electromagnet in Figure A-1 with a flat surface A_g can exert, neglecting leakage and fringing as well as iron losses, is given by:

$$F_{flat} = \left(\frac{B_{air}^2}{\mu_0} \right) A_g \qquad \text{(A-1)}$$

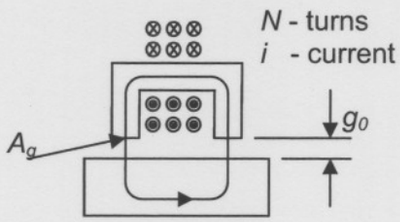

Figure A-1 Electromagnet with a flat surface

Consider now an electromagnet with a rounded surface as shown in Figure A-2. The perpendicular area of one leg is given by:

$$A_{iron} = l\,w \qquad \text{(A-2)}$$

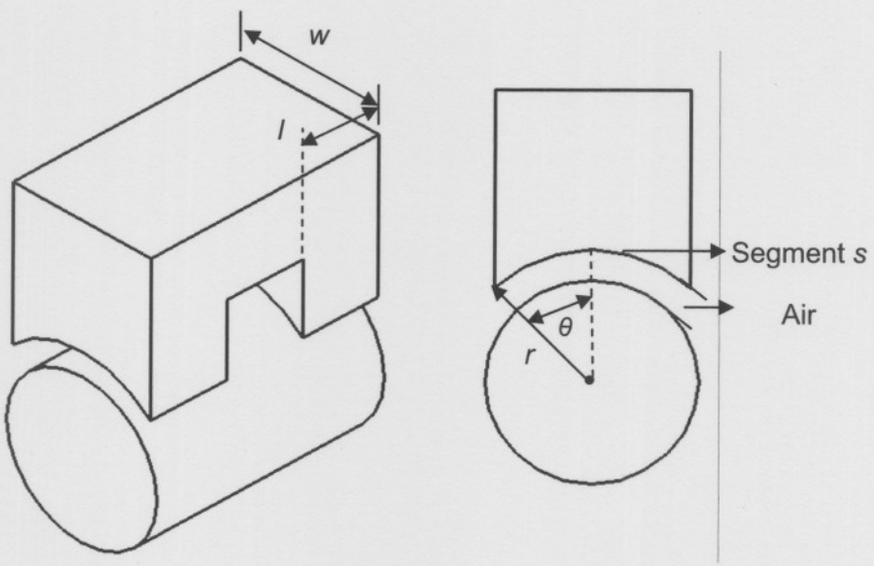

Figure A-2: Electromagnet of a Radial AMB

The segment s makes an angle of 2θ with the centre of the shaft. To determine the force that one leg of the electromagnet can exert, the segment s is divided into very small segments ds. The effective area of the surface between the airgap and the iron is then given by (A-3).

$$dA_{gap} = l\,ds \tag{A-3}$$

The distance ds can be expressed in terms of the angle θ and the radius of the segment r so that

$$\begin{aligned} ds &= r\,d\theta \\ \therefore dA_{gap} &= l\,r\,d\theta \end{aligned} \tag{A-4}$$

The force is perpendicular to the area A_{gap} so that for a small area dA_{gap} the force is given by (A-5).

$$\begin{aligned} dF &= \frac{B_{gap}^2\,d\,A_{gap}}{2\mu_0} \\ &= \frac{B_{gap}^2\,l\,r\,d\theta}{2\mu_0} \end{aligned} \tag{A-5}$$

The force in the vertical direction is then given by (A-6).

$$dF = \frac{B_{gap}^2\,l\,r\,d\theta}{2\mu_0}\cos(\theta) \tag{A-6}$$

The vertical force across the complete sector is obtained by integration.

$$\begin{aligned} F &= \int_{-\theta}^{\theta} dF \\ &= \int_{-\theta}^{\theta} \frac{B_{gap}^2\,l\,r}{2\mu_0}\cos(\theta) \\ &= \frac{B_{gap}^2\,l\,r}{2\mu_0}\sin(\theta)\Big|_{-\theta}^{\theta} \\ &= \frac{B_{gap}^2\,l\,r}{2\mu_0}\left(\sin(\theta) - \sin(-\theta)\right) \\ &= \frac{B_{gap}^2\,l\,r}{2\mu_0}\left(\sin(\theta) + \sin(\theta)\right) \\ &= \frac{B_{gap}^2\,l\,r}{\mu_0}\left(\sin(\theta)\right) \end{aligned} \tag{A-7}$$

The flux density in the airgap (B_{gap}) and in the iron (B_{iron}) is not the same because the effective areas are different. Since the divergence of a magnetic field is zero:

$$B_{iron}A_{iron} = B_{gap}A_{gap} \qquad \text{(A-8)}$$
$$\therefore B_{gap} = \frac{A_{iron}B_{iron}}{A_{gap}}$$

By substituting (A-8) into (A-7), (A-9) is obtained.

$$F = \left[\frac{A_{iron}B_{iron}}{A_{gap}}\right]^2 \frac{l\,r}{\mu_0 g}(\sin(\theta))$$
$$= \frac{B_{iron}^2 A_{iron}}{\mu_0 g}\left[\frac{A_{iron}}{A_{gap}^2} l\,r(\sin(\theta))\right] \qquad \text{(A-9)}$$

Using trigonometry the areas of the iron and the air gap are respectively given by (A-10).

$$A_{iron} = l\,2r\sin(\theta) \qquad \text{(A-10)}$$
$$A_{gap} = l\,2r\theta$$

Substitute A_{gap} and A_{iron} into (A-9):

$$F = \frac{B_{iron}^2 A_{iron}}{\mu_0}\left[\frac{l\,2r\sin(\theta)}{(l\,2r\theta)^2} l\,r(\sin(\theta))\right]$$
$$= \frac{1}{2}\frac{B_{iron}^2 A_{iron}}{\mu_0}\frac{\sin^2(\theta)}{\theta^2}$$

For two air gaps the total force is twice this value:

$$F_t = \frac{B_{iron}^2 A_{iron}}{\mu_0}\frac{\sin^2(\theta)}{\theta^2} \qquad \text{(A-11)}$$

The force correction factor (*FCF*) due to pole geometry is thus as given by (A-12).

$$FCF = \frac{\sin^2(\theta)}{\theta^2} \qquad \text{(A-12)}$$

Appendix B: Cadkey manufacturing drawings

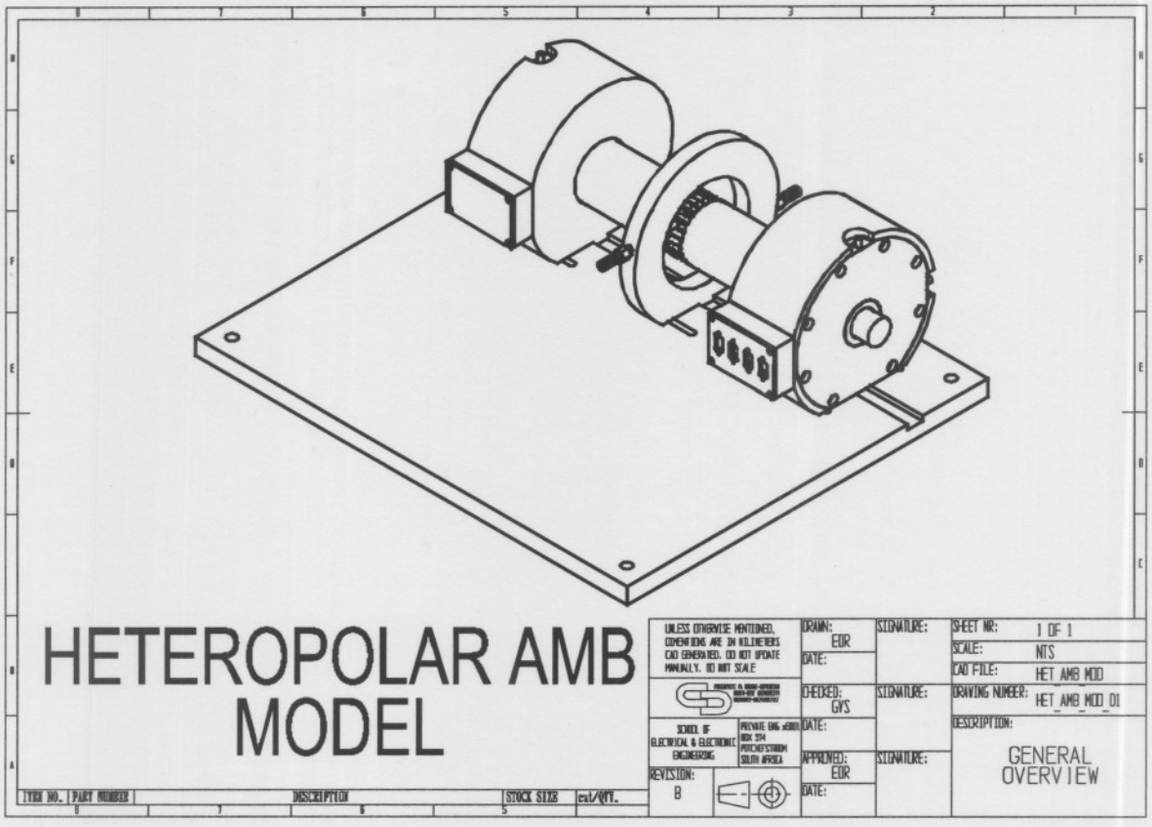

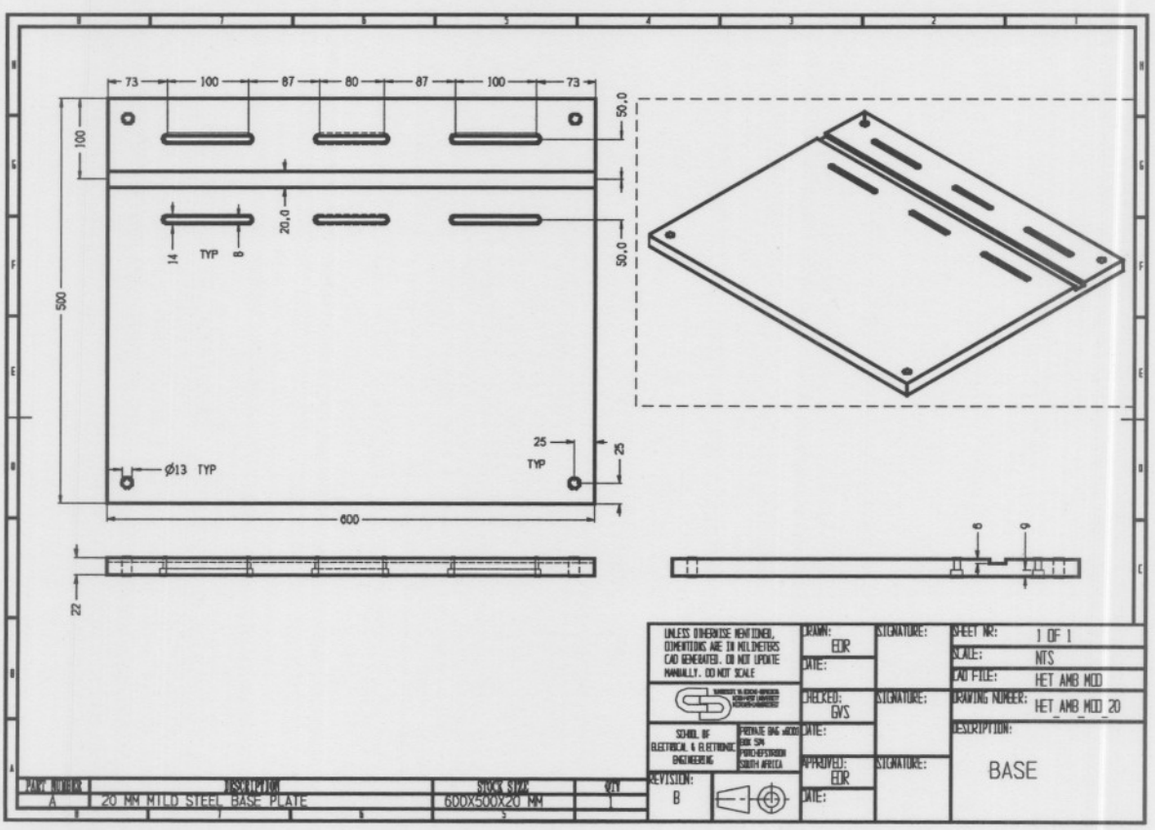

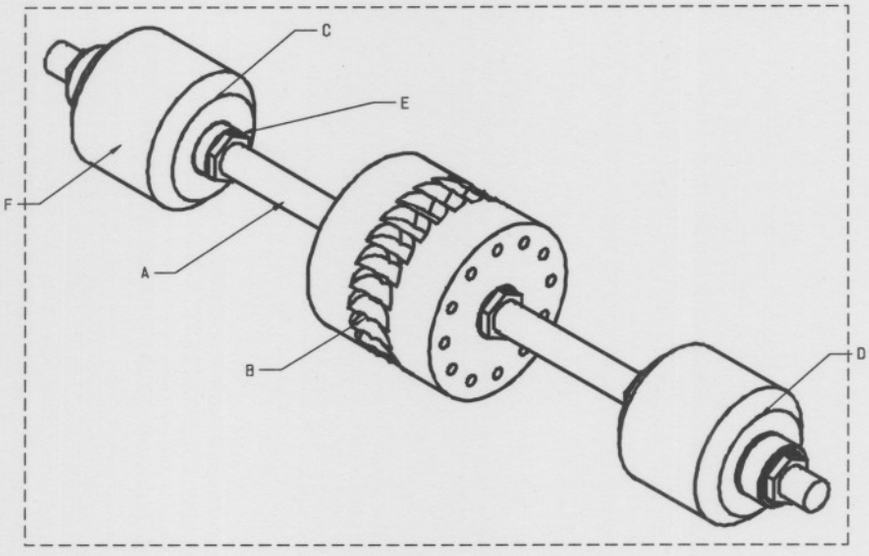

PART NUMBER	DESCRIPTION	STOCK SIZE	QTY
A	16 MM AISI 304 STAINLESS STEEL BRIGHT BAR	Ø16 MM X 500 MM	1
B	CENTRE MASS Ø90 MM MILD STEEL	Ø90 MM X 80 MM	1
C	PRESS FIT BOBBIN FOR LAMINATIONS MILD STEEL	Ø70 MM X 81 MM	2
D	END STOPS 8 MM MILD STEEL PLATE	Ø70 MM X 8 MM	2
E	TRANTORQUE GT MINIATURE SERIES UNITS	(1	6
F	ROTOR LAMINATIONS (SUPPLIED)	Ø70 MM X 50 MM	2

UNLESS OTHERWISE MENTIONED, DIMENTIONS ARE IN MILLIMETERS CAD GENERATED. DO NOT UPDATE MANUALLY. DO NOT SCALE

SCHOOL OF ELECTRICAL & ELECTRONIC ENGINEERING

PRIVATE BAG X6001 BOX 394 POTCHEFSTROOM SOUTH AFRICA

REVISION: B

DRAWN: EDR DATE:

CHECKED: GVS DATE:

APPROVED: EDR DATE:

SIGNATURE:

SHEET NR: 1 OF 3
SCALE: NTS
CAD FILE: HET AMB MOD
DRAWING NUMBER: HET_AMB_MOD_05
DESCRIPTION: FLEXIBLE ROTOR OVERVIEW

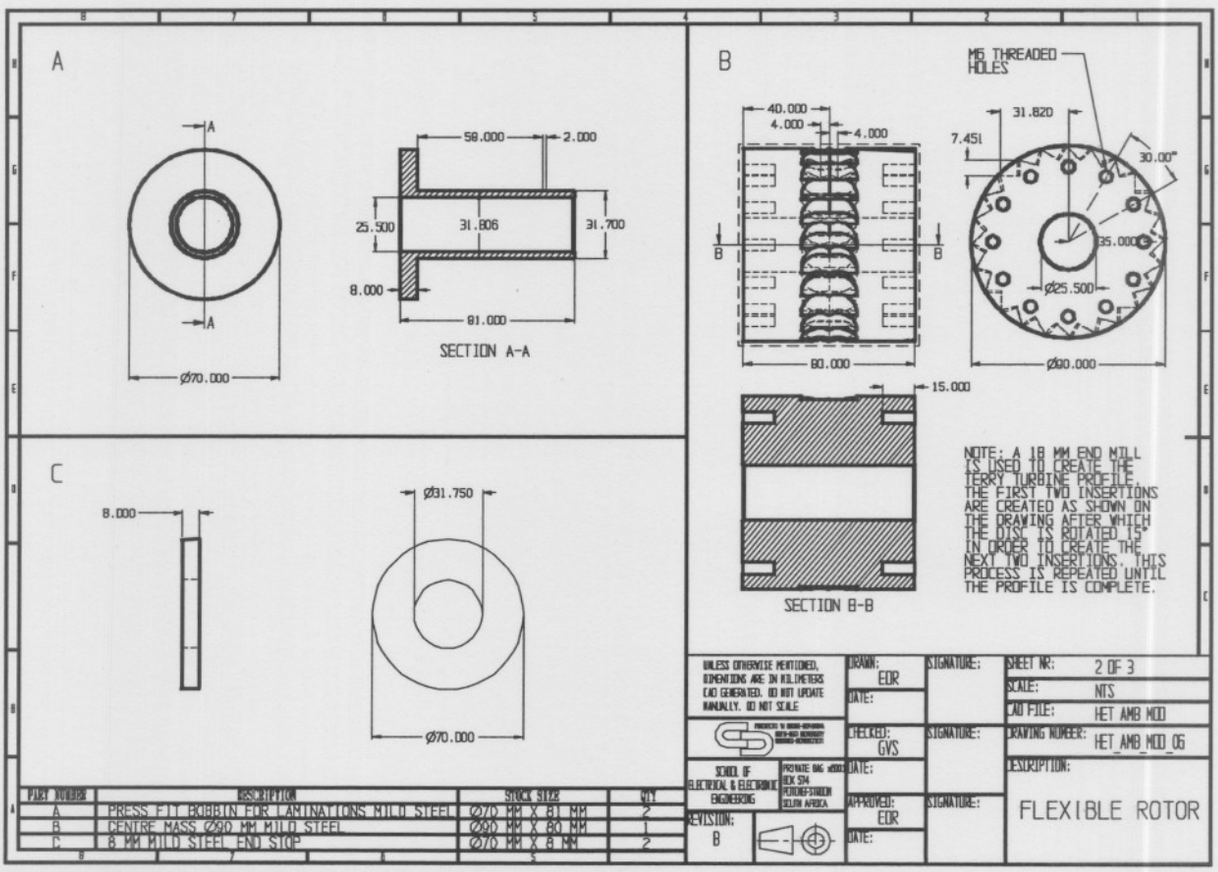

PART NUMBER	DESCRIPTION	STOCK SIZE	QTY
A	PRESS FIT BOBBIN FOR LAMINATIONS MILD STEEL	Ø70 MM X 81 MM	2
B	CENTRE MASS Ø90 MM MILD STEEL	Ø90 MM X 80 MM	1
C	8 MM MILD STEEL END STOP	Ø70 MM X 8 MM	2

UNLESS OTHERWISE MENTIONED, DIMENTIONS ARE IN MILLIMETERS CAD GENERATED. DO NOT UPDATE MANUALLY. DO NOT SCALE

SCHOOL OF ELECTRICAL & ELECTRONIC ENGINEERING

PRIVATE BAG X6001 BOX 394 POTCHEFSTROOM SOUTH AFRICA

REVISION: B

DRAWN: EDR DATE:

CHECKED: GVS DATE:

APPROVED: EDR DATE:

SIGNATURE:

SHEET NR: 2 OF 3
SCALE: NTS
CAD FILE: HET AMB MOD
DRAWING NUMBER: HET_AMB_MOD_06
DESCRIPTION: FLEXIBLE ROTOR

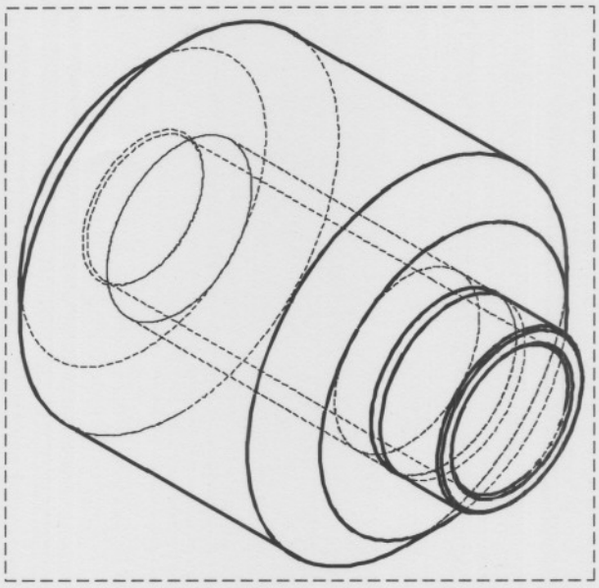

NOTE: THE SILICON STEEL LAMINATIONS ARE PRESS FITTED ONTO THE MILD STEEL BOBBIN WITH THE MILD STEEL END STOP. THE LAMINATIONS TOGETHER WITH THE BOBBIN ARE THEN MACHINED TO SIZE. THE MILD STEEL AT THE EDGES OF THE LAMINATION PACK IS MACHINED AT AN ANGLE OF 45° AS CAN BE SEEN.

UNLESS OTHERWISE MENTIONED, DIMENTIONS ARE IN MILLIMETERS CAD GENERATED. DO NOT UPDATE MANUALLY. DO NOT SCALE	DRAWN: EDR	SIGNATURE:	SHEET NR: 3 OF 3
	DATE:		SCALE: NTS
	CHECKED: GVS	SIGNATURE:	CAD FILE: HET AMB MOD
SCHOOL OF ELECTRICAL & ELECTRONIC ENGINEERING, PRIVATE BAG X6001, BOX 394, POTCHEFSTROOM, SOUTH AFRICA	DATE:		DRAWING NUMBER: HET_AMB_MOD_07
REVISION: B	APPROVED: EDR	SIGNATURE:	DESCRIPTION: FLEXIBLE ROTOR
	DATE:		

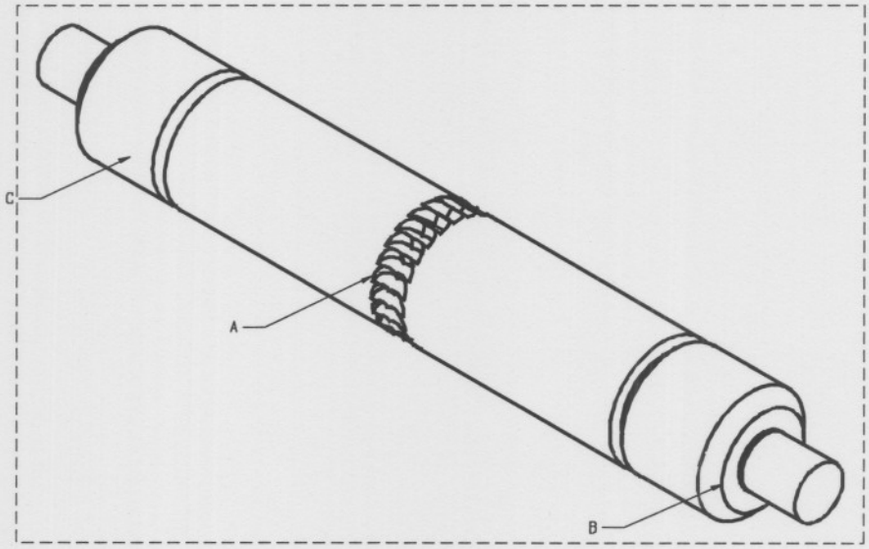

PART NUMBER	DESCRIPTION	STOCK SIZE	QTY
A	70 MM MILD STEEL SHAFT	Ø70 MM X 500 MM	1
B	8 MM MILD STEEL PLATE END STOP	Ø70 MM X 8 MM	2
C	SILICON STEEL LAMINATION PACK (SUPPLIED)	Ø70 MM X 50 MM	2

UNLESS OTHERWISE MENTIONED, DIMENTIONS ARE IN MILLIMETERS CAD GENERATED. DO NOT UPDATE MANUALLY. DO NOT SCALE	DRAWN: EDR	SIGNATURE:	SHEET NR: 1 OF 3
	DATE:		SCALE: NTS
	CHECKED: GVS	SIGNATURE:	CAD FILE: HET AMB MOD
SCHOOL OF ELECTRICAL & ELECTRONIC ENGINEERING, PRIVATE BAG X6001, BOX 394, POTCHEFSTROOM, SOUTH AFRICA	DATE:		DRAWING NUMBER: HET_AMB_MOD_02
REVISION: B	APPROVED: EDR	SIGNATURE:	DESCRIPTION: RIGID ROTOR
	DATE:		

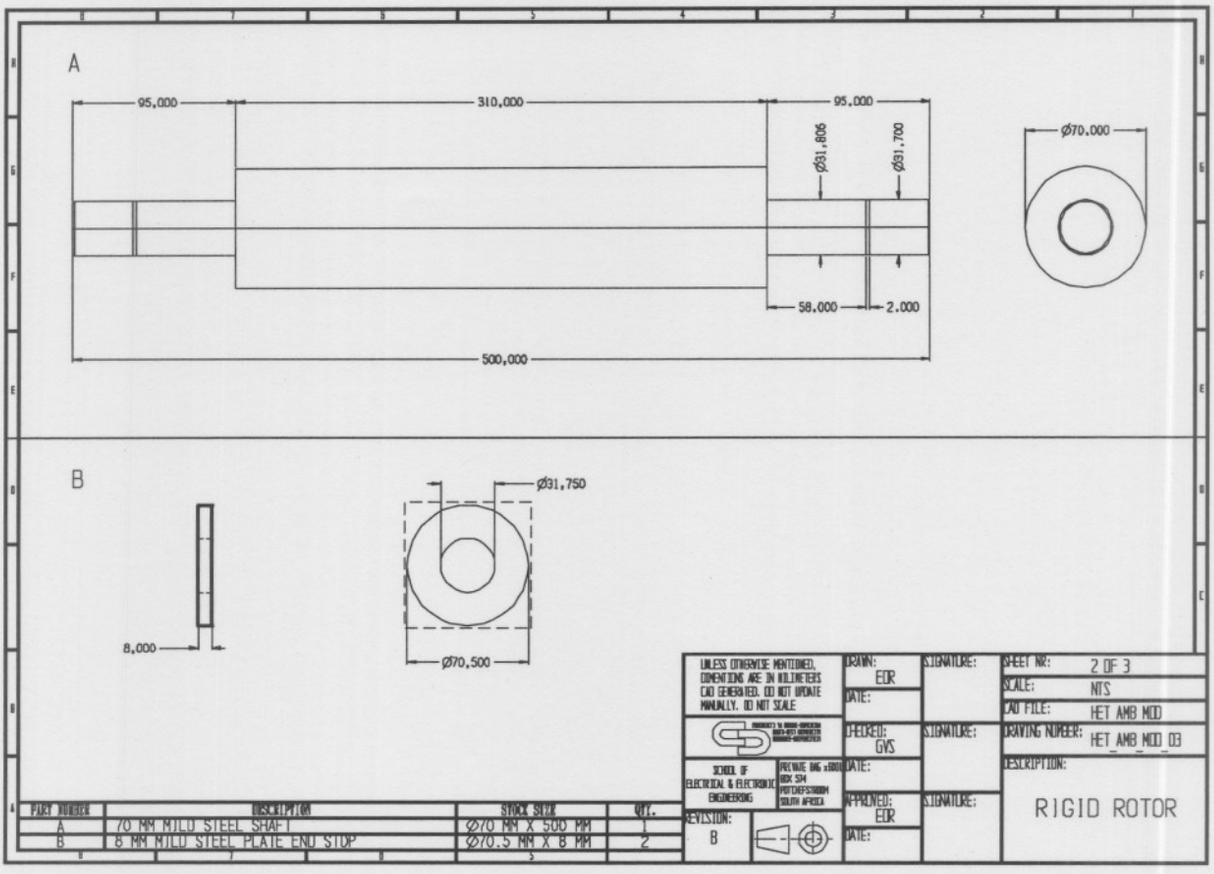

PART NUMBER	DESCRIPTION	STOCK SIZE	QTY.
A	70 MM MILD STEEL SHAFT	Ø70 MM X 500 MM	1
B	8 MM MILD STEEL PLATE END STOP	Ø70.5 MM X 8 MM	2

UNLESS OTHERWISE MENTIONED, DIMENTIONS ARE IN MILLIMETERS CAD GENERATED. DO NOT UPDATE MANUALLY. DO NOT SCALE

SCHOOL OF ELECTRICAL & ELECTRONIC ENGINEERING

PRIVATE BAG X6001 BOX 394 POTCHEFSTROOM SOUTH AFRICA

REVISION: B

DRAWN: EDR DATE:

CHECKED: GVS DATE:

APPROVED: EDR DATE:

SIGNATURE:

SHEET NR: 2 OF 3
SCALE: NTS
CAD FILE: HET AMB MOD
DRAWING NUMBER: HET_AMB_MOD_03
DESCRIPTION: RIGID ROTOR

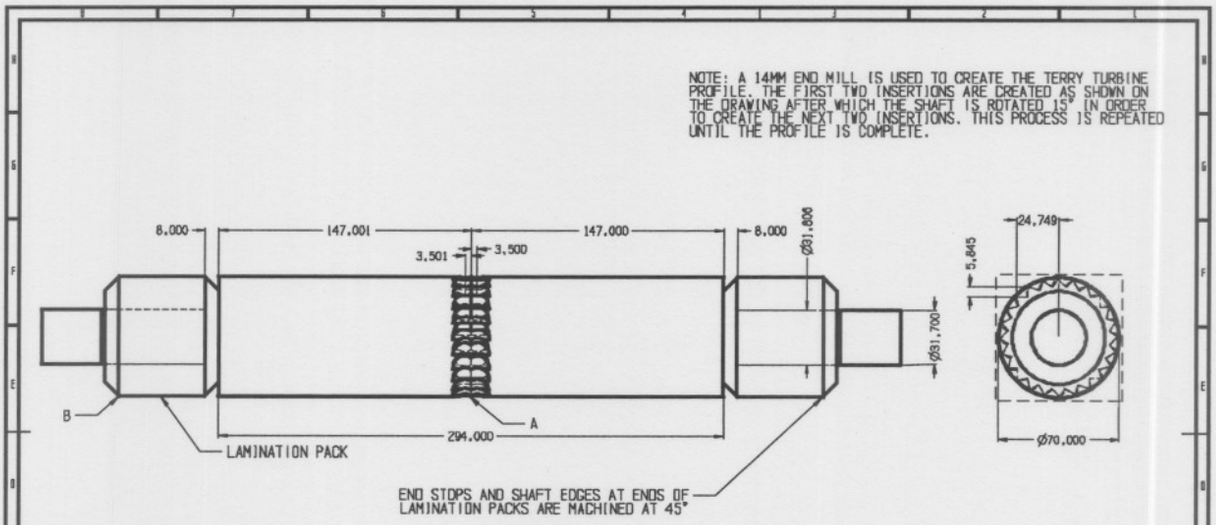

NOTE: THE SILICON STEEL LAMINATION PACKS ARE PRESS FITTED ONTO THE MILD STEEL SHAFT WITH THE MILD STEEL END STOPS. THE LAMINATIONS TOGETHER WITH THE SHAFT AND END STOPS ARE THEN MACHINED TO SIZE. THE MILD STEEL AT THE EDGES OF THE LAMINATION PACKS IS MACHINED AT AN ANGLE OF 45° AS CAN BE SEEN.

PART NUMBER	DESCRIPTION	STOCK SIZE	QTY
A	70 MM MILD STEEL SHAFT	Ø70 MM X 500 MM	1
B	8 MM MILD STEEL PLATE END STOP	Ø70 MM X 8 MM	2

UNLESS OTHERWISE MENTIONED, DIMENTIONS ARE IN MILLIMETERS CAD GENERATED. DO NOT UPDATE MANUALLY. DO NOT SCALE

SCHOOL OF ELECTRICAL & ELECTRONIC ENGINEERING

PRIVATE BAG X6001 BOX 394 POTCHEFSTROOM SOUTH AFRICA

REVISION: B

DRAWN: EDR DATE:

CHECKED: GVS DATE:

APPROVED: EDR DATE:

SIGNATURE:

SHEET NR: 3 OF 3
SCALE: NTS
CAD FILE: HET AMB MOD
DRAWING NUMBER: HET_AMB_MOD_04
DESCRIPTION: RIGID ROTOR

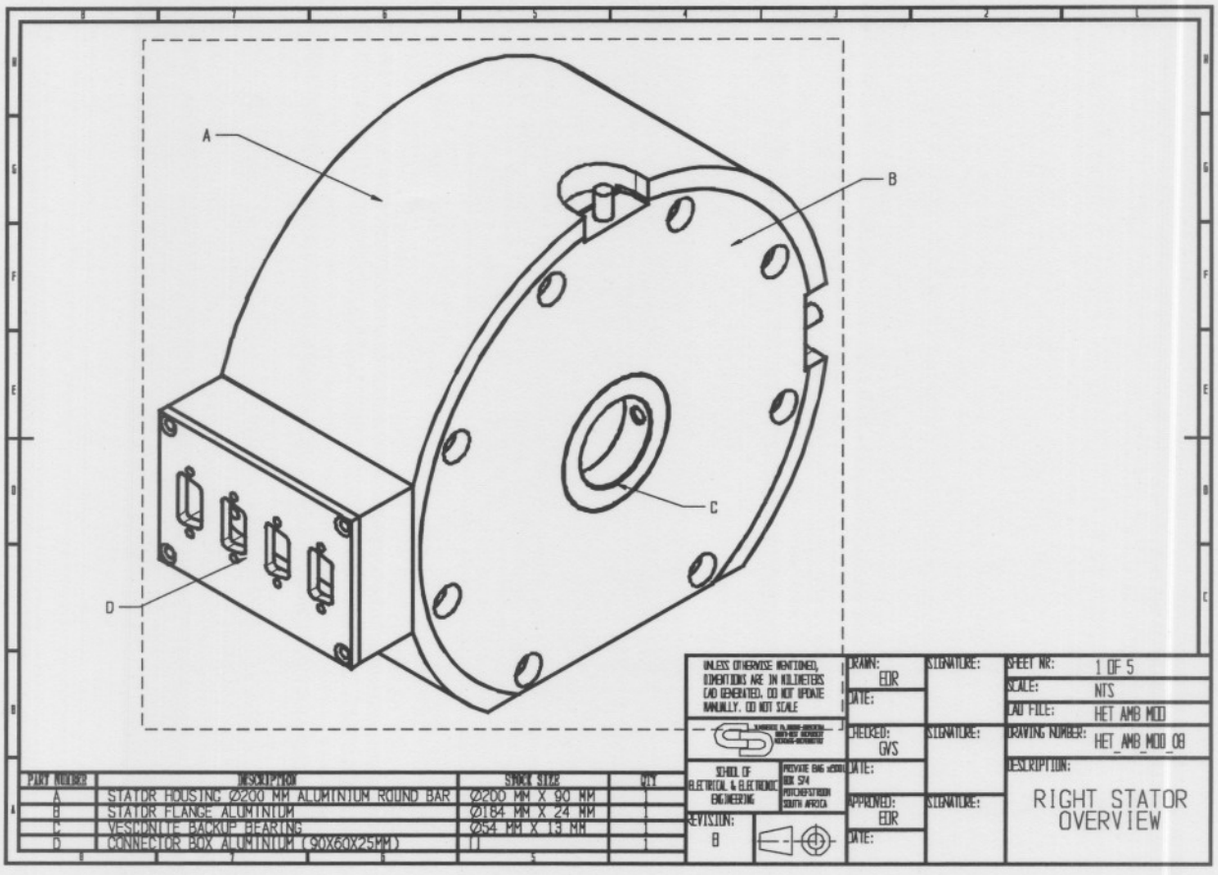

PART NUMBER	DESCRIPTION	STOCK SIZE	QTY
A	STATOR HOUSING Ø200 MM ALUMINIUM ROUND BAR	Ø200 MM X 90 MM	1
B	STATOR FLANGE ALUMINIUM	Ø184 MM X 24 MM	1
C	VESCONITE BACKUP BEARING	Ø54 MM X 13 MM	1
D	CONNECTOR BOX ALUMINIUM (90X60X25MM)		1

UNLESS OTHERWISE MENTIONED, DIMENTIONS ARE IN MILLIMETERS CAD GENERATED. DO NOT UPDATE MANUALLY. DO NOT SCALE

SCHOOL OF ELECTRICAL & ELECTRONIC ENGINEERING

PRIVATE BAG X6001 BOX 514 POTCHEFSTROOM SOUTH AFRICA

REVISION: B

DRAWN: EDR | DATE: | SIGNATURE:
CHECKED: GVS | DATE: | SIGNATURE:
APPROVED: EDR | DATE: | SIGNATURE:

SHEET NR: 1 OF 5
SCALE: NTS
CAD FILE: HET AMB MOD
DRAWING NUMBER: HET_AMB_MOD_08
DESCRIPTION: RIGHT STATOR OVERVIEW

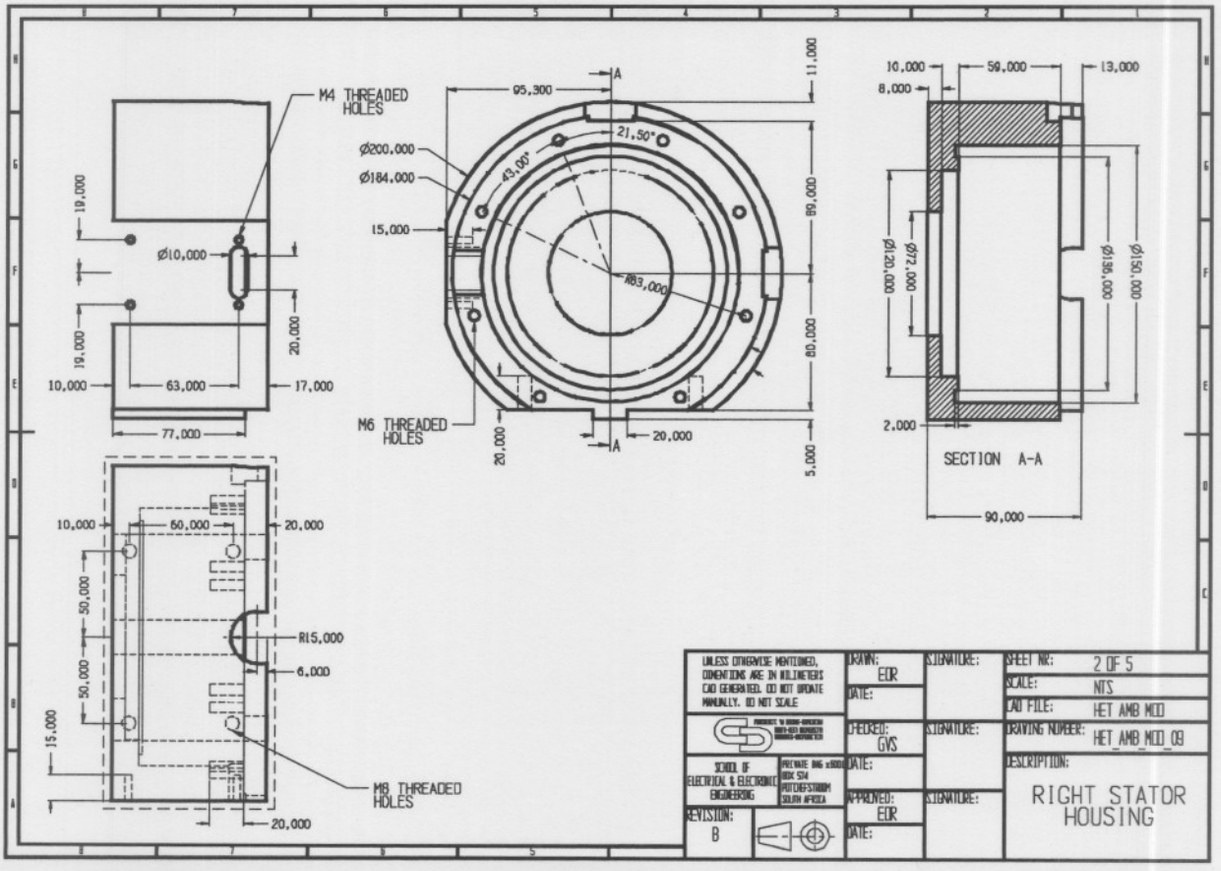

UNLESS OTHERWISE MENTIONED, DIMENTIONS ARE IN MILLIMETERS CAD GENERATED. DO NOT UPDATE MANUALLY. DO NOT SCALE

SCHOOL OF ELECTRICAL & ELECTRONIC ENGINEERING

PRIVATE BAG X6001 BOX 514 POTCHEFSTROOM SOUTH AFRICA

REVISION: B

DRAWN: EDR | DATE: | SIGNATURE:
CHECKED: GVS | DATE: | SIGNATURE:
APPROVED: EDR | DATE: | SIGNATURE:

SHEET NR: 2 OF 5
SCALE: NTS
CAD FILE: HET AMB MOD
DRAWING NUMBER: HET_AMB_MOD_09
DESCRIPTION: RIGHT STATOR HOUSING

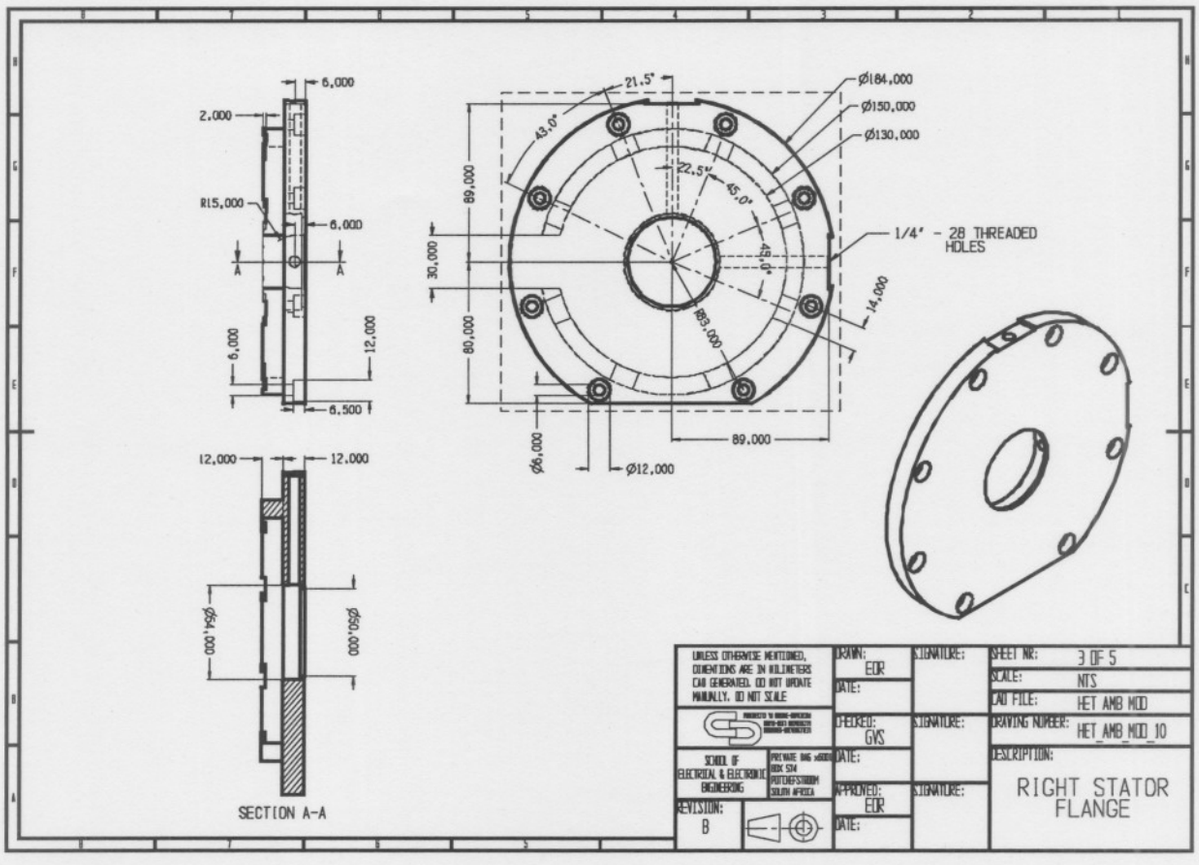
6.000
2.000
R15.000
6.000
A
A
6.000
12.000
6.500
12.000
12.000
Ø54.000
Ø50.000
SECTION A-A
21.5°
43.0°
Ø184.000
Ø150.000
Ø130.000
22.5°
45.0°
45.0°
89.000
30.000
80.000
1/4" - 28 THREADED HOLES
14.000
Ø89.000
Ø6.000
Ø12.000
89.000
UNLESS OTHERWISE MENTIONED, DIMENTIONS ARE IN MILIMETERS CAD GENERATED. DO NOT UPDATE MANUALLY. DO NOT SCALE
DRAWN: EDR
DATE:
SIGNATURE:
CHECKED: GVS
DATE:
SIGNATURE:
APPROVED: EDR
DATE:
SIGNATURE:
SCHOOL OF ELECTRICAL & ELECTRONIC ENGINEERING
PRIVATE BAG X6001 BOX 514 POTCHEFSTROOM SOUTH AFRICA
REVISION: B
SHEET NR: 3 OF 5
SCALE: NTS
CAD FILE: HET AMB MOD
DRAWING NUMBER: HET_AMB_MOD_10
DESCRIPTION:
RIGHT STATOR FLANGE

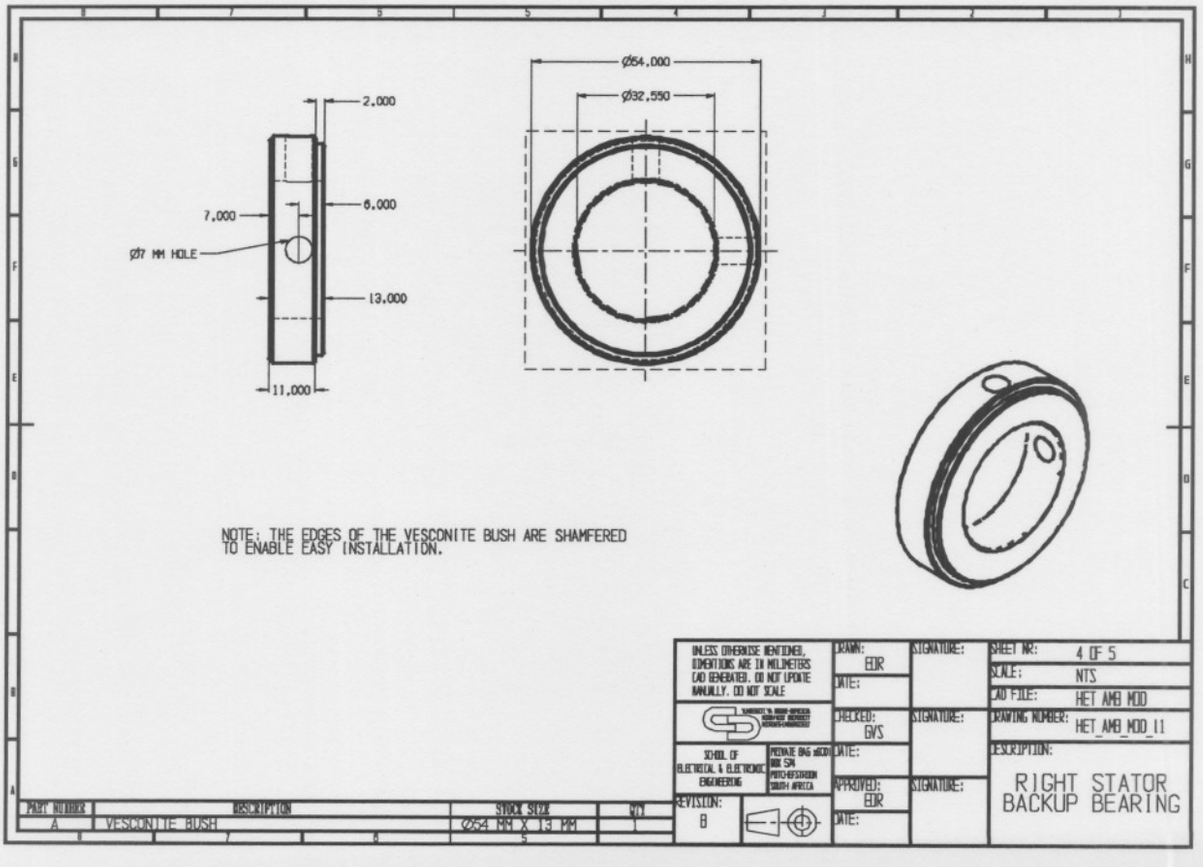
2.000
7.000
6.000
Ø7 MM HOLE
13.000
11.000
Ø54.000
Ø32.550
NOTE: THE EDGES OF THE VESCONITE BUSH ARE SHAMFERED TO ENABLE EASY INSTALLATION.
PART NUMBER
DESCRIPTION
STOCK SIZE
QTY
A
VESCONITE BUSH
Ø54 MM X 13 MM
1
UNLESS OTHERWISE MENTIONED, DIMENTIONS ARE IN MILIMETERS CAD GENERATED. DO NOT UPDATE MANUALLY. DO NOT SCALE
DRAWN: EDR
DATE:
SIGNATURE:
CHECKED: GVS
DATE:
SIGNATURE:
APPROVED: EDR
DATE:
SIGNATURE:
SCHOOL OF ELECTRICAL & ELECTRONIC ENGINEERING
PRIVATE BAG X6001 BOX 514 POTCHEFSTROOM SOUTH AFRICA
REVISION: B
SHEET NR: 4 OF 5
SCALE: NTS
CAD FILE: HET AMB MOD
DRAWING NUMBER: HET_AMB_MOD_11
DESCRIPTION:
RIGHT STATOR BACKUP BEARING

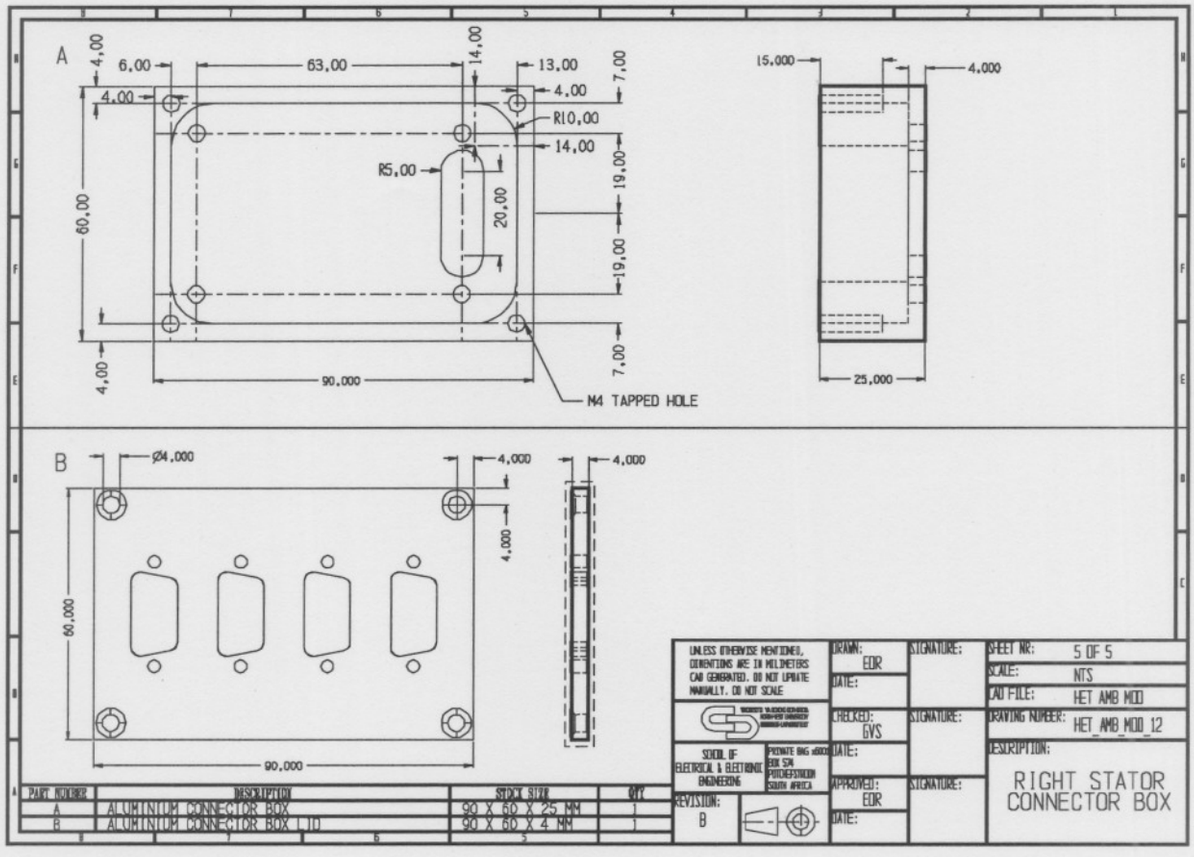
A
4,00
6,00
63,00
14,00
13,00
7,00
4,00
4,00
R10,00
14,00
R5,00
19,00
20,00
60,00
19,00
4,00
7,00
90,000
M4 TAPPED HOLE
15,000
4,000
25,000
B
Ø4,000
4,000
4,000
4,000
60,000
90,000
UNLESS OTHERWISE MENTIONED, DIMENTIONS ARE IN MILIMETERS CAD GENERATED. DO NOT UPDATE MANUALLY. DO NOT SCALE
SCHOOL OF ELECTRICAL & ELECTRONIC ENGINEERING
PRIVATE BAG X6001 BOX 574 POTCHEFSTROOM SOUTH AFRICA
REVISION: B
DRAWN: EDR
DATE:
CHECKED: GVS
DATE:
APPROVED: EDR
DATE:
SIGNATURE:
SHEET NR: 5 OF 5
SCALE: NTS
CAD FILE: HET AMB MOD
DRAWING NUMBER: HET_AMB_MOD_12
DESCRIPTION: RIGHT STATOR CONNECTOR BOX
PART NUMBER | DESCRIPTION | STOCK SIZE | QTY
A | ALUMINIUM CONNECTOR BOX | 90 X 60 X 25 MM | 1
B | ALUMINIUM CONNECTOR BOX LID | 90 X 60 X 4 MM | 1

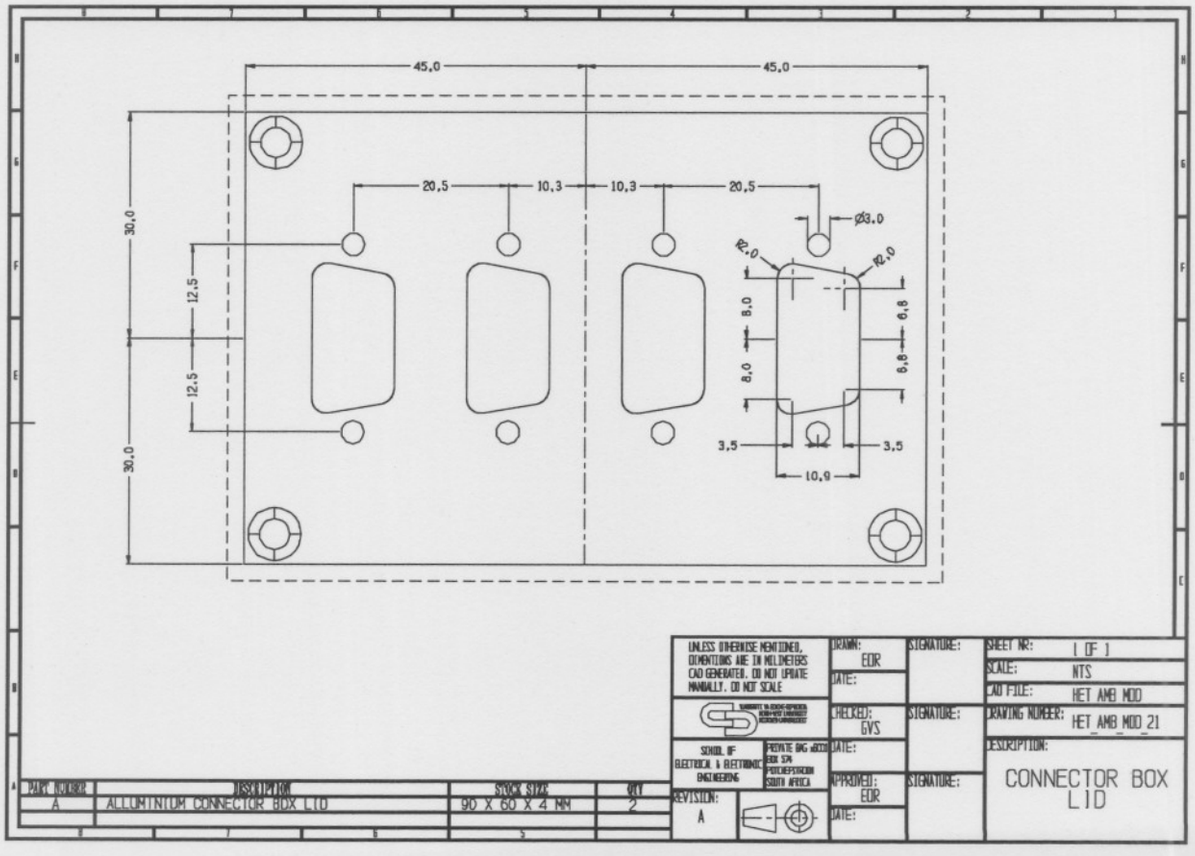
45,0
45,0
20,5
10,3
10,3
20,5
Ø3,0
R2,0
R2,0
30,0
12,5
12,5
30,0
8,0
8,0
6,8
6,8
3,5
3,5
10,9
UNLESS OTHERWISE MENTIONED, DIMENTIONS ARE IN MILIMETERS CAD GENERATED. DO NOT UPDATE MANUALLY. DO NOT SCALE
SCHOOL OF ELECTRICAL & ELECTRONIC ENGINEERING
PRIVATE BAG X6001 BOX 574 POTCHEFSTROOM SOUTH AFRICA
REVISION: A
DRAWN: EDR
DATE:
CHECKED: GVS
DATE:
APPROVED: EDR
DATE:
SIGNATURE:
SHEET NR: 1 OF 1
SCALE: NTS
CAD FILE: HET AMB MOD
DRAWING NUMBER: HET_AMB_MOD_21
DESCRIPTION: CONNECTOR BOX LID
PART NUMBER | DESCRIPTION | STOCK SIZE | QTY
A | ALUMINIUM CONNECTOR BOX LID | 90 X 60 X 4 MM | 2

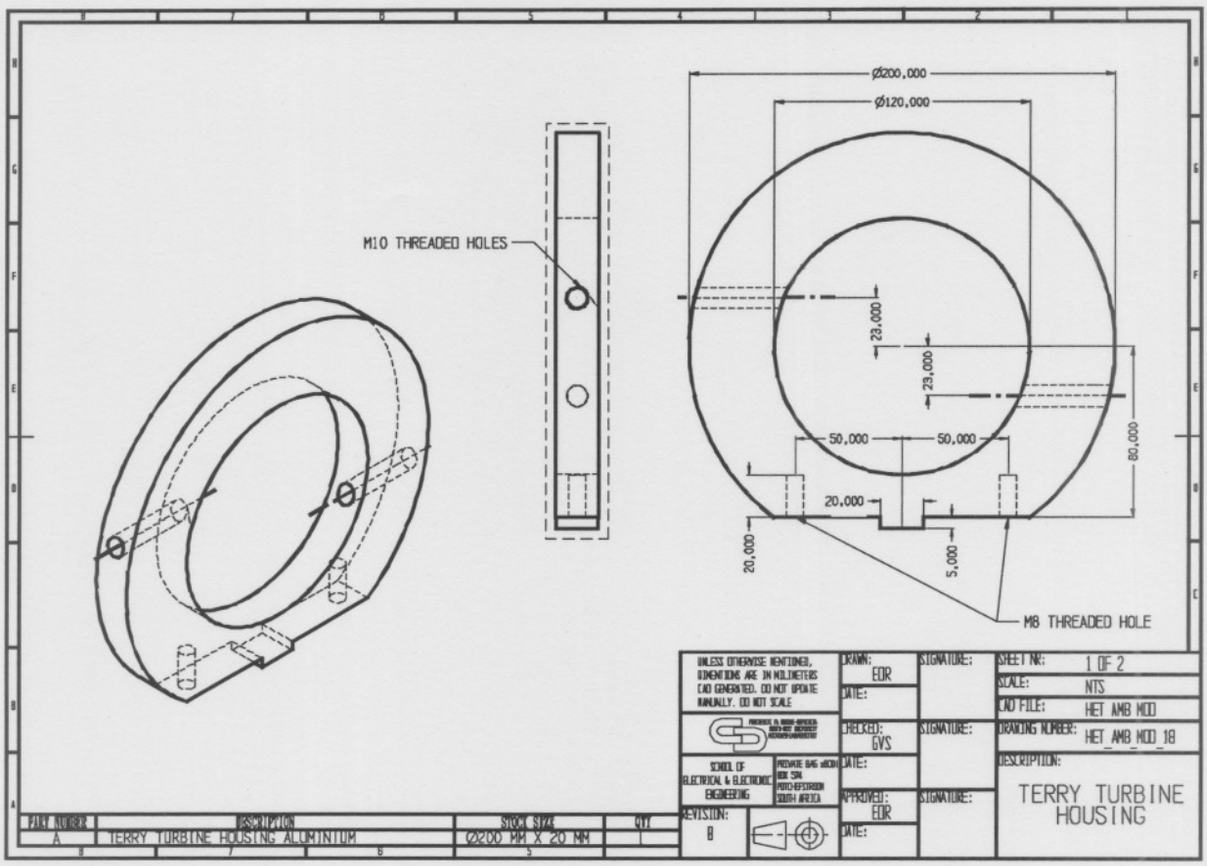
M10 THREADED HOLES
Ø200,000
Ø120,000
23,000
23,000
50,000
50,000
80,000
20,000
20,000
5,000
M8 THREADED HOLE
UNLESS OTHERWISE MENTIONED, DIMENTIONS ARE IN MILLIMETERS CAD GENERATED. DO NOT UPDATE MANUALLY. DO NOT SCALE
DRAWN: EDR
DATE:
CHECKED: GVS
DATE:
APPROVED: EDR
DATE:
SIGNATURE:
SHEET NR: 1 OF 2
SCALE: NTS
CAD FILE: HET AMB MOD
DRAWING NUMBER: HET_AMB_MOD_18
DESCRIPTION:
TERRY TURBINE HOUSING
SCHOOL OF ELECTRICAL & ELECTRONIC ENGINEERING
REVISION: B
PART NUMBER | DESCRIPTION | STOCK SIZE | QTY
A | TERRY TURBINE HOUSING ALUMINTIUM | Ø200 MM X 20 MM | 1

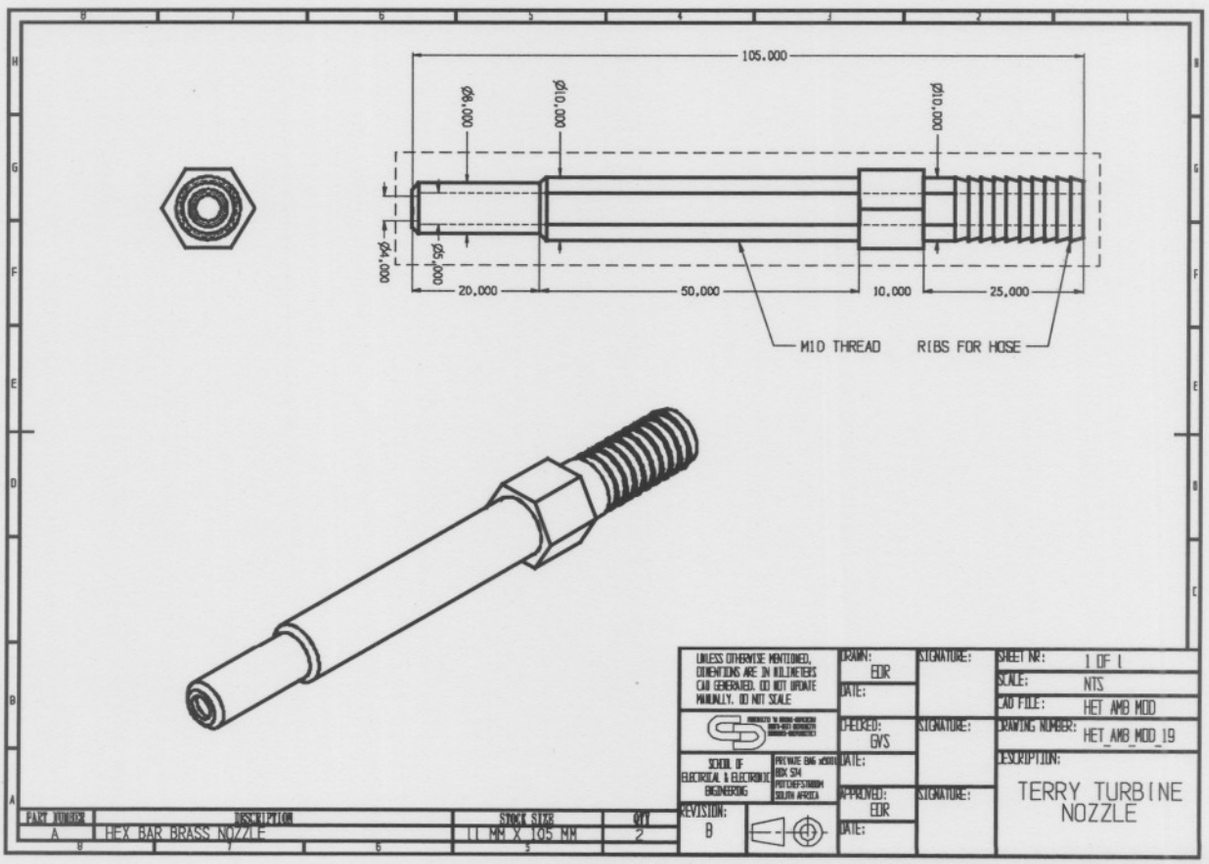
105.000
Ø8,000
Ø10,000
Ø10,000
Ø4,000
Ø5,000
20,000
50,000
10,000
25,000
M10 THREAD
RIBS FOR HOSE
UNLESS OTHERWISE MENTIONED, DIMENTIONS ARE IN MILLIMETERS CAD GENERATED. DO NOT UPDATE MANUALLY. DO NOT SCALE
DRAWN: EDR
DATE:
CHECKED: GVS
DATE:
APPROVED: EDR
DATE:
SIGNATURE:
SHEET NR: 1 OF 1
SCALE: NTS
CAD FILE: HET AMB MOD
DRAWING NUMBER: HET_AMB_MOD_19
DESCRIPTION:
TERRY TURBINE NOZZLE
SCHOOL OF ELECTRICAL & ELECTRONIC ENGINEERING
REVISION: B
PART NUMBER | DESCRIPTION | STOCK SIZE | QTY
A | HEX BAR BRASS NOZZLE | 11 MM X 105 MM | 2

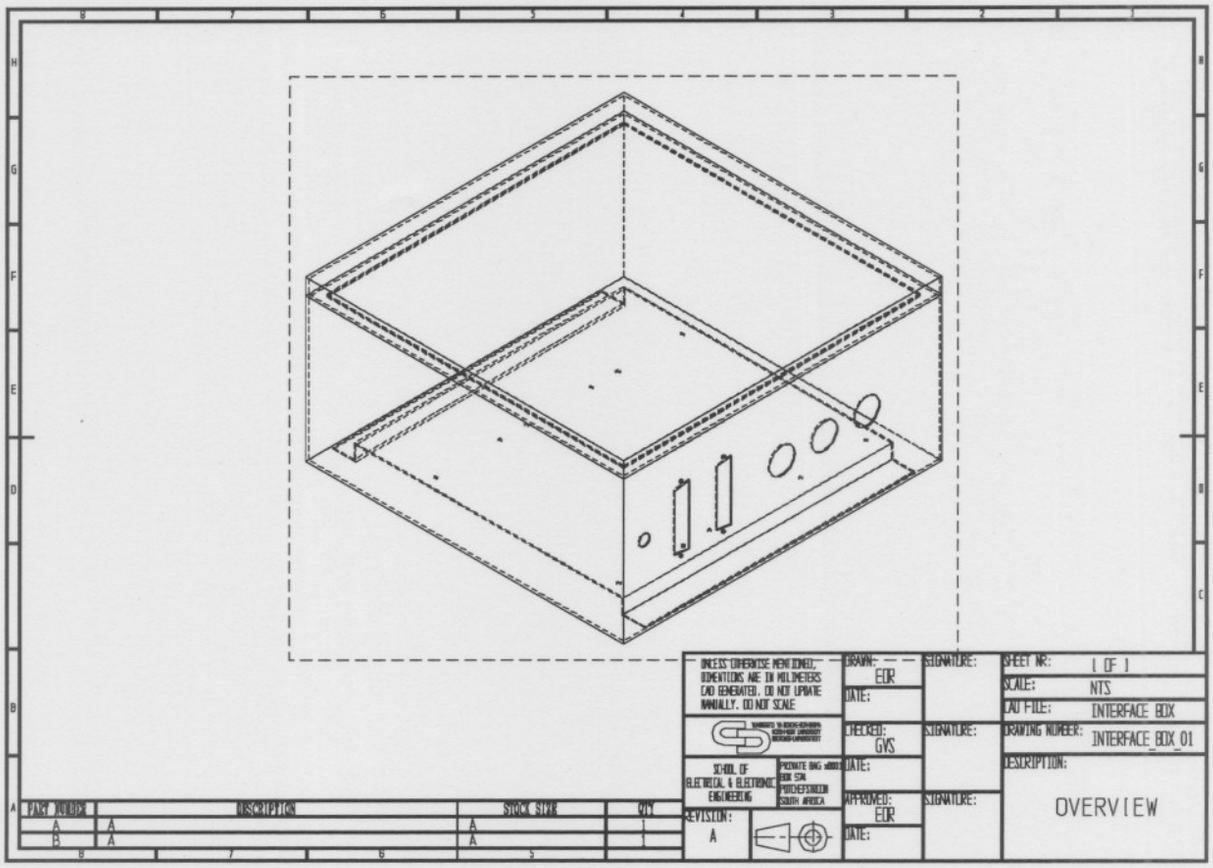
UNLESS OTHERWISE MENTIONED, DIMENTIONS ARE IN MILLIMETERS CAD GENERATED. DO NOT UPDATE MANUALLY. DO NOT SCALE
SCHOOL OF ELECTRICAL & ELECTRONIC ENGINEERING
PRIVATE BAG X6001 BOX 304 POTCHEFSTROOM SOUTH AFRICA
REVISION: A
DRAWN: EDR
DATE:
SIGNATURE:
CHECKED: GVS
DATE:
SIGNATURE:
APPROVED: EDR
DATE:
SIGNATURE:
SHEET NR: 1 OF 1
SCALE: NTS
CAD FILE: INTERFACE BOX
DRAWING NUMBER: INTERFACE BOX 01
DESCRIPTION:
OVERVIEW
PART NUMBER
DESCRIPTION
STOCK SIZE
QTY
A
B
A
A
A
A
1
1

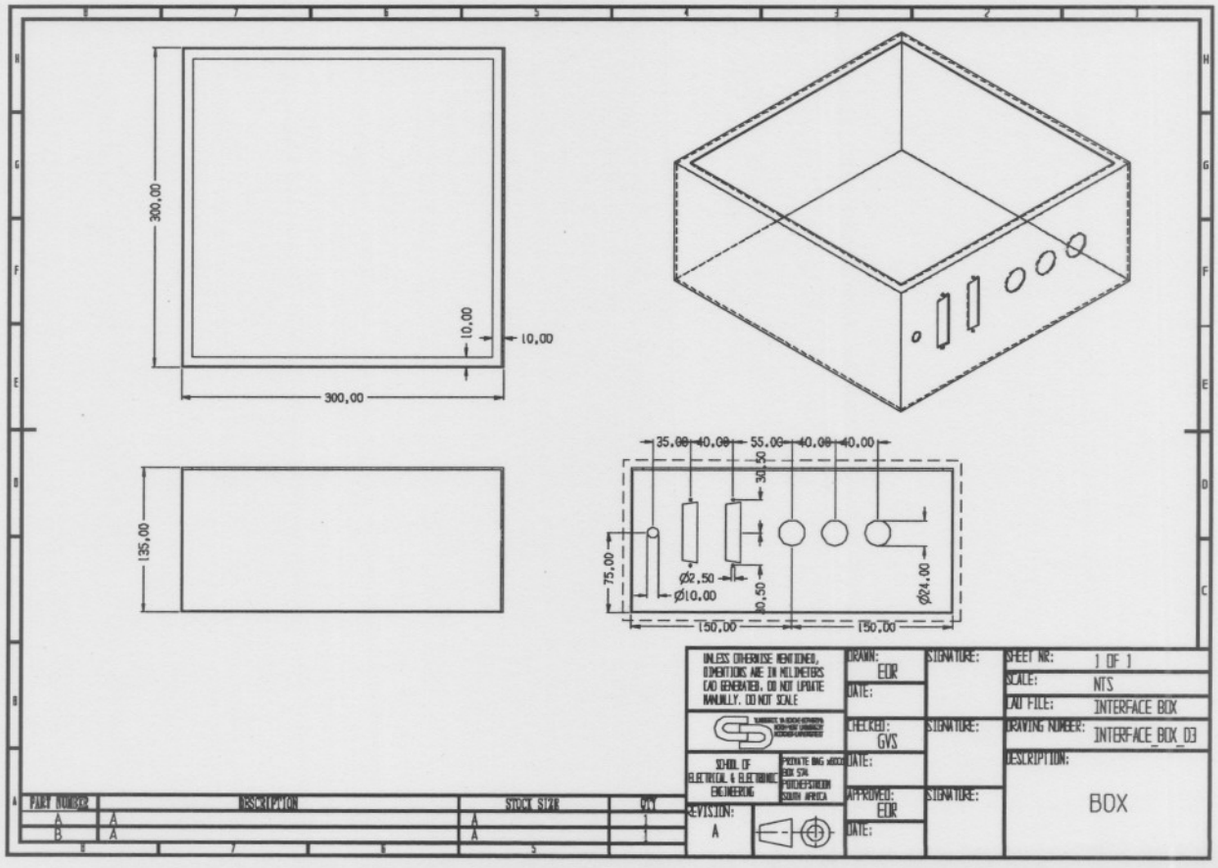
300,00
300,00
10,00
10,00
135,00
35,00
40,00
55,00
40,00
40,00
30,50
30,50
75,00
Ø2,50
Ø10,00
Ø24,00
150,00
150,00
UNLESS OTHERWISE MENTIONED, DIMENTIONS ARE IN MILLIMETERS CAD GENERATED. DO NOT UPDATE MANUALLY. DO NOT SCALE
SCHOOL OF ELECTRICAL & ELECTRONIC ENGINEERING
PRIVATE BAG X6001 BOX 304 POTCHEFSTROOM SOUTH AFRICA
REVISION: A
DRAWN: EDR
DATE:
SIGNATURE:
CHECKED: GVS
DATE:
SIGNATURE:
APPROVED: EDR
DATE:
SIGNATURE:
SHEET NR: 1 OF 1
SCALE: NTS
CAD FILE: INTERFACE BOX
DRAWING NUMBER: INTERFACE BOX 03
DESCRIPTION:
BOX
PART NUMBER
DESCRIPTION
STOCK SIZE
QTY
A
B
A
A
A
A
1
1

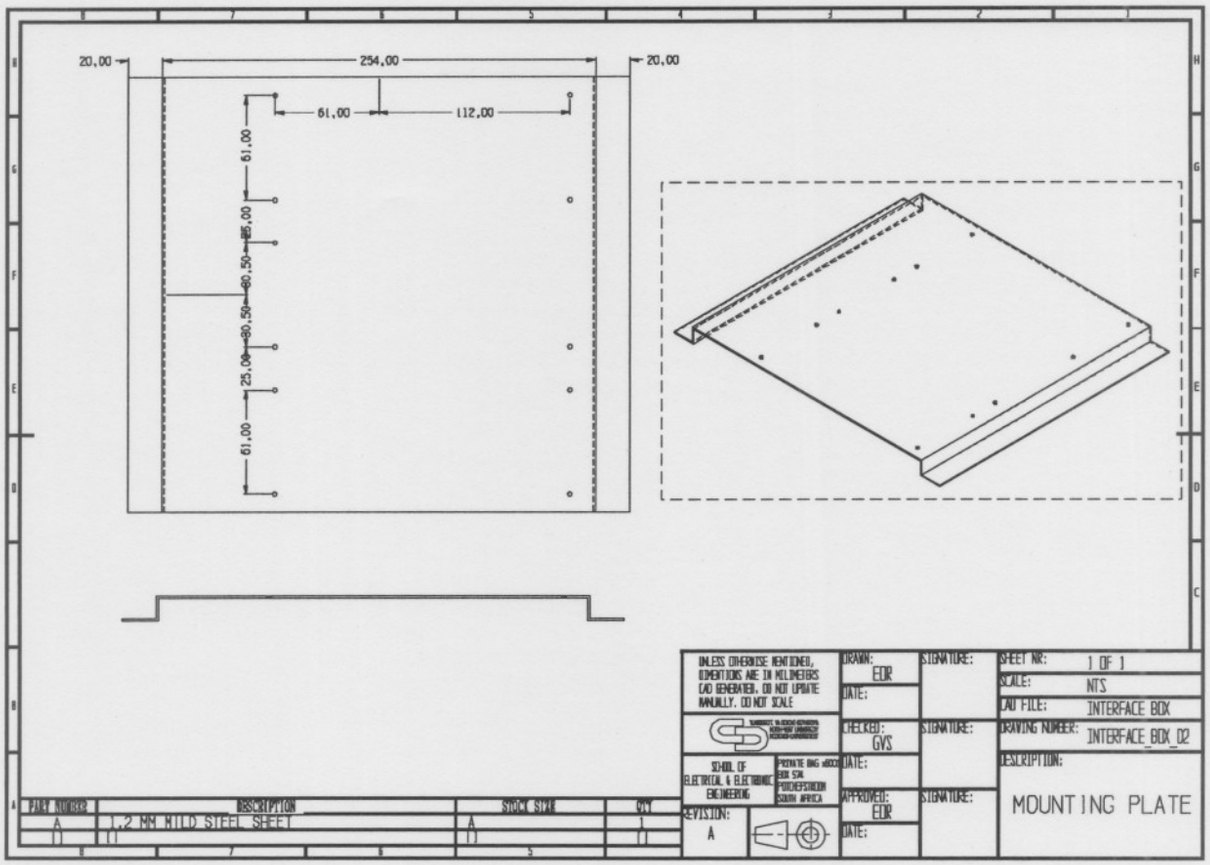
20,00
254,00
20,00
61,00
112,00
61,00
85,00
80,50
30,50
25,00
61,00
UNLESS OTHERWISE MENTIONED, DIMENTIONS ARE IN MILIMETERS CAD GENERATED. DO NOT UPDATE MANUALLY. DO NOT SCALE
DRAWN: EDR
DATE:
SIGNATURE:
CHECKED: GVS
DATE:
SIGNATURE:
APPROVED: EDR
DATE:
SIGNATURE:
SHEET NR: 1 OF 1
SCALE: NTS
CAD FILE: INTERFACE BOX
DRAWING NUMBER: INTERFACE_BOX_02
DESCRIPTION:
MOUNTING PLATE
SCHOOL OF ELECTRICAL & ELECTRONIC ENGINEERING
PRIVATE BAG X6001 BOX 524 POTCHEFSTROOM SOUTH AFRICA
REVISION: A
PART NUMBER
DESCRIPTION
STOCK SIZE
QTY
A
1,2 MM MILD STEEL SHEET
A
1
01
01
01

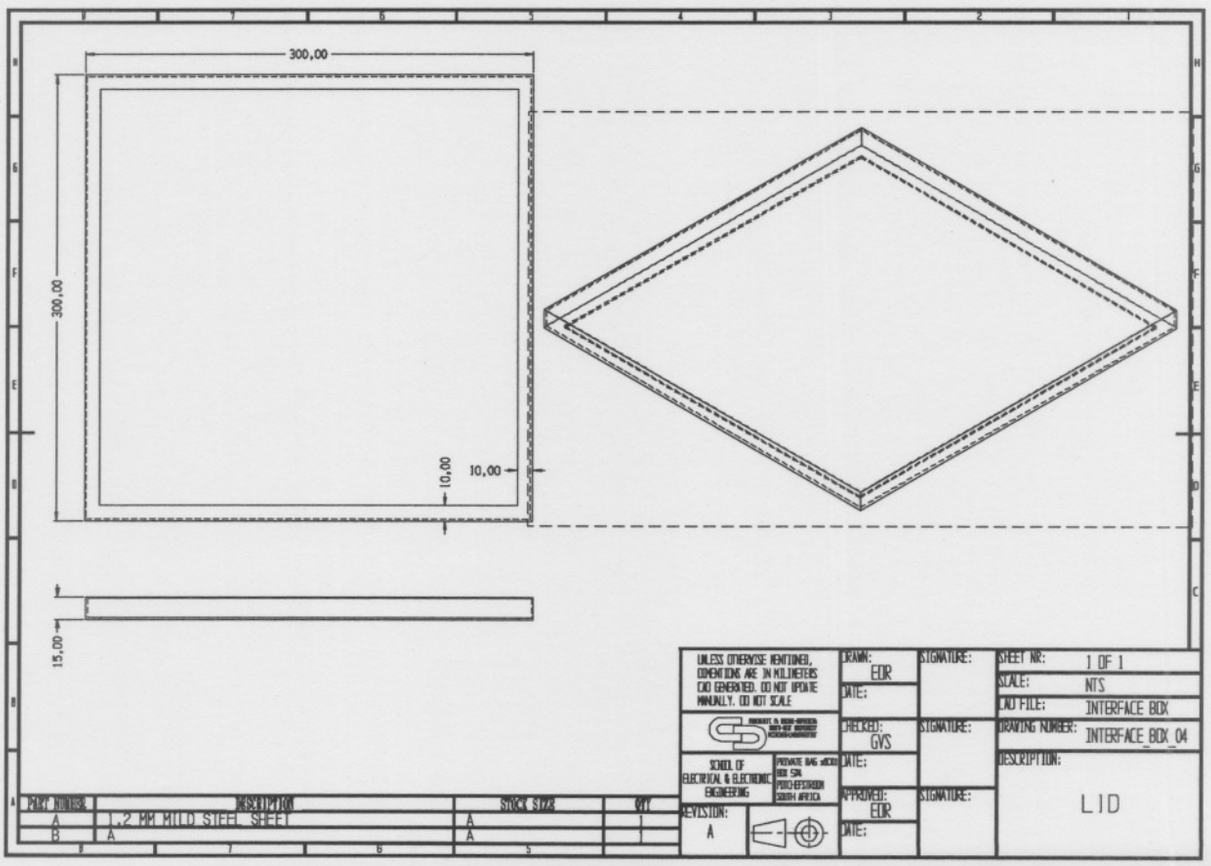
300,00
300,00
10,00
10,00
15,00
UNLESS OTHERWISE MENTIONED, DIMENTIONS ARE IN MILIMETERS CAD GENERATED. DO NOT UPDATE MANUALLY. DO NOT SCALE
DRAWN: EDR
DATE:
SIGNATURE:
CHECKED: GVS
DATE:
SIGNATURE:
APPROVED: EDR
DATE:
SIGNATURE:
SHEET NR: 1 OF 1
SCALE: NTS
CAD FILE: INTERFACE BOX
DRAWING NUMBER: INTERFACE_BOX_04
DESCRIPTION:
LID
SCHOOL OF ELECTRICAL & ELECTRONIC ENGINEERING
PRIVATE BAG X6001 BOX 524 POTCHEFSTROOM SOUTH AFRICA
REVISION: A
PART NUMBER
DESCRIPTION
STOCK SIZE
QTY
A
1,2 MM MILD STEEL SHEET
A
1
B
A
A
1

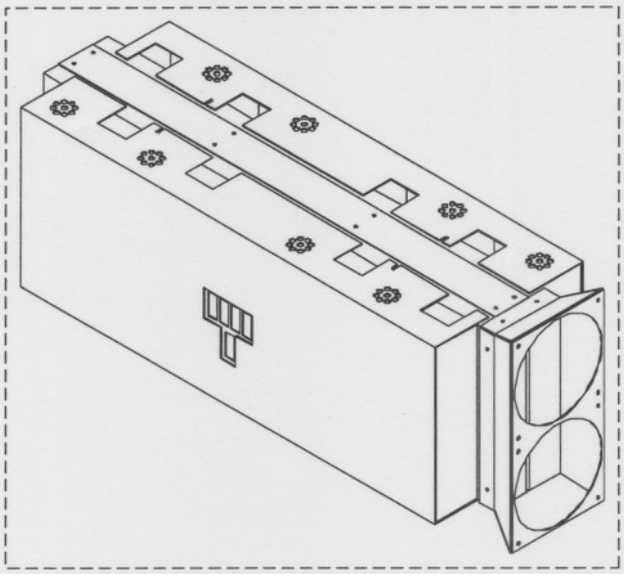

PART NUMBER	DESCRIPTION	STOCK SIZE	QTY
A	A	A	1
B	A	A	1

UNLESS OTHERWISE MENTIONED, DIMENTIONS ARE IN MILLIMETERS CAD GENERATED. DO NOT UPDATE MANUALLY. DO NOT SCALE

SCHOOL OF ELECTRICAL & ELECTRONIC ENGINEERING

REVISION: A

DRAWN: EDR	DATE:	SIGNATURE:	SHEET NR: 1 OF 1
			SCALE: NTS
			CAD FILE: HEATSINK
CHECKED: GVS	DATE:	SIGNATURE:	DRAWING NUMBER: HEATSINK_01
APPROVED: EDR	DATE:	SIGNATURE:	DESCRIPTION: GENERAL LAYOUT

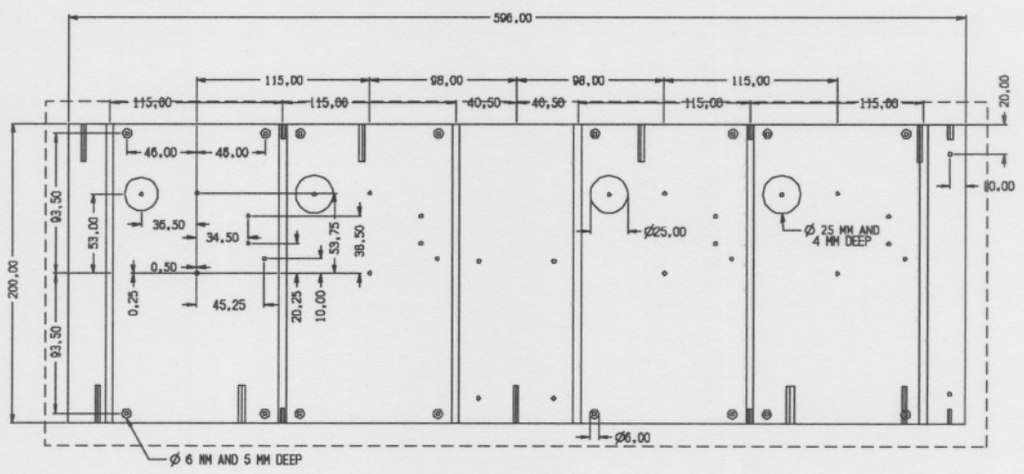

PART NUMBER	DESCRIPTION	STOCK SIZE	QTY
A	A	A	1
B	A	A	1

UNLESS OTHERWISE MENTIONED, DIMENTIONS ARE IN MILLIMETERS CAD GENERATED. DO NOT UPDATE MANUALLY. DO NOT SCALE

SCHOOL OF ELECTRICAL & ELECTRONIC ENGINEERING

REVISION: A

DRAWN: EDR	DATE:	SIGNATURE:	SHEET NR: 1 OF 1
			SCALE: NTS
			CAD FILE: HEATSINK
CHECKED: GVS	DATE:	SIGNATURE:	DRAWING NUMBER: HEATSINK_03
APPROVED: EDR	DATE:	SIGNATURE:	DESCRIPTION: FRONT HEAT SINK DETAIL

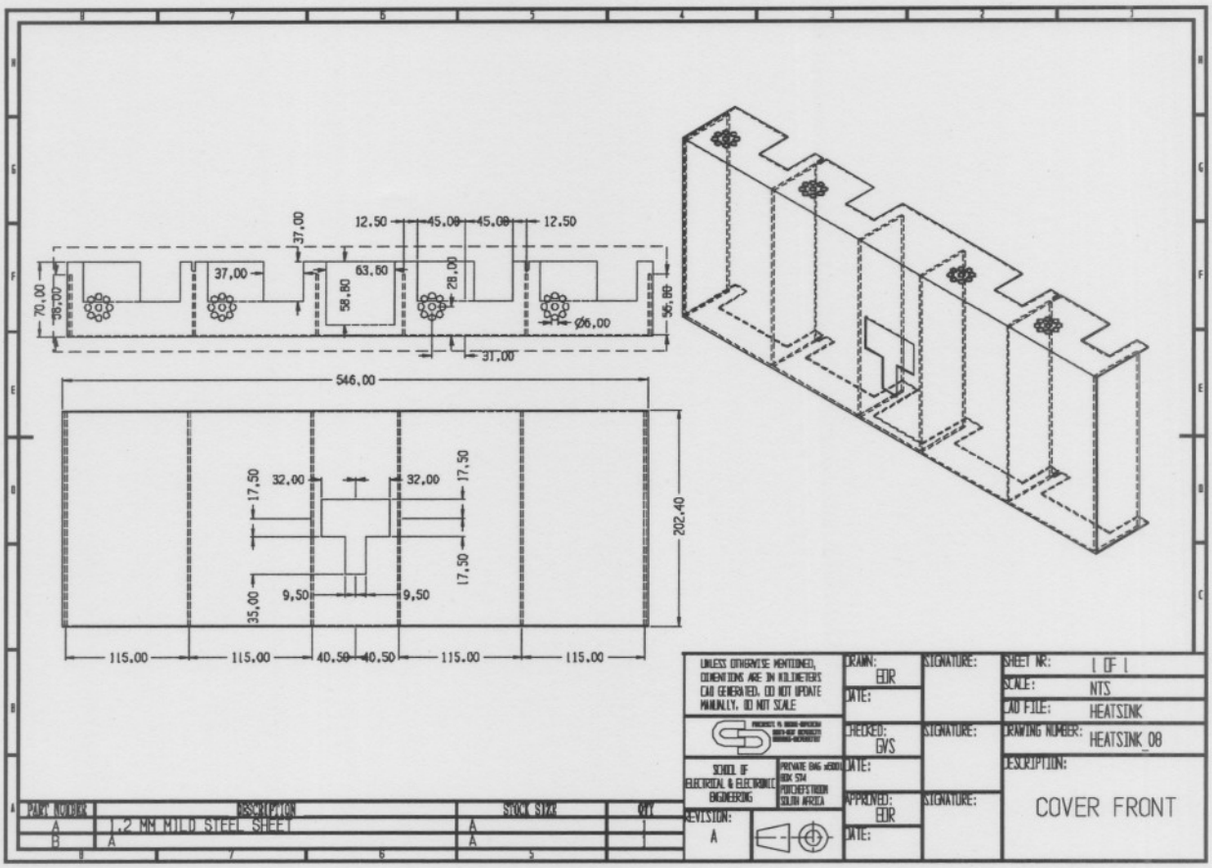
37,00
12,50
45,00
45,00
12,50
70,00
35,00
37,00
63,80
58,80
28,00
96,80
Ø6,00
37,00
546,00
17,50
32,00
32,00
17,50
202,40
17,50
35,00
9,50
9,50
115,00
115,00
40,50
40,50
115,00
115,00
UNLESS OTHERWISE MENTIONED, DIMENTIONS ARE IN MILIMETERS CAD GENERATED. DO NOT UPDATE MANUALLY. DO NOT SCALE
DRAWN: EDR
DATE:
CHECKED: GVS
DATE:
APPROVED: EDR
DATE:
SIGNATURE:
SCHOOL OF ELECTRICAL & ELECTRONIC ENGINEERING
SHEET NR: 1 OF 1
SCALE: NTS
CAD FILE: HEATSINK
DRAWING NUMBER: HEATSINK_08
DESCRIPTION:
COVER FRONT
REVISION: A
PART NUMBER | DESCRIPTION | STOCK SIZE | QTY
A | 1,2 MM MILD STEEL SHEET | A | 1
B | A | A

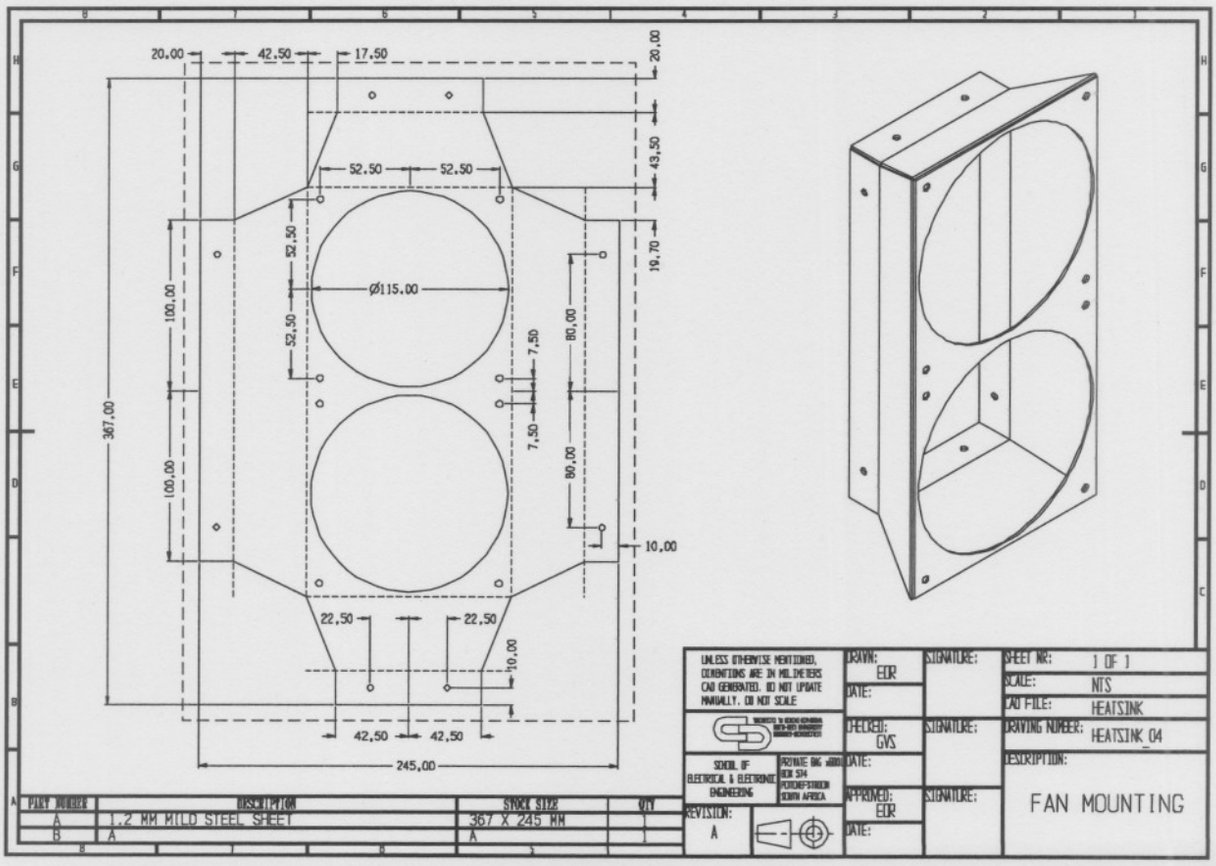
20,00
42,50
17,50
20,00
52,50
52,50
43,50
52,50
19,70
Ø115,00
100,00
52,50
7,50
80,00
367,00
7,50
80,00
100,00
10,00
22,50
22,50
10,00
42,50
42,50
245,00
UNLESS OTHERWISE MENTIONED, DIMENTIONS ARE IN MILIMETERS CAD GENERATED. DO NOT UPDATE MANUALLY. DO NOT SCALE
DRAWN: EDR
DATE:
CHECKED: GVS
DATE:
APPROVED: EDR
DATE:
SIGNATURE:
SCHOOL OF ELECTRICAL & ELECTRONIC ENGINEERING
SHEET NR: 1 OF 1
SCALE: NTS
CAD FILE: HEATSINK
DRAWING NUMBER: HEATSINK_04
DESCRIPTION:
FAN MOUNTING
REVISION: A
PART NUMBER | DESCRIPTION | STOCK SIZE | QTY
A | 1,2 MM MILD STEEL SHEET | 367 X 245 MM | 1
B | A | A

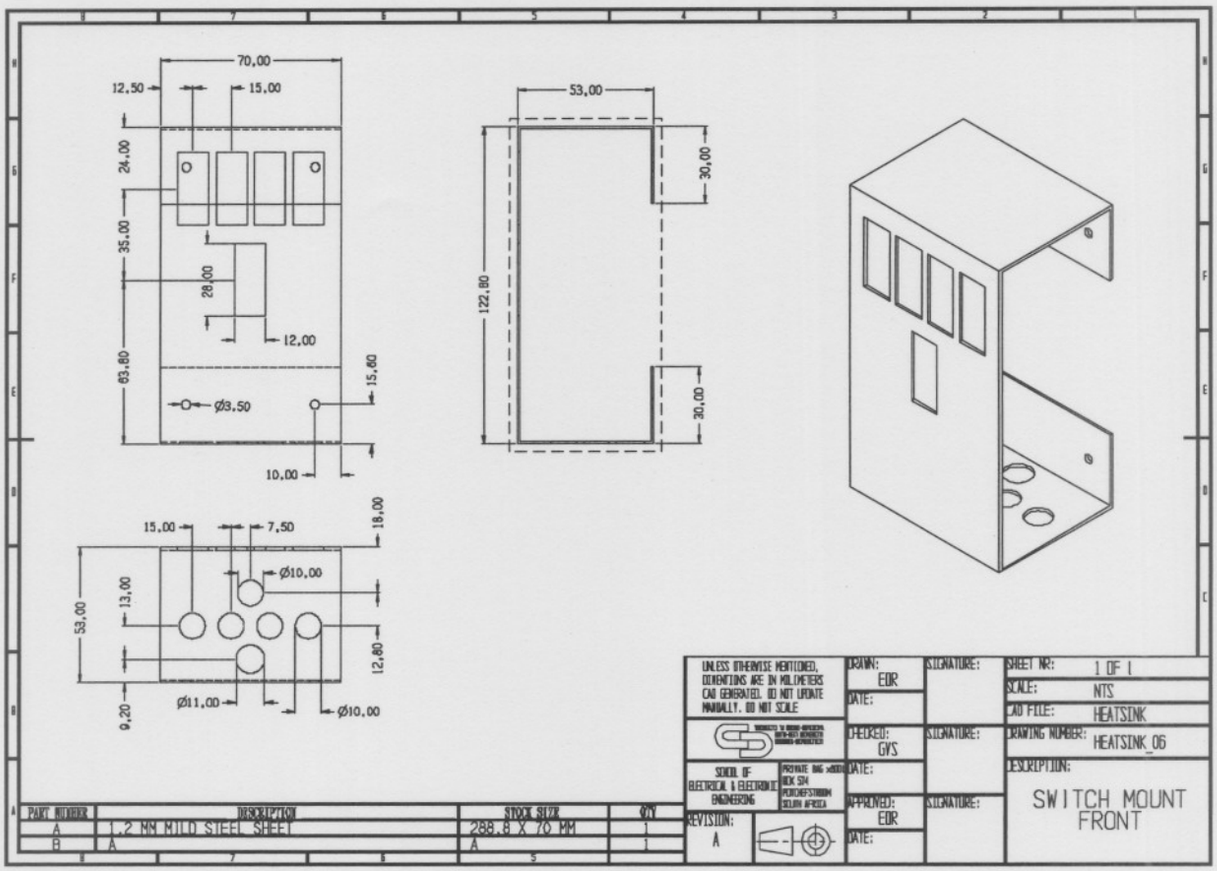
70,00
12,50
15,00
24,00
35,00
28,00
12,00
63,80
15,60
Ø3,50
10,00
53,00
30,00
122,80
30,00
15,00
7,50
18,00
Ø10,00
53,00
13,00
12,80
9,20
Ø11,00
Ø10,00
UNLESS OTHERWISE MENTIONED, DIMENTIONS ARE IN MILLIMETERS CAD GENERATED. DO NOT UPDATE MANUALLY. DO NOT SCALE
DRAWN: EDR
DATE:
CHECKED: GVS
DATE:
APPROVED: EDR
DATE:
SIGNATURE:
SHEET NR: 1 OF 1
SCALE: NTS
CAD FILE: HEATSINK
DRAWING NUMBER: HEATSINK_06
DESCRIPTION:
SWITCH MOUNT FRONT
SCHOOL OF ELECTRICAL & ELECTRONIC ENGINEERING
REVISION: A
PART NUMBER
DESCRIPTION
STOCK SIZE
QTY
A
B
1,2 MM MILD STEEL SHEET
288,8 X 76 MM
1

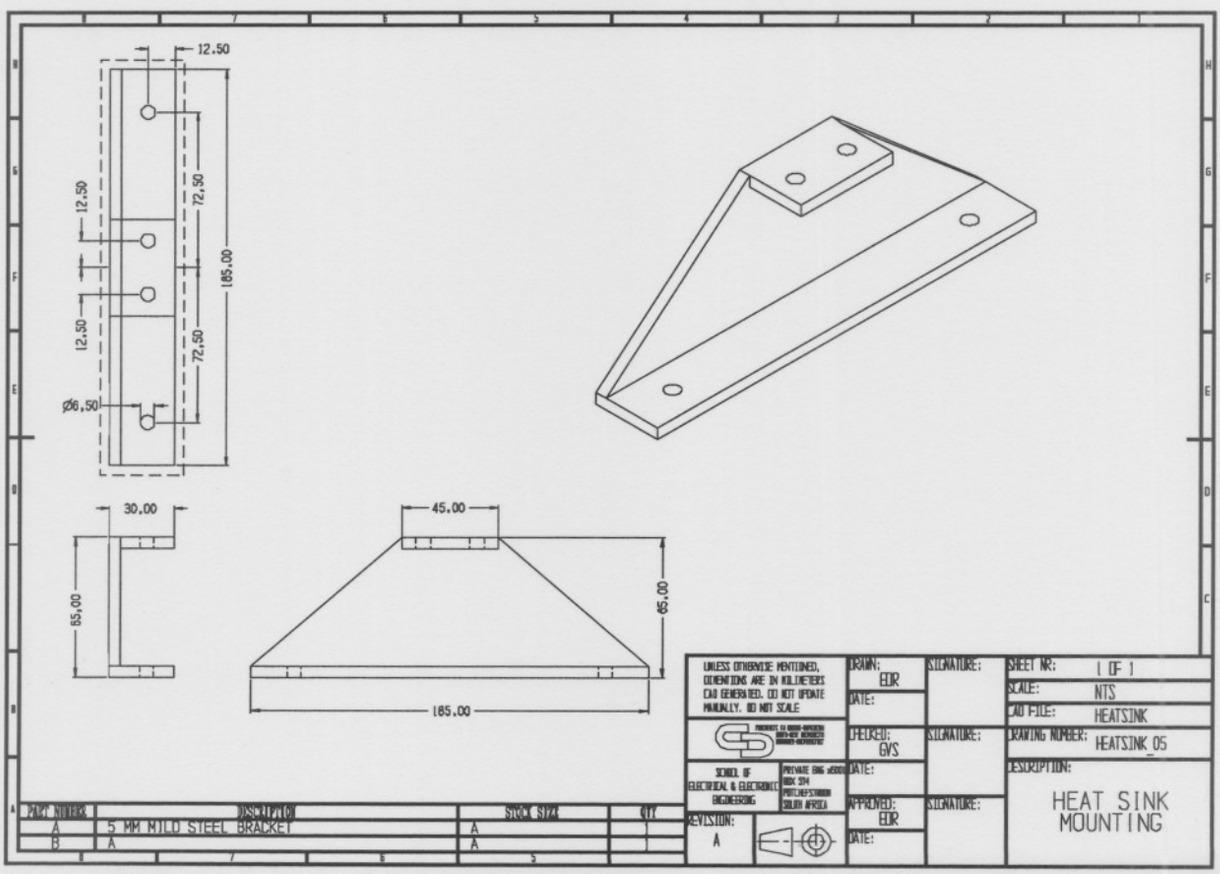
12,50
12,50
72,50
185,00
12,50
72,50
Ø6,50
30,00
65,00
45,00
65,00
185,00
UNLESS OTHERWISE MENTIONED, DIMENTIONS ARE IN MILLIMETERS CAD GENERATED. DO NOT UPDATE MANUALLY. DO NOT SCALE
DRAWN: EDR
DATE:
CHECKED: GVS
DATE:
APPROVED: EDR
DATE:
SIGNATURE:
SHEET NR: 1 OF 1
SCALE: NTS
CAD FILE: HEATSINK
DRAWING NUMBER: HEATSINK_05
DESCRIPTION:
HEAT SINK MOUNTING
SCHOOL OF ELECTRICAL & ELECTRONIC ENGINEERING
REVISION: A
PART NUMBER
DESCRIPTION
STOCK SIZE
QTY
A
B
5 MM MILD STEEL BRACKET

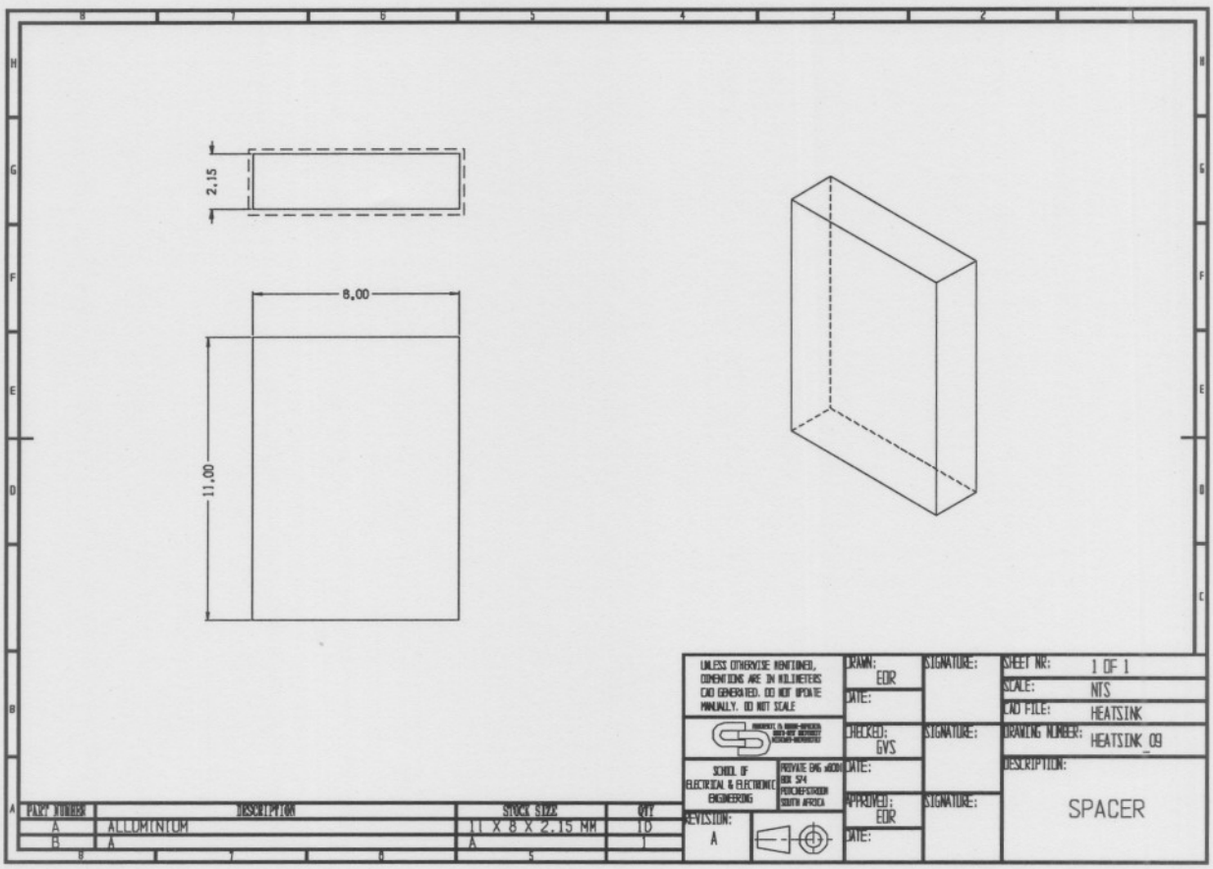
2.15
8.00
11.00
UNLESS OTHERWISE MENTIONED, DIMENTIONS ARE IN MILLIMETERS CAD GENERATED. DO NOT UPDATE MANUALLY. DO NOT SCALE
DRAWN: EDR
DATE:
SIGNATURE:
SHEET NR: 1 OF 1
SCALE: NTS
CAD FILE: HEATSINK
CHECKED: GVS
DRAWING NUMBER: HEATSINK_09
DESCRIPTION:
SCHOOL OF ELECTRICAL & ELECTRONIC ENGINEERING
PRIVATE BAG X6001 BOX 394 POTCHEFSTROOM SOUTH AFRICA
APPROVED: EDR
REVISION: A
SPACER
PART NUMBER | DESCRIPTION | STOCK SIZE | QTY
A | ALLUMINIUM | 11 X 8 X 2.15 MM | 10
B | A | A | 1

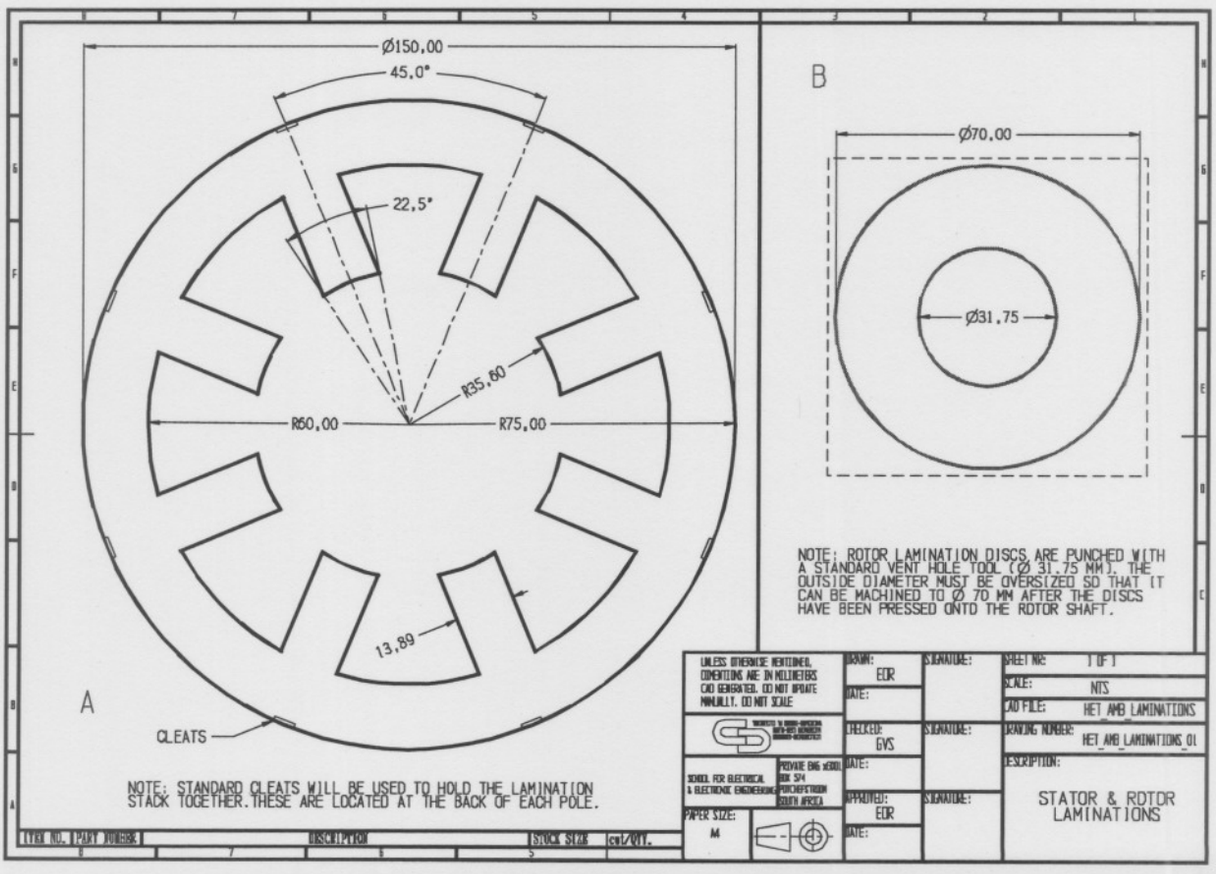
Ø150.00
45.0°
22.5°
R35.60
R50.00
R75.00
13.89
A
CLEATS
NOTE: STANDARD CLEATS WILL BE USED TO HOLD THE LAMINATION STACK TOGETHER. THESE ARE LOCATED AT THE BACK OF EACH POLE.
B
Ø70.00
Ø31.75
NOTE: ROTOR LAMINATION DISCS ARE PUNCHED WITH A STANDARD VENT HOLE TOOL (Ø 31.75 MM). THE OUTSIDE DIAMETER MUST BE OVERSIZED SO THAT IT CAN BE MACHINED TO Ø 70 MM AFTER THE DISCS HAVE BEEN PRESSED ONTO THE ROTOR SHAFT.
UNLESS OTHERWISE MENTIONED, DIMENTIONS ARE IN MILLIMETERS CAD GENERATED. DO NOT UPDATE MANUALLY. DO NOT SCALE
DRAWN: EDR
DATE:
SIGNATURE:
SHEET NR: 1 OF 1
SCALE: NTS
CAD FILE: HET AMB LAMINATIONS
CHECKED: GVS
DRAWING NUMBER: HET AMB LAMINATIONS 01
DESCRIPTION:
SCHOOL FOR ELECTRICAL & ELECTRONIC ENGINEERING
PRIVATE BAG X6001 BOX 394 POTCHEFSTROOM SOUTH AFRICA
APPROVED: EDR
PAPER SIZE: M
STATOR & ROTOR LAMINATIONS
ITEM NO. | PART NUMBER | DESCRIPTION | STOCK SIZE | QTY/QTY.

Appendix C: Power Amplifier Circuit Diagram

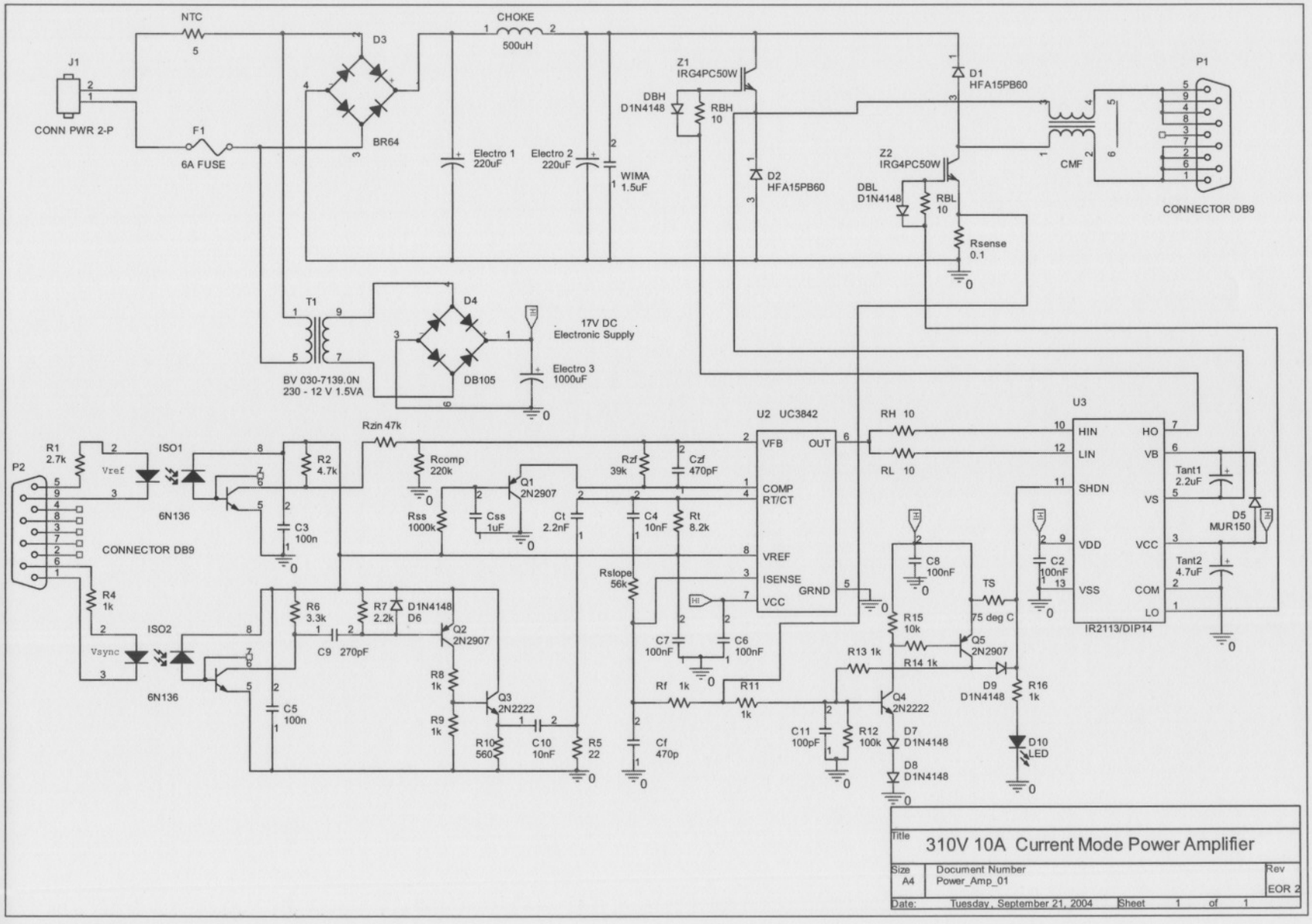

Appendix D: Photos

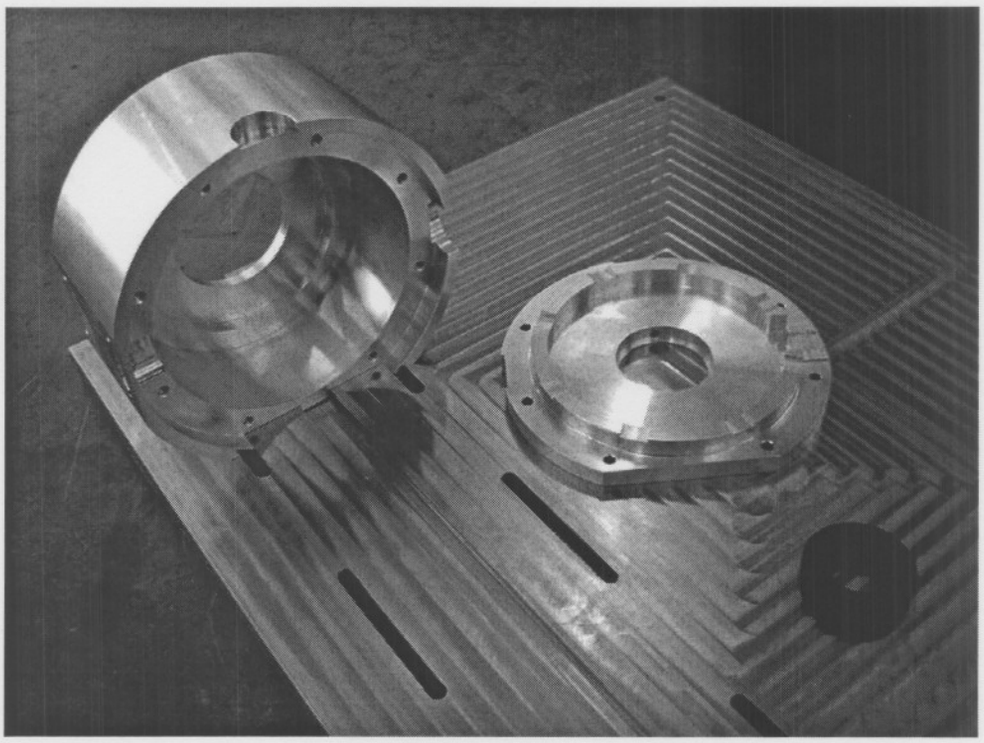

Figure D-1: Left stator housing, flange and backup bearing

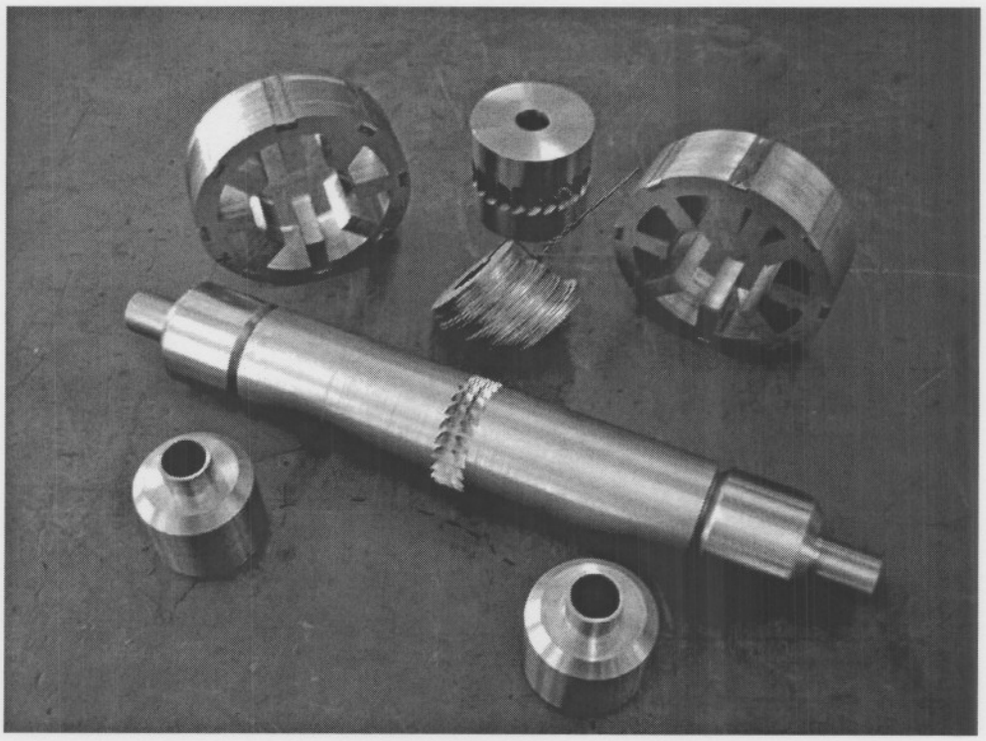

Figure D-2: Various magnetic circuit components

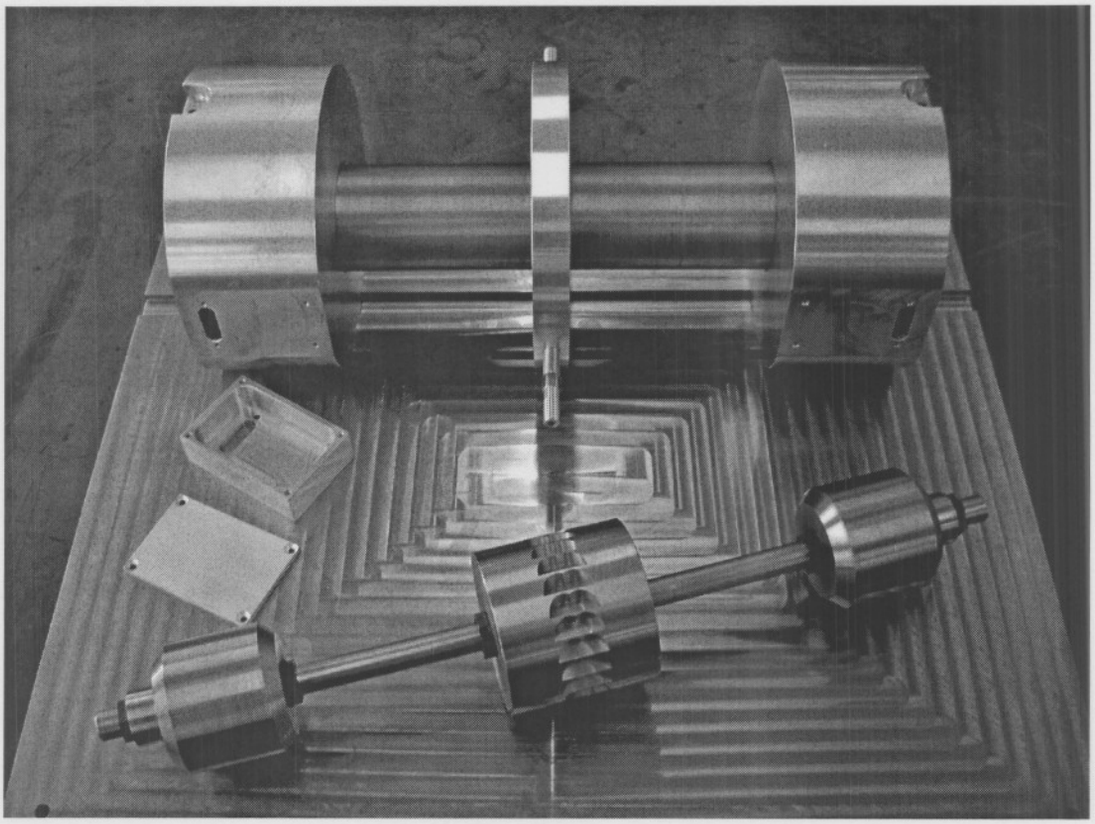

Figure D-3: Flexible rotor and rigid rotor in AMB stators

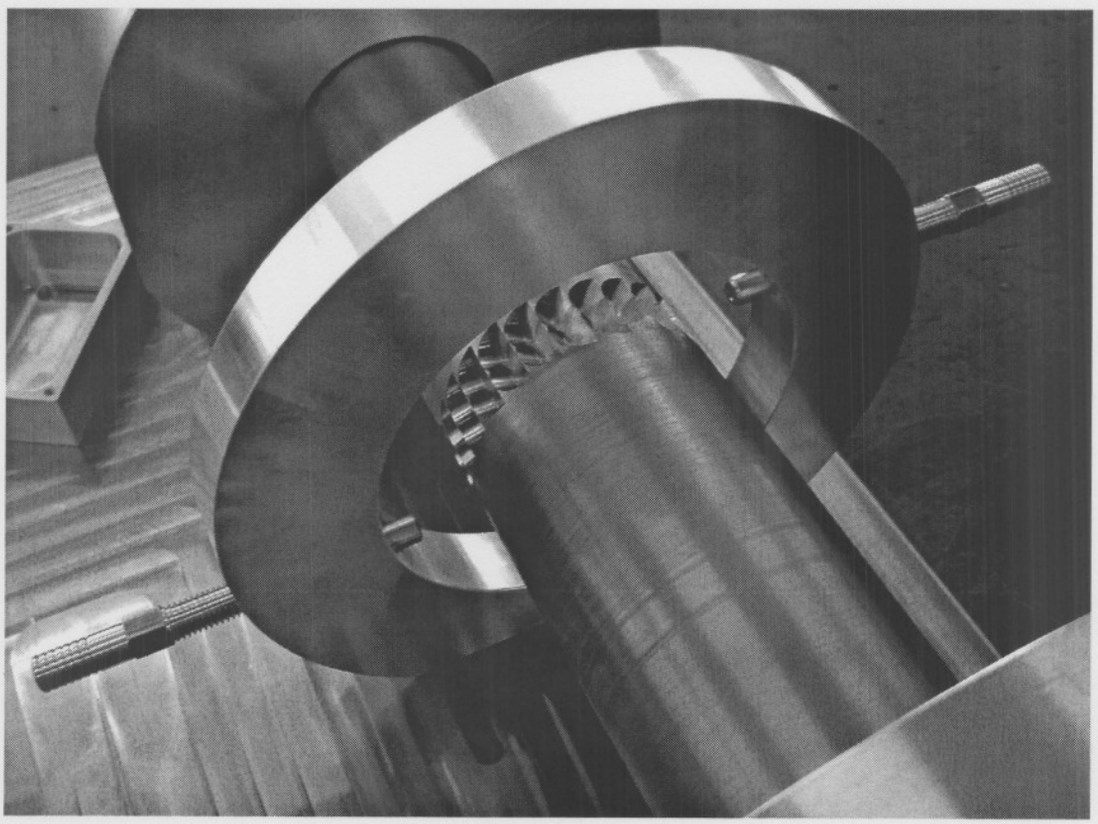

Figure D-4: Air turbine profile and nozzles

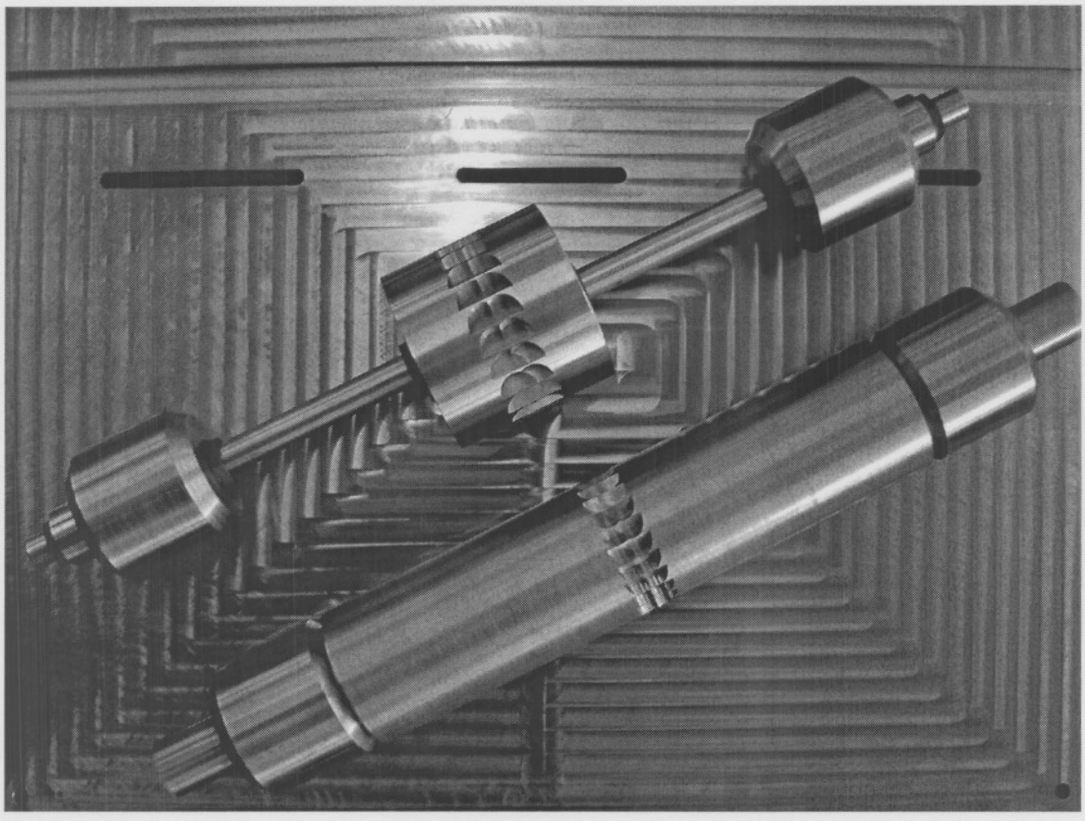

Figure D-5: Interchangeable flexible and rigid rotors

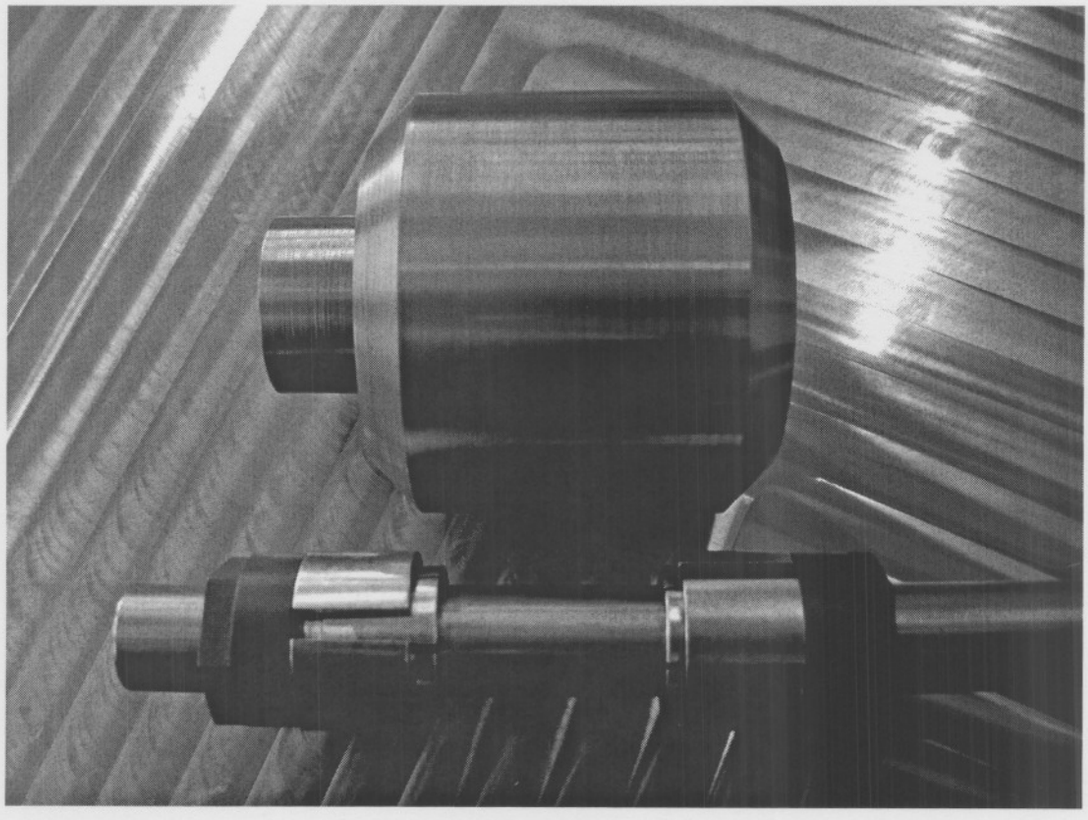

Figure D-6: Trantorque fasteners and flexible rotor journal

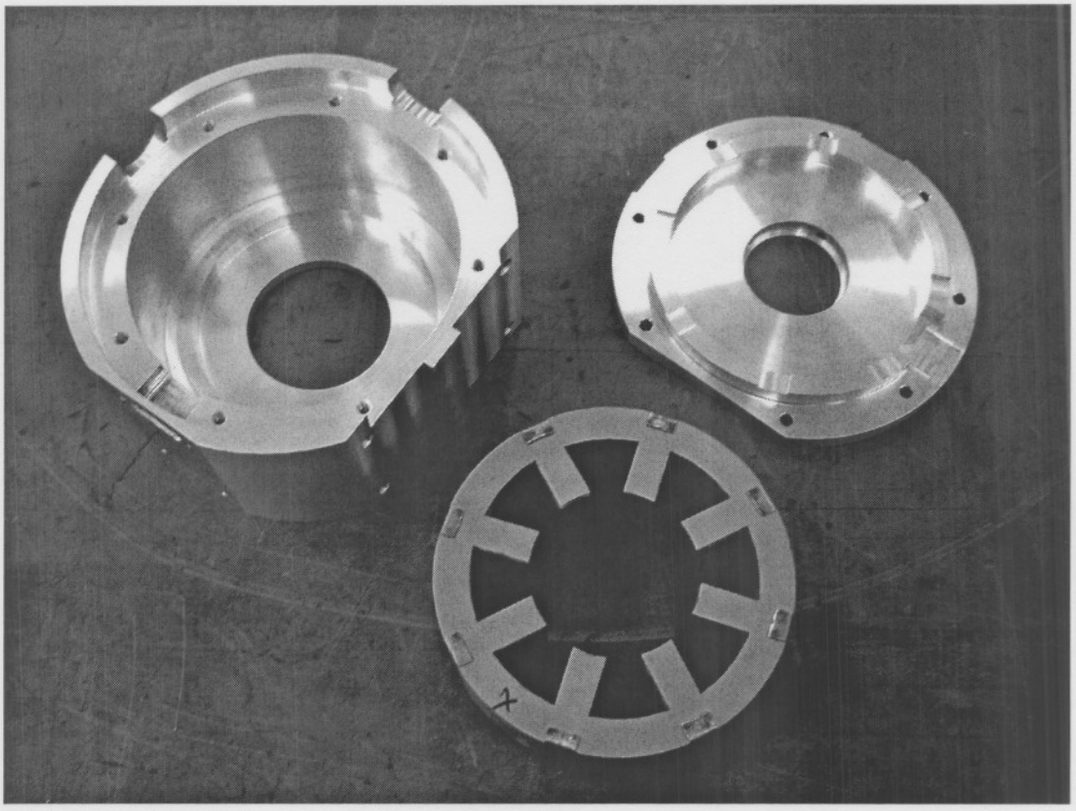

Figure D-7: Stator housing and magnetic circuit

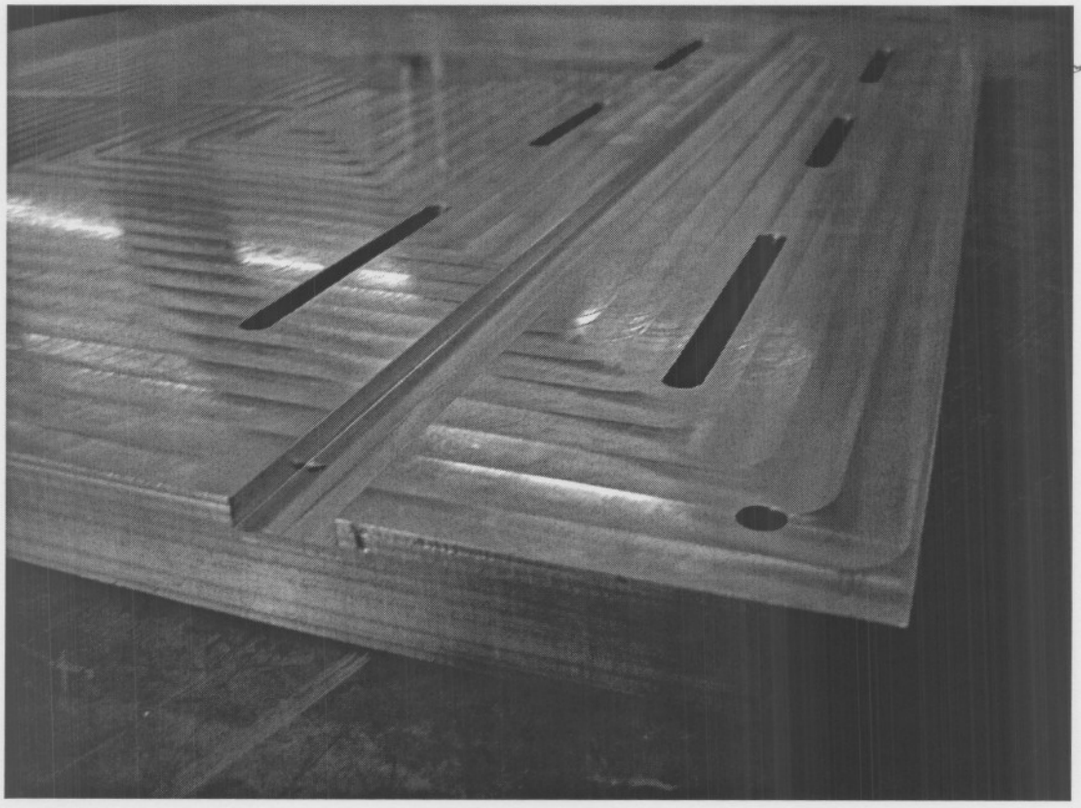

Figure D-8: Base plate with machined profiles

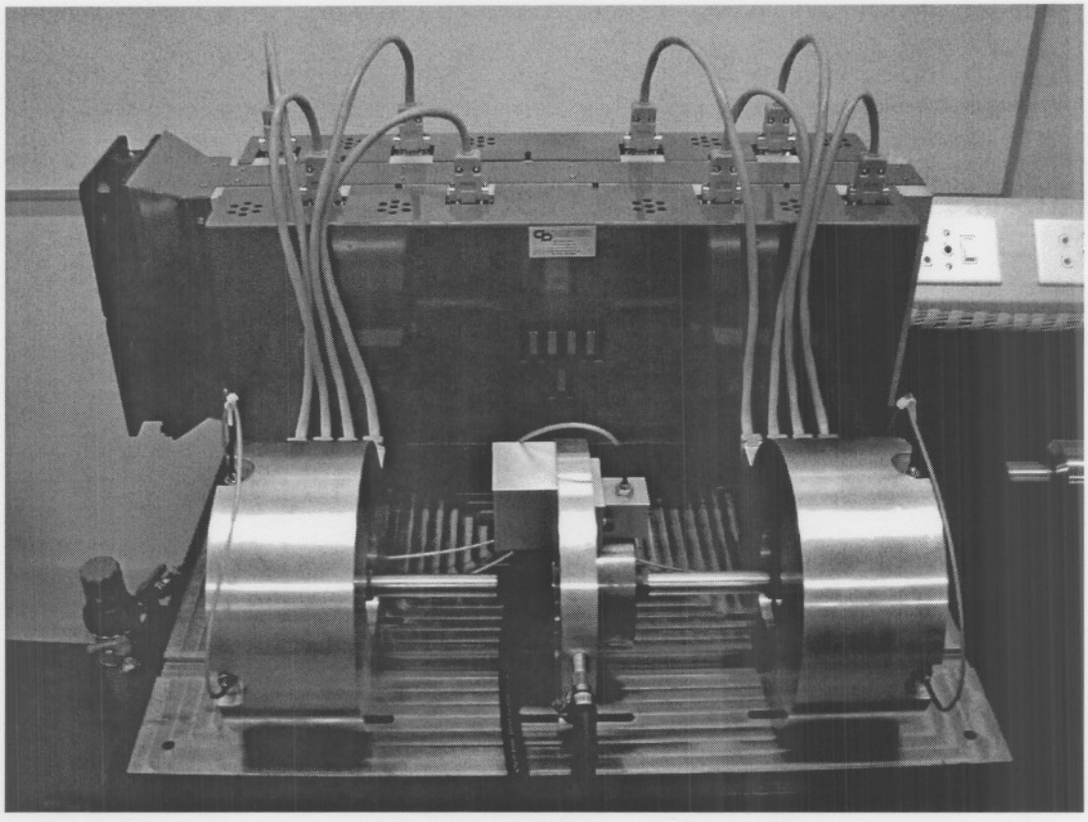

Figure D-9: Double radial flexible rotor model front view

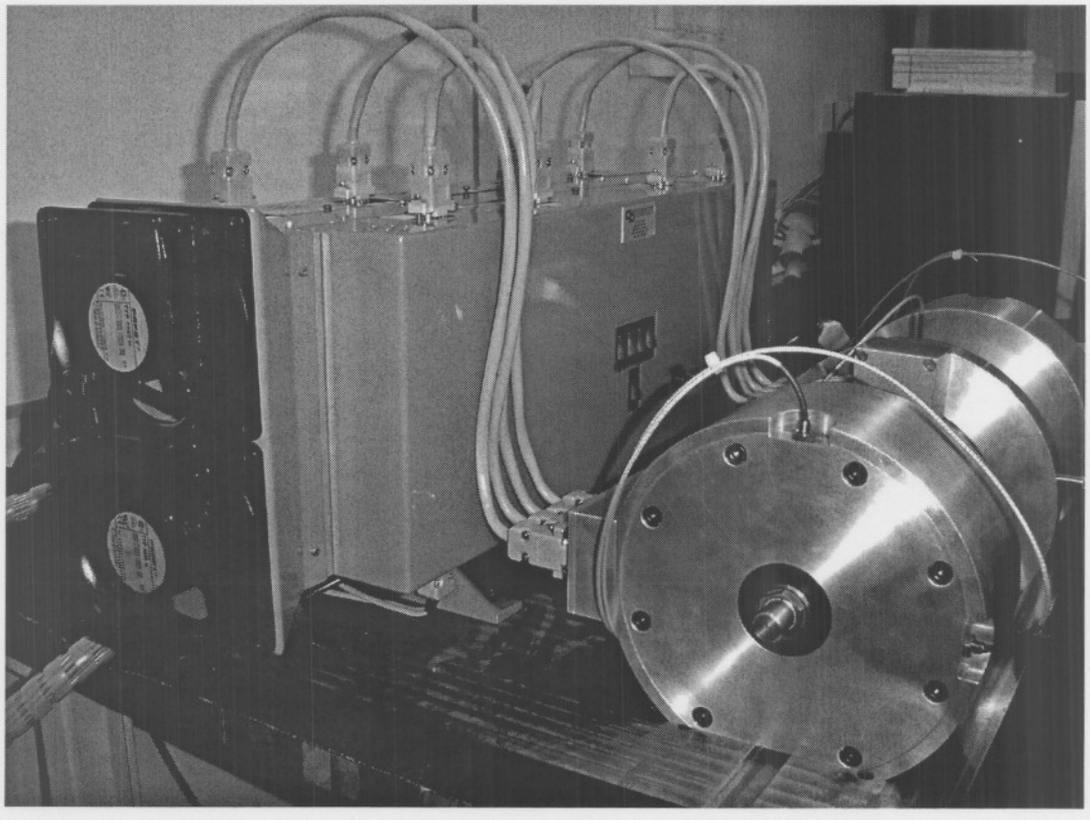

Figure D-10: Double radial flexible rotor model side view

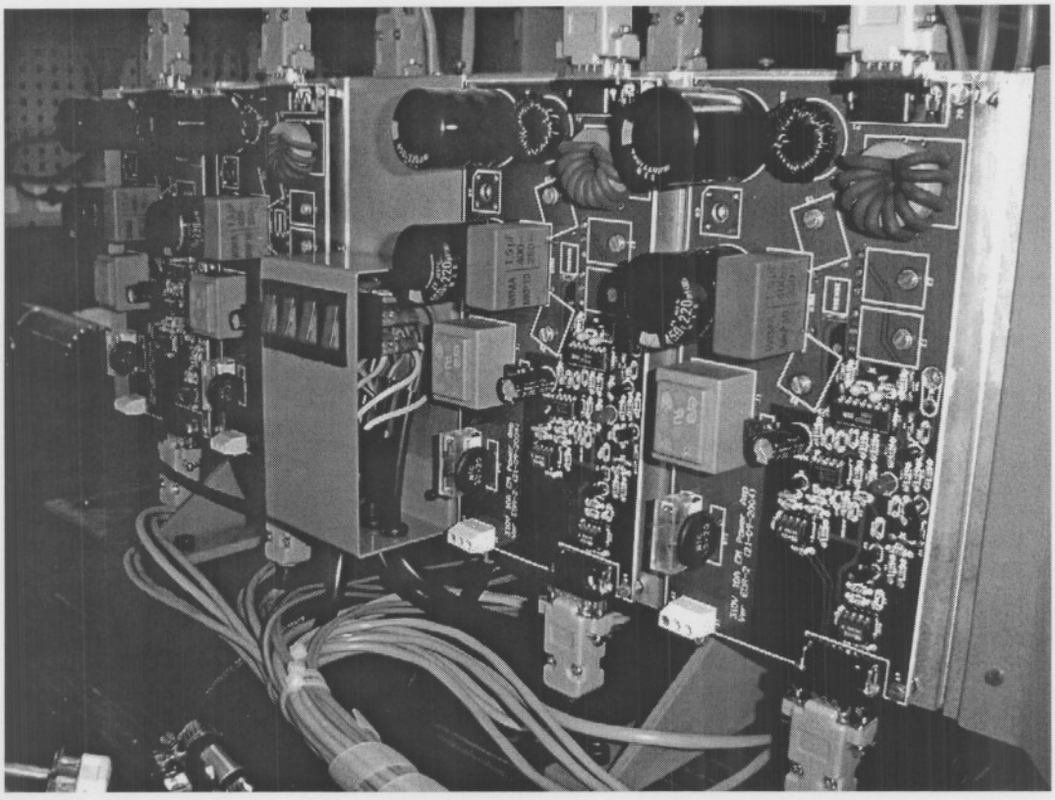

Figure D-11: Power amplifier heat sink layout

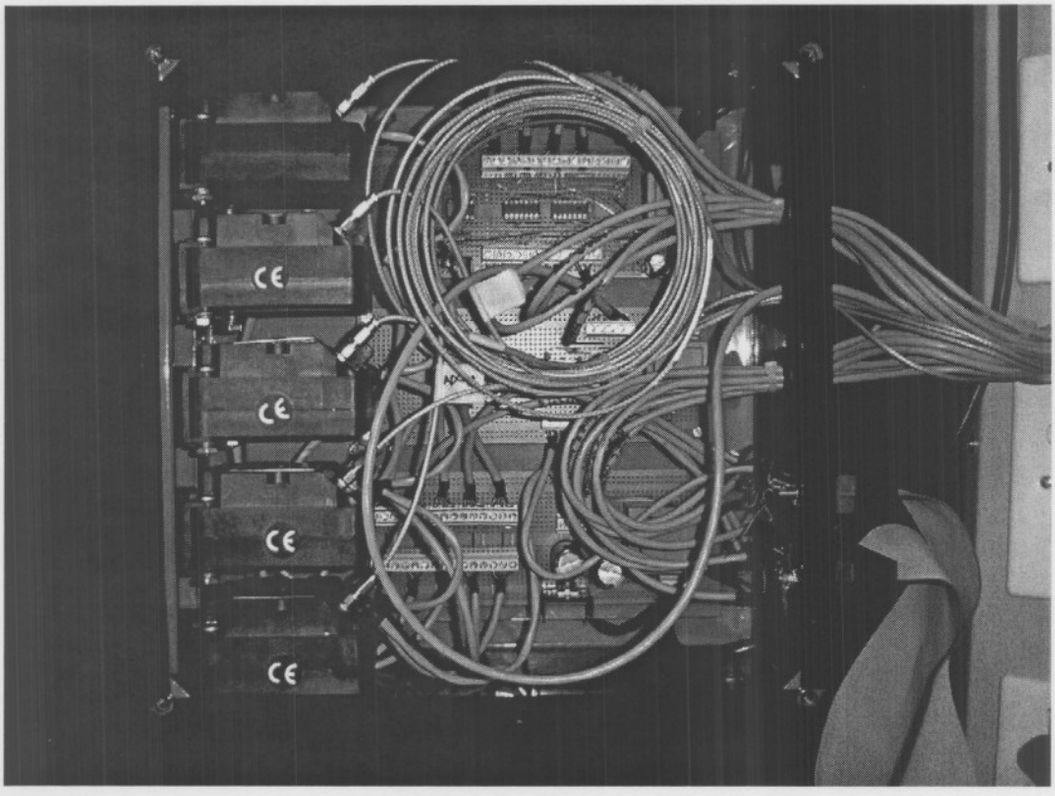

Figure D-12: Electrical interface

Appendix E: Data CD

REFERENCES

[1] A.P. George, "Introduction to the Pebble Bed Modular reactor (PBMR)," PBMR, Pretoria, Tech. Rep. 2001.

[2] M.C. Nieuwoudt and W Kriel, "PBMR operability summary," PBMR, Pretoria, Tech. Rep. Revision: 2D, 2001.

[3] Revolve Magnetic Bearings Inc. Magnetic bearings. [Online]. Available: http://www.revolve.com/ Technology/magbearings.html, [Date of access: February. 2003].

[4] M.E.F. Kasarda, "An Overview of Active Magnetic Bearing Technology and Applications," The Shock and Vibration Digest, vol. 32, No. 2, pp. 91-99, March 2000.

[5] dSPACE. Solutions for Control. [Online] available http://www.dspace.de/ww/en/ pub/home. htm [Date of access: March. 2004].

[6] G. Schweitzer, H. Bleuler, A. Traxler, "Active Magnetic Bearings: Basics, Properties and Applications of Active Magnetic Bearings", Authors Reprint, Zürich, 2003.

[7] M.S. Sarma, "Electric Machines Steady-State Theory and Dynamic Performance," 2nd ed., PSW Publishing Company, Boston, 1996, pp. 34-73.

[8] J.J. Cathey, "Electric Machines Analysis and Design Applying MATLAB®," International Edition, Mc Graw Hill, New York, 2001, pp.49-112.

[9] M. Zeisberger and W Gawalek. (1998). Losses in magnetic bearings. *Materials Science and Engineering.* No. B53, pp 193-197. Available: http:\\www.sciencedirect.com [Date of access: March 2003].

[10] R Hertzog, P. Bühler, *et al*. (1996, Sept). Unbalance compensation using generalized notch filters in the multivariable feedback of magnetic bearings. *IEEE Transactions on control systems technology: Special issue on magnetic bearing control.* Vol. 4, no.5, pp 580-585.

[11] K. Noami and T. Ito. (1996, Sept). μ Synthesis of flexible rotor-magnetic bearing systems. *IEEE Transactions on control systems technology: Special issue on magnetic bearing control.* Vol. 4, no.5, pp 503-511.

[12] F. Matsumura, T. Namerikawa, *et al*. (1996, Sept). Application of gain scheduled H infinity robust controllers to a magnetic bearing. *IEEE Transactions on control systems technology: Special issue on magnetic bearing control.* Vol. 4, no.5, pp484-492.

[13] P. Allaire, C.R. Knospe, *et al*, "Short course on magnetic bearings," Alexandria Virginia United States of America: University of Virginia 1997.

[14] John M. Vance, "Rotordynamics of Turbomachinery," WILEY, New York, 1988, pp. 116-170.

[15] P.E. Allaire, R.R. Humphrits and R.D. Kelm. (1986, June). Dynamics of a flexible rotor in magnetic bearings. ROMAC Report No. 245.

[16] M.E.F. Kaskarda and P.E. Allaire. (1997, Jan). The measurement and characterization of power losses in high speed magnetic bearings. ROMAC Report No. 407.

[17] D.C. Meeker and E.H. Maslen. (1997, May). Prediction of rotating losses in heteropolar radial magnetic bearings. ROMAC Report No. 414.

[18] M.E.F. Kasarda, P.E. Allaire, P.M. Norris, E.H. Maslen, and C. Mastrangelo. (1997, Aug). Comparison of Measured Rotor Power Losses in Homopolar and Hetropolar Magnetic Bearings. *Proceedings of MAG '97*. pp 323-333.

[19] Richard C. Dorf, Robert H. Bishop, "Modern Control Systems", Ninth Edition, Prentice Hall, New Jersey, 2001, pp. 36-47, pp. 227-233.

[20] Jai P. Agrawal, "Power electronic systems: theory and design," Prentice Hall, New Jersey, 2001, pp. 109-137.

[21] International Rectifier. (2003, May). HV Floating MOS-Gate Driver ICs. International Rectifier Application Note. [Online]. AN978-b, pp. 1-10. Available: http://www.irf.com

[22] J. Adams. (2003, May). Bootstrap component selection for control IC's. International Rectifier Design Tip. [Online]. DT 98-2a, pp. 1-4. Available: http://www.irf.com

[23] Unitrode. (2003, May). Modeling, analysis and compensation of the current-mode converter. Unitrode Application Note. [Online]. U-97, pp. 3-43 - 3-48. Available: http://www.ti.com

[24] ISO TC108/SC2/WG7, "Active magnetic bearing – Evaluation of stability margin," ISO CD148393-3, Oct. 7, 2003.

[25] J.D. Nel, "The development of a radial active magnetic bearing," Dissertation M.Eng, North-West University, Potchefstroom Campus, 2004